



**UNIVERSITY  
OF TRENTO - Italy**

**DEPARTMENT OF INDUSTRIAL ENGINEERING**

---

Ph.D. School in Materials, Mechatronics and Systems Engineering

---

---

## **Development of Small-Pitch, Thin 3D Sensors for Pixel Detector Upgrades at HL-LHC**

**3D SI SENSOR OF EXTREME RADIATION HARDNESS**

**D M S Sultan**

**Advisor:**

**Prof. Gian-Franco Dalla Betta  
University of Trento, Italy**

---

---

**June 2017**

# Development of small-pitch, thin 3D sensors for pixel detector upgrades at HL-LHC

## 3D Si SENSOR OF EXTREME RADIATION HARDNESS

D M S Sultan

E-mail: [dms.sultan@unitn.it](mailto:dms.sultan@unitn.it)

### Approved by:

Prof. Gian Franco Dalla Betta, Advisor  
Department of Industrial Engineering  
*University of Trento, Italy.*

### Ph.D. Commission:

Prof. Cinzia Da Via,  
School of Physics and Astronomy  
*University of Manchester, UK.*

Dr. Ulrich Parzefall,  
Institute of Physics,  
*Albert Ludwig University of Freiburg,  
Germany.*

University of Trento,  
Department of Industrial Engineering

June 2017

**University of Trento – Department of Industrial Engineering**

**Doctoral Thesis**

**June – 2017**

**Published in Trento (Italy) – by University of Trento**

**ISBN: - - - - -**

## *Acknowledgements*

I have been privileged for having the opportunity to work with Prof. Gian-Franco Dalla Betta, an exemplary person of work ethics, and a wonderful mentor who introduced me to sensor technology of extreme radiation hardness and led growing with it. I would like to share my sincere thanks to Dr. Roberto Mendicino, Prof. Lucio Pancheri, members of Electronics Laboratory, UniTN for sharing their precious technical experiences. Nevertheless, all wonderful colleagues of Department of Industrial Engineering and Administration, UniTN are receiving thanks for remaining the inspiring figures throughout this exciting journey.

The entire team of FBK foundry, Dr. Maurizio Boscardin, Dr. Sabina Ronchin, Dr. Stefano Girardi are receiving my special gratitude for their sincere and unfailing supports. I am particularly grateful to Dr. Nicola Zorzi, who has always been a step ahead in sharing his experienced opinions in making the critical investigations.

I would like to recall Dr. Joern Lange, IFAE, Spain, Dr. Hideyuki Oide, Dr. Claudia Gemme, INFN-Genova, Italy for being the wonderful colleagues at test-beam campaigns. Nevertheless, I am sharing my gratitude here to the people of University of Freiburg, Germany, who shared their plausible input during my visit. Nevertheless, all fascinating people in Pixel-Group shall be in my remembrance who has been so friendly during my internship at CERN.

Finally, I am thanking my parents, who have made me believing, endeavours are always paid off. My thesis dissertation is dedicated to them.

## *Abstract*

3D Si radiation sensors came along with extreme radiation hard properties, primarily owing to the geometrical advantages over planar sensors where electrodes are formed penetrating through the active substrate volume. Among them: reduction of the inter-electrode distance, lower depletion voltage requirement, inter-columnar high electric field distribution, lower trapping probability, faster charge collection capability, lower power dissipation, and lower inter-pitch charge sharing. Since several years, FBK has developed 3D sensors with a double-sided technology, that have also been installed in the ATLAS Insertable B-Layer at LHC. However, the future High-Luminosity LHC (HL-LHC) upgrades, aimed to be operational by 2024, impose a complete swap of current 3D detectors with more radiation hard sensor design, able to withstand very large particle fluences up to  $2 \times 10^{16} \text{ cm}^{-2}$  1-MeV equivalent neutrons. The extreme luminosity conditions and related issues in occupancy and radiation hardness lead to very dense pixel granularity ( $50 \times 50$  or  $25 \times 100 \mu\text{m}^2$ ), thinner active region ( $\sim 100 \mu\text{m}$ ), narrower columnar electrodes ( $\sim 5 \mu\text{m}$  diameter) with reduced inter-electrode spacing ( $\sim 30 \mu\text{m}$ ), and very slim edges ( $\sim 100 \mu\text{m}$ ) into the 3D pixel sensor design. This thesis includes the development of this new generation of small-pitch and thin 3D radiation sensors aimed at the foreseen Inner Tracker (ITk) upgrades at HL-LHC.

**KEYWORDS:** 3D Si Sensor, HL-LHC, Small-pitch 3D Pixels, Radiation hard sensor.

## ***List of Publication(s) on Ph.D. Thesis***

- [1] A. Bagolini, M. Boscardin, P. Conci, M. Crivellari, G. Giacomini, F. Mattedi, C. Piemonte, S. Ronchin, N. Zorzi, M.A. Benkechke, G.-F. Dalla Betta, R. Mendicino, L. Pancheri, M. Povoli, **D M S Sultan**, “*Micromachined Silicon Radiation Sensors - Part 1: Design and Experimental Characterization*”, XVIII AISEM Annual Conference Record, 2015, (DOI: 10.1109/AISEM.2015.7066825).
- [2] A. Bagolini, M. Boscardin, P. Conci, M. Crivellari, G. Giacomini, F. Mattedi, C. Piemonte, S. Ronchin, N. Zorzi, M. A. Benkechke, G. -F. Dalla Betta, R. Mendicino, L. Pancheri, M. Povoli, **D M S Sultan**, “*Micromachined silicon radiation sensors - Part 2: Fabrication technologies*”, XVIII AISEM Annual Conference Record, 2015, (DOI: 10.1109/AISEM.2015.7066822).
- [3] **D M S Sultan**, R. Mendicino, M. Boscardin, S. Ronchin, N. Zorzi and G.-F. Dalla Betta, “*Characterization of the first double-sided 3D radiation sensors fabricated at FBK on 6-inch silicon wafers*”, Journal of Instrumentation, 2015, 10(C12009).
- [4] Gian-Franco Dalla Betta, Maurizio Boscardin, Roberto Mendicino, Sabina Ronchin, **D M S Sultan**, and Nicola Zorzi, “*Development of new 3D pixel sensors for phase 2 upgrades at LHC*”, IEEE Nuclear Science Symposium and Medical Imaging Conference (NSS/MIC), Conference Record, 2015, (DOI: 10.1109/NSSMIC.2015.7581946).
- [5] G.-F. Dalla Betta, N. Ayllon, M. Boscardin, M. Hoferkamp, S. Mattiazzo, H. McDuff, R. Mendicino, M. Povoli, S. Seidel, **D M S Sultan**, “*Investigation of Leakage Current and Breakdown Voltage in Irradiated Double-Sided 3D Sensors*”, Journal of Instrumentation, 2016, 11 (P09006).
- [6] G.-F. Dalla Betta, M. Boscardin, M. Bombend, M. Brianzie, G. Calderini, G. Darbo, R. Dell’Orso, A. Gaudiello, G. Giacomini, R. Mendicino, M. Meschini, A. Messineo, S. Ronchin, **D M S Sultan**, and N. Zorzi, “*The INFN-FBK “Phase-2” R&D program*”, Nuclear Instruments and Methods in Physics Research A, 2016, 824 (388–391).

- [7] G.-F. Dalla Betta, M. Boscardin, G. Darbo, R. Mendicino, M. Meschini, A. Messineo, S. Ronchin, **D M S Sultan**, and N. Zorzi, “*Development of a New Generation of 3D Pixel Sensors for HL-LHC*”, Nuclear Instruments and Methods in Physics Research A, 2016, 824 (386–387).
- [8] **D M S Sultan**, R. Mendicino, M. Boscardin, S. Ronchin, N. Zorzi and G.-F. Dalla Betta, “*First Production of New Thin 3D Sensors for HL-LHC at FBK*”, Journal of Instrumentation, 2017, 12(C01022).
- [9] **D M S Sultan**, et. al., “*Development of small-pitch, thin 3D sensors for pixel detector upgrades at HL-LHC*”, (in preparation)

## ***List of Presentation(s) on Conferences/Workshops***

- [2] **D M S Sultan**, et al., “*Investigation of the Electrical Characteristics of DoubleSided 3D Sensors after Proton and Neutron Irradiation up to HL-LHC Fluencies*”, 10<sup>th</sup> ‘Trento’ Workshop on Advanced Silicon Radiation Detectors (3D and p-type), Trento, Italy, 2015, (DOI: 10.13140/RG.2.1.2892.5605).
- [2] **D M S Sultan**, et al., “*Radiation hardness study on double sided 3D sensors after proton and neutron irradiation up to HL-LHC Fluencies*”, RADFAC, Legnaro, Italy, 2015, (DOI: 10.13140/RG.2.1.3941.1360).
- [3] **D M S Sultan**, et al., “*Characterization of the First Double-Sided 3D Radiation Sensors Fabricated at FBK on 6-inch Silicon Wafers*”, 17<sup>th</sup> International Workshop on Radiation Imaging Detectors (iWoRiD2015), DESY, Hamburg, Germany, 2015, (DOI: 10.13140/RG.2.2.17930.47041).
- [4] **D M S Sultan**, et al., “*Thin 3D Silicon Radiation Sensors for HL-LHC*”, 4<sup>th</sup> EIROforum School of Instrumentation, Munich, Germany, 2015, (DOI: 10.13140/RG.2.2.12722.20163).
- [5] **D M S Sultan**, et al., “*Initial results from new thin 3D Sensors for HL-LHC*”, 18<sup>th</sup> International Workshop on Radiation Imaging Detectors (iWoRiD2016), Barcelona, Spain, 2016, (DOI: 10.13140/RG.2.1.2592.9208).

## ***List of Publication(s) on associate Ph.D. activities***

- [1] F. Benetti, M. Buccella, A. Caciagli, N. Cozza, F. Deirmina, **D M S Sultan**, G. Giusti, E. Schneider, S. Tondini, “*Identification of Colored-masterbatch Process-parameter with Greater Influence on Pigment Dispersion and Color Perception*”, Industrial Problem Solving with Physics, Trento, Italy, 2014, (DOI: 10.13140/RG.2.1.1658.0962).
- [2] B. Marcello, T. Karola, A. L. Rosa, H. Oide, M. Antinio, A. Rozanov, N. S. Dann, M. Rimoldi, D. Ferrere, **D M S Sultan**, “*Observation of radiation induced effects in the ATLAS Insertable B-Layer readout chip*”, CERN Technical Note in preparation, 2017, (Available: <https://cds.cern.ch/record/2221954>).
- [3] **D M S Sultan**, et. al., “*Calibration and Commissioning the Dose Rate of X-RAD iR160 for Semiconductor Devices*”, (in preparation).

# *Table of contents*

## **Chapter I**

<b>Introduction.....</b>	<b>001</b>
--------------------------	------------

## **Chapter II**

<b>3D Silicon Radiation Detectors: State of the Art &amp; Applications ....</b>	<b>004</b>
---	------------

<b>2.1. Silicon Radiation Detectors .....</b>	<b>004</b>
---	------------

2.1.1. Semiconductor and Dopants.....	005
---------------------------------------	-----

2.1.2. p-n Diodes and relevant concepts for Silicon Detectors .....	007
---	-----

2.1.3. Silicon as a Detector Material .....	009
---	-----

2.1.4. Radiation Damage in Silicon .....	011
--	-----

2.1.5. Remedy to Radiation damage.....	018
--	-----

<b>2.2. 3D Silicon Detectors .....</b>	<b>021</b>
--	------------

2.2.1. Technological Simulation .....	023
---------------------------------------	-----

2.2.2. Evolution of 3D Si Sensors .....	025
---	-----

2.2.3. Experimental results.....	029
----------------------------------	-----

2.2.4. State of Art 3D-DDTC IBL Production .....	036
--	-----

2.2.5. Applications.....	042
--------------------------	-----

## **Chapter III**

<b>High Energy Physics at CERN .....</b>	<b>047</b>
--	------------

<b>3.1. Large Hadron Collider .....</b>	<b>047</b>
---	------------

<b>3.2. Upgrades of LHC.....</b>	<b>049</b>
----------------------------------	------------

<b>3.3. ATLAS Experiment .....</b>	<b>050</b>
------------------------------------	------------

3.3.1. Components of ATLAS Particle Detector .....	051
--	-----

3.3.2. ATLAS Pixel Detector and Readouts .....	056
--	-----

3.3.3. Semi-Conductor Tracker (SCT) .....	069
---	-----

<b>3.4. CMS Experiment .....</b>	<b>071</b>
----------------------------------	------------

3.4.1. Components of CMS Particle Detector .....	072
--	-----

3.4.2. CMS Pixel Detector and Readouts .....	072
--	-----

3.4.3. CMS Si Strip Tracker .....	075
-----------------------------------	-----

## Chapter IV

<b>Radiation Hardness of FBK 4-inch 3D DDTC Si Sensors .....</b>	<b>077</b>
<b>4.1. Two Prime Double-Sided 3D Sensors.....</b>	<b>079</b>
<b>4.2. Irradiation Campaigns .....</b>	<b>082</b>
<b>4.3. Experimental Setups .....</b>	<b>084</b>
<b>4.4. Comparative Experimental Studies.....</b>	<b>087</b>
4.4.1. Before Irradiation.....	087
4.4.2. X-ray and $\gamma$ -ray Irradiation .....	088
4.4.3. Neutron Irradiation .....	090
4.4.4. Proton Irradiation.....	096
4.4.5. Annealing Campaign.....	100
<b>4.5. Summary Insight.....</b>	<b>101</b>

## Chapter V

<b>FBK 1<sup>st</sup> 6-inch Pilot Production of Modified 3D DDTC Si Sensor ...</b>	<b>108</b>
<b>5.1. Fabrication.....</b>	<b>108</b>
5.1.1. Process Design .....	109
5.1.2. Process Characterization .....	110
<b>5.2. Wafer Layout .....</b>	<b>112</b>
<b>5.3. Electrical Characterization.....</b>	<b>113</b>
5.3.1. Before Irradiation.....	113
5.3.2. After $\gamma$ -ray Irradiation .....	117

## Chapter VI

<b>New Small-Pitch and Thin 3D Si Sensors for HL-LHC .....</b>	<b>120</b>
<b>6.1. Fabrication.....</b>	<b>121</b>
6.1.1. Process Design .....	121
6.1.2. Process Characterization .....	124
<b>6.2. Wafer Layout .....</b>	<b>125</b>
<b>6.3. Simulation.....</b>	<b>126</b>
6.3.1. Simulation for Non-irradiated devices .....	127
6.3.2. Simulation for Irradiated devices.....	130

<b>6.4. Experimental Results .....</b>	<b>133</b>
6.4.1. Before Irradiation.....	133
6.4.2. After Irradiation.....	144
<b>6.5. 2<sup>nd</sup> Production of Small-pitch, Thin 3D Radiation Sensors at FBK .....</b>	<b>159</b>

## **Chapter VII**

<b>Conclusions .....</b>	<b>166</b>
<b>References .....</b>	<b>171</b>

# Chapter I

## Introduction

The ATLAS experiment is vastly dependent on the performance of silicon pixel detectors in order to identify and determine the paths of particles that are produced in the LHC proton-proton collisions. The rate of the particles and the radiation levels produced put heavy constraints on the sensor and front-end electronics that are part of the pixel system. The foreseen upgrades of High Luminosity Large Hadron Collider (HL-LHC) by 2024 will come with integration of new radiation hard technologies to be applied in the next generations of tracking devices that will be required to withstand extremely high radiation doses. High Energy Physics (HEP) experiments at the LHC are expecting to reach five to ten times the nominal instantaneous luminosity of the current LHC and an integrated luminosity up to  $3000 \text{ fb}^{-1}$ . To maintain the detector performance new pixel technologies have to be developed. In this sense, one of the most promising candidates is silicon 3D detector technology, that realizes columnar electrodes penetrating vertically into the silicon substrate and thus decoupling the active volume from the inter-electrode distance. 3D detectors were first proposed by S. Parker and collaborators in the mid '90s as a noble engineered geometry intended to mitigate the effects of radiation damage in silicon.

Recently, 3D sensors have emerged as a viable solution for the innermost layers of the upgraded pixel detector. The 3D technology is already used in the current ATLAS detector. In May 2014, a new innermost layer of the ATLAS Pixel detector called Insertable B-layer (IBL) was installed. Planar and 3D silicon sensor technologies were proven to fulfil the radiation requirements of the IBL, maintaining high efficiency ( $> 97\%$ ) after a fluence of  $5 \times 10^{15} \text{ n}_{\text{eq}}/\text{cm}^2$  (1 MeV neutron equivalent) [78]. Owing to several outstanding features over planar sensors, like, the comparatively lower bias voltage, the faster charge collection and the lower trapping probability, 3D sensors are still attracting a growing interest for future HEP applications. It is also true that the fabrication of 3D Sensors still holds more complex and expensive in comparison to the planar one. Despite these limitations, in the ATLAS Inner Tracker (ITk) upgrade of forthcoming HL-LHC, 3D Sensors shall hold a significant portion of all technologies because of their lower power dissipation and enhanced radiation hardness. The IBL generation of 3D sensors will be completely swapped with the newer design of 3D to cope with the more demanding radiation conditions and higher occupancy. The high particle densities impose the need for smaller pixel sizes, which also offer increased position resolution. Within the international framework of the ATLAS ITk project, and in tight contact with the CERN RD53 Collaboration, which is developing the new read-out chips in 65 nm CMOS technology, FBK-INFN-Italy, CNM-IMB-Barcelona, and

SINTEF-Univ. Oslo-Norway are the three 3D sensor design groups working in parallel to develop the suitable designs including the maximum possible enhancement. Since the beginning, SINTEF-Norway is engaged in producing 3D sensors using single-sided process, where both junction and ohmic columns are passing through, but their yield has not yet been satisfactory. CNM-IMB-Barcelona instead follows the double-sided process to form both non-passing through junction and ohmic columns. FBK-INFN-Italy adopted as well the double-sided process to accomplish both junction and ohmic passing through column design for the ATLAS IBL. However, the double-sided fabrication approach at FBK is not favoured for the foreseen upgrades at HL-HLC, mainly because of the thin active layers involved. A modified, single-sided design with handle wafer has been considered to this purpose. Keeping in mind all design constraints suggested from RD53A collaboration, i.e., the small-pitch sensor ( $50 \times 50 \mu\text{m}^2$  or  $25 \times 100 \mu\text{m}^2$ ) and thin active substrate ( $\sim 150 \mu\text{m}$ ), the first ever thin 3D production using single-sided process was released early in 2016. This thesis comprises all the efforts made in the design, fabrication and characterization of these newer small-pitch thin 3D detectors produced at FBK.

In chapter 2, there has been an extensive summary on theoretical aspects of 3D Si radiation sensors, and their evolution in the perspective of being deployed in LHC, state of art design fabricated at FBK and their comparative performance among other foundries. A brief note on other possible applications of these 3D sensors is also attached in this chapter.

In chapter 3, the main application of this thesis work to High Energy Physics Experiments has been elaborated. To understand better the scope of newer design, it is worth to look back at the entire experimentations possible at CERN. The technological aspects of all relevant state of art readout electronics (FE-I4, PSI46 etc.) as well the forthcoming RD53A readout electronics have been enclosed within this section.

Chapter 4 comprises in-depth comparative electrical investigations made between the state-of-art IBL sensors and modified junction column non-passing through technology, fabricated at FBK. This study has highlighted the limitations present in IBL pixel sensors and the corresponding enhancement made in a modified double-sided process.

In chapter 5, a brief report has been made on the first 6 inch pilot production of double-sided modified junction column non-passing through technology. Critical investigations from layout design and process involved within this batch enlightened a greater possible improvement for the first small-pitch single sided 3D Production.

In chapter 6, a comprehensive discussion of all the efforts made in design, fabrication and characterization of these newer small-pitch thin 3D detectors produced

at FBK has been addressed. A brief section on TCAD simulation and the corresponding agreement with experimental results from FBK sensors of the first thin 3D production, from both the electrical and the functional points of view have been reported. At the end a brief discussion on the design aspects that were improved and aggregated already in the next layout as per the expertise earned so far.

Conclusions follow in chapter 7.

## Chapter II

### 3D Silicon Radiation Detectors: State of the Art & Applications

In various scientific, medical and industrial applications, silicon radiation detectors have been extensively used for many years [1,2]. One of the prime advantages of this technology is to produce electron-hole pairs with relatively low mean ionization energy (3.6 eV) than any gas based ionization ( $\sim 20\text{eV}$ ), thus providing better energy resolution.

A major breakthrough in Si detector technology came in the early 80s owing to J. Kemmer, who pioneered the use of the planar fabrication process, derived from microelectronics [3]. By using the passivation properties of silicon dioxide and keeping the thermal budget to a minimum, allowing the fine pitch segmentation of electrode and very low leakage currents within the implanted detectors, Si-based device has already been possible to produce in large scale. The evaluation on silicon detector technologies have been continuously advancing ever since then. More complex and reliable detectors could be obtained, featuring outstanding performance in terms of energy, timing and/or position resolution, long-term stability and radiation tolerance.

In the recent history of radiation sensors, another milestone is represented by the introduction of detectors with three-dimensional electrodes (3D detectors), which were first proposed by S. Parker and collaborators in 1997 [4]. Differently from planar detectors, where the electrodes are confined to the wafer surfaces, in 3D detectors electrodes penetrate entirely through the substrate (perpendicularly to the surface). This architecture offers a number of substantial advantages with respect to the planar one, making 3D detectors ideal candidates for some critical applications, especially in High Energy Physics (HEP). However, this comes at the expense of a more complicated and expensive fabrication process, which combines microelectronic and MEMS (Micro-Electro-Mechanical-Systems) technologies.

A comprehensive and up-to-date review of 3D detectors is presented in this chapter, covering all relevant aspects: relevant background theory, device description and simulation, fabrication technologies and design issues, selected experimental results from different 3D sensor generations until the current state of the art, and application fields.

#### 2.1 *Silicon Radiation Detectors*

Since early 1970s semiconductor detectors became the frontier in particle detection. Silicon (Si) was chosen as the best studied semiconductor and one of the cheapest and most abundant materials on earth. The progressing maturity in

processing technologies over the last decades, made Si as one of the prime candidates for complex structures, especially 3D technologies, to produce the extreme radiation hard detector. The understanding of semiconductor physics is well established and discussed in several books. A more complementary reference for the understanding of the usage of semiconductor materials and relative electronics should be found from literature available from the wider community [5,6,7].

### 2.1.1 Semiconductor and Dopants

Semiconductors have a small band gap. For silicon at room temperature, it is 1.12 eV, which means that electrons can be lifted into the conduction band by thermal excitation. A semiconductor is called intrinsic if contains a negligible amount of impurity atoms in its crystal. In this case, the probability of electrons occupying the conduction band is given by the Fermi-Dirac equation,  $F(E)$ :

$$F(E) = \frac{1}{1 + e^{\frac{(E-E_F)}{KT}}} \approx e^{-\frac{(E-E_F)}{KT}} \quad (2.1)$$

where  $E_F$  is the energy of Fermi level,  $T$  is the absolute temperature in °K, and  $k$  is the Boltzmann constant. At the Fermi energy, the occupation probability is exactly 0.5. The number of free electrons per unit volume  $n$  in a semiconductor can be calculated by integrating the product  $N(E)F(E)$  over the energy  $dE$ .  $N(E)$  is the density and the interval ranges from the bottom to the top of the conduction band. Solving the equation of probability density function [5] with respect to the Fermi-Dirac equation,  $F(E)$ , the concentration of free carriers (electron,  $n$  and hole,  $p$ ) can be retrieved from the following equations:

$$n = N_C e^{-\frac{(E-E_F)}{KT}} \quad (2.2),$$

$$p = N_V e^{-\frac{(E-E_F)}{KT}} \quad (2.3).$$

Here,  $N_C$  and  $N_V$  are the notation of effective density states of conduction and valance band. In the intrinsic semiconductor, the concentration of electrons and holes remains equal ( $n = p = n_i$ ). This relationship changes for doped materials. However, the product of both concentrations at thermal equilibrium is independent of the Fermi level and so 'np' is also independent of the doping concentration. For silicon,  $n_i$  has a value of  $9.65 \times 10^9 \text{ cm}^{-3}$  at room temperature [8].

$$n_i^2 = np = N_C N_V e^{-\frac{E_g}{KT}} \quad (2.4).$$

The properties of a semiconductor can be changed by inserting impurities (extrinsic materials) into its lattice. An Atom with additional valence electron than the semiconductor material is called donor (n-doped). The energy level of donors is close to the conduction band. Due to small ionization energies for donors, the excessive electrons are lifted into the conduction band which leads to a high concentration of free

electrons in the semiconductor. In silicon, it requires an energy of approximately 0.03 eV to be ionized. Phosphorus, Arsenic, Antimony of group V of the periodic table are normally used as donors.

Acceptor atom instead have one valence electron less than the semiconductor and their energy level is close to the level of the valence band. Thus, electrons are attracted by the impurities and consequently, a hole is produced in the valence band. The holes are treated effectively as particle with a positive charge. Holes keep mobility at reasonable temperatures and thus can act as charge carriers. Boron of group III of the periodic is widely used as an acceptor. Normally, thermal energy is enough to ionize all donors and acceptors in doped silicon detectors in silicon sensors. Thus, the number of majority free charge carriers is  $n = N_D$  in n-doped material and  $p = N_A$  in p-doped semiconductors.

The displacement of free charge carriers due to thermal movement is random and overall it remains zero. However, if the concentration of the free electrons and holes differs in the charge carrier density, they start to diffuse. On average charge carriers diffuse from a region with a large density into the one with smaller density. The total current density  $J$  in the semiconductor is given by the sum of the drift and diffusion components. If the carrier concentration changes in x-direction and an external electric field  $E$  in x-direction is present, then the current density equations for electrons  $J_n$  and holes  $J_p$  are written as:

$$J_n = qn\mu_n E - qD_n \frac{\partial n}{\partial x} \quad (2.5),$$

$$J_p = qp\mu_p E + qD_p \frac{\partial p}{\partial x} \quad (2.6).$$

Here,  $q$  is the elementary charge electron drift mobility,  $\mu_n$ , and  $\mu_p$  are the electron and hole mobilities, respectively,  $D_n$  and  $D_p$  are the electron and hole diffusion coefficients, respectively, which can be expressed from Einstein relation as proportional to the mobilities:

$$D_{n,p} = \frac{KT}{q} \mu_{n,p} \quad (2.7).$$

Silicon detectors are often used in the presence of a magnetic field in order to allow measurements of the particle momentum. However, the magnetic field influences not only the particle that is passing through the sensor but also the free charge carriers moving inside the silicon sensor. Thus created electron-hole pairs drifting towards the electrodes (in the presence of an electric field) are deflected by the Lorentz force. The change in drifting direction is generally described by the opening angle,  $\theta_L$  measured with respect to the direction of the electric field. Typical values of the so called Lorentz angle range between a few and  $20^\circ$  and the equations for electrons  $\theta_{L,n}$  and holes  $\theta_{L,p}$  are :

$$\tan\theta_{L,n} = \mu_{H,n} B_\perp \quad (2.8),$$

$$\tan\theta_{L,p} = \mu_{H,p} B_{\perp} \quad (2.9).$$

Here  $\mu_H$  is the hall mobility and  $B_{\perp}$  is the magnetic field component that is perpendicular to the direction of the charge carrier drift. The hall mobility can be derived from the drift mobility:  $\mu_H = r\mu$ . The Lorentz factor 'r' is slightly temperature dependent and its value is 1.15 for electrons and 0.72 for holes at 0° [9].

In real environment, carrier generation and recombination plays a vital role to the device performance. Indirect band-gap present in silicon leads it to minimize the direct band-to-band recombination highly since electrons at the bottom of the conduction band and holes are at top of the valence band hold different crystal momentum. A direct transmission conserving both energy and momentum is not possible without lattice interactions. The recombination in silicon is dominated by Shockley-Read-Hall (SRH) process that uses localized energy band-gap, that are mainly induced in silicon from lattice imperfection or unwanted impurities (e.g. Au, Cu, Fe). These localized band-gap states directly influence the carrier lifetimes and especially in Si and they can lead to the severe decrease of lifetime values. More details on SRH process could be found in reference [5].

### 2.1.2 p-n Diodes and Relevant Concepts for Silicon Detectors

Two layers of silicon by p and n doped material forms a p-n junction diode, that is used for semiconductor sensors. The general principle of semiconductor p-n junctions is illustrated in figure 2.1.

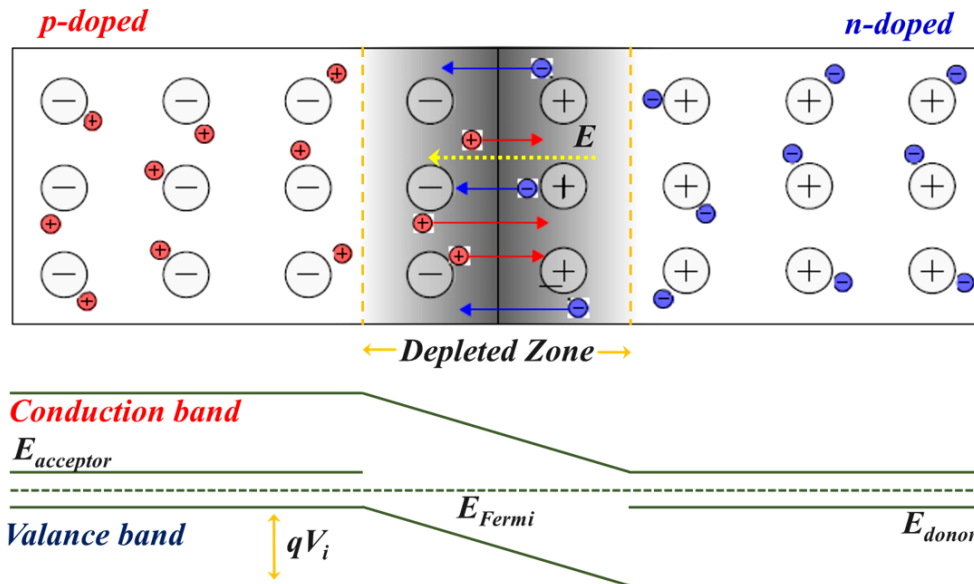


**Figure 2.1:** Schematics of p-n junction. Grey-shaded region is representing the space charge region created at thermal equilibrium.

In the n-doped part the majority carriers are electrons, where holes dominate the p-type region. In the region where both types are joined, charge carriers diffuse across the junction. Electrons diffuse into the p-doped side, while holes diffuse into the

n-doped semiconductor. The diffusion leads to the creation of region in close proximity of the p-n junction that is depleted of free charge carriers (depleted region). As a result, a negative space charge is created in the p-side of the sensor and a positive charge is formed in the n-doped region. The space charge leads to an electric field in opposite direction of the carrier's diffusion. This effect prevents further diffusion of charge carriers into the area around junction. As soon as thermal equilibrium is reached, the values of the electron and hole current at the junction decreases to exactly zero and the Fermi level remains constant in the whole diode.

The built-in voltage  $V_{bi}$  of the junction is the potential difference built at thermal equilibrium between the p-side and the n-side. The size of the depleted region 'w', surrounds the junction region, is a function of ' $V_{bi}$ '. Both values can be derived by solving the Poisson equation in the p-n junction. Assuming all donors and acceptors are ionized the following equation can be derived for built-in voltage:

$$V_{bi} = \frac{KT}{q} \ln\left(\frac{N_A N_D}{n_i^2}\right) \quad (2.10).$$

In order to able to detect the radiation induced charges, an external electric field,  $V_{bias}$ , is applied in the same direction of  $V_{bi}$ . The width of depletion region can be formulated as:

$$w = \sqrt{\frac{2\epsilon_s}{q} \left(\frac{1}{N_A} + \frac{1}{N_D}\right) (V_{bias} + V_{bi})} \quad (2.11).$$

Where  $\epsilon_s$  is the dielectric constant of silicon. The silicon bulk of silicon detectors is generally low-doped ( $10^{-12} \text{ cm}^{-3}$ ) while implants acting as electrodes are generally highly doped ( $10^{-18} \text{ cm}^{-3}$ ). In case n-type bulk material is used and the built-in potential remains very low as compared to the applied external voltage ( $V_{bi} \ll V_{bias}$ ), eq<sup>n</sup> 2.11 can even be simplified:

$$w = \sqrt{\frac{2\epsilon_s}{qN_D} V_{bias}} \quad (2.12).$$

The maximum electric field inside a typical p-n junction can be estimated as:

$$E_{max} = \frac{2V_{bias}}{w} \cong \sqrt{\frac{2qN_D}{\epsilon_s} V_{bias}} \quad (2.13).$$

The full depletion voltage  $V_{fd}$ , is the externally applied voltage required to extend the depleted Space Charge Region (SCR) to the entire sensor thickness. The full depletion voltage depends upon the square of the inter-electrode distance. If the applied  $V_{bias}$  exceeds  $V_{fd}$ , the device leads to a so-called over-depleted condition. The steady state leakage or dark current present within the device has multiple components: (i) the diffusion of free carriers from the non-depleted volume into the SCR and the thermal contributions from generation-recombination centers at the depleted surface (ii) and in the depleted bulk (iii) of the device. The third component generally remains dominant over the first and second ones. The leakage current

density of a reverse biased p-n junction associated to contribution (iii),  $J_{vol}$ , can be approximated to:

$$J_{vol} \cong -\frac{qn_i w}{\tau_g} \cong -\frac{n_i}{\tau_g} \sqrt{\frac{2q\epsilon_s}{N_D}} V_{bias} \quad (2.14).$$

Here,  $\tau_g$  represents the carrier generation lifetime. Such leakage current vastly depends upon temperature since both  $n_i$  and  $\tau_g$  inherently depend on device operating temperature. This phenomenon suggests to operate the device in cool environment in order to decrease the leakage current. The leakage current at temperature  $T_2$  can be predicted with reference to leakage current at temperature  $T_1$ , using the following equation [169]:

$$\frac{I(T_2)}{I(T_1)} = \left(\frac{T_2}{T_1}\right)^2 \exp\left[-\frac{E_{eff}}{2k} \left(\frac{T_2 - T_1}{T_1 T_2}\right)\right] \quad (2.15).$$

Here the effective band-gap,  $E_{eff}$ , is 1.21eV. At sufficiently large reverse bias voltage, the thermally generated free carriers gain large kinetic energy, so they can break the covalent bonds and release electron-hole pairs by hitting in the silicon lattice. This process is also known as impact ionization and it can eventually induce avalanche breakdown. During the self-sustained impact ionization at relative large reverse bias voltage, the leakage current can increase by many orders of magnitude than the usual operation, possibly leading the device to the state of thermal runaway. The reverse bias limit ( $V_B$ ) can be estimated using the following equation:

$$V_B \cong \frac{\epsilon_s}{2qN_D} E_B^2 \quad (2.16).$$

Here,  $E_B$  is the critical electric field for avalanche multiplication in silicon at  $T=300^\circ\text{K}$  and its value  $\sim 3 \times 10^5$  V/cm.

The full depletion voltage  $V_{fd}$  can also be estimated from the bulk capacitance of Si device. The bulk capacitance of silicon device can be approximated using the equation below:

$$C_{bulk} \cong \begin{cases} A \sqrt{\frac{\epsilon_s}{2\mu\rho V_{bias}}}, & V_{bias} \ll V_{fd} \\ A \frac{\epsilon_s}{w_{depl}} = const., & V_{fd} > V_{bias} \end{cases} \quad (2.17).$$

From, the above equation, it is clear that full depletion of device occurs while the bulk capacitance becomes minimum.  $1/C^2$  or log-log plots are typically used to show the arrival of full depletion.

### 2.1.3 Silicon as a Detector Material

Charged particles lose part of their energy as they pass through matter. Particles with sufficient energy and a mass larger than the electron mass lose their

energy primarily by ionization and excitation of electrons, which is the desired behaviour in particle sensors. Additional interactions of highly energetic particles also lead to non-ionising energy losses, which have a negative impact on the sensor performance. The average energy loss per distance (stopping power) is given by the Bethe-Bloch equation:

$$-\frac{dE}{dx} = 4\pi N_A r_e^2 m_e^2 c^2 z^2 \frac{Z}{A} \frac{1}{\beta^2} \left[ \frac{1}{2} \ln \left( \frac{2m_e c^2 \beta^2 \gamma^2 T_{MAX}}{I^2} \right) - \beta^2 - \frac{\delta(\gamma)}{2} \right] \quad (2.18).$$

Here,  $z$  is the charge of the incident particle,  $T_{max}$  denotes the maximum kinetic energy that can be imparted to a free electron produced from a single collision,  $Z$  is the atomic number and  $A$  is the atomic mass of the considered material,  $I$  denotes the mean excitation energy,  $N_A$  is Avogadro's number,  $m_e$  is the electron mass,  $c$  is the speed of light,  $r_e$  is the classical electron radius,  $\beta=v/c$ ,  $\gamma = \frac{1}{\sqrt{1-\beta^2}}$ , and  $\delta$  is the density correction function.

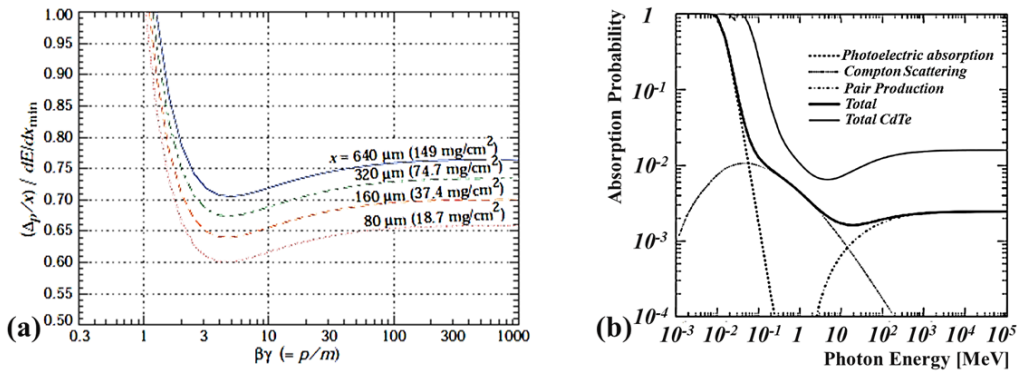


**Figure 2.2:** (a) Straggling functions in silicon for 500 MeV pions, normalized to unity at the most probable value  $\Delta/x$ .  $\Delta$  is the most probable loss and  $w$  is the width of full width at half maximum. (b) Probability of Photon Absorption in 300 $\mu$ m silicon. For the comparative understanding, high  $Z$  material CdTe is also shown in the plot [9].

Particles providing such minimum values of energy loss are called Minimum Ionizing Particles (MIPs) and each detector system must have an intrinsic noise low enough to detect these particles. Figure 2.2 (a) demonstrate stopping power for 500 MeV pions with normalized depth of silicon where  $\beta_\gamma$  is around 4 showing the MIP position. When a particle interacts with a material, some statistical fluctuations in the number of collisions occur. This can be modelled by Poisson distribution. At the same time, energy transfer per scattering also remains and it can be described with a straggling function. In rare cases,  $\gamma$ -rays or  $\delta$ -electrons produced by the interaction, hold sufficient energy to produce ionizing particles. Such phenomenon can be represented by an asymmetry spectrum, with a longer tail toward higher energies. This resulting spectrum distribution is known as Landau distribution [10]. The most probable value of energy transfer is generally about 30% lower than the average value. In silicon, the average energy to create an electron and hole pair is about 3.6eV ( $\sim 3$  times higher than Si band-gap), since  $2/3^{\text{rd}}$  of it is spent for phonon generation. For a MIP,

the most probable number of generated electron-hole pairs in Si is  $72 \mu\text{m}^{-1}$ , with an average value of  $108 \mu\text{m}^{-1}$ . Thereby, a device of  $300 \mu\text{m}$  active thickness can produce almost 21,600 e-h pairs ( $300 \mu\text{m} \times 72$ ). An important effect to consider when dealing with charged particles, is the so called Multiple Scattering. The trajectory of a particle traversing a medium is scattered multiple times by small angles, mainly due to Coulomb interaction with the nuclei of the material.

Silicon is sensible to electromagnetic radiation from the visible light up to the  $\gamma$ -ray range, where photons interact with silicon by three different processes: (i) photoelectric effect, (ii) Compton effect and (iii) pair production. In the photoelectric absorption and pair production modes, the photon is completely absorbed. In this context, Compton mode is scattered by a large angle. Beer's law in equation 2.19 gives the relation of photon absorption over penetration depth ( $x$ ) of active thickness:

$$I(x) = I_0 e^{-\mu x} \quad (2.19).$$

Here,  $I_0$  is the incident photon flux and  $\mu$  is the permittivity of silicon. Figure 2.2 (b) shows the probability of photon interaction in a  $300 \mu\text{m}$  silicon layer as a function of the photon energy comparing it with the one for CdTe, to show the difference between silicon and high-Z materials.

Moving charge carriers produced by a passing particle that drift in an electric field induce electric charge on the electrodes of the detector. The collected charge in the readout electronics is then converted into an output signal. The Shockley-Ramo theorem [24] offers a simple way to calculate the induced charge,  $Q$ , in an electrode by a free moving point charge  $q$ . For the calculation only one electrode of the sensor is selected. A charge  $q$  moving from point  $\vec{x}_i$  to  $\vec{x}_f$  induces the following charge:

$$Q_L = \int_{\vec{x}_i}^{\vec{x}_f} q \vec{E}_0 \cdot d\vec{x} = -q [\varphi_0(\vec{x}_f) - \varphi_0(\vec{x}_i)] \quad (2.20).$$

Here,  $\vec{E}_0$  is the weighting field and  $\varphi_0$  is the weighting potential. The weighting field and potential can be estimated by selecting an electrode, which is set to the dimensionless unit potential 1, keeping other electrodes at ground potential. As a result, all charges are removed. The solution is not so complex, that can be done easily by the Poisson equation for the given configuration (where the layout of the detector electrodes is known). The weighting potential could thus take values between 0 and 1 and it describes the induced charge on the electrode as a fraction of the free moving charge.

#### 2.1.4 Radiation Damage in Silicon

Radiation damage effects in the ATLAS pixel detector become increasingly visible with the advancing run time of the LHC. The effective depletion voltage and the depletion depth are key values for the pixel-monitoring to access the radiation damage

made at them. Continuous monitoring of these values is eminent to ensure that the expected performance of the pixel detectors is met until they be replaced.

For sensor design, it is also expected that the depletion voltage decreases up to the point of type-inversion, after which the sensor bulk becomes effectively p-type silicon. After type-inversion the depletion voltage increases constantly with the accumulated radiation fluence. Due to the bulk induced effect, the full depletion voltage increases and it limits charge collection efficiency in efficient manner by limiting the maximum operating voltage. The pixel sensors are then intended to be designed to be operated in partially depleted condition when the depletion voltage exceeds their maximum operation voltage. Radiation damage in silicon sensors can be separated into two categories: bulk damage and surface damage. Surface damage comprises all defects that are located close to the surface of the silicon crystal as well as in the interface area between the silicon and passivation layer. Bulk defects are located deeper inside the silicon sensor. The creation of bulk damage is described by the so called Non Ionising Energy Loss (NIEL) hypothesis.

### **Surface Damage**

Most of the surface damage induced in silicon devices can be realized from the damage made on silicon dioxide ( $\text{SiO}_2$ ) layer. Interface trap charge and oxide charge are the two common defects remain even if  $\text{SiO}_2$  is still well fabricated. Due to structural defects, oxidation defects, metal impurities or radiation induced bond breaking, positive or negative charges are induced. Interface states (interface traps) basically locate at Si- $\text{SiO}_2$  interface, that highly contribute to surface recombination and consequently, take part to the increase of leakage current. Oxide charge in  $\text{SiO}_2$  can play a major role for the device. Positive oxide near the Si- $\text{SiO}_2$  interface attract electrons near the interface and modulate the electric field. The phenomenon ultimately affects major electrical properties of the device and enhance the operation anomalies, i.e. threshold voltage shifting. Ionizing radiation or avalanche injection like mechanisms lead to enhance the negative or positive oxide, also known as oxide trapped charge, which can be recovered by sintering process.

In irradiation condition, high energy particles pass through the  $\text{SiO}_2$  and generate electron-hole (e-h) pairs. Most of them recombine but a fraction of them can not do. Since in silicon oxide the electron mobility is very high ( $\mu_n \cong 20 \text{ cm}^2/\text{Vs}$ ) in comparison to the hole mobility ( $\mu_p \cong 2 \times 10^{-5} \text{ cm}^2/\text{Vs}$ ), electrons drift much faster. The holes instead diffuse to interface traps and enhance the positive oxide charges. Increment of surface recombination velocity and leakage current increase due to irradiation are reported in figure 2.3. For the accumulated Total Ionizing Dose (TID) and no device biasing condition, the oxide charge density is enhanced by at least 1 order magnitude. In case of bias condition, the oxide charge enhancement within device could increase even further. It is interesting to notice that the oxide charge

concentration within the device saturates after certain accumulated TID since the dangling bonds of oxide are fully terminated. On the other hand, the leakage current shows an incremental trend with ionizing radiation damage due to surface generation.

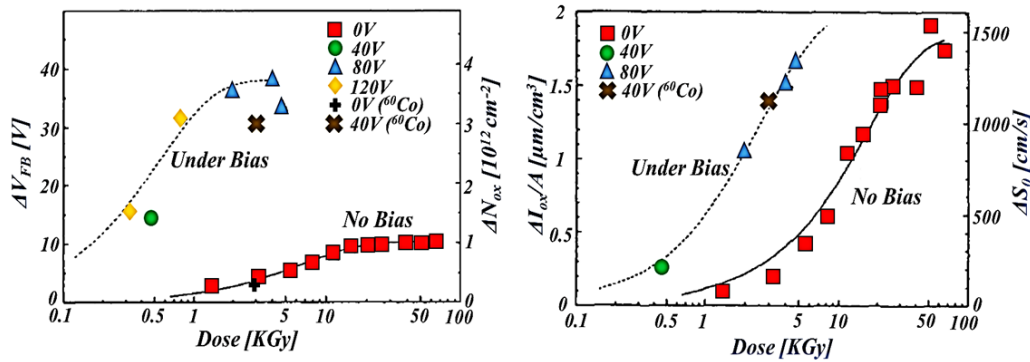


**Figure 2.3:** MOS with  $\text{SiO}_2$  dielectric layer under proton irradiation: **left** figure represents the oxide charge enhancement with different applied voltage condition at accumulated TID and **right** figure represents the leakage current enhancement with different applied voltage condition at accumulated TID. Plus (+) and Cross (X) represent data relevant to  $\gamma$ -ray irradiation with  $^{60}\text{Co}$  source [11].

### Bulk Damage

A passing particle can knock silicon atoms off of their lattice position and thus is able to create defects in the silicon crystal. The displacement of atoms in the lattice leads to the creation of Vacancy-Interstitial (V- I) pairs (Frenkel-defect). The minimum energy necessary to create a Frenkel pair is approximately 25 eV [5]. The energy of a neutron creating such a point defect is about 175 eV or more, while electrons need at least an energy of 260 keV to create such displacements [12].

Displaced silicon atoms by interactions with a passing particle are called Primary Knock-on Atoms (PKAs). At lower particle energies no further defects are created. However, if the PKA has received sufficient energy, it travels through the crystal, that would create further Frenkel defects. In addition to single point defects, high energetic PKAs also create clusters with a high density of defects in a relatively small area. Clusters are usually created when the silicon atom already has lost most of its energy. Thus, they are in general located at the end of the PKA's path. For very high energies, it is possible that point defects created by the PKA also possess enough energy to create additional defects. These atoms are called secondary knock-on atoms.

A PKA with an energy of 50 keV can create up to 1000 additional defect pairs, while approximately 600 of them recombine again. A simulation of a PKA creating further defects is shown in Figure 2.4. The exact distribution varies from event to event of course. The example shows a structure created by one PKA with an energy of 50 keV. This is a typical energy for 1 MeV neutron scattering in silicon. A tree-like structure and several sub-clusters are clearly visible. Sub-clusters are created by secondary

knock-on atoms with lower energy. If the PKA energy is increased above 50 keV, a larger tree with several branches can be observed [13].

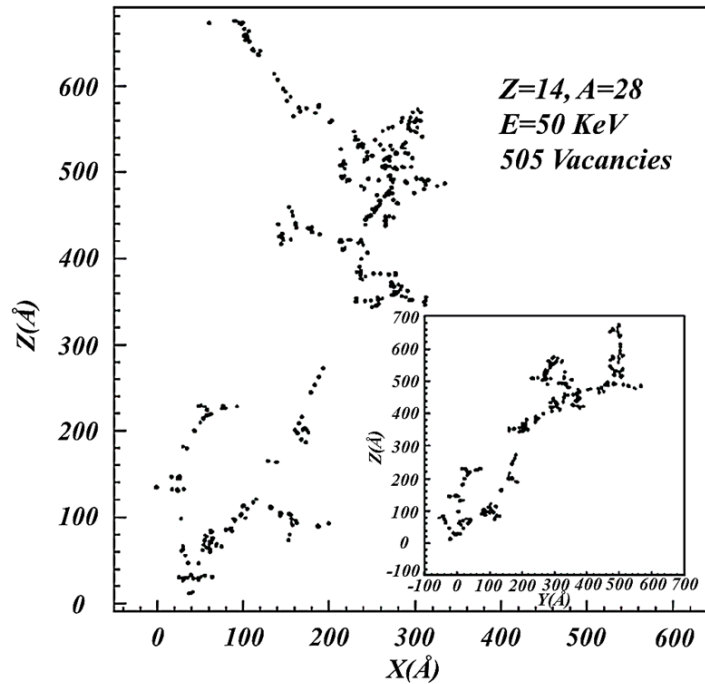


**Figure 2.4:** Simulated point and cluster defect in Silicon by PKA of 50 KeV. Inset is showing the transverse projection [12].

Neutral particles and charged particles interact with matter in different way. Charged particles interact electrically with the nuclei which increases the probability of the creation of point defects. Neutrons instead interact via nuclear force only inside nucleus. Impinging particles could create cluster like defects due to their elastic scattering process and interaction with atoms within the crystal. Highly energized impinging particles can displace the atoms from their original position in the crystal lattice and the consequent sufficiently earned kinetic energy of the displaced atoms allow them to displace more atoms. This cascaded process of defect formation creates cluster alike defects at the end path [9].

The NIEL scaling technique is used in the case of comparative analysis of irradiated samples (with different types of particles). The impact of the radiation damage of highly energetic particles is scaled to the damage of 1 MeV neutrons as a reference. The equation,  $\phi_{eq} = k\phi_p$  is used generally to calculate the neutron equivalent fluence where  $\phi_{eq}$  is the neutron equivalent fluence,  $k$  is hardness factor and  $\phi_p$  is the total fluence. The created point defects are mobile and thus are able to move through the silicon crystal. Many of them again recombine as it has stated earlier. However, stable defects are also formed with this process. Various types of stable defects can be created: defects that react with each other or with impurity atoms. These stable defects as well as defect clusters can be electrically active and are thus remain as the source of the measurable radiation damage effects in silicon.

Several kinds of defects, i.e. vacancy, di-vacancy, interstitials etc. could induce in Si crystal lattice from irradiation. Any kind of defect initiates intermittent energy states within the intrinsic bandgap, those act as recombination-generation centres. These newer states capture electrons and holes through recombination process or emit their kind by thermal excitations. Shallow defects which have an energy level close to the valence or conduction band on the other hand act as trapping centres due to the fact that they can capture free charge carriers temporarily. The trapped charge carriers are re-emitted after a time delay. Finally, some of the defects also possess energy levels that are similar to the ones of acceptors and donors. All of these defect characteristics lead to a visible change in the behaviour of silicon sensors, as it shall be explained in the following.

### **Damage Effect on Sensor Performance**

The microscopic defects accumulate over time and have an increasing impact on the sensor performance, which ultimately limits the lifetime of silicon sensors used in high energy experiments. The properties of the sensor are altered in three main ways that are important for detector operation:

- The leakage current increases with the increase of recombination-generation centres, which affects the signal to noise ratio, the power consumption and the cooling system of the pixel detector.
- The effective doping concentration of the sensor is modified in dependence of defects density, which has an impact on the depletion voltage. Overall, p-type defects are more created than n-type, which lead to type-inversion of the sensor in case substrate is initially of n-type.
- The charge collection efficiency decreases as the trapping centers increase. The resultant lower hit efficiency has a negative impact on the b-tagging performance and track resolution of the detector at the end.

The impact of radiation damage is not usually constant after irradiation but they can be improved through annealing treatment. Some defect like silicon interstitial and vacancies can recombine and stable defects can transform and become inactive, which become beneficial for the sensor performance eventually. However, Inactive defects can also be reactivated again and thus increase the impact of radiation damage.

### **Leakage Current**

An example of the increase in the leakage current per unit of volume  $\Delta I/V$  in several types of silicon is shown in figure 2.5. In these measurements the leakage current was measured before and after irradiation in order to estimate its increase. An important factor that needs to be taken into account for a precise measurement is the dependence of the leakage current on the temperature. In this case all current

measurements were normalised to a reference temperature of 20°C [14]. The increase in the measured leakage current is proportional to the particle fluence and it is clearly visible, it does not depend on the silicon type. The relationship between the leakage current and the collected fluence can thus be written as:

$$\Delta I = \alpha \Phi_{eq} V \quad (2.21).$$

Here,  $V$  is the sensor volume and  $\alpha$  is the current related damage rate.

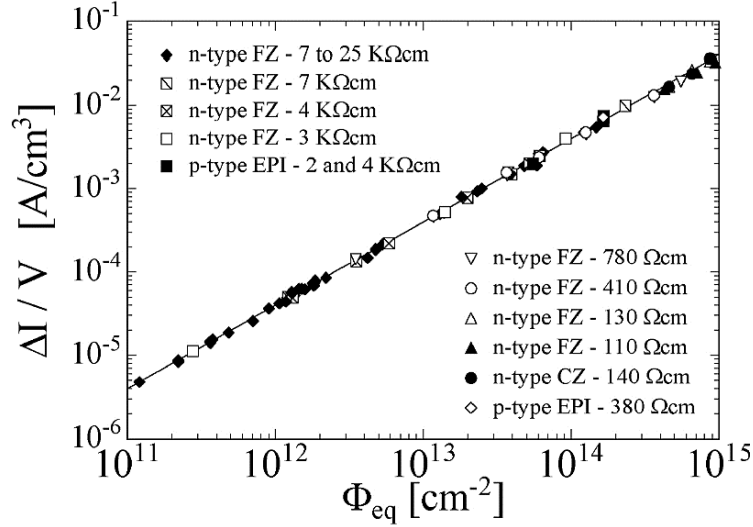


**Figure 2.5:** The leakage current behavior in term of the neutron equivalent fluence, for different types of silicon. All the measurements were taken after annealing the sensor to 60°C for 80 minutes [12].

Annealing effects can be described by the current related damage rate, which is therefore a function of time,  $\alpha(t)$ . The value of  $\alpha$  was found to decrease over time [14]. This indicates that annealing effects are beneficial for the leakage current. Several models has been already exist to describe the impact of annealing. However, the long term behaviour of  $\alpha$  can be described by a fit function,

$$\alpha(t) = \alpha_I \exp\left(-\frac{t}{\tau_1}\right) + \alpha_0 - \beta \cdot \ln\left(\frac{t}{t_0}\right) \quad (2.22).$$

Here,  $\alpha_I$ ,  $\alpha_0$  and  $\beta$  are the fit parameter and time  $t_0$  refers 1<sup>st</sup> minute.

The time constant  $\tau_1$  is based on the Arrhenius equation, which describes reaction rates as a function of the temperature. A growing leakage current increases the noise in the sensor as well as the power consumption. Due to the fact that the leakage current can reach the magnitude of mA in case of highly irradiated sensors, this could lead them to the condition of thermal runaway. The heat dissipation caused by a current of this magnitude is large enough to induce avalanche process, leading to an even higher heat dissipation. This self-amplifying loop could finally destroy the sensor. Thus, it is thus crucial to ensure the proper cooling for silicon detectors during operation at the highly radiative environment.

## Effective Doping Concentration and Depletion Voltage

Acceptor-like defects and donor removal lead to a change in the effective doping concentration in the silicon bulk. Donor removal can occur if foreign donor atoms such as phosphorus are combined with a vacancy. This creates a new defect, which has different electrical properties. As an example, measurement for an initially n-type doped sensor is shown in figure 2.6.

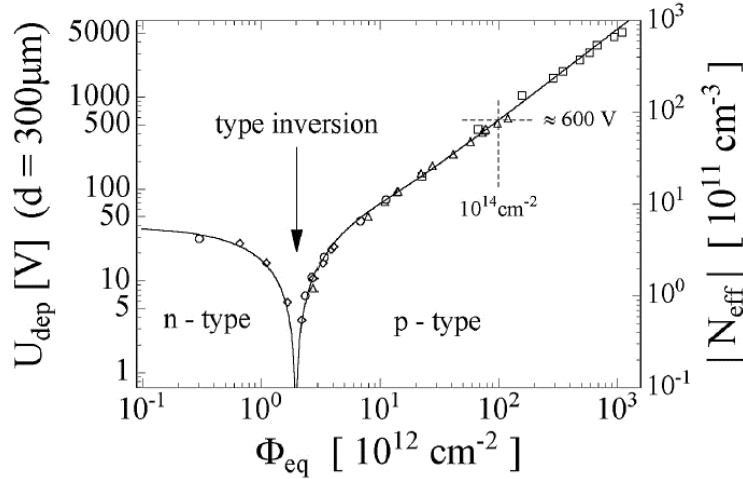


**Figure 2.6:** Change in effective doping concentration (and full depletion voltage) as a function of neutron equivalent fluence [12].

The effective doping concentration as well as the depletion voltage decrease at the beginning up to the point of type-inversion. Afterwards, the silicon reaches to the state as effectively p-doped. Later, the doping concentration as well as the depletion voltage increases continuously in dependence of the accumulated particle fluence. The change of the effective doping concentration can be quantified in term of time and temperature. The effective doping concentration  $N_{eff}(\Phi_{eq}, t(T_a))$  is described as:

$$N_{eff}(\Phi_{eq}, t(T_a)) = N_{eff,0} - \Delta N_{eff}(\Phi_{eq}, t(T_a)) \quad (2.23).$$

Here,  $N_{eff,0}$  is the initial doping concentration, and  $\Delta N_{eff}(\Phi_{eq}, t(T_a))$  is the change in concentration induced by irradiation, where time (t), is the dependant function of temperature,  $T_a$ . More details can be found in reference [14].

The formation of oxygen vacancies into the ATLAS pixel detector during operation can be treated as a measurable parameter of radiation damage [15]. However, after years of operation, the maximum voltage of the power supplies is about to be reached and the sensor might need to be swapped in near future. Time dependent annealing effect into the effective doping concentration is presented in figure 2.7. However, due to the n-in-n sensor design that is used in the ATLAS pixel detector, it is possible to operate the detector partially depleted after type-inversion. A bit detail on this phenomenon will be discussed in chapter 3.

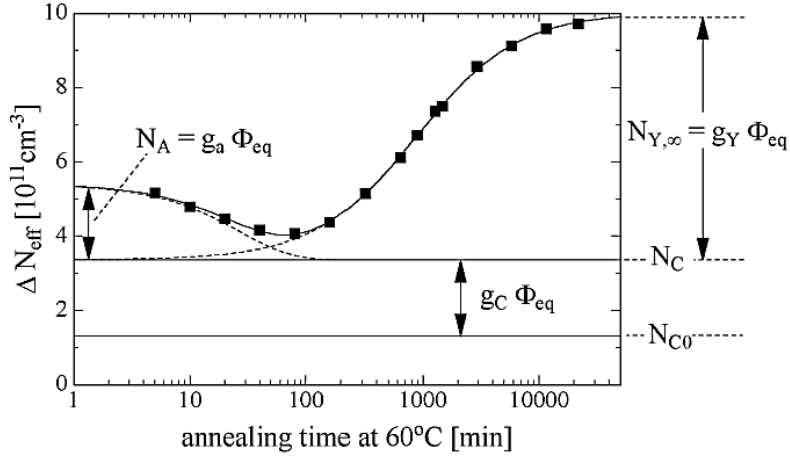


**Figure 2.7:** Change in the effective doping concentration  $\Delta N_{\text{eff}}$  as a function of time. The sample was irradiated at  $1.4 \times 10^{13} \text{ n}_{\text{eq}}/\text{cm}^2$  at  $60^\circ\text{C}$  [14].

### Degradation of CCE due to Charge Trapping

A fraction of the free charge carriers drifting towards the electrodes in the silicon sensor are trapped for a limited time by defects. If the trapping time is longer than the time available for readout, then the charge carriers do not contribute to the signal and its amplitude will decrease. The trapping time depends highly on the type of trap. Only traps with energy levels very close to the valence/conduction band may release the holes/electrons fast enough so that the charge collection is not affected. Traps, and thus the charge carrier loss in the silicon sensor, are characterised by the trapping time constant,  $\tau^+(\Phi)$ . This trapping time constant describes the average time that a charge carrier stays trapped, which is inversely proportional to the fluence [11]:

$$\frac{1}{\tau^+(\Phi)} = \frac{1}{\tau_0^+} + \gamma\Phi \quad (2.24).$$

Both parameters were measured and the values were found to be  $\tau_0^+ = 0.51 \times 10^6 \text{ s}^{-1} \pm 12\%$  and correction factor,  $\gamma = 0.24 \text{ cm}^2\text{s}^{-1}$ . The quoted values are valid for electrons and holes, however, they cannot be used for fluences larger than  $\Phi = 8.8 \times 10^{12} \text{ cm}^{-2}$  [11].

### 2.1.5 Remedy to Radiation damage

In order to improve the Si-device performance, several radiation hardening techniques are being adopted in processing foundry. The subsection is highlighting their significance.

#### Counteract to Surface Damage

The built positive oxide charge due to irradiation leads device to be run into several adversities. This built oxide charges in p-in-n devices affect the electric field distribution at the devices strongly, which leads to early breakdown. In case of n-in-p and n-in-n devices, oxide charge inverts surface layer with electrons that eventually

shorts all the segmented  $n^+$  readout electrodes. This anticipates the impossibility of position sensing. Si foundry generally adopts the surface isolation techniques to prevent the surface inversion due the enhanced positive oxide charges from irradiation. The p-spray, p-stop and moderated p-spray are the three different surface isolation techniques widely used today. Numerical simulation provides a good understanding of each respective technique and has well been discussed in literature [16].

Each isolation technique come with some benefits but the choice of a specific technique should be optimally chosen by the requirement of device application. The target breakdown voltage, that defines the device ultimate operating range before and after irradiation, inter-electrode capacitance, inter-electrode resistance as well as the cost of processing steps are the prime parameters of choice.

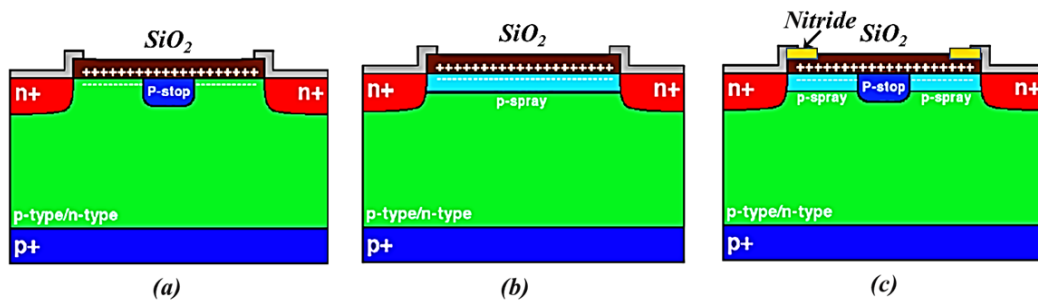


**Figure 2.8:** Different isolation techniques: (a) p-stop, (b) p-spray and moderated p-spray [17].

The **p-stop** isolating is a common technique that introduces a high dose p - implant between the strips as shown in figure 2.8(a). This is done by an additional photolithographic step. The alignment of the p-stop mask with respect to the  $n^+$ -pixels is critical as an over-lapping of the two high dose implants would result in Zener breakdown. The minimum spacing between two  $n^+$ -implants is therefore limited by the necessary alignment tolerances. The advantage of this technique is that a typical dose of about  $10^{14}$  boron (B) ions per square centimeter is a good choice in any case to ensure proper isolation. The adjustment of the implantation dose is not at all critical at this context. The finely processed non-irradiated device typically has a very low oxide charge, resulting in a low electric field. The value of the oxide charge increase after an irradiation dose of  $\sim 20\text{kGy}$  may be close to its saturation value, that results an accumulation of electrons close to the interface and consequently in a strong increase of the electric field. The potential of the p-stop depends of course on the implant geometry, the backside bias and the substrate doping. As the two latter values also are very high in a highly irradiated sensor, the potential difference between n -pixels and the p -stops increases with ongoing irradiation. This leads to a comparatively smaller increase of the electric field in addition. The operation of devices featuring p-stops in a strong radiation field is thereby limited by their decreasing high voltage capability.

In the **p-spray** isolation technique (figure 2.8(b)), the dose of boron implant is matched to the saturation value of the oxide charge which is of the order of  $3 \times 10^{12}$  e/cm<sup>2</sup>. The boron concentration is so small that it can actually be placed between n<sup>+</sup>-implants, without leading into breakdown. The dedicated mask, which was used separating both implantations in p-stop processing, can be omitted here and the whole surface is then covered by the medium dose boron implant. The reduction of this processing step eminently comes with cost benefit and also permits narrower spacing between the neighbouring n<sup>+</sup>-implants (as there are no alignment tolerances needed between two different masks). Initially, p-spray implanted nonirradiated device shows the highest electrical field and the consequent lowest breakdown voltage. With the increase of the oxide charge to its saturation value the shallow p-spray layer moves into the depleted state and so, the electric field decreases. Sooner the boron implant matches exactly the saturation value of the oxide charges, the electric field reaches to it's the lowest. However, the isolation could not be ensured if the dose implantation remains too low. Considering the process induced non-uniformity, one usually chooses an a bit higher implant dose than the necessary. The increase of the effective substrate doping concentration results an expected increase of the electric field. Therefore these devices are characterized by an improved high voltage performance after irradiation.

In order to improve the pre-radiation high voltage stability of p-spray devices while keeping their good post-irradiation behavior, the **moderated p-spray** technique can be an interesting choice (figure 2.8(c)) [17]. Here the p-spray implant is performed later in the production process. As shown in the schematic, nitride is integrated the in the doping profile. Boron dose in the middle of the gap is implanted between two pixels, as high enough to ensure inter pixel isolation (almost twice the expected saturation value of the surface charge). At the same time, boron dose in the surrounding of the lateral p-n junction is optimized for the best high voltage performance. Here, the dose is considered to be close to the expected saturation value of the surface charge. Since the nitride layer is a standard step in the process of many detector vendors, this technology in most cases does not need an additional photolithographic step. However, very small gaps between the pixel implants is limited in the moderated p-spray technology because the moderation becomes only effective which has a minimum width of moderated p-spray layer is about 3-5 $\mu$ m.

### **Counteract to Bulk Damage**

Counteracting the bulk damage in device can be adopted by implementing through a blended solution of material engineering and device engineering. Material engineering mainly consist in engineering of new material properties of semiconductors that will better withstand the high radiation doses. Since long the use of oxygenated substrates remains a stronger technique. During the process, oxygen is believed to capture the vacancies in stable and neutral point defects. This leads to a diminished effective doping modification after irradiation [18]. However, this is limited

only to the stable damage and reverse annealing and is restricted to charged hadrons irradiation. Another option is to use the different kinds of semiconductors. In this sense, diamond has remained an attracting choice due to its very low leakage current and high radiation hardness, because of owing a larger band gap. The main disadvantage of diamond is the extremely high cost of its substrates and the complexity in yielding them at a large scale.

Where the device engineering would be a concern, it can be applied in order to enhance device performances, or can lead in adopting a newer architectural enhancement. Enhanced modified junction column non-passing through technology or the newer small-pitch and thin 3D sensors designs fall within this scope (shall be discussed in later chapters). As previously described, from the point of view of leakage current, there have been limiting scopes except for cooling.

## **2.2 3D Silicon Detectors**

3D detectors consist of an array of doped columnar electrodes of both p and n types arranged in adjacent cells and oriented perpendicularly to the wafer surface. The columns are formed by etching process through a high-resistivity silicon substrate [4]. Electric field lines begin at one electrode type and end at the closest electrode of the opposite type in parallel with respect to the wafer surface. Similarly to standard planar detectors, the strength of the electric field is controlled by the bias voltage. In order to have several kinds of detectors (e.g., pixel, strip, pad, etc.), either single-column or multi-column arrangements can be adopted utilizing the diffusion and/or metal surface connections.

In standard planar detectors, the electrodes are implanted on the top and bottom surfaces of the wafer, so that the depletion region grows vertically and the full depletion voltage depends on the substrate thickness (figure 2.9 (b)). On the contrary, 3D detectors allow to decouple the electrode distance ( $L$ ) and the substrate thickness ( $\Delta$ ) as shown in figure 2.9 (a). The depletion region grows laterally between the electrodes, whose distance can be made much smaller ( $\sim 10x$ ) than the substrate thickness. This leads the full depletion voltage to be dramatically reduced in comparison to planar detectors. This property is extremely useful to the applications where full depletion of planar detectors can be limited to achieve because of junction breakdown and/or thermal runaway problems. Among them, thick detectors used in the field of X- and  $\gamma$ -ray detection and heavily irradiated detectors in HEP applications. As per the concern of the leakage currents that could be also very high in planar type sensor, the related savings in terms of power consumption in 3D sensors can act the crucial role to ease the realization of complex systems.

The charge collection properties of 3D architecture is superior to the planar one in several respects. A high energy particle traverses through the detector and produces a uniform electron-hole (e-h) pair density (MIP) along its track, as reported in figure 2.9

(a) and (b). At the same substrate thickness, the amount of generated charge remains same for both kind of detectors. However, the charge collection distance is much shorter in 3D detectors, and high electric fields as well as carrier velocity saturation can be achieved at very low bias. The charge collection times can then be even much faster (in the order of a few ns, to be compared to a few tens of ns for planar detectors).

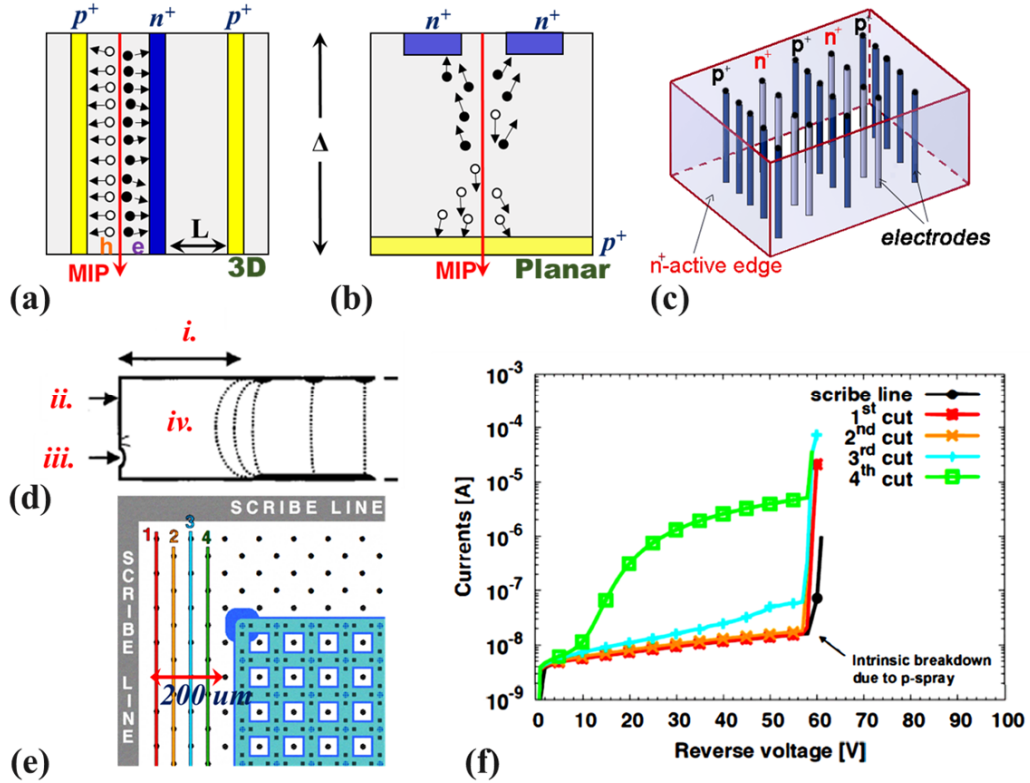


**Figure 2.9:** Schematic cross-sections: (a) of 3D detector emphasizing the decoupling of active thickness ( $\Delta$ ) and collection distance ( $L$ ) in 3D detectors and (b) of planar detector. (c) Schematic of 3D sensors with active edge. (d) Schematic cross-sections of edge-region in a standard planar detector showing the reason of having large insensitive region: i. places hold for adapting guard ring, ii. defects induce from saw-cut process and iii. the bulge at the edge of the electric field in the depletion region, that should keep far away from defect [21]. (e) Schematic of slim-edge made on 3D Si sensors, and (f) experimental I-V curves of double-sided 3D diodes with slim edge of 200  $\mu\text{m}$  with corresponding dicing made as reported in (d) [22].

In particular, using Ramo's theorem [see, section 2.1.3], one can estimate the signal current from the carrier velocity and the weighting field. In planar detectors, each charge carrier is generated at a different distance from the collecting electrodes, thus inducing its peak signal at different times. This effect is efficiently handled in 3D detectors, where all charges along the ionization track are generated within a much shorter distance from the electrodes (viz. figure 2.9(a)). In non-irradiating condition, such effect is not significantly different between these planar and 3D sensors. However, in the field of very high speed applications at HEP experiments, 3D technology act as remedy to the charge trapping effects due to high levels of radiation

induced damage. Finally, due to their particular structure where a sort of self-shielding effect sustains in each cell, charge sharing between adjacent electrodes is considerably reduced in 3D detectors with respect to planar detectors with smaller pixel sizes, an eminent requirement for photon imaging applications [19]. Aside all these advantages presented here, this technology comes with several challenges, like the signal response to particles is not spatially uniform because of the existence of dead region (very low field) within the active volume. This phenomenon leads charge carriers generated in these regions to diffuse first towards the region with the sufficient electric field, thus delaying the signal response and possibly contribute to lower the charge collection efficiency. The small spacing between the electrodes and their deep extension all through the substrate cause the capacitance to be quite high. This degrades the noise performance at short shaping times, which is the major interest for these fast detectors.

In standard processes, sensors are separated from the wafer using diamond saw. In planar detectors (see figure 2.9 (d)), the active region is normally kept far away (~1mm) from the dicing line so the electric field does not reach the defects (e.g., cracks, chipped regions) created from the saw cut. Multiple guard rings generally adopted in planar sensor is aimed at evenly distributing the lateral voltage drop and enhancing the breakdown performance [20] are also normally present at the periphery. If the depletion region reaches these defects a large amount of current start injecting in the device, eventually leading to an early breakdown. The schematic of having a large insensitive edge region has pictorially demonstrated in figure 2.9(d). Active edge around the sensors active area can be defined as an additional boundary condition in order to restrict the depletion enlargement not beyond [21]. A schematic of it is shown in figure 2.9(c) by means of 3D technology. A deep trench is etched all around the active area of the device, which is later doped and passivated. Such trench act in fact as an ohmic contact filled by poly-silicon. This technique requires a support wafer, adding further complications to the fabrication process and is literally not feasible for double-sided process, adopted in IBL production.

A different edge concept for double-sided 3D Si sensors is the slim edge by columnar fence wall (figure 2.9(e)). Since the process of slim-edge does not require the substrate wafer, it was used in all double sided 3D processing batches at FBK. A slim edge approach is able to restrict edge depleted electric field in less than 100 $\mu$ m [22]: an experimental saw cut to slim edge (figure 2.9(e)) and the corresponding I-V behavior of a sensor as reported in figure 2.9(f) are endorsing the fact.

### **2.2.1 Technological Simulation**

Understanding 3D detector performance can be predicted by numerical device simulations, e.g. by SILVACO or SYNOPSIS software, before the fabrication. Simulated electrical and functional results were reported in [4] relevant to the static

and dynamic characteristics of 3D detectors. A typical unit cell in a 3D detector of  $25\mu\text{m}$  pitch between columns is shown in figure 2.10(a). Different bulk doping concentrations can be chosen. Because of symmetry considerations, the simulation domain can be reduced to a quarter of the unit cell only, in order to ease the computational complexity for using the minimal nodes possible in account. In order to predict the device performance only relevant to bulk, 3D sensor structure allows to perform a 2D simulation on a slice of the full 3D structure (taken from the middle of the substrate).

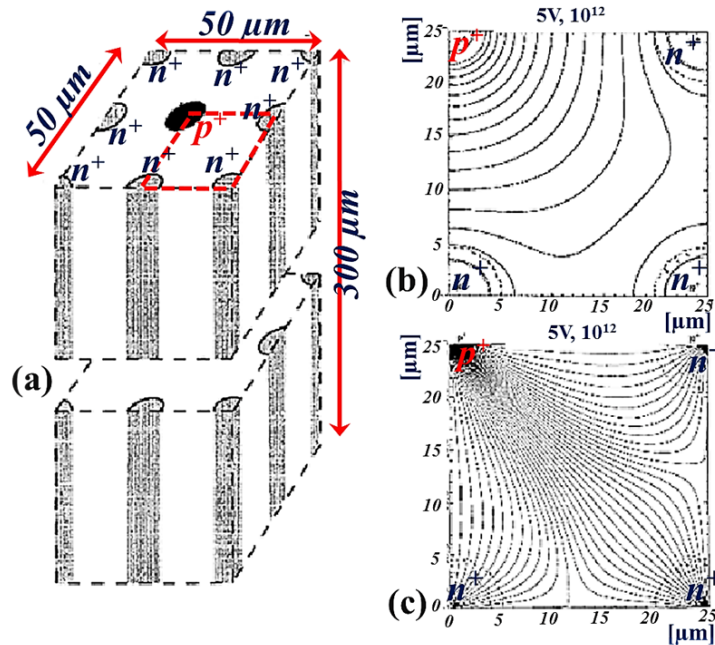


**Figure 2.10:** (a) 3D Simulated schematic of a unit cell in a 3D detector, (b) equipotential lines for one-quarter of the unit cell (red dotted marked in (a)) with  $10^{12}\text{cm}^{-3}$  p-type substrate doping concentration at 5-V reverse bias voltage, (c) drift lines in the same condition as in (b) [4].

Simulations on electrical quantities are typically performed grounding one type of electrode while a reverse bias ramp is applied to the other electrode type. In case of a detector made on p-type substrate, for a doping concentration  $N_A=10^{12}\text{cm}^{-3}$ , simulations predict a full depletion voltage of just 1.6 V (including the contribution from the built-in voltage). The full depletion voltage could even be increased to 8.8 V at  $N_A=10^{13}\text{cm}^{-3}$ . As an example, the equipotential lines in a quarter-cell with  $N_A=10^{12}\text{cm}^{-3}$  is reported in figure 2.10(b) at a reverse bias of 5V. Figure 2.10(c) shows the corresponding drift lines. From both figure 2.10 (b) & (c), the less dense mesh schematic of electric field along  $n^+$  columnar electrodes represents the dead regions of almost zero field region ( $\sim 2\text{-}3\mu\text{m}$  [4]). This anticipates a non-uniform spatial response to a charge particle passing through it. However, the carrier drift is strongly correlated to the particle impact position. Electrons and holes generated at the cell center can be collected within 1ns, whereas it could take longer time up to 5 ns if charge is generated at the zero field between  $n^+$ -electrodes [4]. The signal response

in terms of time is reported in figure 2.11. Figure 2.11 (a) reports current pulses on the electrodes while particles hit perpendicularly to the detector surface in cell center and the corresponding signal response behavior for particles hit between  $n^+$ -electrodes is shown in figure 2.11 (b). However, for the particles hit in null point, signals are still much faster in 3D detector in comparison to planar one, with much lower peak fields.

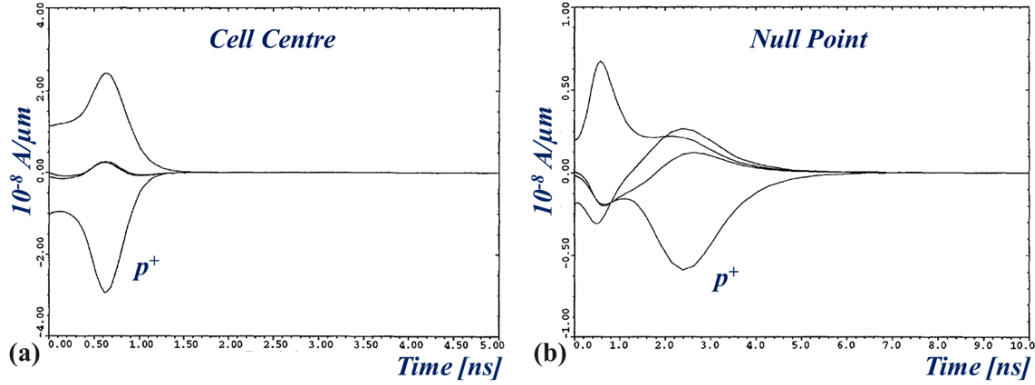


**Figure 2.11:** Current pulses on the electrodes in response to an MIP for a single track parallel to the electrodes that passing (a) through the cell center and (b) through the null point in between two  $n^+$  electrodes (doping concentration  $10^{12} \text{ cm}^{-3}$ , reverse bias 10 V) [4].

RC time constants related to the electrodes resistance and capacitance is in the order of 100-200ps [4], which is small enough for most applications. Here, it should stress out that both static and signal characteristics deviate from simulated prediction, close to the top and bottom surfaces. Electron accumulation layer at the interface as an effect of oxide fixed charges as well as the surface isolation structures using p-spray or p-stops deviate the prediction within these regions. Thus the charge collection properties are also affected in this context. In order for these effects to be accurately predicted, 3d simulations should be used, that of course involve a much higher computational effort.

## 2.2.2 Evolution of 3D Si Sensors

The viable production of 3D detectors has become possible since there has been a rapid development of MEMS technologies in '90s. By means of the availability of Deep Reactive Ion Etching (DRIE) equipment, the high aspect ratio of depth to diameter of columnar electrodes remains achievable. In DRIE-based production, etching rates could be higher than  $3 \mu\text{m}/\text{min}$ , selectivity to masking materials can set higher than 70:1, and non-uniformities can be lower than 5% only. The so called "Bosch process" is currently a standard for DRIE. The process repeats several times a 2-phase etching cycle based on fluorine compounds, alternating nearly isotropic plasma etching steps (by  $\text{SF}_6$ ) and sidewall passivation steps (by  $\text{C}_4\text{F}_8$ ), so as to achieve a high anisotropy in the overall etching profiles [23]. Aspect ratios can be maintained in the order of 30:1 nowadays within this process but the value should require a careful optimization to the current limits in the 3D technology.

The process details of the first few prototypes production at Stanford Nanofabrication Facility, SNF (Stanford, USA) was reported in [24]: it had been indeed quite a long and complicated processing cycle, and it resulted in a relatively small yield due to incorporating all the non-standard processing steps. Later, Norwegian Foundation for Scientific and Industrial Research, SINTEF (Oslo, Norway) took charge of the possible industrial production of SNF recommended process. The viable modified 3D architectures adopted by Fondazione Bruno Kessler, FBK (Italy), Technical Research Centre of Finland, VTT (Finland) and Centro Nacional de Microelectronica, CNM (Spain) in collaboration with large research groups made the 3D Si sensor production simplified and of higher yield. The first simplified 3D Si sensors made at FBK was with single non-passing through columnar electrode ( $n^+$  doped) while the back side was kept uniformly doped with  $p^+$  material (figure 2.12 (a)), that is called 'Single Type Column' 3D detector (3D-STC) [25]. The columnar electrodes remained hollow at this stage. FBK also proposed another 3D-STC detector concept with passing-through columns and back-side, grid-shaped ohmic contact (figure 2.12(b) [25]), which however was never fabricated. A single columnar similar approach was also fabricated at VTT, the only difference being that electrodes were  $p$ -type doped and filled with  $p$ -type poly-Si [26]. Another single type columnar approach was proposed by Brookhaven National Laboratory, BNL (Upton, NY, USA) in collaboration with CNM [27], where the  $p^+$  regions are patterned and implanted on the front-side (figure 2.12 (c)) rather than on the back side.

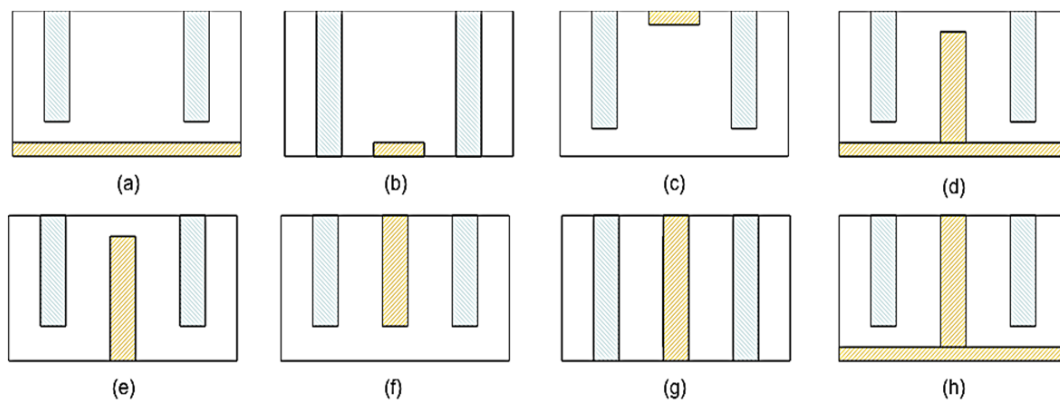


**Figure 2.12:** Schematic cross sections describing the modified 3D detector architectures so far reported: **(a)** single-type column 3D detectors, also called semi-3D detectors, with back-side ohmic contact, independently proposed by FBK [25] (3D-STC) and VTT [26] (Semi-3D); **(b)** an alternate version of (a) with passing-through column, proposed by FBK [25]; **(c)** single-type column 3D detectors with front-side ohmic contact, proposed by BNL/CNM [27]; **(d)** and **(e)** double-sided, double-type column detectors with slightly different back-side configuration, independently proposed by FBK [29] and CNM [30], respectively; **(f)** single-sided, double-type column detector proposed by BNL [31]; **(g)** and **(h)** alternate versions of double-sided, double-type column detectors proposed by FBK featuring passing-through columns [33, 34].

Single type column only 3D Si sensors among all these versions come with a major simplification in the fabrication technology with respect to standard process

followed for full 3D detectors. Evidently, such architectures have to deal the slower response times and limited charge collection efficiency and radiation resistance [28]. The revolutionary Double-type-column 3D detectors (3D-DDTC) were then independently proposed by FBK [29] and CNM [30] as it could be seen in figure 2.12(d) & (e). The fabricated solution of these 3D-DDTC came up with better performance comparing to single columnar type solutions owing to fully shielding property. In both approaches followed by FBK and CNM, columnar electrodes are etched from both wafer sides. In particular to CNM approach (figure (e)), both types of electrodes stop a short distance from the opposite surface. This solution still provides several advantages from the viewpoint of process complexity, owing in particular to the absence of a support wafer. FBK detectors (figure (d)) slightly differ from CNM ones for the fact that they feature a uniform doping layer on the wafer back-side between the ohmic columns in order to feature a singular ohmic contact region. These columns remained hollow rather than being partially filled with poly-Si. Also for double-type-column detectors, BNL proposed a one-sided alternative [31] (figure 3.12(f)), for which, however, no results are available.

The main process steps for the fabrication of 3D-DDTC detectors on n-type substrate at FBK are presented in figure 2.13 [29].

- i. A thick oxide is grown to be used also as a mask for the first DRIE process on the back-side.
- ii. The thick oxide is etched from the back-side and Phosphorus is diffused from a solid source into the columns and at the surface. Later a thin oxide layer is grown to prevent the dopant from diffusing out.
- iii. The oxide layer on the front-side is patterned and DRIE step is performed on the top surface defining readout electrodes.
- iv. The thick oxide is removed from a circular region around columns and boron is diffused into the columns and on the surface to ease the contact formation.
- v. A thin oxide layer is grown to prevent the dopant out-diffusion. Contact holes are defined and etched through the oxide, aluminum is sputtered and patterned.
- vi. A final passivation layer is deposited and patterned to define the access to the metal layer, while on the back-side aluminum is sputtered to have a metal back electrode.

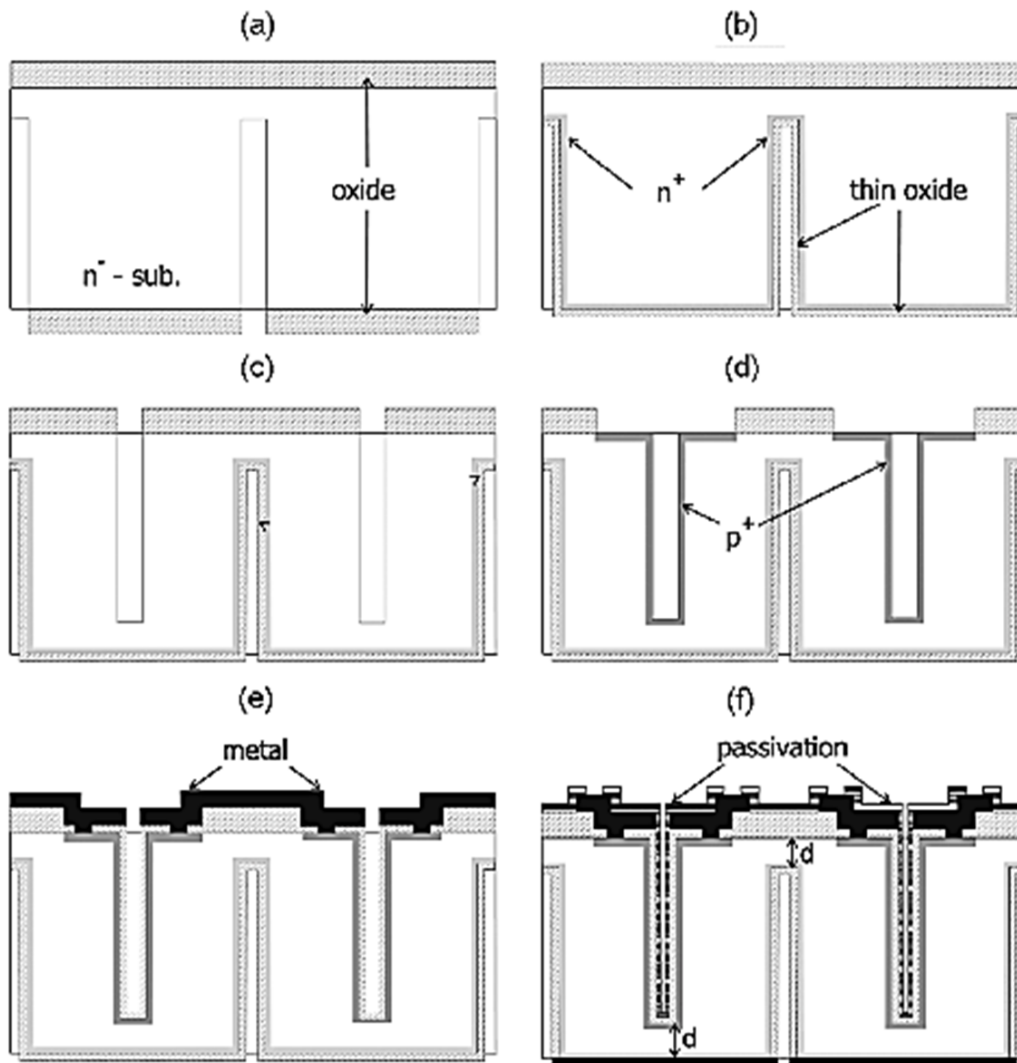


**Figure 2.13:** Schematic of the main steps of the fabrication of 3D-DDTC detectors on n-type substrates at FBK [29].

The fabrication steps for 3D-DDTC detectors made on p-type substrate are similar yet there has been an inversion of the column doping types and an additional process step to implement p-spray surface isolation between n-columns. If p-stop or a combination of p-stop/p-spray are employed, an additional mask for the p-stop patterning is needed. Other designs of 3D-DDTC detector were developed at FBK, as an example the device shown in figure 2.12(g) has passing-through columns of both doping types, are obtained using a relatively thin stack of passivation layers as an etch stop for DRIE [32]. Finally, the device shown of figure 2.12(h) keeps junction columns stopped at a short distance from the opposite surface, whereas ohmic columns remain passing-through. The wafer back-side is uniformly doped in this structure as well in order to facilitate a singular ohmic contact region [33].

## 2.2.3 Experimental Results

### Full 3D Detectors (Stanford)

The first ever electrical characteristics made on 3D detector having p-type 121  $\mu\text{m}$  active thickness reported leakage current densities at around  $1\text{nA}/\text{mm}^3$ , breakdown voltages at around 60V and the full depletion voltage 8V up to 200  $\mu\text{m}$  electrode pitch design [24]. However, values of the capacitance ( $\sim 0.1\text{ pF}/\text{column}$ ) are very close to those numerical predictions [4]. The charge collection characteristics in response to X-rays and  $\beta$  particles are reported first in [34]. This study assured the low charge sharing between adjacent cells with readout shaping time of 1 ns. As of  $\beta$ -scan is concerned, an effective response was demonstrated with combination of coincidental scintillators and fast electronics for  $^{106}\text{Ru}$  source. The first irradiation made on this devices with 24 GeV/c proton for  $5 \times 10^{14}\text{ cm}^{-2}$  accumulated fluence and with 55 MeV protons up to a fluence of  $10^{15}\text{ cm}^{-2}$ . The depletion voltage degraded to 105V for the largest fluence even though leakage current remained in expected level (damage constant rate was  $4 - 5 \times 10^{-17}\text{ A}/\text{cm}$  only) [35]. Some irradiated devices with 55 MeV proton were studied in University of New Mexico demonstrated the active volume extension up to 5  $\mu\text{m}$  for the devices owing the wall-electrodes through infrared microbeam tests [36,37]. This had been an indeed good agreement for the similar study made on planar type sensors, irradiated with 12.5 keV X-ray [38]. Charge collection efficiency reported up to 60% for  $10^{15}\text{ cm}^{-2}$  proton irradiated samples [39]. In another study using 12.65 keV X-ray synchrotron beam reported that the signal for particles passing through columnar dead area are still possible to collect but with a strong reduction in scale, since the induced charges have to diffuse first to the active region of sufficiently high electric field [40, 41].

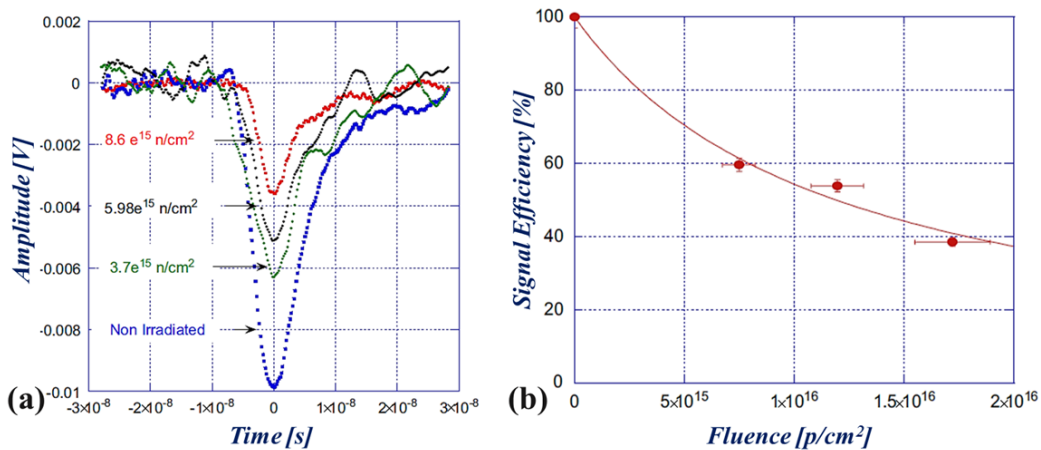


**Figure 2.14:** (a) Averaged (1,000 samples) oscilloscope traces of 3D detector signals in response to fast IR pulses at 1,060-nm wavelength. Data relevant to different irradiation fluences are compared. (b) Signal efficiency of 3D detectors irradiated with neutrons versus the fluence, which was converted to proton equivalent using the Non Ionizing Energy Loss (NIEL) scaling to 24 GeV/c  $\text{cm}^{-2}$  [42].

Figure 2.14 (a) shows the signals of a 3D detector with 71  $\mu\text{m}$  inter-electrode pitch in response to IR laser pulses up to  $8.6 \times 10^{15} \text{ cm}^{-2}$  neutron irradiation fluences [41]. The corresponding Charge Collection Efficiency (CCE) of 24 GeV/c CERN proton irradiated device can also be found in figure 2.14 (b). For the foreseen requirement at the High-Luminosity LHC, CCE is tending to be about 38%. This limitation can be overcome through a device engineering into 3D detectors with narrower pitch between the electrodes [42]. In the same paper, a study of the noise is reported for 3D pixel detectors with different electrode configurations (bump-bonded to the ATLAS FEI3) highlighting the impact of the capacitance dependence upon the number of electrodes.

FE-I3 type 3D pixelated sensors having a test-beam campaign with 100 GeV pion at CERN Super Proton Synchrotron (SPS) reported hit efficiency is  $95.9\% \pm 0.1\%$  for orthogonal incidence of the particles and  $99.9\% \pm 0.1\%$  in case of  $15^\circ$   $\epsilon$  rotation [43]. As an example, figure 2.15 compares the measured Landau distributions of the cluster charge in the two cases with tracks orthogonal to the detector surface (figure 2.15 (a)) and tracks impinging with an inclination of  $15^\circ$  (figure 2.15(b)). Low charge entries affecting the  $0^\circ$  plot due to the non-uniform spatial inefficiency. The broad tails present in the Landau distribution of  $15^\circ$  incidence gave a clear indication that signal charge detection was effectively lower in these devices. Another test-beam campaign made with 24 GeV/c proton reported the device signal efficiency reached up to 21% for 5V bias reference [44].

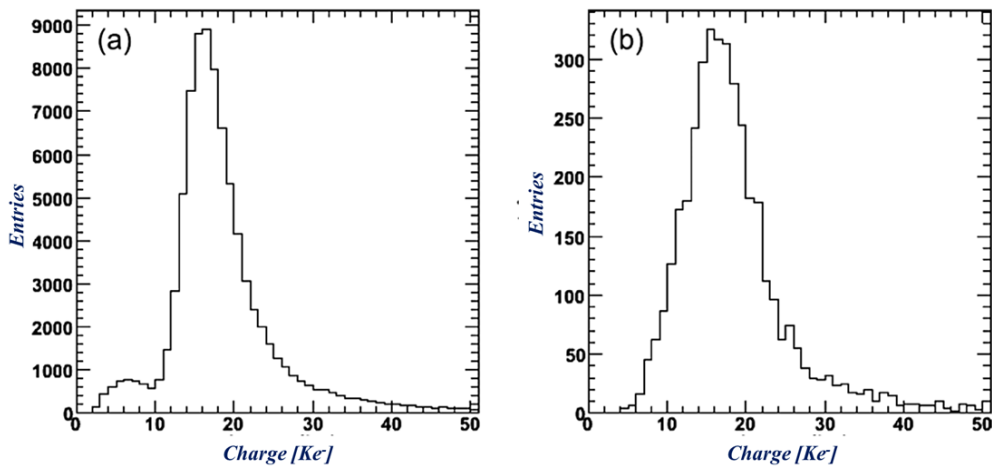


**Figure 2.15:** Measured distributions of cluster charge for 100-GeV pion tracks under different inclination angles: **(a)**  $0^\circ$  angle of incidence (i.e., orthogonal to the detector surface) and **(b)**  $15^\circ$  angle [43].

### 3D-STC (Semi-3D) Detector (FBK, VTT)

For the Semi-3D sensors shown in figure 2.12(a), the full depletion occurs in two stages: lateral depletion in between the columnar electrodes first and then vertical depletion from column tips to backside [45]. Since all columns are of the same doping type, once lateral depletion is reached, the electric field at the very mid-point of

columnar electrodes cannot be further increased, and it depends only on the substrate doping concentration. Signal response for a MIP hitting at semi-3D type structure on the very mid-point of columnar electrodes, is almost 100 times lower than a MIP hitting at semi-3D type structure on impact position near columnar electrode [25]. There is a fast signal component of few ns due to electrons and holes drifting horizontally towards the nearest electrode and towards the center of the structure respectively. The collection time of electrons strongly depends on the impact position, as can be understood from the different peak positions in the two considered cases (figure 2.16). Then, the induced signal has a long tail lasting for several microseconds due to the slow diffusion of holes towards the back plane. This part of the signal does not depend on the impact position. During their motion to the back-side, holes start drifting only when they reach the region below column tips, where the vertical electric field is greater than zero. Due to this slow signal component, ballistic deficit effects can occur in case fast electronics is used for the read-out [25, 46].

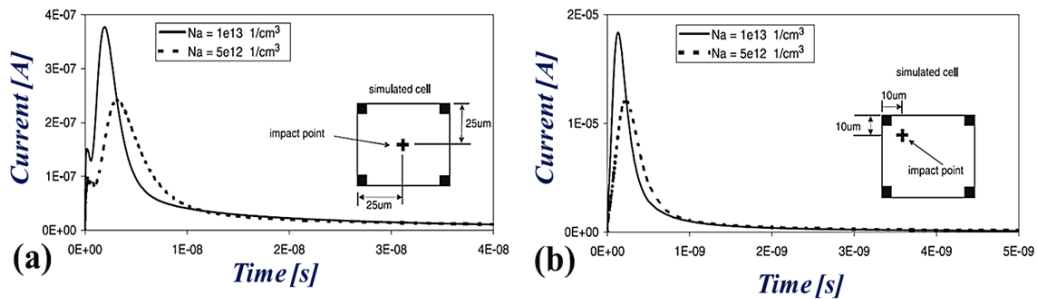


**Figure 2.16:** Simulation of the current signals induced by a MIP particle impinging a 3D-STC detector in two different positions (see insets) [25].

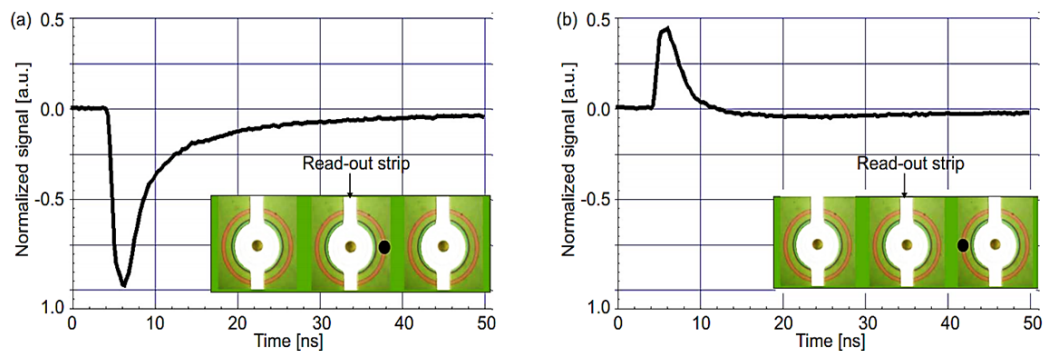


**Figure 2.17:** TCT signal induced on the central strip by a 1060-nm pulsed laser (black spot) in the case of (a) a beam focused near the readout strip and (b) a beam focused near the adjacent strip [46].

Since the fabrication was made an extensive experimental studies was made on this 3D-STC detectors [45,47,48,49,50]. Transient Current Technique (TCT) measurements were performed at JSI with a system based on a 1060 nm pulsed laser for 3D microstrip sensors showed (Figure 2.16) the induced signal response there had been a fast component of few ns and a long tail of few microseconds irrespective to

particle hit, a good agreement with simulations. This behavior is known also for planar strip detectors and can be explained with the aid of Ramo's theorem (see, section 2.1.3). Since the induced signal on the adjacent strip is not negligible, an increased spatial resolution could be obtained in 3D-STC detectors. On the other hand, if the charge is generated underneath a strip rather than in the interstrip region (figure 2.17), the fast signal component would be attenuated since a positive and a negative fast signals would be induced on two columns of the same strip.

Sensors were irradiated up to  $5 \times 10^{15} \text{ cm}^{-2}$  neutrons and up to fluences of  $5 \times 10^{15} \text{ cm}^{-2}$  and exploited through TCT technique, reported signal efficiency reaches around 10% only for particle hit in the same center. Such confirmation of the non-uniform response of 3D-STC detectors gave a clear indication that charge collection efficiency after high irradiation levels could be ever not estimated.

Similar single type column 3D sensors production at VTT reported leakage current density few pA per column at 100 V (well beyond full depletion), per column capacitance  $\sim 90 \text{ fF}$ . Irradiated sample at  $6.0 \times 10^{15} \text{ cm}^{-2}$  CERN PS proton reported the depletion voltage below 100V [51]. However, some sensors bonded with Medipix2 read-out chip reported good imaging properties for 35 keV X-ray [52].

### **3D-DDTC Detector (FBK, CNM)**

3D Double-sided Double-type Column (3D-DDTC) detectors were independently proposed by FBK and CNM in slightly different versions (figure 2.12). This detector concept aims at achieving performance comparable to full 3D detectors while reducing the process complexity. TCAD simulations made 3D-DDTC detector with  $80 \text{ }\mu\text{m}$  pitch for A quarter-volume cell of  $40 \times 40 \times 250 \text{ }\mu\text{m}^3$  between readout columns fabricated on p-type substrate (Figure 2.18 (a)). The substrate doping concentration is  $2 \times 10^{12} \text{ cm}^{-3}$ , oxide charge and p-spray isolation are included as well, with values typical of FBK technology. Different geometries were compared, in order to investigate how the distance  $d$  affects the performance. For the full passing through design ( $d=0$ ) p-spray isolation was included also on the back surface. Figure 2.18(b) is reporting the electric field configuration along the diagonal of the simulated cell of Figure 2.19(a) at 16V (beyond full depletion). As it could be seen, the electric field lines in full 3D are horizontal and very homogeneous between columns, a part from regions close to the surfaces, due to the effect of p-spray. At higher gap, 'd', values, the electric field becomes more distorted and only in a small region at the center the field lines remain comparably similar to those of full 3D. Low field regions near the top and bottom surfaces of 3D-DDTC detectors lead degrading the charge collection efficiency. However, increasing bias voltages beyond the full depletion value increases the electric field between columns and the carrier drift velocity, thus reducing the collection time in compassion to 3D-STC.

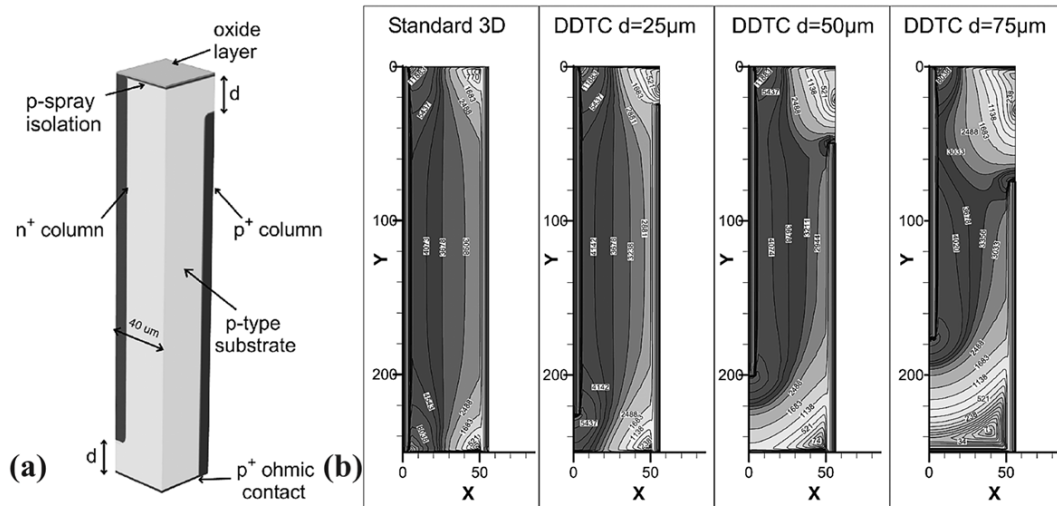


**Figure 2.18:** (a) Sketch of a 3D-DDTC detector of 80  $\mu\text{m}$  pitch on p-type substrate. The cell represents a quarter of typical pattern present in the layout. (b) Electric field distribution of a simulated 2D cross section taken across the diagonal of the quarter cell. The column junction is placed at  $x=0$  and the ohmic column is at  $x=40$ . The four plots (from left to right) are referred to a full 3D and three 3D-DDTC with  $d=25 \mu\text{m}$ ,  $d=50 \mu\text{m}$ ,  $d=75 \mu\text{m}$  [32].

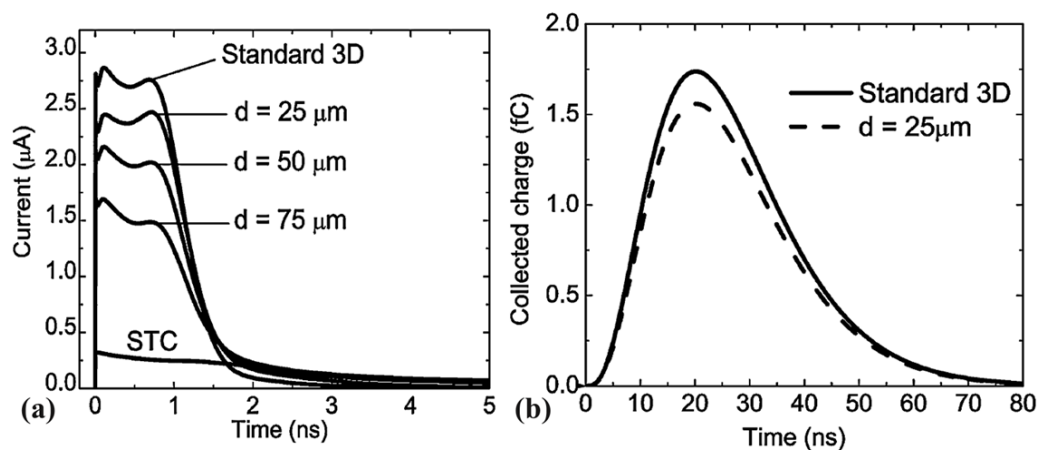


**Figure 2.19:** (a) Transient current signals in 3D detectors with different geometries taken from simulation at a bias of 16V in response to an MIP particle, (b) Simulated transient signals in 3-D detectors of different geometries irradiated at  $10^{16} \text{ cm}^{-2}$  1-MeV neq fluence, at the output of a semi-Gaussian CR-(RC)<sup>3</sup> filter with a shaping time of 20ns [32].

Figure 2.19 shows the induced currents of transient simulation, where a MIP particle impinging the cell at few microns from the ohmic  $p^+$ -column, for junction columns of different depth at 16V. As expected from the static electric field simulations, the shorter is the distance  $d$ , the higher is the current peak and the shorter is the collection time (see, the tails). Simulations accounting for bulk radiation damage ( $10^{16} \text{ cm}^{-2}$  1-MeV neq fluence) were also performed (figure 3.20(b)), demonstrating that full 3D and 3D-DDTC with  $d=25 \mu\text{m}$  yield comparable charge collection efficiency [32]. Another interesting observation of leakage current, depletion voltage, collected

charge, capacitance and related noise in variance of electrode configurations of these 3D detector in comparison to the current ATLAS pixel design was reported in [53].

3D-DDTC detectors fabricated on 300  $\mu\text{m}$  thick n-type substrates at FBK reported very promising results, although the structures were not optimized from the point of view of the column overlap. The reported leakage current were very good,  $\sim 0.1\text{pA/column}$  at full depletion [32]. Functional characterization was carried out on 3D-DDTC strip detectors connected to the ATLAS SCT ABCD3T readout module (20 ns shaping time) with a  $^{90}\text{Sr}$  beta source system. Sensors under test had  $1\text{cm}^2$  area with 102 strips and 102 columns per strip [54] reported higher charge collection efficiency with respect to 3D-STC even if device capacitance was higher in that generation. The tracking performance measured in a beam test was also very good in terms of efficiency, charge sharing and position resolution [55, 57].

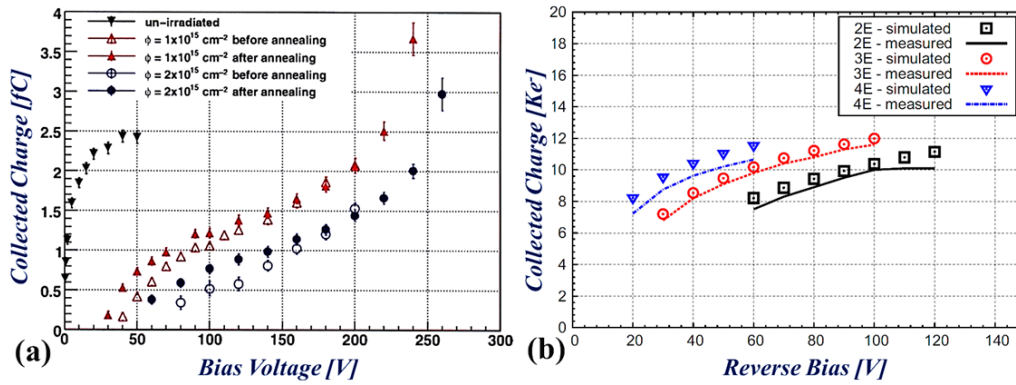


**Figure 2.20:** (a) Charge collection of two 3D-DDTC detectors irradiated with 25-MeV protons at  $1 \times 10^{15} \text{ cm}^{-2}$  and  $2 \times 10^{15} \text{ cm}^{-2}$  fluences. The figure includes data measured before and after an annealing step at  $60^\circ$  for 80 min aimed at taking benefit from the short term annealing [56]. (b) Comparison between measured and simulated collected charge as a function of reverse bias voltage for pixel sensors with different electrode configurations (2E, 3E, 4E) irradiated with 25-MeV protons at  $1 \times 10^{15} \text{ neq cm}^{-2}$  [64].

3D-DDTC detectors were irradiated with 25-MeV protons at three different fluences up to  $2 \times 10^{15} \text{ cm}^{-2}$ . After irradiation the samples were annealed for 80 minutes at  $60^\circ\text{C}$  to exploit beneficial annealing and to reach minimum depletion voltage. Figure 2.20 (a) plots the collected charge for the detectors irradiated at the two higher fluences of  $1 \times 10^{15} \text{ cm}^{-2}$  and  $2 \times 10^{15} \text{ cm}^{-2}$ . It should stress that the annealing step reduced the effective doping concentration as the lateral depletion of both detector occurred at lower voltages after the annealing. Higher trappings made at higher fluences significantly reduce collected charge with respect to the pre-irradiation value. At 150 V bias reference, sensors irradiated at  $1 \times 10^{15} \text{ cm}^{-2}$  and  $2 \times 10^{15} \text{ cm}^{-2}$  can collect up to 1.5 and 1 fC, respectively. Beyond this voltage, all 3D-DDTC detectors exhibit an exponential increase in the collected charge. This phenomenon could be ascribed as avalanche multiplication triggered by particles, possibly enhanced by high electric field effects at the column tips, as predicted by TCAD simulations [58]. The other 3D-DDTC

batches fabricated at FBK on 200-220  $\mu\text{m}$  thick p-type substrates, obtaining a larger column overlap (from 100 to 150  $\mu\text{m}$ ), which allowed for an improvement in the performance [59,60,61,62]. The sensor behavior before irradiation was also assessed in a high energy pion beam test at CERN, with and without a 1.6T magnetic field [63]. The 3D-DDTC performance was found to be comparable to that of full 3D sensors, with no sizeable effect from the magnetic field and very little charge sharing between cells. After irradiation, the performance of the first 3D-DDTC pixel sensors from FBK was limited by the non-optimized column depth, which resulted in the presence of low field regions and charge trapping effects. As an example, figure 2.20(b) shows the collected charge of sensors with different electrode configurations irradiated with 25-MeV protons at  $1 \times 10^{15}$   $\text{neq cm}^{-2}$  and tested with a  $^{90}\text{Sr}$  beta source [66]. As expected, depending on the inter-electrode spacing in characterization of the different configurations, the charge saturates at different reverse bias voltages. The collected charge is in fact in good agreement with TCAD simulations (also shown in figure 2.20(b)) though the signal efficiency remained limited to 70%. These sensors and other sensors irradiated with neutrons up to  $1 \times 10^{15}$   $\text{neq.cm}^{-2}$ , were further characterized in several beam tests that reported good results in terms of hit efficiency, charge collection, and charge sharing [65].

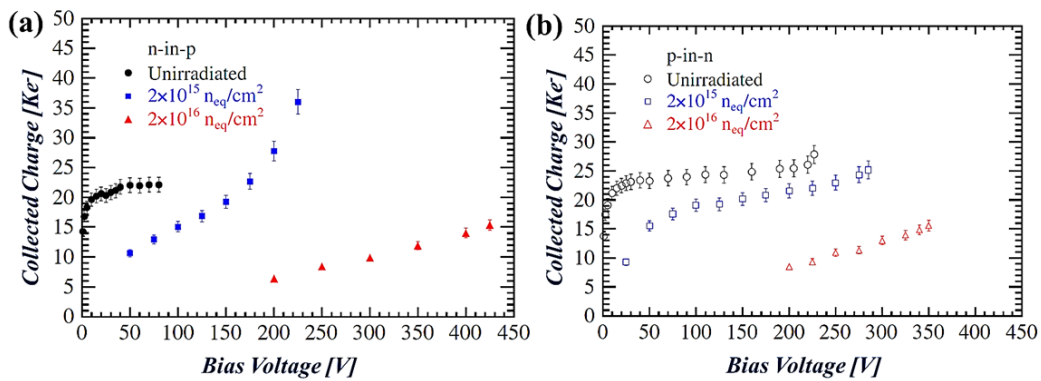


**Figure 2.21:** Signal as a function of the reverse voltage for different irradiation fluences measured with (a) n-in-p sensors and (b) p-in-n sensors. Measurements were performed at temperatures of  $T = -16^\circ\text{C}$  (before irradiation),  $T = -40^\circ\text{C}$  ( $2 \times 10^{15}$   $\text{neq.cm}^{-2}$ ) and  $T = -43^\circ\text{C}$  ( $2 \times 10^{16}$   $\text{neq.cm}^{-2}$ ) [70].

The first results reported for CNM 3D detectors refer to double-sided devices having 250 $\mu\text{m}$  deep electrodes on 300 $\mu\text{m}$  thick, n-type Si wafers. Initial electrical tests show low depletion voltages (a few Volts), good leakage currents ( $\sim 1\text{pA/column}$ ) and breakdown voltages higher than 60V [66,67]. Functional characteristics of pixel detectors bump-bonded to Medipix2 readout are reported in [68]. The result of X-ray campaigns reported the low depletion voltage  $\sim 2\text{V}$  for lateral depletion,  $\sim 9\text{V}$  for full depletion. However, a spectroscopic test using monochromatic 15-keV X-rays from a synchrotron show a substantially reduced charge sharing process with respect to planar detectors. Owing to an optimized column overlap, 3D-DDTC sensors made at CNM showed excellent results after irradiation up to very large fluences. In particular,

sensors in the strip configuration, connected to an Alibava read-out system, were thoroughly tested after irradiation up to  $2 \times 10^{16}$  neq  $\text{cm}^{-2}$  [69,70]. Both p-in-n and n-in-p sensors, with a distance of about  $56 \mu\text{m}$  between n- and p-electrodes, were tested and compared. The collected charge measured as a function of the reverse voltage in different irradiation conditions is reported in figure 2.21. It can be seen that sensors are fully efficient after  $2 \times 10^{15}$  neq. $\text{cm}^{-2}$ . Moreover, due to a charge multiplication effect at high voltage, the signal efficiency exceeds 100% for accumulating  $2 \times 10^{15}$  neq. $\text{cm}^{-2}$  fluence and can still reach 70% at 350 V after  $2 \times 10^{16}$  neq. $\text{cm}^{-2}$  [70]. Higher induced trappings in p-substrate from  $2 \times 10^{16}$  neq. $\text{cm}^{-2}$  campaign made the maximum signal measured limited to  $\sim 15 \text{ Ke}^-$  only.

## 2.2.4 State of Art 3D-DDTC IBL Production

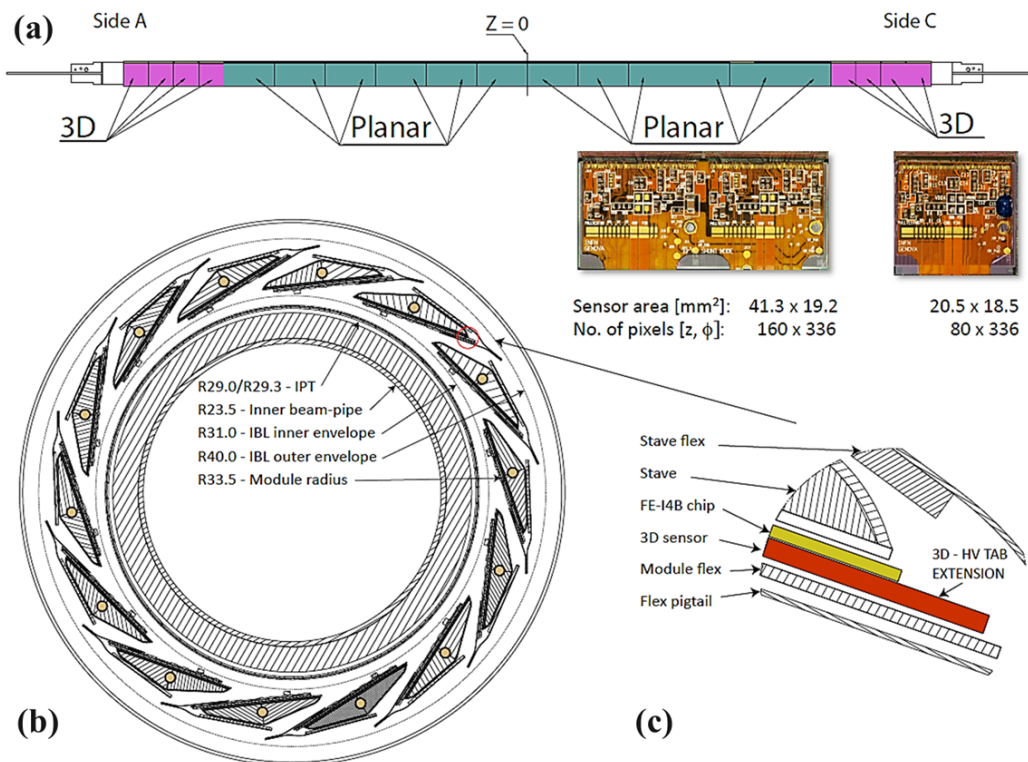


**Figure 2.22:** (a) Stave layout with the organization of planar and 3D sensor modules. (b) Layout of the IBL detector with the 14 staves around the IBL positioning tube (IPT) and (c) zoom of one stave side where a 3D sensor module is visible [91].

Over past few years, a remarkable production maturity has been achieved in the development of 3D sensors, with the great efforts made by the ATLAS 3D Sensor Collaboration over more than a decade [71]. Since 2009, the main efforts were devoted to the ATLAS pixel Insertable B-Layer (IBL), a new pixel layer to be inserted as close as 3.4 cm from the proton beams inside the existing pixel layers of the ATLAS experiment in order to improve the physics performance [72]. In 2011, there was two years long shutdown for IBL installation and the relevant sensor technology was reviewed on the basis of the built module prototypes with planar and 3D sensors. The

measured performance of the 3D module prototypes, before and after irradiation, was convincing in order to include them in IBL. The proposal of a mixed-sensor IBL layout having planar sensors in the central region and 3D in the forward/backward part was aimed to exploit benefit of a more uniform charge collection across the sensor depth during tracking. The IBL layout is shown in figure 2.22. There are 14 staves in a turbine structure; each staff has 12 modules with double-chip planar sensors in the center and 4 forward single-chip 3D sensors at the two extremities. In order to produce the 3D sensors of the required volume for ATLAS IBL, the four 3D silicon processing facilities belonging to the ATLAS 3D Sensor Collaboration (namely SNF, SINTEF, CNM, and FBK) agreed to combine their efforts. A common design and joint processing effort made during this collaboration brought several features: the full mechanical compatibility and equivalent functional performance of the 3D sensors, while maintaining the specific flavors of the different technologies [73]. An improved 3D-DDTC processing for passing-through columns was developed at FBK [32]. The production of 3D pixel sensors cover one quarter of the forward part of the ATLAS IBL staves (112 modules) [77].

All the sensors design were optimized to pixel requirement of FEI4, a readout of 130nm CMOS technology [74]. It contains  $80 \times 336$  pixels having pitch dimension of  $50 \times 250 \mu\text{m}^2$ . Considering the processing within this 3D technology, the large sensor size was a major concern in terms of production yield and so the single sensor tiles were chosen in pairs to be mounted in the modules. Sensors active thickness is  $230 \mu\text{m}$  which has been a good trade-off between signal/noise and mechanical robustness for double-side processing. A more details on this readout can be found in the following chapter.

SNF/SINTEF sensors went with active edge design whereas CNM and FBK sensors exploited the slim edge design in general [76]. In terms of slim edge, FBK design consists of a multiple ohmic column fence where CNM one had a guard ring fence using 3D electrodes, and surrounded by a fence of ohmic columns. Such design actually brings a beneficial feature to sink the leakage current originating from the cut line. Considering the IBL specification of having  $200 \mu\text{m}$  dead region at the edge between sensors in the direction parallel to the beam (Z), all foundries decided to go with slim edge approach.

CNM and FBK sensors features the substrate biasing from the back-side, similar to standard planar sensors. SNF/SINTEF sensors are instead strict in substrate biasing from the front-side, the same side where readout connecting bump bonding is placed. In order to bias the SNF/SINTEF sensors, all sensors were extended on one side by  $\sim 1.5 \text{ mm}$  more for accessing the bias tab beyond the physical edge of the front end chip. Since, both CNM and FBK sensors require biasing through the bias tab at back side, a  $400 \mu\text{m}$  wide edge was implemented.

Bump bonding of the sensor to readout has always been a complex and expensive process, and so it was necessary identifying bad pixel sensors initially. For this purpose, SNF/SINTEF and FBK deposited a temporary aluminum layer which allows current-voltage (I-V) tests to be performed in each tile shorting an array of pixels. The total current can thus be probed. As an example, figure 2.23 shows a comparison between the I-V curves measured on wafer with a temporary metal and on the assembly after bump bonding and flip chip. A very good qualitative agreement is reported. It would worth to notify that the leakage current remained smaller after the front end assembly, that can be anticipated from the additional surface current contribution (MOS effect) caused by the temporary metal [32].

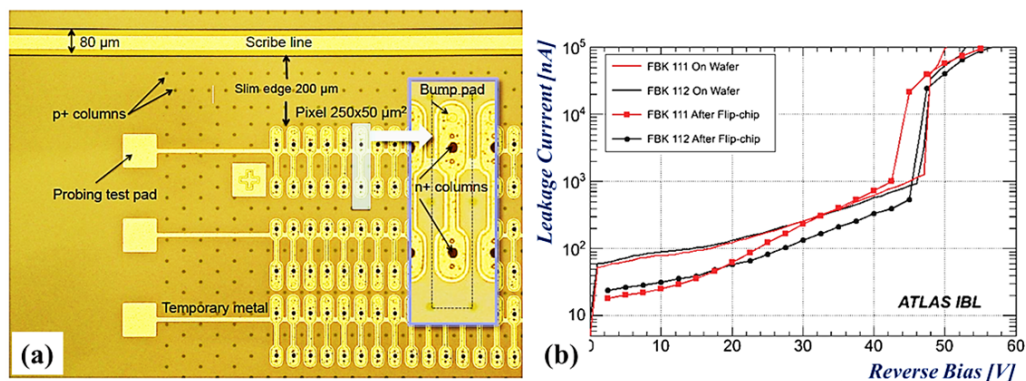


**Figure 2.23:** (a) Temporary metal used at FBK to select the working pixel row at wafer level investigation and (b) comparison of total current versus voltage curves from an FBK sensor measured on wafer with temporary and after bump bonding [76].

The temporary metal pattern used in CNM sensors was not fully compatible with the available testing equipment. The qualification of these sensors was made by guard ring only. However, the technique followed in this case was not accurate since the actual current drawn by the sensor can not be estimated [77]. The qualification phase of these sensors was limited to the installation schedule, fixed for the first long shut down of the LHC in 2013-2014. Thereby, it was not possible to fully exploit the qualification of SNF/SINTEF sensors and FBK and CNM were chosen by the 3D ATLAS Collaboration for the IBL production at the end. The electrical characterization made on the sensors reported the depletion voltage  $V_{\text{depl}}$  less than 15V, breakdown voltage  $V_{\text{bd}}$  greater than 25V whereas the full sensor leakage current was limited to  $2\mu\text{A}$  [73]. Operation voltage was decided around 20 V at  $-15^\circ\text{C}$ . Keeping in account the cost involved in bump bonding, processed wafer that has at least 3 working pixelated sensor was sent for final bump bonding only. Several assemblies of FBK and CNM sensor with FEI4 read-out chip at IZM (Berlin, Germany) were tested both before and after irradiation in laboratory and test beams that reports a maximum leakage current of 100 nA/pixel, a maximum power dissipation of  $200\text{ mW}\cdot\text{cm}^{-2}$ , and an in-time hit efficiency  $> 97\%$  after a benchmark fluence of  $5 \times 10^{15}\text{ n}_{\text{eq}}\cdot\text{cm}^{-2}$  at  $15^\circ$  track inclination angle at  $-15^\circ\text{C}$  [77].

During the IBL qualification, several assemblies were irradiated with protons with 25 MeV protons at KIT, Germany and neutrons up to  $6 \times 10^{15} \text{ neq.cm}^{-2}$  at Ljubljana, Slovenia. Sensors received TID equivalent to  $\sim 750 \text{ Mrad(Si)}$  at proton campaign, a much higher scale than the IBL requirement (250 Mrad). All assemblies were annealed for 120 minutes at  $60^\circ\text{C}$  before testing. Beam tests were also made with 120GeV pions at CERN SPS and with 4GeV positrons at DESY. Both irradiated and non-irradiated assemblies were distributed in different beam test campaigns, where a planar sensor was kept as a reference. Data were taken for both the beam incident to perpendicular to the module, and to a  $\epsilon$  rotation of  $\pm 15^\circ$  [77].

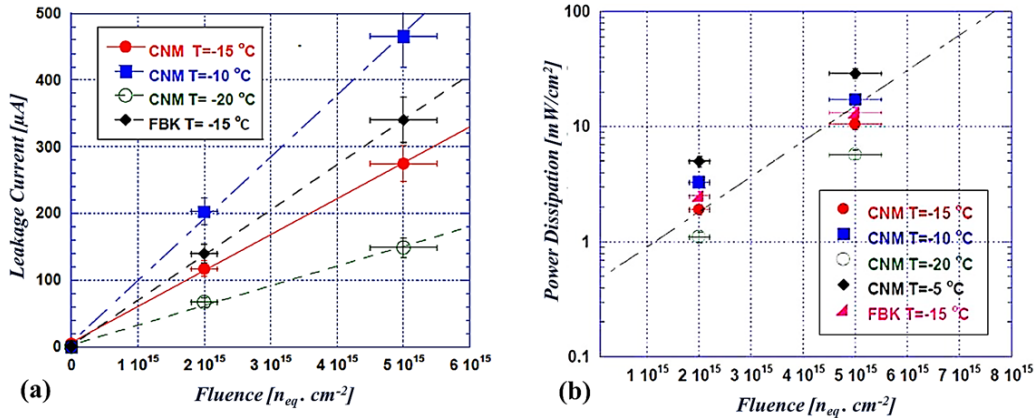


**Figure 2.24:** (a) Leakage current and (b) power dissipation versus fluence at different temperatures for CNM and FBK pixel sensor assemblies irradiated with 25 MeV protons  $-15^\circ\text{C}$  [79].

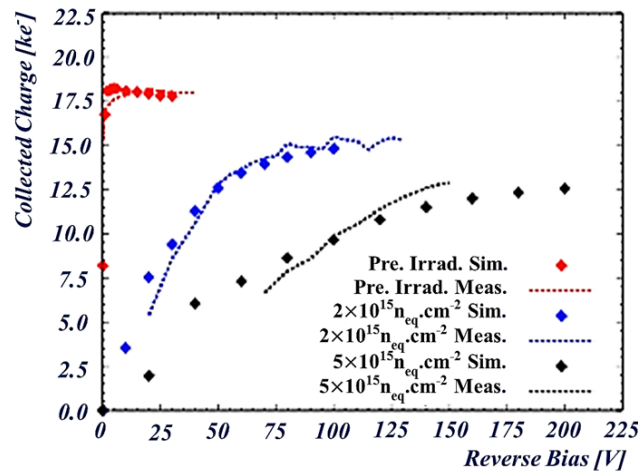


**Figure 2.25:** Comparison between measured and simulated collected charge as a function of reverse bias voltage for IBL pixel sensors from FBK before irradiation and after 25-MeV proton irradiation at  $2 \times 10^{15} \text{ neq.cm}^{-2}$  and  $5 \times 10^{15} \text{ neq.cm}^{-2}$  [80].

Figure 2.24 reports the leakage current and power dissipation as a function of fluence, measured at different temperatures for proton irradiated CNM and FBK sensor based modules [79]. In reference to  $5 \times 10^{15} \text{ neq cm}^{-2}$  fluence, both the power dissipation ( $\sim 15 \text{ mW.cm}^{-2}$ ) and the leakage current ( $\sim 10 \text{ nA/pixel}$ ) remained 10 time

lower than the IBL qualification requirement. 3D sensor modules, although they have higher capacitance of 200 fF per pixel, reported a similar noise level found in planar sensor assemblies (from 150 to 200 e<sup>-</sup>) irrespective to irradiation condition during the measurement made in test-beam and laboratory [76]. Different FBK sensors of IBL generation were exposed to a <sup>90</sup>Sr beta source and the corresponding charge collection as a function of bias voltage is reported in figure 2.25. It is clearly visible that the collected charges reaches to the full saturation plateau at less than 10V (fully depleted). At irradiated condition (5×10<sup>15</sup> cm<sup>-2</sup>), the sensors were able to collect the charges up to 60%, that had been in good agreement with TCAD simulated predictions [80] as it could be seen in the same figure. Simulations were performed with “Perugia” trap model taking account of radiation damage at a set fluence, the inter-electrode spacing and the effective drift length [81,82]. Simulated data plotted in the same figure seconding their validity while being compared with experimental results having account all uncertainty possible: calibration errors, beam uniformity, and annealing conditions [76,78,79,80].

**Table 2.1:** Summary of the main results from the 2011 beam tests at CERN. (\*) Results relevant to FBK87 sensor were obtained from a beam test at DESY in April 2012. All results were obtained with a tuning of 10 ToT at 20 ke<sup>-</sup> signal.

Sensor ID	Bias (V)	Tilt Angle (°)	Irradiation	Fluence (n <sub>eq</sub> cm <sup>-2</sup> )	Threshold (e <sup>-</sup> )	Hit Efficiency (%)
CNM55	20	0	No	-	1600	99.6
FBK13	20	0	No	-	1500	98.8
CNM34	140	0	25-MeV protons	5×10 <sup>15</sup>	1500	97.6
CNM34	160	0	25-MeV protons	5×10 <sup>15</sup>	1500	98.1
CNM97	140	15	25-MeV protons	5×10 <sup>15</sup>	1800	96.6
CNM34	160	15	25-MeV protons	5×10 <sup>15</sup>	1500	99.0
CNM81	160	0	Reactor neutrons	5×10 <sup>15</sup>	1500	97.5
FBK90	60	15	25-MeV protons	2×10 <sup>15</sup>	3200	99.2
FBK11	140	15	25-MeV protons	5×10 <sup>15</sup>	2000	95.6
FBK87(*)	160	15	25-MeV protons	5×10 <sup>15</sup>	1500	98.2

The most important results from the beam tests performed at CERN in 2011 in different assembly arrangements during the module qualification phase has summarized in table 2.1. Non-irradiated samples were measured with perpendicular tracks, where the high efficiency was still achievable already at low voltage due to the smaller inter-electrode spacing in comparison to planar sensor. It is still worth to note that FBK 3D sensors cannot exploit the full efficiency at the condition where particles pass perpendicularly to the assemblies because full passing through columnar are

dead regions. In this respect, CNM sensors perform better than FBK ones because they can collect charge from the regions between the column tips. The hit efficiency is still pretty good also after irradiation and compatible with the IBL specification. Inclined tracks at  $\pm(10-25)^\circ$  increase the hit efficiency. As it can be seen from Table 2.1, increasing the bias voltage from 140 V to 160 V while reducing the threshold to 1500 e<sup>-</sup> allowed for a significant increase of the hit efficiency since the higher electric field at higher bias reference optimize more the charge sharing.

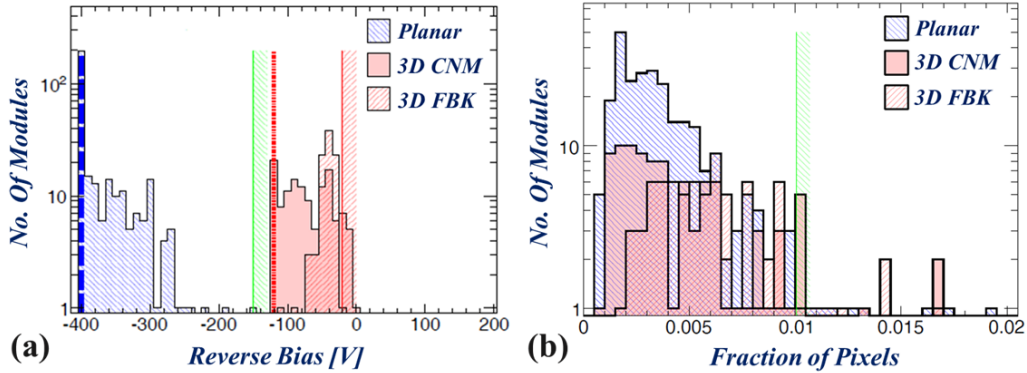


**Figure 2.26:** (a) Distribution of modules' breakdown voltage of different kind of IBL sensors measured with FE chip at room temperature (20°C) during qualification phase. The blue dashed vertical line indicates the maximum measurement bias set for planar sensor (-400 V) and the red dotted indicates the maximum measurement bias set for FBK and CNM 3D Sensors. The acceptance margin for planar sensor was set to be installed (having  $V_{bd}$  greater than 120V) shown as green combo-line, where as it was (30V) for 3D sensors marked with red combo line [72]. (b) The distribution of the fraction of pixels failing in any test of breakdown or <sup>241</sup>Am source scan.

During the qualification phase, sensor breakdown voltage was chosen as a qualifying factor. Figure 2.26 (a) reports the distribution of breakdown voltage for all assembled modules and the set threshold to qualify them finally for IBL installation. Measurements were made with FE-I4 readout keeping current compliance at 10  $\mu$ A. Since the set operating voltage for IBL 3D sensor was 20V, all bump bonded modules having breakdown voltage below 30V were rejected. However, as it is already discussed that the CNM sensor qualification with temporary metal probing was not accurate enough, the distribution of accepted CNM 3D sensor module was quite poor in number as it could be seen from figure 2.26 (a). Aside this CNM sensor were suffering with higher surface generated leakage current, that made the breakdown voltage determination process quite complicated [72]. Hence, a wider distribution for CNM sensor can be observed from figure 2.26(a) in comparison to FBK one. With the accumulated TIDs and bulk damages over the long LHC run, this effect can be mitigated. Bump bonding yield on the sensor module was verified by a functional test using <sup>241</sup>Am source. A pixel was considered as failing if it had less than 5% or more than 450% of the mean pixel occupancy during the test. As an example figure 2.26 (b) is reporting the failing test statistics as per the sensor types. This distribution is taking

account both  $V_{bd}$  test and functional test by  $^{241}\text{Am}$  source. In this case, number of failing per module below 1% were finally chosen for the IBL installation.

## 2.2.5 Applications

Extreme radiation tolerance, low bias voltage and power dissipation, well-defined detection volume, high speed and four-side tiling capability of 3D silicon sensor gave the greater sense to include 3D Si sensor since the first upgrade of pixel system of the ATLAS experiment in 2014 at CERN LHC. This innovative technology can also be used in medical and biological applications to overcome challenges still unresolved by traditional semiconductor imagers. This section is covering some exemplary fields where 3D Si sensors could be an interesting option.

### High Energy Physics (HEP)

As already been discussed earlier, the radiation tolerance of 3D sensors is defined by its geometry. Numerically calculated signal, which can be collected in 3D sensors, shows a direct dependence on the ratio of the carrier trapping time and the distance between the two electrodes. Therefore, the inverse relation between the signal and the sensor's inter-electrode distance suggests, the smaller distance would bring the larger signal. This is possible also in planar sensors. However, in concern of 3D columns placement along the thickness of sensors wafer can therefore bring more compromising radiation hardness properties in terms of collecting the charges at shorter distance.

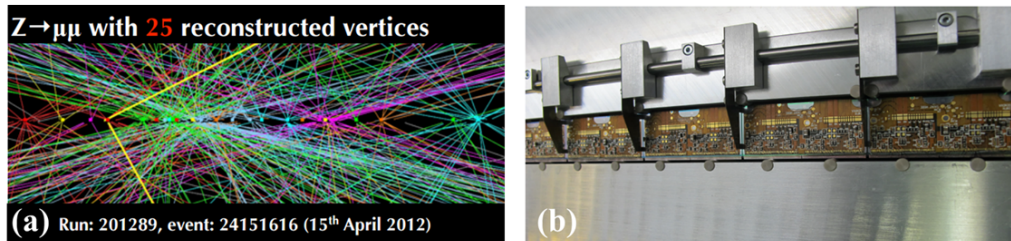


**Figure 2.27:** (a)  $Z \rightarrow \mu\mu$  event (run number 201289, event number 24151616) from 15 April 2012,  $L = 4 \times 10^{33} \text{ cm}^{-2} \text{ s}^{-1}$ , 25 vertices, and (b) a picture of a stave composed by planar and 3D modules (ATLAS Experiment © 2014 CERN ).

High energy physics requires tracking sensor with high speed and 3D sensor is capable to detect signal in time resolution of 31ps [162]. In LHC, proton-proton collision generates an unprecedented amount of particles and it requires very high multiplicity of tracking detectors. As an example of such multiple vertex events from the ATLAS experiment could be seen in figure 2.27 (a) where a  $Z \rightarrow \mu\mu$  event is visible from the 15 April 2012 run with an integrated luminosity of  $4 \times 10^{33} \text{ cm}^{-2} \text{ s}^{-1}$  [83]. Since June 2014, 112 staves of tracking sensors combined with both planar and 3D sensors were installed in the ATLAS Insertable B-Layer. One quarter of them has been the 3D Si sensor and they are placed surrounding the beam pipe at just 3.4 cm away from the beam (figure 2.7(b)).

In addition to the installation of the IBL, 3D sensors could be a fascinating choice for the additional tracking stations in ATLAS, in aim to study the diffractive proton-proton scattering. ATLAS Forward Proton (AFP) detectors have conceptualized to be installed in both upstream and downstream of ATLAS detector in a placement of about 210 m from the ATLAS interaction point, divided into two different detector boxes: one at 206 m and the other at 214 m. In the first station (AFP1) it is planned to install a small pocket containing 6 layers of silicon tracking detectors, to reconstruct the trajectory of the scattered protons. In the second station (AFP2), another pocket containing silicon detectors is planned and, in addition, one containing a timing detector. In diffractive scattering process two protons does not collide, they pass instead so close to each other that the energy exchanged between them create Pomeron like particle with increasing spin. During the formation of Pomeron, proton momentum get changed and to detect these two special protons AFP detector is needed to be placed as close as possible to the beam (at reasonable distance from the point where the two protons met). Extracting the physics information related to the optical properties of these protons is set goal of this target investigation, which requires again the fastest possible detector to ensure that the proton is coming from the core of vertex. Owing the following benefits over planar sensor: smaller inter-electrode distance, higher field uniformity in over depleted condition, the lower  $\delta$ -ray (recoil particle caused by secondary ionization) contribution, 3D sensors should be a greater choice for ATLAS Forward Physics experiments [84].

Chapter 3 is dedicated to give a greater insight on high energy physics experiments of LHC, integrated detector and related readout systems.

### **Medical Imaging**

In the field of X-ray imaging the contrast of specimen identify the object, like the contrast of fat, bone etc., appears differently due to their different densities. The X-ray absorption efficiency process within in the silicon detector depends on its active thicknesses and is strongly dependent on the photon energy. A photon is a massless and neutral particle, for which the interaction mechanisms with semiconductors are Photoelectric, Compton or Pair Production (if their energy is high enough). Depending on the atomic number  $Z$  and the photon energy itself, the required sensor thickness varied within this imaging field. Si is thereby a suitable candidate for the X-ray photon having energy below 20keV. However, all the X-ray imaging systems are using today require photon energy greater than 60keV. In this context, thick planar Si sensor (~1 mm) could not demonstrate a feasible solution to collect all impinging photons, that leads to achieve efficiency up to few percent only. The intrinsic reason behind such anomaly is the active volume that remains partially depleted even at high bias reference. This leads charge carrier (induce from impinging photon) to diffuse first where the most portion of them recombines and so the resultant signal efficiency become quite low. In case of 3D Si sensor architecture, the inter-electrode distance

could be much smaller while maintaining a large active thickness. Exploiting such geometrical efficiency could be a great input to this application. Aside this, shielding effect enabled within the neighboring pixels will bring another optimization to the better image quality [85].

### Micro-Dosimetry

Irradiation exposure is dangerous to human health in general concept while its usage to cancer cell is known to be a revolutionary remedy. However, it is eminent to predict the associated risk caused by the radiation and to understand the radiobiological properties of the radiation absorbed by our tissues for which dosimetry type instrument is used widely. In this context, microdosimetry-approach involves measuring the probabilistic lineal energy deposition in the applied specimen on event basis. The device deals the energy deposition on micron scale volume, a very close dimension of human cell. Charge particle induce from irradiation could be either from impinging radiative particle or the secondary interaction possible with nucleus. Fine spatial monitoring possible in micron regime, microdosimetry helps to control the required dose in aim to be deposited into the tumor cells only, without effecting surrounding healthy tissues. Pioneering work of this type of device was performed by Anatoly Rozenfeld and his co-workers at the University of Wollongong in Australia.

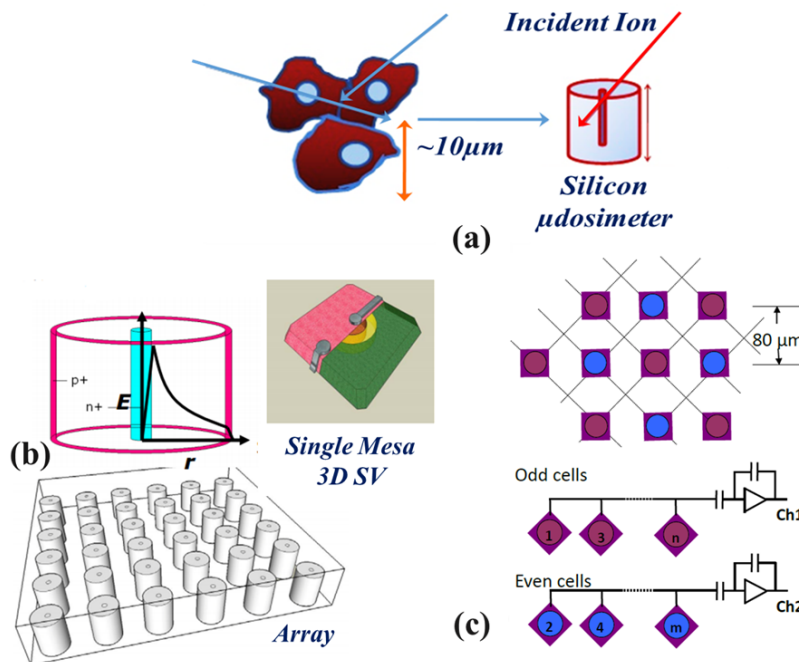


**Figure 2.28:** (a) A micro-dosimetry with molecular sized Sensitive Volume (SV), (b) 3D Si coaxial Array fabricated in SNF, USA, and (c) A schematic of the design of the array of 3D sensing elements [86].

Active edge 3D Si sensors could be an interesting choice in this context because of the geometrical advantages where sensing volume can be defined in more aggressive way in comparison to planar sensor. In planar process, it is not possible

pattern the surface anymore than 1-2  $\mu\text{m}$  whereas 3D technology avails forming the electrodes within entire substrate. A coaxial schematic of 3D micro dosimetry cell is reported in figure 2.28 (a), where junction column is formed as 3D electrode and ohmic column remains as p-type trench. An array combination of such 3D silicon coaxial structure is shown in figure 2.27(b), that would enhance the signal output collecting charge all together by using a fast readout electronics chip. The readout chip holds two independent channel connected even and odd 3D cell respectively, to track the position of impinging particle. A schematic of this concept is reported in figure 2.28 (c). A mushroom type 3D structure forming junction column by DRIE process into 10  $\mu\text{m}$  thick SOI wafer being filled with poly-silicon while p-type ohmic trench fabricated surround the junction column is recently being investigated at SINTEF, Norway. The aim of this development would be studying in relative biological effectiveness in neutron field of aviation, space and accelerating science.

### **Neutron Detection**

Through the therapeutic irradiation, many secondary particles are produced by the beam interacting with tissues in the patient body. The correlation between the beam energy loss and the emission point, allows to monitor the dose delivery and the beam range by sensing the generated secondary radiation. Among the produced secondary charged particles, photons from  $\beta^+$  annihilation and prompt gammas production have already been well investigated. Still, to date, nothing fully efficient experimental characterization of the abundant secondary neutron could be made due to not having highly efficient neutron detector in the field medical imaging. The neutron tracking principle is based on the reconstruction of two consequent elastic scattering interactions of a neutron with a target tissue [87]. In case of an elastic scattering interaction with a hydrogen nucleus, the neutron and the scattered proton momenta are correlated. Thus one can obtain the energy of the incoming neutron by reconstructing the kinematics of the photon originated from a neutron-photon interaction. In the field of neutron-based nuclear medicine and diffraction techniques, the detection of neutron with spatial resolution of  $\sim 100 \mu\text{m}$  is desirable. The challenge is the active characterization in radiotherapy environments because the radiative pulse remains as a mixed form of neutron and  $\gamma$ -ray background. Typical planar neutron Si sensors have  $\sim 10 \mu\text{m}$  thickness, allows a high  $\gamma$  rejection, that is eminent to segregate the neutron signal from neutron-  $\gamma$  combo-pulse. Moreover, a scattering and capture reaction is required in sensors active region to detect the incident neutron, so it may lead to the generation of e-h pairs to be collected. In order to make it possible  $^{10}\text{Boron}$  or  $^6\text{Lithium-fluoride}$  like moderator is used. However the highest reported efficiency remains less than 5% in the planar-sensor context [88]. In 3D architecture shown in figure 2.29, composed with neutron converting materials, avails the scattering interaction process more between incident neutron with moderator as well as the thin

Si slab remains from  $n^+$  electrode to back  $p^+$  electrode ensures high  $\gamma$  rejection. Such kind of 3D optimization could enhance the neutron detection efficiency up to 50% [89].

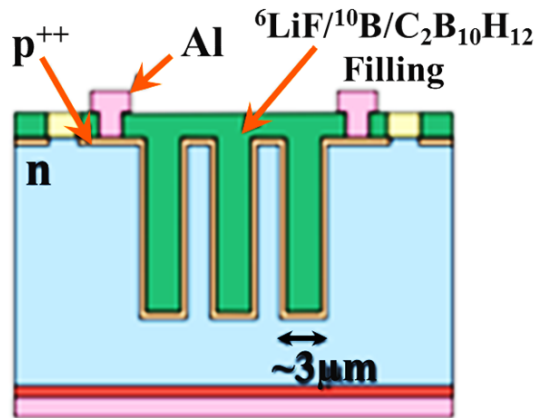


**Figure 2.29:** Schematic cross section of a 3D sensor for neutron detection [89].

Since the introduction of 3D detection technology almost 20 years back, it has reached today an emerging candidate to cope with the challenging demands of future HEP experiments. Results reported in this chapter gave a solid impression of 3D Si sensors in terms of signal efficiency, speed, and radiation hardness. Owing to the active edge feature, sensitivity to within few micrometers from the physical edge opens the way to be a special interest with imaging domain. The increased noise due to a higher electrode capacitance was shown to be tolerated by properly designed readout chips and actually overcompensated by a superior signal robustness. From chapter 4 to onwards, the advanced R&D made recent years to achieve the extreme hardness within these detector as per the requirement of HL-LHC shall bring more exciting insights.

## Chapter III

### High Energy Physics at CERN

High Energy Physics (HEP) holds quite a broad research domain, covering by heterogeneous science drivers to explore the elementary particles of matter and energy, their interactions and their nature in space and time. Its execution is spanned in three main edges: experimental innovation, and their related efforts in theory and computation. However, it also advances new accelerator, detector and computational tools for enabling the science, and making them available to the wider audience. This thesis work contributed to the development of next generation of detectors aimed at CERN HL-LHC.

#### 3.1 *Large Hadron Collider*

The Large Hadron Collider (LHC) is the largest and most powerful yet particle accelerator in the world, founded between 1998 and 2008 with the strong collaboration of European organization of nuclear research, named Conseil Européen pour la Recherche Nucléaire (CERN). The main objective of the accelerator is to experimentally investigate and validate the derived particles through supersymmetry theories. It also gives the opportunity to experimentally investigate the theories relevant to Higgs, Dark Matter extra dimension, etc. The accelerator consists of 27km long and 3.7m wide undergrounded two rings of the superconducting proton-proton collider, that evolved from the Large Electron-Positron Collider (LEP) from 2000 [90]. The evolution of LHC alike proton machine over LEP does not have the same synchrotron radiation problem and would ideally have longer arcs and shorter straight sections for the same circumference where the already built was a cost-effective solution. The superconductive RF cavities and electromagnets at 2 K and lower temperature have been used in the design by imposing Helium for compensating the monotonously decreasing superconductivity with increasing magnetic field. The enhanced heat transport property, the low bulk viscosity, enables Helium to permeate to the heart of magnet windings and maintain the thermal stabilization during LHC operation.

One of the aims of the LHC remains that to reveal the physics beyond the Standard Model with centre of mass collision energies of up to 14 TeV and unprecedented luminosity ( $10^{34} \text{ cm}^{-2}\text{s}^{-1}$ ). This interest is to study the number of events per second, generated in the LHC collisions given by:

$$N_{event} = L\sigma_{event} \quad (3.1)$$

where  $\sigma_{event}$  is the cross section for the event under study and  $L$  is the machine luminosity. The machine luminosity depends only on the beam parameters and can be written for a Gaussian beam distribution as:

$$L = \frac{N_b^2 n_b f_{rev} \gamma_r}{4\pi \varepsilon_n \beta^*} F \quad (3.2)$$

where  $N_b$  is the number of particles per bunch,  $n_b$  is the number of bunches per beam,  $f_{rev}$  is the revolution frequency,  $\gamma_r$  is the relativistic gamma factor,  $\varepsilon_n$  is the normalized transverse beam emittance,  $\beta^*$  is the beta function at the collision point, and  $F$  is the geometric luminosity reduction factor due to the crossing angle at the interaction point (IP), which in turn is given by:

$$F = \left( 1 + \left( \frac{\theta_c \sigma_z}{2\sigma^*} \right)^2 \right)^{-\frac{1}{2}} \quad (3.2).$$

Here  $\theta_c$  is the full crossing angle at the IP,  $\sigma_z$  is the RMS bunch length, and  $\sigma^*$  is the transverse RMS beam size at the IP. The above expression assumes round beams, with  $\sigma_z \ll \beta$ , and with equal beam parameters for both beams. In order to investigate the rare events from LHC collisions, both high beam energies and high beam intensities are required.

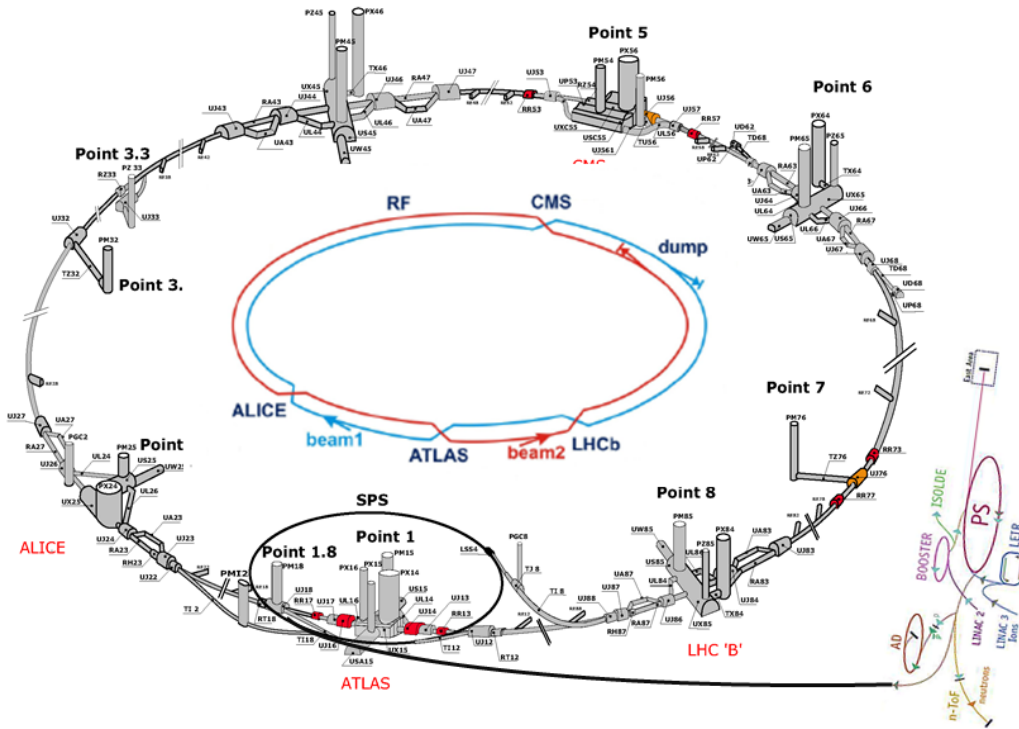


**Figure 3.1:** LHC Layout. Inset of the bigger ring showing the two parallel beam lines and four collision points of dedicated experiments: ATLAS, CMS, ALICE and LHCb [91].

The basic layout of current LHC is reported in figure 3.1. The LHC is equipped with eight arcs and eight straight sections. Four of the straight sections host the LHC experiments whereas the other four are used for auxiliary services and beam abort. Two of the straight sections (points 1 and 5 in Figure 3.1) host the **A Toroidal LHC**

**Apparatus** (ATLAS) detector and the **Compact Muon Solenoid** (CMS) detector respectively with collaboration of **Large Hadron Collider forward** (LHCf) at point 1 and **TOTAL** cross section, **Elastic scattering and diffraction dissociation Measurement** at the LHC (TOTEM) at point 5. The other two experiments, **A Large Ion Collider Experiments** (ALICE) and **Large Hadron Collider beauty** (LHCb), are placed at point 2 and point 8 respectively for studying the outcome of the sizable collision between Pb-Pb and p-Pb. Pb-Pb collision is made with a design luminosity of  $10^{27}\text{cm}^{-2}\text{s}^{-1}$  at the center of mass energy of 5.5 TeV per nucleon pair to produce the tiny quantities of such matter. They are known as the quark-gluon plasma, and studying them leads to understand the evolution of universe today. LHCb instead studies the charge parity violation of b-hadrons in order to explain the Matter-Antimatter asymmetry of the universe. The ring is composed by 9600 magnets in combination of dipoles, quadrupoles, sextupoles, octupoles, decapoles, etc., among which 1232 dipole magnets are used to maintain particles in a circular path. The higher order multiple magnets are used for focusing the beam in order to enhance the particle interactions in four intersection points of dedicated experiments.

The CERN accelerator is a complex system that accelerates particles to higher energies on the successive increasing orders. Each singular component of LHC boosts the beam energy, before transferring the beam into the next one in the successive accelerating sequence. In the Large Hadron Collider (LHC), the last accelerating component of this gigantic instrument, beams are accelerated up to the record energy of 6.5 TeV. Bottle of hydrogen gas works as the source of protons where an electric field is used to strip hydrogen atoms to yield protons only. Linac 2, the first accelerator in the chain, accelerates the protons in order to achieve the energy of 50 MeV. The beam is then pushed into the Proton Synchrotron Booster (PSB) and reaches 1.4 GeV energy scale. Later, Proton Synchrotron (PS) boosts the beam to 25 GeV scale and forwards it into the Super Proton Synchrotron (SPS). Here, the accelerated protons gain energy up to 450 GeV. The protons are finally transferred to the two beam pipes of the LHC, where one beam circulates clockwise while the other one circulates in anticlockwise fashion. The whole process requires 4 minutes and 20 seconds to fill singular LHC ring, and 20 minutes in total to reach their maximum energy for the protons (~6.5 TeV). Under normal operating condition, beams can be circulated for long periods of time. Once the beams reach to the targeted highest energy, they are directed into four colliding nodes, which are ALICE, ATLAS, CMS and LHCb detectors. The total energy at the collision point becomes 13 TeV.

### **3.2 Upgrades of LHC**

LHC-CERN has achieved a new record for energy levels by having proton-proton collision successfully at a huge 13 trillion electron volts, by year 2016. The prior highest energy reported was 8 TeV in 2012. Factually, as soon as the collider reaches

to its highest operational performance, experiments open the platform to be fully probed in the TeV energy scale. In this capacity, it leads to explore the electroweak symmetry breaking and the Higgs phenomenon and also opens new possibilities for super-symmetry, extra dimensions of space and time, and other “Beyond the Standard Model (BSM)” physics.

The LHC began its operation in late 2009 and had been producing collisions at 6.5 TeV center of mass energy until the end of 2011. During the Phase-0 upgrade, there had been the first long shutdown from the beginning of 2013 to the end of 2014. The machine was optimized to reach the nominal luminosity up to  $10^{34} \text{ cm}^{-2}\text{s}^{-1}$ , with center mass energy up to 14 TeV and 25ns bunch spacing. The primary modifications made during this long technical shutdown were relevant to the machine enhancement in order to reach the maximum performance without making massive mechanical upgradation in tunnel, i.e., the inclusion of Insertable B-Layer. In accordance to the CERN technical report released in July of 2010, more significant modifications shall be made in coming years in order to comply with the luminosity growth to much higher values than the current one.

In forthcoming Phase ‘1’ upgrade, there shall be the second long technical shut down, which is expected from 2018 to 2020. In this period, the detector and the corresponding compatible readout like electronics will be changed in order to exploit the upcoming luminosity  $2 \times 10^{34} \text{ cm}^{-2}\text{s}^{-1}$  with the center mass energy up to 14 TeV and at 25 ns bunch spacing. No major hardware swap is still being expected at this stage to LHC tunnel architecture.

In the ultimate upgrade of ‘Phase 2’ after 2022, there will be a major machine upgrade with an extended shutdown. This upgrade targets to achieve considerably higher values of integrated luminosity, possibly 5 times higher than the one achieved at the end of Phase 1. The energy of center of mass shall still remain 14 TeV. However, LHC would eventually need an upgrade to increase the total number of collisions by a factor of 10. The more powerful future-LHC would provide more accurate measurements of new particles and enable observation of rare processes that remain still unexplored below the present sensitivity level.

The focus of this thesis is the development of thin and small pitch 3D radiation Si sensors that will eventually be deployed at HL-LHC environment after necessary qualification phase into the ATLAS Inner Tracker (ITk) and CMS Silicon Tracker particle detectors.

### **3.3 ATLAS Experiment**

ATLAS is one of the four major experiments at LHC. It runs general-purpose particle physics experiment within a wide international collaboration. Together with CMS, it has been designed and upgraded to exploit the full discovery potential in the

huge range of physics fields, especially in particle physics. ATLAS physicists test the predictions of the Standard Particle Model, which helps the current understanding of building blocks of matter and their process of interaction. These studies can lead to ground-breaking discoveries, such as the state of art LHC discovery of the Higgs boson presence. They also open the platforms to think beyond the Standard Model and the related development of new theories.

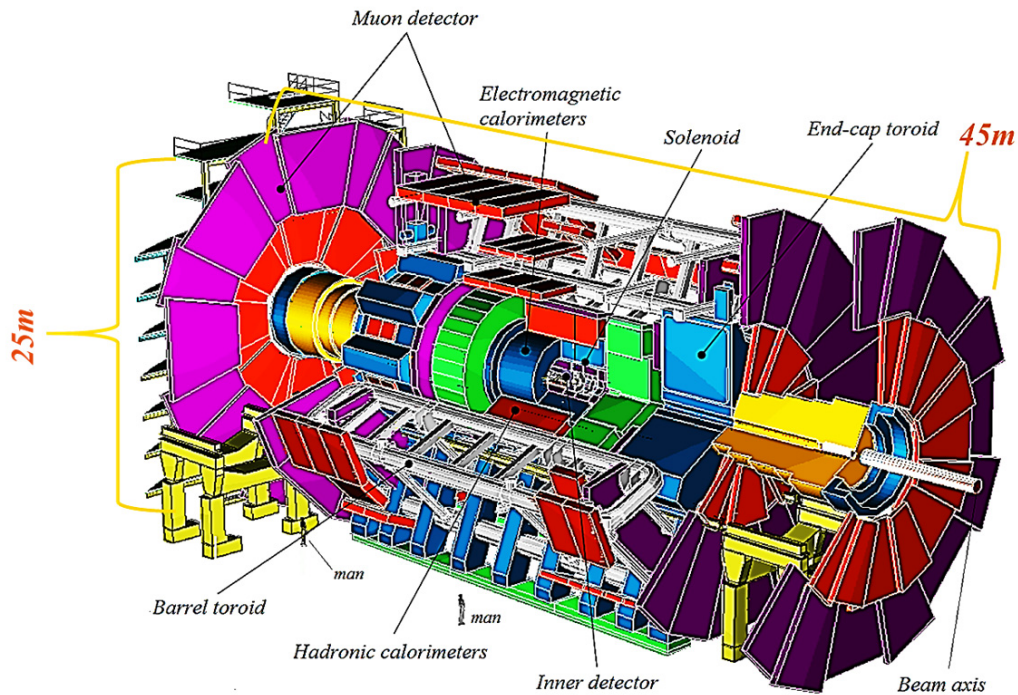


**Figure 3.2:** Schematics of ATLAS particle detector layout [91].

The heart of this experiment consists of an immensely complex machine, which is 45m long, 25m wide in diameter and has weight around 7,000 tons (Figure 3.2). ATLAS detector is a many-layered instrument designed to detect some of the tiniest yet most energetic particles ever created on earth. It consists of six different detecting subsystems wrapped concentrically in layers. Around the collision point, this detector helps to record the trajectory, momentum, and energy of particles, allowing them to be individually identified and measured. A huge magnet system used in the system bends the paths of the charged particles, so that their momenta can be measured as precisely as possible.

### 3.3.1 Components of ATLAS Particle Detector

The ATLAS detector is nominally forward-backward symmetric with respect to the interaction point. The magnet configuration comprises a thin superconducting solenoid surrounding the inner-detector cavity, and three large superconducting toroids (one barrel and two end-caps). An eight-fold azimuthal symmetry is present around the calorimeters. Tracking, calorimetry and muon spectrometry are the three main prime performances of this particle detector.

## Inner Detector (ID)

The inner detector is the first part of ATLAS to see the decay products of the collisions, so it is very compact and highly sensitive. It consists of three different systems of sensors: pixel detector, semiconductor tracker (SCT), and transition radiation tracker (TRT). All of them are integrated into a magnetic field, parallel to the beam axis. The Inner Detector measures the direction, momentum, and charge of electrically-charged particles produced from each proton-proton collision.

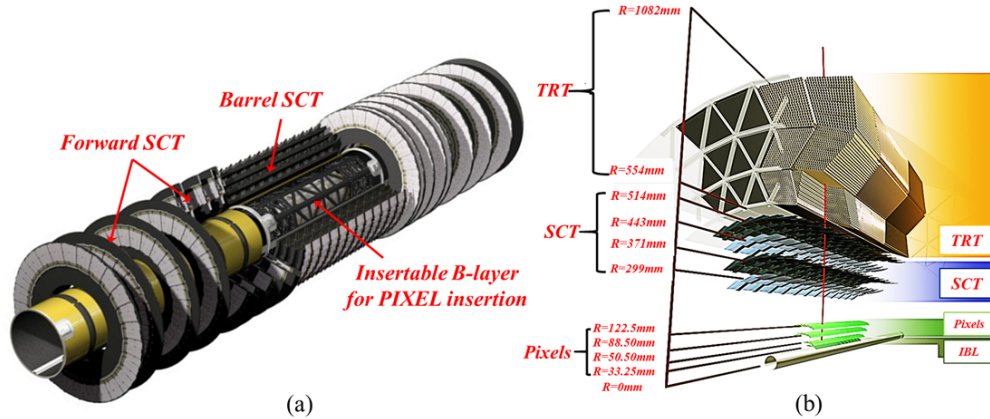


**Figure 3.3:** Sensor topology of the ATLAS inner detector (a) and cross-section of the inner detector with inclusion of TRT and Insertable B-layer (IBL) [91].

The inner detector combines high-resolution detectors at inner radii and the continuous tracking elements at the outer radii. All are contained in the central solenoid, which provides a nominal field of 2 T. The highest granularity is achieved around the vertex region using semiconductor pixel detectors followed by silicon microstrip detectors. Typically for each track, the pixel detector contributes three space points and the strips contribute additional four. At the larger radii, typically 36 tracking points can be observed by the straw tube tracker. The relative precision of the measurement is well matched so that no single measurement dominates the momentum resolution. The outer radius of the inner detector is 1.15 m and the total length 7 m. In the barrel region, the high-precision detectors are arranged in concentric cylinders around the beam axis, while the end-cap detectors are mounted on disks perpendicular to the beam axis. The barrel TRT straws and all end-cap tracking elements are located in planes parallel to the beam direction. Details of different layers deposition are presented in figure 3.3.

Inner Detectors are dedicatedly installed to find the short-lived particles such as B-hadrons. The system consists of three barrels at average radii of  $\sim 5$  cm, 9 cm, and 12 cm (1456 modules), and three disks on each side, between radii of 9 and 15 cm (288 modules). Each module is 62.4 mm long and 21.4 mm wide, with 46,080 pixel elements read out by 16 chips, each is serving an array of 18 by 160 pixels. The 80 million pixels cover an area of 1.7 m<sup>2</sup>. These integrated readout chips were qualified to withstand over 300 kGy of ionizing radiation (over  $5 \times 10^{14}$  n<sub>eq</sub> cm<sup>-2</sup>) over ten years

of operation. The modules are overlapped on the support structure to give hermetic coverage. The thickness of each layer is expected to be about 2.5% of a radiation length at normal incidence. Since the Insertable B-layer is the state art layer integrated with 3D Si Sensors, details of it are presented in a separate section below.

The SCT system is designed to provide eight precision measurements per track in the intermediate radial range to investigate the measurement of momentum, impact parameter and vertex position. In the barrel SCT, there have been eight layers of silicon microstrip detectors which provide a precision point in the  $r$ - $\phi$  and  $z$  coordinates. Each silicon detector is  $6.36 \times 6.40 \text{ cm}^2$  in size having 780 readout strips of  $80 \text{ }\mu\text{m}$  pitch. The barrel modules are mounted on carbon-fiber cylinders at radii of 30.0, 37.3, 44.7, and 52.0 cm. The end-cap modules are very similar in construction but use tapered strips with one set aligned radially. Since the primary objective of this thesis remains semiconductor detectors, both the Pixel Detector and Semi-Conductor Tracker shall be explained in 3.3.2 and 3.3.3 in extensive format.

Transition radiation Tracker (TRT) [92] is based on the use of straw detectors, which can operate at the expected high rates due to their small diameter and the isolation of the sense wires within individual gas volumes. Electron identification capability is added by employing Xe gas to detect transition radiation photons created in a radiator between the straws. Each straw is 4 mm in diameter and equipped with a  $30 \text{ }\mu\text{m}$  diameter gold-plated W-Re wire. The maximum straw length is 144 cm in the barrel, which contains about 50,000 straws. The end-caps contain 320,000 radial straws, with the readout at the outer radius. The total number of channels that are read out is 420,000. Each channel provides a drift time measurement, giving a spatial resolution of  $170 \text{ }\mu\text{m}$  per straw, and two independent thresholds. These allow the detector to discriminate between tracking hits, which pass the lower threshold, and the transition radiation hit, which passes the higher one.

### **Insertable B-Layer (IBL)**

In order to amplify the precision in vertex reconstruction especially increasing the b-tagging efficiency, a new pixel layer IBL has been installed in the first long shutdown between 2013 and 2014. The layer has been mounted between the pixel B-layer and the beam pipe. Initially, the old envelope allowed only 8.5mm of radial free space, too narrow for the insertion of a new layer. Hence, a newer beam pipe with reduced diameter was replaced within the IBL volume (which contains the staves and the services). This volume holds the space between the inner positioning tube (IPT), a precision mechanical support and the external inner support tube (IST) fixed on the pixel structure. This design features the fast removal of IBL packages or the beam components. While the existing pixel sensors were being repaired during 2014, the IBL layer including the newer beam pipe was installed into their respective positions. A schematic of the entire ATLAS tracking system is presented in figure 3.4 where the IBL layer is highlighted with red rectangular boundary.

There have been 14 staves having length 330.15 mm occupying 32 front ends per staff. Each staff is holding 20 modules among which 8 are based on 3D sensors. In order to minimize the dead region, modules are glued on the staff with a physical gap of 200  $\mu\text{m}$  in between. Staves are in 14° tilting position with 1.82° overlaps. For geometrical reasons, 3D sensors are less affected by charge drifting through Lorentz angle, whereas the staff inclination is quite beneficial for the installed planar sensors at IBL. However, this also helps to increase the charge collection efficiency of 3D modules from the perpendicular track incidence to the columnar dead regions. The IBL has been placed 33.5 mm away from the interaction point covering a pseudorapidity,  $\eta$  less than 3. The r- $\phi$  view and the staff schematic of IBL layer can be found in figure 3.4. Moreover, a zoomed inset of cylindrically arranged IBL module is given in figure 3.5.

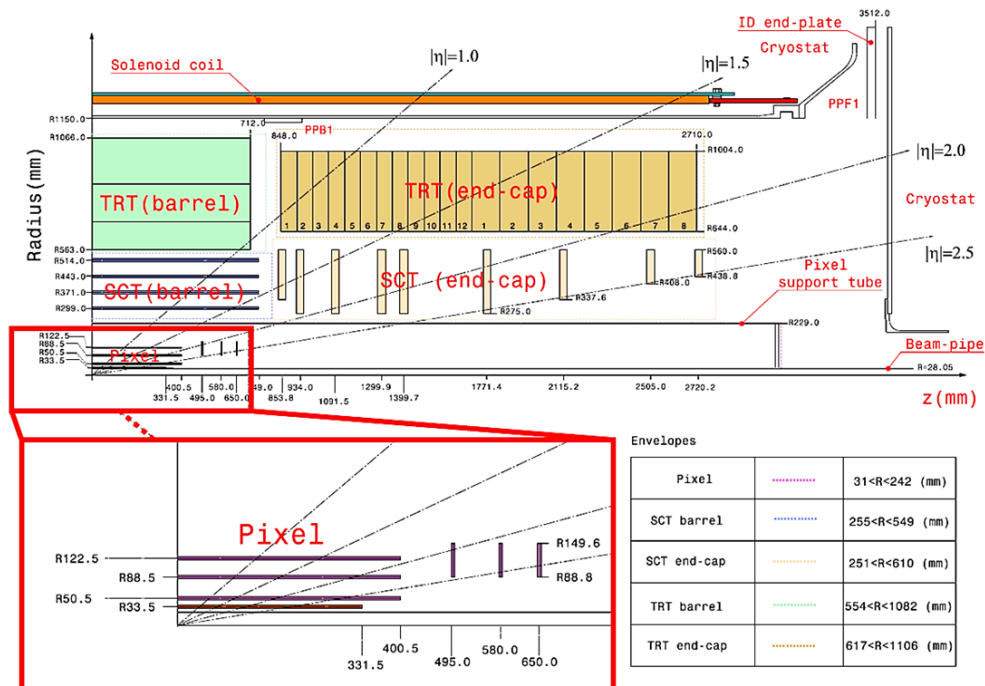


Figure 3.4: The upgraded ATLAS tracking system with Insertable B-Layer (IBL).

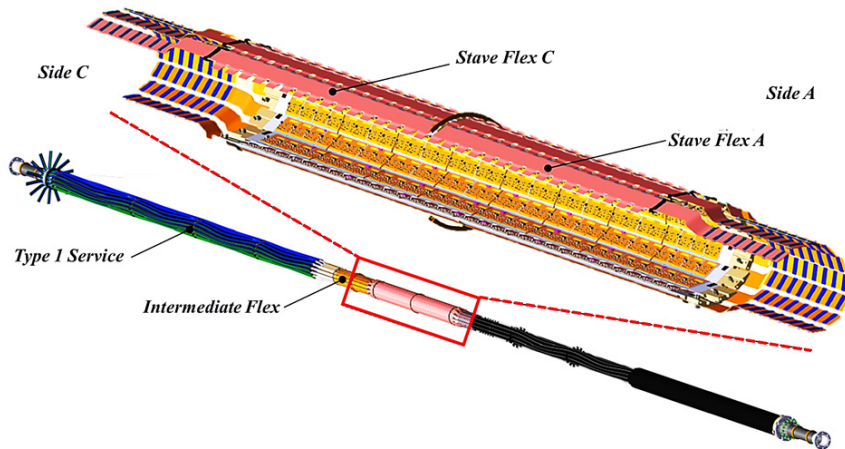
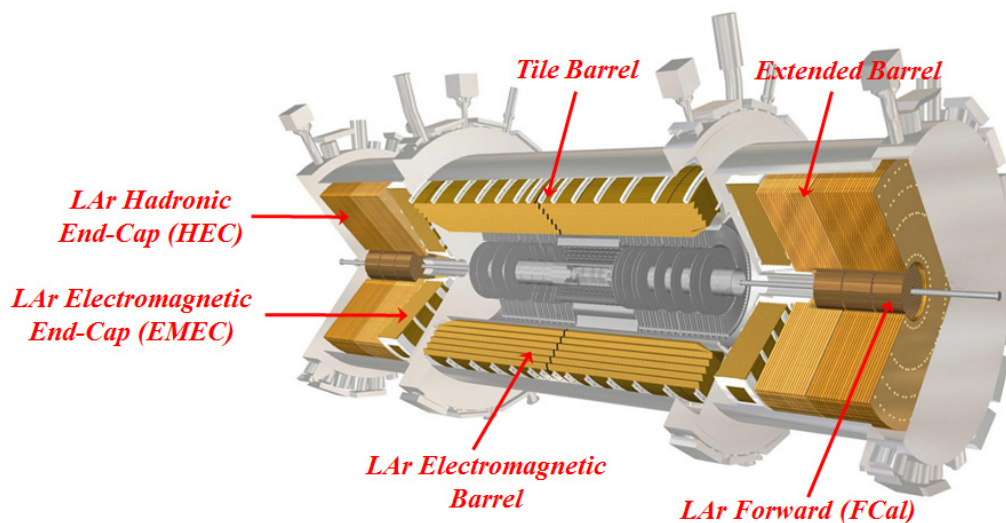


Figure 3.5: Schematic of IBL detector and related services. The zoomed inset is showing cylindrically arranged modules within detector and around the beam pipe.

To be more specific, the ID detector provides charged particle tracking with high efficiency in the  $\eta < 2.5$  covering the full azimuthal range. The original B-Layer for its radial proximity delivers vital information for the reconstruction of charged particles trajectories, multiple collision vertices, and higher b-tagging performance in upper level. The IBL also helps maintaining the tracking performance and robustness when the B-Layer starts to deteriorate from radiation damage. A complete evaluation of the expected tracking and vertex reconstruction performance has been reported in [72].

## Calorimeters

Calorimeters measure the energy of particles passing through the detector. Such detector is dedicatedly designed to stop the particles in terms of absorbing their entire energy. This is generally made by high-density material like lead. The innermost spacing among the Layers is typically filled with liquid argon. The ATLAS calorimeter holds two distinctive portions: the Barrel part and two End-Caps. A detailed CAD schematics is represented in figure 3.6. Electromagnetic calorimeters measure the energy of electrons and photons as they interact with matter. Hadronic calorimeters sample the energy of hadrons (particles that contain quarks, such as protons and neutrons) as they interact with atomic nuclei. This detector is capable of absorbing most of the known particles except muons and neutrinos. The highly precise electromagnetic calorimeters absorb the energy of charged particles (electrons and photons) while a tracking information can also be made.



**Figure 3.6:** Computer Aided Design of ATLAS Calorimeters [91].

The Hadronic End-Cap calorimeter (HEC) is a Liquid Argon (LAr) sampling calorimeter which has parallel Cu plate absorbers orthogonal to the beam axis and consists of two consecutive wheels with absorber thickness of 25 and 50 mm, respectively [93]. The task of the Hadronic Calorimeter is to measure the energy of hadron like particles and any radiative energy loss (within the pseudo-rapidity,  $1.5 < |\eta| < 3.2$ ).

## Muon Spectrometers

Muon Spectrometers made an important contribution to the discovery of the Higgs boson through a precise tracking of Muons. Muons are particles like electrons but having 200 times higher weight. They are the only detectable particles that can traverse all the calorimeter absorbers without being stopped. The muon spectrometer is constructed around the calorimeter and is able to determine their momenta with high precision. It is a very large system (figure 3.7) which consists of thousands of charged particle sensors placed in three large superconducting toroidal coils: one is the circumferencing barrel type detector that can cover  $\eta$  up to 1.1 and the other two are the Muon End-caps. Each Muon End-Cap detector can produce the trajectory information for  $1.1 < |\eta| < 2.7$  [94]. The sensors are similar to the straws described for the inner detector but have a larger tube diameter. The system provides a standalone measurement of Muon transverse momentum with the uncertainty of 3% at 100 GeV to about 10% at 1 TeV, while the trigger threshold is set below few GeV.

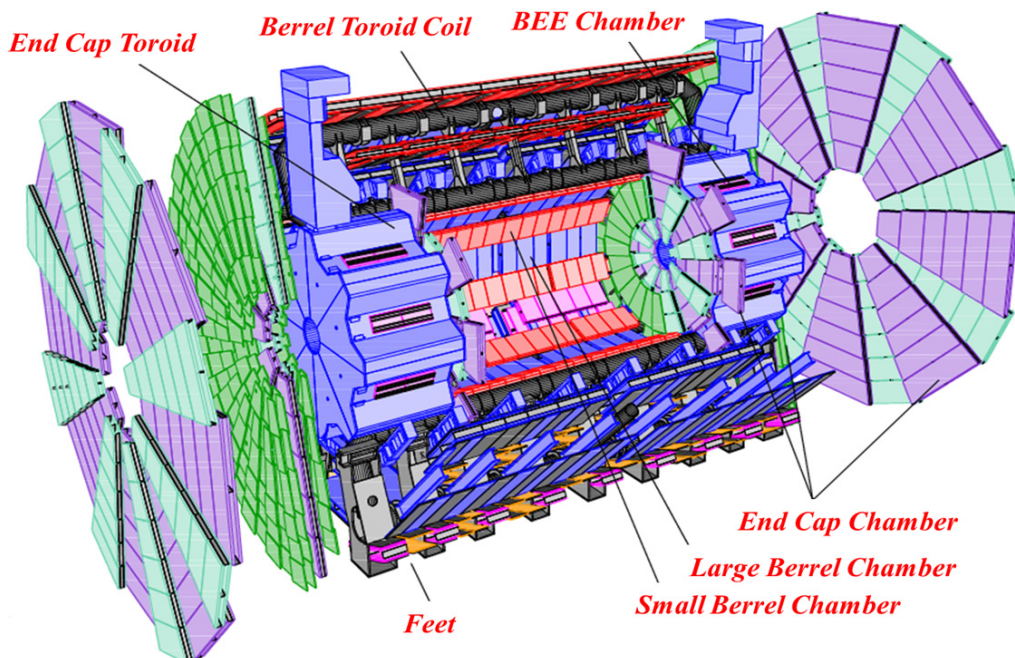


**Figure 3.7:** Sketch of ATLAS Muon Spectrometer [91].

Interestingly, the muon spectrometer is visibly responsible for the enormous size of the entire ATLAS detector holding around 1,150 MDT chambers and more than 350,000 drift tubes. Complying the requirement of HL-LHC, the relevant groups of ATLAS are studying and developing the next generation muon electronics of extreme hardness.

### 3.3.2 ATLAS Pixel Detector and Readouts

The ATLAS pixel detector consists of three barrel layers and it is designed to cover a pseudorapidity region,  $|\eta| < 2.5$ . Layers 0, 1, and 2 have radii of 50.5, 88.5, and 122.5 mm [95]. The innermost pixel layer (layer 0 or b-layer) is composed of 22

staves, while layer 1 consists of 38 staves and layer 2 of 52. A single staffe holds 13 pixel modules and the cooling pipes of the detector. The disks consist of 48 modules, resulting in a total of 1744 pixel modules having a sensitive area of about 1.7 m<sup>2</sup>. A schematic view of the pixel detector can be found in Figure 3.8.

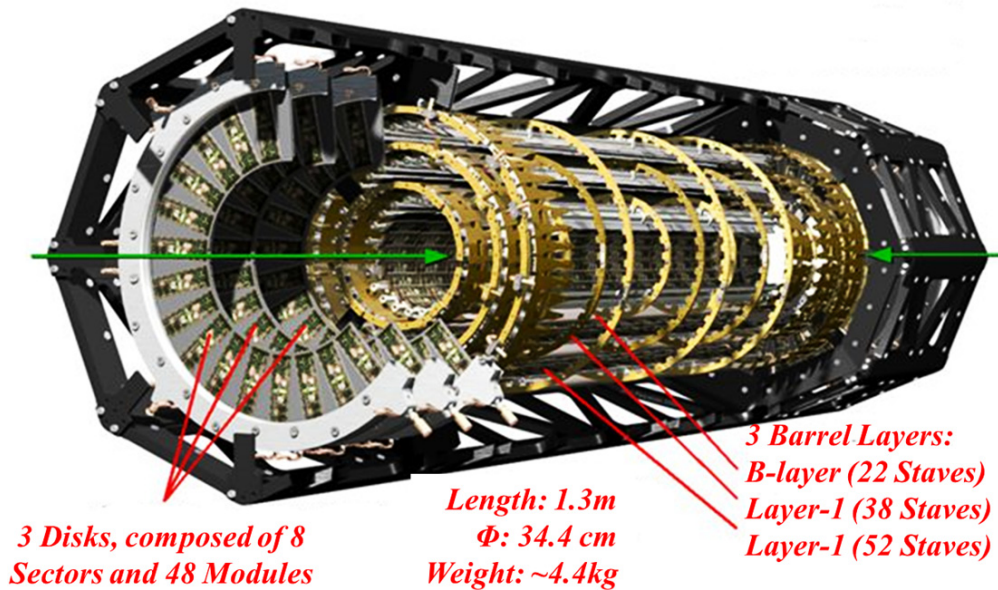


**Figure 3.8:** Sketch of the ATLAS pixel detector active region representing the barrel and the end-cap disks [91].

### Flex Module

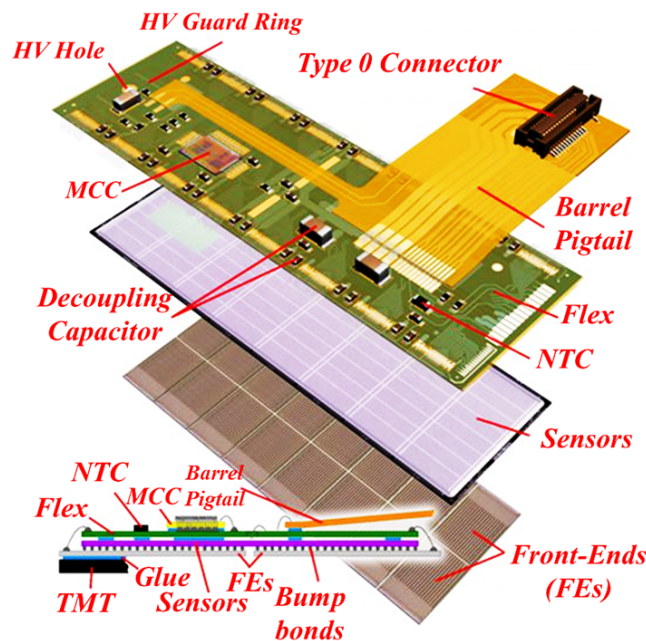


**Figure 3.9:** Schematic drawing of the pixel module. A single module consists of the flex hybrid, the sensor, and the FE-chips. The electric connection between the sensor and the FE chips is illustrated. Small metal spheres, Bump Bonds, are used to establish the connection between sensors and front ends [91].

The flex-hybrid is a double-sided flexible printed circuit board with a thickness of approximately 100  $\mu\text{m}$  (figure 3.9). It holds the control chip, the Negative Temperature Coefficient (NTC) sensor, the electrical connections for high and low voltage power supplies, and data input and output lines. The NTC is used for the monitoring of the module temperature. An interlock system powers the module off quickly if the temperature is too high. The Module Control Chip (MCC) needs to operate in a highly radiative environment with a time resolution of 25 ns.

It has three main tasks. First, the MCC configures itself and the FE chips before a data-taking run or after power-up. Second, the MCC is responsible for the distribution of timing signals such as bunch crossing, L1 triggers and resets, and readout signals for the FE chips. Third, event building is done by the MCC. It is the most complicated task where data coming from the FE chips is buffered and used by the event builder in order to prepare them for the transmission of an event out of the pixel module. External signals and the supply voltage are transmitted through the pigtail in barrel modules, while for the disk module wires are soldered directly to the flex (without the pigtail).

### FE-I3 Compliant Pixel Sensors

The sensitive area of the pixel detector is the sensor side with high resistivity area. It has a  $256 \pm 3 \mu\text{m}$  thick n-type bulk. As an example, in the planar sensor,  $n^+$  pixel implants are located on the readout side of the bulk. The backside of the sensor is p-doped in order to create a p-n junction. Each sensor consists of 47,232 pixel implants [96]. The pixel pitch dimension is  $50 \times 400 \mu\text{m}^2$ . The gap between two FE chips is 400  $\mu\text{m}$  wide and thus needs to be covered by a special type of pixel. Figure 3.10 shows the pixel region at the edge of the FE chips. Elongated pixels with a length of 600  $\mu\text{m}$  cover the gaps in the long pixel direction, while ganged pixels are used to cover the gap in the short pixel direction. At the corner of each FE chip, elongated + ganged pixels are used in order to achieve the full coverage.

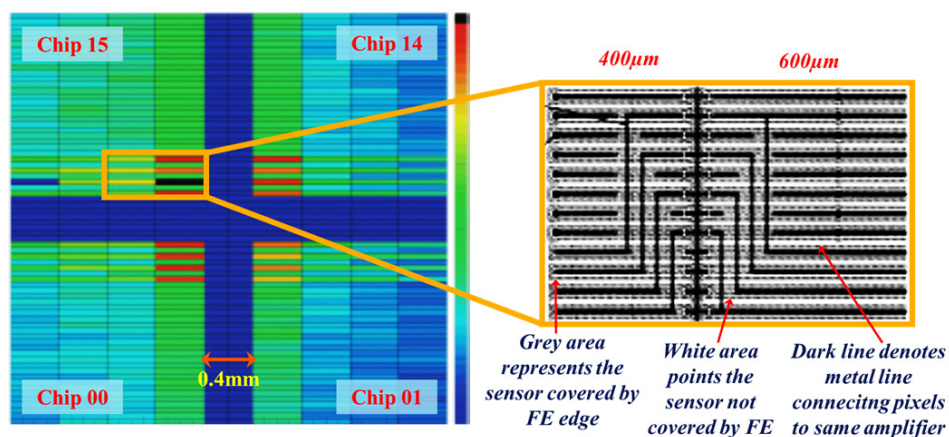


**Figure 3.10:** Schematic of the inter-chip region of FE-I3 readout compliant planar pixel detector. Long and ganged pixels are used to cover the gap between the FE chips.

Four ganged pixels are connected to four pixels at the edge of each FE chip. In order to minimize the effect on track reconstruction ganged pixels are always

connected to the next but one neighboring pixel below the FE chip. The signal between the bump-bonded and the ganged pixel hits can be distinguished because a hit in two neighboring ganged pixels is recorded as a hit in non-neighboring bump bonded pixels. If the edges of the sensors are damaged by the cutting of the pixel sensors, this would lead to crystal defects in the silicon close to the sensor edge. These defects can even create shorts and increase the leakage current if this region is depleted. Thus, 17 guard rings are implemented to decrease the potential stepwise towards the cutting edge of the sensor.

This ATLAS planar pixel sensor is actually a double-sided n<sup>+</sup>-in-n device structure with the pixelated electrodes (n<sup>+</sup>) at the front side and a uniform p<sup>+</sup> implantation on the backside, combined with several guard-rings at the edge. This structure uses n<sup>+</sup> electrodes for read-out, so the collected charge remains electrons that had been one of the requirements of the read-out chip, ensuring faster signal response since the mobility of electrons in Si is higher than that of holes, also leading to better radiation hardness properties. The n-type Float Zone silicon undergoes type-inversion at a relatively low irradiation fluence, at which the effective doping of the bulk is transformed into p-type and starts enhancing the full depletion voltage with the increasing irradiation. If devices were of standard p<sup>+</sup>-in-n silicon detectors, the junction would move to the opposite side of the pixel after certain fluence, and thus the correct operation would require a very high reverse bias voltage to be fully depleted (e.g., ~2000 V in a 300 μm active thickness). At n<sup>+</sup>-in-n silicon device, the junction proceeds from the backside before irradiation, when full depletion voltage remains yet at an acceptable value. After heavy irradiation and type-inversion, the depletion proceeds from the pixel side, thus ensuring the operation as a pixel device even if full depletion is not reached [95]. Surface isolation on the pixel side of the sensor is made through moderated p-spray implants, a reliable processing technique up to doses of 500 kGy. Pixel modules are expected to withstand a radiation fluence up to  $1 \times 10^{15} \text{ n}_{\text{eq}} \text{ cm}^{-2}$  at least.

A single sensor tile, made of 16 pixel detectors, is composed of 47,232 pixels arranged in 144 columns and 328 rows. In 128 of these columns, the implant size for a simple pixel is of  $382.5 \times 30 \text{ μm}^2$ , with a pitch size of  $400 \times 50 \text{ μm}^2$ , while in 16 columns pixels have implant size of  $582.5 \times 30 \text{ μm}^2$  with a pixel pitch of  $600 \times 50 \text{ μm}^2$ . In each column, eight pairs of pixels are connected together to a common readout (figure 3.10), bringing the total number of independent readout rows to 320 or 46,080 readout channels. This particular arrangement is needed in order to allow the connection of a sensor tile to 16 readout chips consecutively.

Silicon sensors and readouts are connected together by means of bump-bonding and flip-chip. This process is costly and complicated and so, it is eminent to select good devices only for the bump-bonding process. For the selection process, each pixel on the device is connected to a bias metal grid by punch-through, which

allows a measurement of the total sensor current before the bump-bonding. The 3D version of this kind of sensors has already been introduced in chapter 2.

### FE-I3 Pixel Readout Chip

Each module of the ATLAS pixel detector is read out by 16 FE chips. The FE-I3 readout chip is implemented in a standard  $0.25\ \mu\text{m}$  CMOS process with a radiation tolerant layout [96, 97, 98]. The chip consists of 2880 pixel cells, arranged in 18 columns and 160 rows. The cells are designed to digitize the signals coming from the corresponding pixel in the sensor.

An overview of the analog readout part is shown in Figure 3.11. The sensor and the FE chips are connected via bump bonds. The unit cell contains two amplifiers and a discriminator with an adjustable threshold. A capacitor ( $C_f = 6.5\ \text{fF}$ ) is charged by the induced current and it is discharged through a constant feedback current. The outcome is a nearly triangular signal shape, where the rising edge is defined by the collected charge in the sensor, and the falling edge is defined by the feedback current.

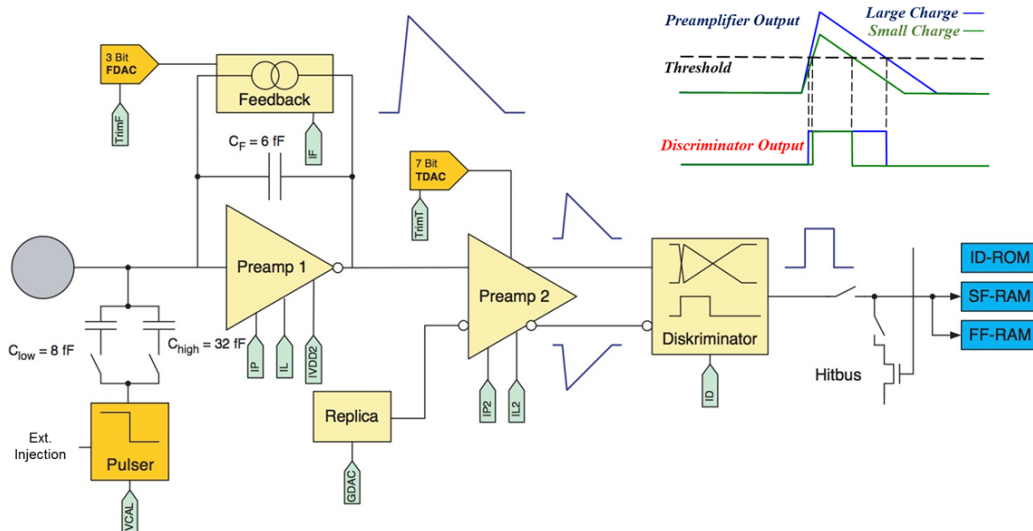


**Figure 3.11:** Schematic of the analog part of the pixel unit cell in the FE-I3 chip. Inset at right corner represents the digitization process of the signal.

The amplitude of the feedback current is tuned globally for every FE chip with an 8-bit DAC1 (IF DAC) and locally for every pixel with a 3-bit DAC (FDAC). A calibration circuit is included in each unit cell. The capacitors  $C_{low}$  and  $C_{high}$  are used to inject predefined amounts of charge into the pixel unit cell. The discriminator output is a logical one as long as the incoming signal is above the adjustable threshold. The value that is saved is the Time over Threshold (ToT), i.e. the total time that the signal exceeds the discriminator threshold. Two cases are shown, a signal with a large amount of collected charge and a smaller one. The ToT value is proportional to the collected charge in the sensor and it is measured in units of 25 ns. The threshold of the discriminator can be tuned globally with a 5-bit Global DAC (GDAC) and locally with a 7-bit Trim DAC (TDAC).

The hit coordinate and a timestamp for the leading edge of the discriminator output signal are temporarily stored in one of the 64 buffers per column pair until the readout selection is made by the trigger of 3.2  $\mu\text{s}$ . Hits selected for readout are sent to the module controller chip (MCC) which builds events containing the hit information of all 16 FE chips. Hit information without trigger is not taken into account. NMOS leakage current explosion with the damage through higher TID could become a threat to nominal operation in the LHC long run and so, in order to make this chip radiation hard, a special design rule, i.e., enclosed layout, had been adopted which ensured its tolerance up to 100 Mrad.

### **FE-I4 Compliant Pixel Sensors**

FE-I4 compatible pixel planar sensors also used the n<sup>+</sup>-in-n design. The sensors are based on the current ATLAS pixel sensor design. Planar sensors are 200  $\mu\text{m}$  thick and the pixel size is 50 $\times$ 250  $\mu\text{m}^2$  [98]. Guard rings are implemented close to the cutting edge in order to decrease the potential in a controlled way. The guard ring design has been adapted to find the slimmest possible edge design that still allows safe depletion [99]. The new design reduces the inactive region at the edge of the sensors significantly and thus minimizes the impact of a stave design that has no overlap in the z-direction. In total, 13 guard rings are used at each cutting edge. The outermost pixel column consists of long pixels with a length of 500  $\mu\text{m}$ . The overlap between the guard ring region and the last pixel column is 250  $\mu\text{m}$  wide. Planar sensors are influenced by the magnetic field whereas 3D-type sensors are unsusceptible to the magnetic field for owing the horizontal charge drifting feature [99,100,101]. At IBL, ~25% modules are 3D type only and an initial discussion on 3D sensors has already made on them in chapter 2 whereas more details on the IBL 3D sensors shall be found in chapter 4. A summary of the most important features of the Pixel detector used in upper layer and IBL is reported in Table 3.1.

### **FE-I4 Readout Chip**

The 18.8 $\times$ 20.2 mm<sup>2</sup> sized FE-I4 readout was developed to compensate the limitation of FE-I3 chip radiation hardness as well as to optimize the large number of IBL compliant readout chip occupancy at the small radius. The FE-I4 integrated circuit holds readout circuitry for 26,880 hybrid pixels arranged in 80 columns on the 250  $\mu\text{m}$  pitch by 336 rows on the 50  $\mu\text{m}$  pitch. It is designed in a 130 nm feature size bulk CMOS process. The state of art this kind is FE-I4B, where 'B' refers to the design revision intended for the production of the IBL detector. Following the predecessor FE-I4 was FE-I4A, in FE-I4B, the chip logic and power supply design have been enhanced and a few additional circuitries have been included.

DC coupled sensors are flipped and bump-bonded with FE-I4 readout chip for negative charge collection. Each FE-I4 pixel contains an independent, free running amplification stage with adjustable shaping, followed by a discriminator with

independently adjustable threshold. The chip keeps track of the firing time of each discriminator as well as the Time over Threshold (ToT) with 4-bit resolution, in counts of an externally supplied clock, nominally 40 MHz. Information from all discriminator firings is kept in the chip for a latency interval, programmable up to 255 cycles of the external clock. Within the latency interval, the information can be retrieved by supplying a trigger. The data output is serial over a current-balanced pair (similar to LVDS). The primary output mode is 8b/10b encoded with 160 Mb/s rate. Serial LVDS input synchronization of FE-I4 is done by the external clock. In each trigger of 25ns resolution bunch crossing, ToT code of a cluster (of 4 pixels) is recorded, that simultaneously accounts for the hit in the adjacent region and eventually relaxes the time-walk function of the analog circuitry. The higher amount of memory inclusion for raw data storage and faster emptying capacity introduced in FE-I4B readout chip led to decrease the hit loss by about a factor of 3 with respect to the FEI3 readout chip [102].

**Table 3.1:** Summary of the main characteristics of the pixel detector and the IBL detector.

	Pixel	IBL
Active Surface (m <sup>2</sup> )	1.73	0.15
Number of channels (x 10 <sup>6</sup> )	80.36	12.04
Pixel size (μm <sup>2</sup> )	50×400	50×250
Pixel array (FE chip)	18×160	80×336
Chip size (mm <sup>2</sup> )	7.6×10.8	20.2×19.0
Active Fraction (%)	74	89
Analog current (μA/pixel)	26	10
Digital current (μA/pixel)	17	10
Analog voltage (V)	1.6	1.4
Digital voltage (V)	2.0	1.2
Data out transmission (MBit/s)	40-160	160
Sensor type	planar	planar / 3D
Sensor thickness (μm)	250	200 / 230
Layer thickness (% X <sub>0</sub> )	2.8	1.9
Cooling fluid	C <sub>3</sub> F <sub>8</sub>	CO <sub>2</sub>

A 2-stage amplifier configuration is used to implement the analog front end, shown schematically in figure 3.12. The “Preamp” is a cascode amplifier with NMOS as an input device and the second stage (“Amp2”), AC coupled to the preamp, is a folded cascode PMOS input amplifier. The main motivation of this 2-stage system is to provide enough gain before the discriminator while permitting optimization in the choice of the preamp feedback capacitor ( $C_{f1}$ ). The discriminator is built with a 2-input voltage comparator and a threshold voltage generator. Signal shaping is only done by the preamp with an adjustable return to baseline, while the second stage provides only voltage gain (given by the ratio of  $C_d/C_{f2}$ ). The return to baseline and discriminator

threshold are individually adjustable in each pixel, with globally determined range and offset. Altogether 13 bits are available for the configuration of the analog pixel which are stored locally in custom-made, Single Event Upset (SEU) tolerant latches. Two selectable capacitors are provided for analog calibration injection. The extracted values including layout parasitic are 1.95 fF and 3.90 fF. Both can be selected in parallel (~5.85 fF) whereas a parasitic capacitance will be of order 0.1 fF if none of them are selected. A calibration of the combined 5.85 fF can be performed on a chip-by-chip basis.

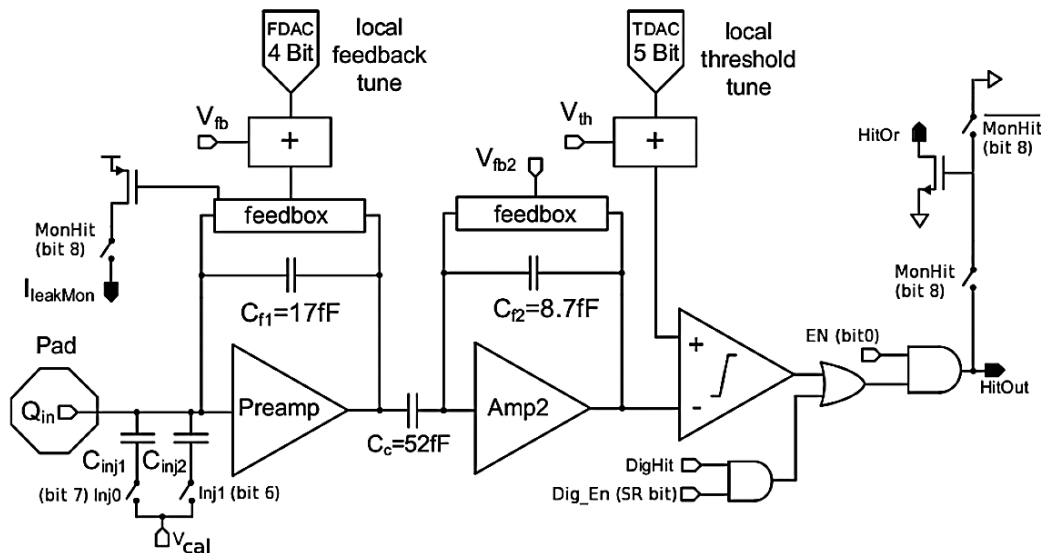


**Figure 3.12:** Schematic of FE-I4 Pixel Analog Circuitry. Input pins remain open here whereas the output of each stage is presented with a solid line.

The preamp feedback has a low-frequency active filter for DC leakage current compensation, and the amount of DC leakage is mirrored to a column-parallel output. The comparator output is fed to the digital pixel region through logic gates which allow the logic OR operation with a digital test signal. Additionally, the comparator output is fed to the column-parallel wired-OR circuit. This "HitOR" function can be disabled and should be off for the normal operation to avoid parasitic crosstalk. When a negative charge  $Q_{in}$  is deposited at the input, a positive going pulse appears at the output of the preamp. In an ideal system, the amplitude of this pulse would be  $Q_{in}/C_{f1}$ . Since there has been a fast shaping (return to baseline) requirement, the amplifier is non-ideal in practice, and the actual amplitude will be less. The shorter the (adjustable) shaping, the smaller the pulse amplitude for the same input charge. The return to baseline is implemented by a feedback system very similar to that of the FE-I3 through discharging  $C_{f1}$  with a quasi-constant current source. The negative going pulse at the output of the second stage feeds the negative input of the comparator, with a threshold voltage at the positive input.

The FE-I4 contains 40 Digital Double Columns (DDC) connected together via the End of Double Column Logic (EODCL). Each DDC contains 168 Pixel Digital

Regions (PDR) grouped into 7 units of 24 PDRs each. Each PDR processes the data from 4 pixel discriminators (2 rows by 2 columns). ToT is independently counted per pixel. PDR holds groups of 5 pixel memories, where each memory stores 4 bits of ToT plus a 1 bit neighbor flag. The 4 bit counter of ToT starts when the digital threshold is applied in the discriminator with an integration of shift register. If both the input and output of the discriminator remains high, the hit signal passes through the digital threshold and is counted as big hit and set the ToT counter to '0000'. The reset value of ToT counter is '1111' and pixels for which discriminator does not fire ToT code '1111' is used.

Radiation hardness properties of these FE-I4 were enhanced with respect to FE-I3 readout chips. Non-ionizing Energy Loss (NIEL) effects at FE-I4 remain non-significant since the doping densities used in active devices (MOSFETs) is much larger than the radiation-induced concentration within the sensor and so, CMOS active region is insensitive to changes instead in the effective doping concentration. From the TID point of view, the chip remained still operational after 250 Mrad from 800 MeV Protons at Los Alamos [103]. Linear Energy Transfer (LET) of the irradiating particle would make an additional contribution instead to the low-level trap (border/shallow traps) by oxygen vacancies and also to the deep level trap (interface trap) dislocating nuclei near Si-SiO<sub>2</sub> interface. The drift velocity of the electrons in the dielectric is much faster than the holes and so, the generated electrons sweep away in shorter time during biasing and the holes would remain trapped in neutral oxygenated vacancies (shallow trap). The trapped holes are transported to the deeper trap region of the Si-SiO<sub>2</sub> interface. This process introduces fixed positive oxide charge (Figure 3.13 (b)).

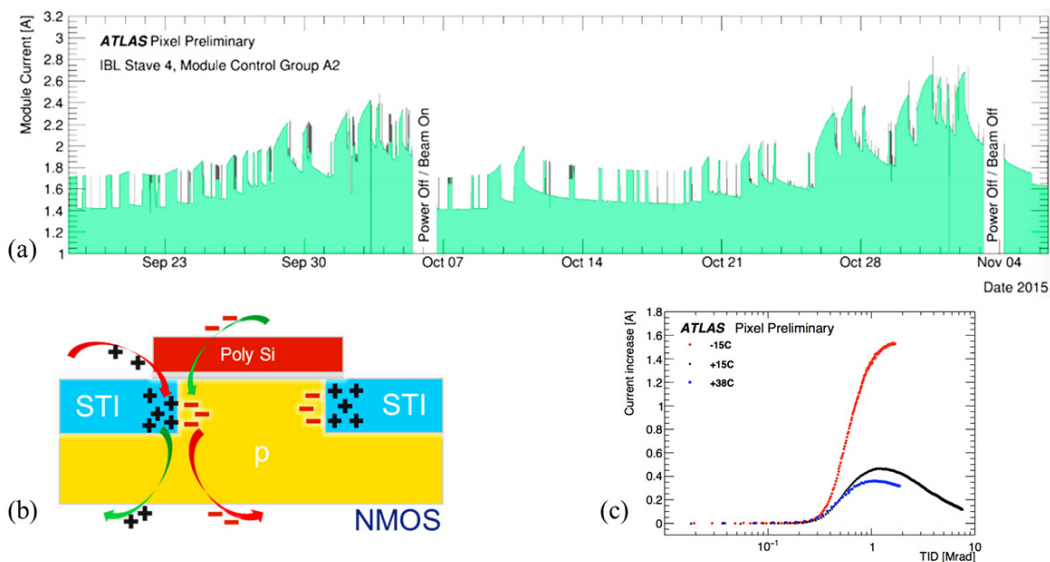


**Figure 3.13:** (a) Evolution of low-voltage current drift of four FE-I4 chips from the middle of September until the beginning of November 2015. Lower level inside denotes the chip standby mode (no data taking) and higher level point the ready mode (data taking) [104], (b) schematic of TID induced low voltage current drift and (c) laboratory data of TID induced current drift dependence on chip operation temperature.

The amount of oxide charge vastly depends on the dose rate and the device operating temperature during experimentation. The lower temperature shrinks the thermal diffusion process and the high dose rate accumulates the higher oxide charge in shorter time. The combination of these effects leads the device to be operated more adversely. The threshold voltage and the leakage current behavior of the CMOS structure follow different trends due to the formation of fixed oxide charges into the oxide layer and the dielectric interface. Since the PMOS within the CMOS structure builds up both positive fixed oxide charges and positive interface traps at a level of the corresponding accumulated TIDs, it plays only increasingly varying the threshold voltage of such parasitic condition, where the leakage current contribution remains negligible. On the contrary, in radiation-induced parasitic NMOS structure, TID plays the vital role in the decreasingly shifting threshold voltage and the leakage current increase till rebound process becomes active. This leakage current increase can be anticipated by the effect of negatively charged interface traps in NMOS. It is also worth to note that the rebound process becomes active when the positive oxide charge density reaches the saturation point between 1-2 Mrad TID, as it has been reported for the 130nm CMOS technology from different foundries [105]. Such phenomenon could lead the FE-I4 readout chip into operation runaway, as it had been demonstrated by the four modules' current drift due to TID effects (figure 3.13(a)). At the end of 2015 LHC run, it was observed that the mean current per module was around 700mA (per module operating limit is ~800mA). Thereby, a thorough study was made of such FE-I4 low voltage leakage current in dependance of operating temperature and X-ray irradiation dose. CERN public plot (figure 3.13 (c)) shows that the higher the FE-I4 operation temperature, the lower the contribution to leakage current enhancement, due to thermal diffusion effects on the Si-SiO<sub>2</sub> interface. A new compact X-ray irradiator XRAD-iR-160 was installed, calibrated and commissioned by the CERN Pixel Operation group [106]. A thorough investigation of such studies gave the essential guideline to the Pixel operation group to tune LHC temperature during operation to 5°C, which ensured a smooth operation of LHC throughout the entire 2016 run. The FE-I4 came with a newer voltage regulator, called Low DropOut (LDO). The LDO is a linear voltage regulator capable of maintaining the output even when the input voltage is very close to the output target. These LDOs have a much simplified design than the conventional DC to DC switching converters though they are featuring a penalty of power dissipation along the converting circuitries. It is worth to note here that the fixed oxide charge introduced during irradiation leads the CMOS circuits of LDOs to face an additional challenge, where the threshold voltage reference changes with accumulated TID. In fact, the energy states produced within the intrinsic bandgap during irradiation make the threshold reference shifted. Such anomalies made the readout chip to be operated instead at an endanger condition (in terms of current consumption beyond the limit) when the analog input voltage requirement reaches above 1.6V [107].

Linear Energy Transfer (LET) from charged heavy particles drives the FE-14 digital readout logic additionally to suffer from a transient effect. Such particles, in particular ions created in hadronic interactions of the silicon lattice with neutrons or charged hadrons, when hitting the depleted region of a transistor, can change the state of memory cells by depositing large amounts of charge. This effect is called Single Event Upset (SEU). SEUs can lead to the wrong information to be stored in latches or transmitted by the chip, and the chip can enter an unrecoverable state due to change of chip configuration registers at the worst scenario.

### **HL-LHC Compliant Detectors**

The High Luminosity Large Hadron Collider (HL-LHC) targets the phase-II upgrade where integrated luminosity is expected to be greater than  $5 \times 10^{34} \text{ cm}^{-2}\text{s}^{-1}$ . The ATLAS inner tracker, ITK, will be a Silicon based strip and pixel system, both consisting of a barrel and two end-caps to provide tracking coverage at high  $|\eta|$ . There are three main working groups associated with different sensor technologies and different detector geographical locations. These are pixels, barrel strips, and end-cap strips systems. There have been on-going tests of silicon sensors over the last several years though the standardization of pixel spatial geometry has not yet finalized. The extensive R&D programs are collaborating in the development of such detectors. ITk compliant pixelated sensors have focused more aggressive designs to make them more radiation hard as per requirement of HL-LHC. The predicted higher event pile-up (140 events/bunch-crossing) and integrated luminosity of  $3000 \text{ fb}^{-1}$  at HL-LHC run would come with the replacement of the currently installed entire tracking detector. The design constraint has pushed to develop sensors of thinner active region ( $\sim 100 \mu\text{m}$ ), denser pixel granularity ( $50 \times 50$  or  $25 \times 100 \mu\text{m}^2$ ) and slimmer edge ( $\sim 100 \mu\text{m}$ ). Planar pixel sensors shall still follow n<sup>+</sup>-in-n with active thickness of about  $100 \mu\text{m}$ . The details on HL-LHC compliant 3D sensors could be found in chapter 6.

### **Forthcoming Inner Tracker (ITk)**

The Inner tracker update in phase 2 shall feature: the measurement of the transverse momentum and direction of isolated particles (in particular electrons and muons), the reconstruction of the piled-up vertices, the correlation of the vertex with the hard interaction, the identification of secondary vertices in b-jets with high efficiency and purity, the good tracking resolution and a low rate for fake track reconstruction. In addition, such tracker will be able to identify the decay of tau leptons, including impact parameter information while reconstructing the track with associated converted protons. The final design of ITk holds the pseudo-rapidity coverage extends up to  $\eta = 4$ .

The ITk will be wrapped up in the magnetic field from a 2 T solenoid where pixel modules are expected to be integrated at the inner radii, surrounded by silicon micro-strip modules at larger radii. The active length of the tracker will be 6 m long and will

include 3 more pixel disk during the first upgrade (covering  $\eta$  up to 2.7) in comparison to present Inner Detector in the forward and downward the stream. The number of pixel disks and strip disks will be increased up to 12 and 6 respectively in any direction in order to extend the coverage to the targeted  $\eta = 4$ . Initial proposal of this extended ITK architecture from Letter of Intent (LOI) brought a new feature of keeping R- $\phi$  plane tilted with respect to the tangent of foreseen installed staves [170]. In this case, a track at large  $\eta$  produces a cluster with many pixels, with a length given by  $N = t/(p \tan\theta) + 1$ , where 't' is the sensor thickness, 'p' is the pitch, and ' $\theta$ ' the incidence angle. This long cluster provides information about the impact position, a continuous measurement along a short segment of the trajectory, including direction and precision  $dE/dx$ . Delta rays information can be retrieved as well by checking the cluster shape compatibility with the track prediction. Moreover, it could even be possible to obtain the equivalent of two space-points by using such long cluster: one for the inner and another for the outer sensor surfaces (provided that an adequate pattern recognition making adequate use of the extra information is available). This expectation can be so challenging since the long cluster may be separated in different parts due to Pixel ineffectiveness, or signal under threshold, or there could be an overlap between clusters generated by different tracks especially in the HL-LHC operating conditions. However, such long track shall eminently traverse through a large amount of materials, which could be particularly harmful at low momenta, and the readout bandwidth (especially for the inner layer) can also be saturated for the increasing channel occupancy by the use of large number of pixels crossed per track.

To address this challenge, another baseline ITK layout has proposed, denoted as 'Inclined ITK'. In this architecture, the staves shall be placed as perpendicular as possible to the R- $\phi$  plane. This approach minimize the traversed material by keeping a close to normal incident angle to each module, as it can be seen from figure 3.14. However, the solution shall bring additional cost of complexity in terms of stave fabrication, the consequent module loading and the later thermal management during HL-LHC operation. The Inner Inclined layout, is a mixture of the previous two layouts, where the innermost part of the Pixel detector has inclined modules (as in the Inclined layout) while the outer barrel has only straight modules (as in the Extended layout). For the outer Pixel barrel, inclining the sensors at the end of the staves is primarily a way to reduce the sensor surface needed, for which a rather aggressive layout design rule was chosen. The sensor module in the tilting position within the inner layer shall be placed around 56 degrees in order to cover the pseudo-rapidity,  $\eta$ , up to 1.1. Small pitch 3D design is to be integrated within this inclined section, shall bring an enhanced opportunity to track the dense b-jet where the position resolution of them cannot predicted at this moment (since it vastly depends on SNR, cluster size distributions and reconstruction algorithms). Moreover, to overcome the thermal management issue, the suitable micro-channel [171] cooling 3D integration is also expected to deploy within ITK modules.

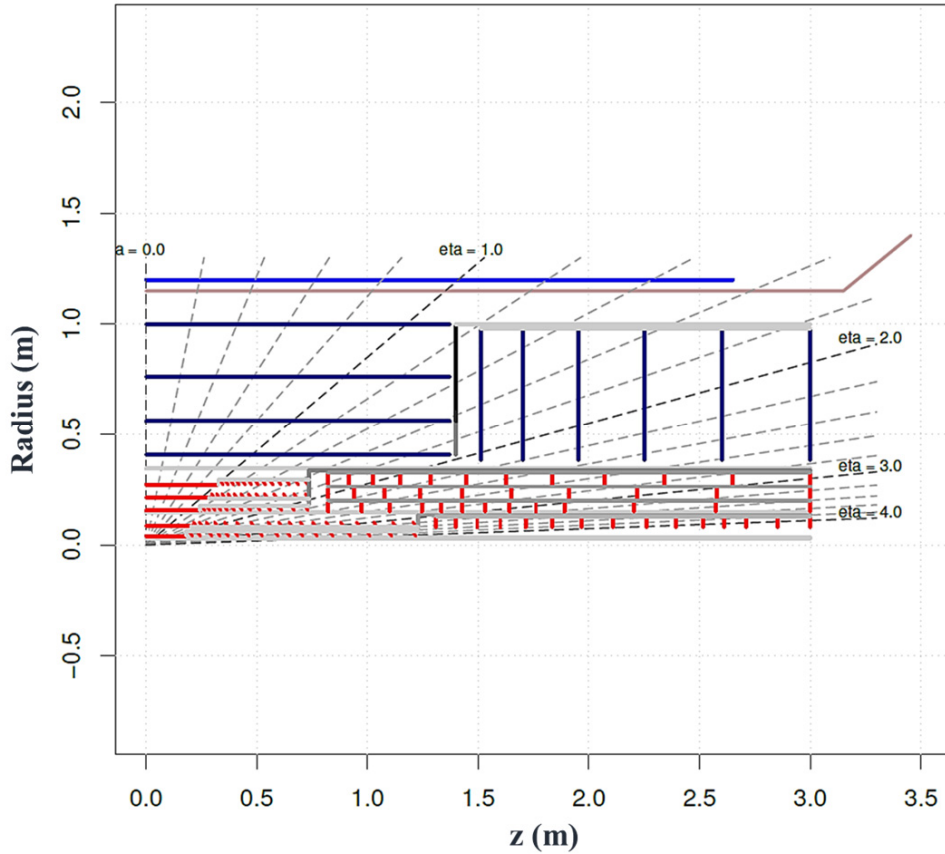


**Figure 3.14:** Schematic cross-section of the ATLAS ITk inclined tracker showing the coverage of the pixel detector in red and strip detector in blue. The pseudo-rapidity coverage extends up to  $\eta = 4$ . Horizontal and vertical lines represent barrel and end-cap layers, respectively.

### HL-LHC Compliant Readout Chip (RD53A)

The RD53A prototype is aimed at demonstrating a large format IC in 65nm CMOS processing technology. The design considered the required radiation tolerance, the stable low threshold operation, and the high hit and trigger rate capabilities for phase-II upgrades of ATLAS and CMS. A list of specification was made with a tolerance of 1000Mrad (Si) TID [108]. To cope with the foreseen occupancy, the pixel area has been set to  $2500 \mu\text{m}^2$ . The active pixel area will hold  $400 \times 192$  pixels with  $50 \mu\text{m}$  by  $50 \mu\text{m}$  regular neighbouring bump-pad distance (figure 3.15).

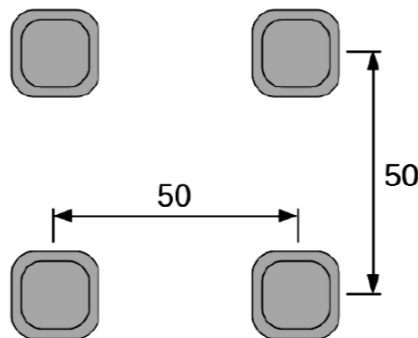


**Figure 3.15:** Schematic of RD53A bump pattern [108].

A  $600e^-$  threshold has been set to fire the discriminator even in case of a 50% charge loss after radiation damage in case of MIPs crossing a  $50\mu\text{m}$  layer. This implies a Landau peak of approximately  $2000e^-$  and in-time threshold of  $1200e^-$  at 25ns bunch crossing. Per sensor pixel capacitance has been targeted to 50 fF (design specification is 100fF), so one may operate with slightly higher threshold in order to achieve the same required hit efficiency of 99%. Average rate of signal pulse is set to 75 kHz per pixel in order not to lose a new hit at in-pixel pileup system of alike free running discriminator while the discriminator is still high from a prior hit. The prototype input must contain all needed Trigger, Timing, and Control (TTC) information on a single differential pair (link). It is also expected to support multiple chips to share a single TTC link. Each chip would have a 3-bit hard wired address.

### **HL-LHC Compliant CHIPIX65**

The CHIPIX65 is a  $3.5 \times 5.1\text{mm}^2$  ASIC prototype readout designed by CHIPIX65 project, part of RD53 collaboration, for a pixel detector at HL-LHC [160]. This consists of  $64 \times 64$  matrix of  $50 \times 50\ \mu\text{m}^2$  pixels, a miniature version of RD53A. The digital architecture has been developed with withstanding particle efficiency above 99.9% at 3 GHz/cm<sup>2</sup> pixel rate, 1 MHz trigger rate with 12.5  $\mu\text{s}$  latency. Two analog front-end designs, one synchronous and one asynchronous, are implemented. Charge is measured with 5-bit precision and the analog dead-time is below 1%. IP-blocks (DAC, ADC, BandGap, SER, sLVS-TX/RX) and very front ends are silicon proven, irradiated up to 800Mrad. Analog part of this readout consists of both synchronous and asynchronous modules having occupied 50% each of the total analog module. Each of them consist of single preamplifier in order to reduce the power consumption. Krummenacher feedback has been used to provide both leakage current compensation and constant current feedback capacitor discharge, along with a calibration circuit to inject an input charge. The average current consumption in synchronous module is 5  $\mu\text{A}$  and the chip has demonstrated its radiation hardness up to 600Mrad. The asynchronous architecture features instead a folded cascode amplifier, followed by a fast comparator composed of a transconductor stage and a transimpedance amplifier. A 4-bit DAC has been included for local threshold trimming. The average current consumption in this module is about 4  $\mu\text{A}$ . Till 800 Mrad campaign the asynchronous module did not show any significant degradation. An enhanced version of FE-I4 design was used with groups of  $4 \times 4$  pixels and centralised latency buffer, obtaining an optimised sharing of the digital circuitry.

### **3.3.3 Semi-Conductor Tracker (SCT)**

The ATLAS SemiConductor Tracker (SCT) is a key precision tracking detector in the ATLAS experiment. Since the first operation in 2009, 99% of 63 million SCT strips remains operational. The SCT consists of  $62\text{m}^2$  strip modules and is immersed in a 2 T magnetic field. There are over 4000 individual modules in the SCT: 2112 in

the barrel and 988 in each end-cap. The modules come in several shapes, two of which are shown in figure 3.16.

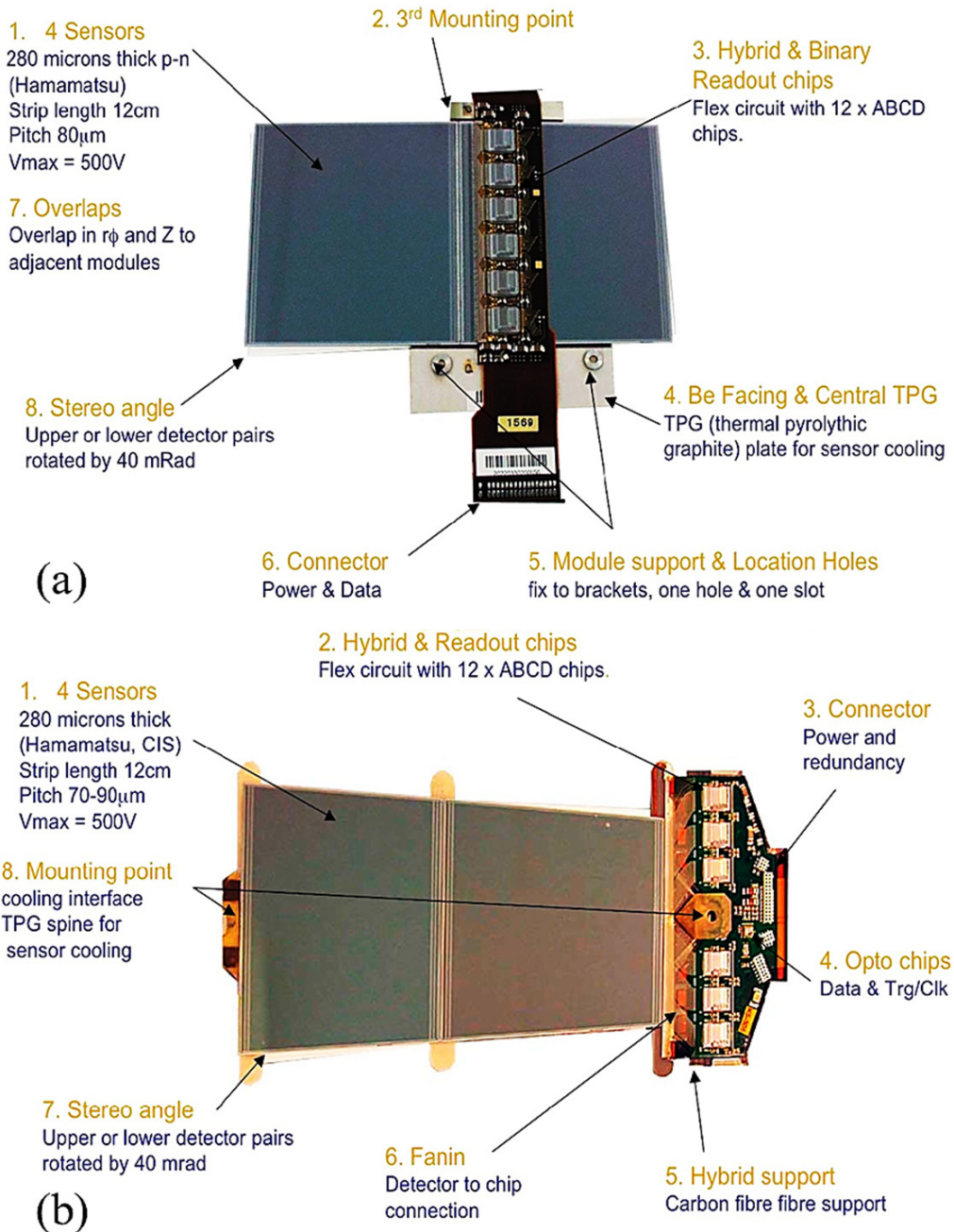


**Figure 3.16:** SCT (a) barrel module and (b) end cap.

Planar p-in-n silicon strip of 285µm active thickness detectors were glued in the support structure and the two layers of sensors can be rotated with respect to another by a 40 milliradian stereo angle. All SCT detectors become depleted under 100V reverse biasing and non-irradiated sensors are typically reversed biased with 150V while after irradiation, the full depletion might be accomplished with larger reverse biasing (~500V) due to NIEL effects. The inner detector measures the trajectories of charged particles within the pseudorapidity range  $|\eta| < 2.5$  [109]. The strip pitch in LHC

remains 80 $\mu\text{m}$ . In HL-LHC compliant SCT design a much smaller pitch ( $\sim 50\mu\text{m}$ ) has been explored with thinner active layer of around 100 $\mu\text{m}$ .

ABCD3TA is a 128-channel ASIC with binary architecture for the readout of silicon strip particle detectors in the Semiconductor Tracker of the ATLAS experiment. The chip comprises fast front-end and amplitude discriminator circuits using bipolar devices, a binary pipeline for first level trigger latency, a second level derandomizing buffer and data compression circuitry based on CMOS devices. It has been designed and fabricated in a BiCMOS radiation resistant process and initially optimized and tested to be operated up to  $2 \times 10^{14} \text{ n}_{\text{eq}} \text{ cm}^{-2}$  (10 Mrad(Si)). The preamplifier-shaper circuit delivers signals with a peaking time of 25 ns. The output of the preamplifier passes through the integrated discriminator that fires for the arrived signal at a level corresponding to 1fC. The noise occupancy is kept below  $5 \times 10^{-4}$ , for which the Equivalent Noise Charge (ENC) is set to 1500e $^-$ . 128 discriminator channels are controlled by 8 bit DAC and in addition holds 4bit TrimDAC, a fixed global threshold controller for all channels [110].

### 3.4 CMS Experiment

The Compact Muon Solenoid (CMS) detector is situated 100 m underground at the French village of Cessy and is another notable particle detection system, measuring 21m in length, 15m in diameter and weighing a total of 14,000 tons. The detector is a bit smaller than ATLAS but its operation is similar, reconstructing high-energy proton-proton collisions produced by LHC.

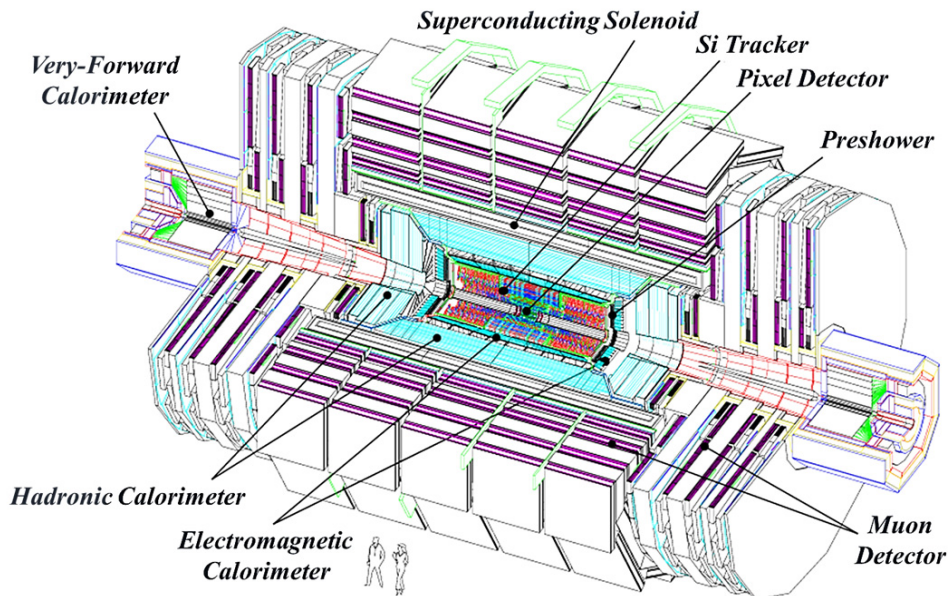


**Figure 3.17:** Schematic of Compact Muon Solenoid (CMS) detector.

The key element of the CMS detector (figure 3.17) is the superconducting solenoid operated to produce a magnetic field of 3.8 T within its volume. Inside the solenoid, from outside to inside, there is a fully hermetic brass-scintillator hadron

calorimeter, a highly granular crystal electromagnetic calorimeter and an all-silicon tracking detector. Outside the solenoid, embedded in the iron yoke, there are gaseous detectors to identify muons and reconstruct their trajectories and momenta together with the inner tracker.

### 3.4.1 Components of CMS Particle Detector

The most important aspect of the overall CMS detector is the choice of a superconducting high magnetic field solenoid to accurately measure muon and other charged particle momenta. The field is returned through a 1.5 m of Fe structure, which houses four muon stations with wide geometric coverage. The bore of the magnetic coil accommodates the tracking detector and the calorimeters. The cylindrical tracker volume is 6 m long and 2.6 m in diameter. To deal with high track multiplicities, the Silicon Strip Tracker (SST) uses ten layers of silicon microstrip detectors with fine granularity to provide high tracking precision. Three silicon pixels layers placed close to the interaction region, improving the measurement of the impact parameter of the charged particle tracks and the position of secondary vertices. The particles then encounter the calorimeters: the electromagnetic calorimeter (ECAL), which employs lead tungstate ( $\text{PbWO}_4$ ) crystals for the measurements of the energy of photons and electrons. The ECAL is surrounded by a brass/scintillator sampling hadron calorimeter. The forward calorimeters provide geometric coverage to  $|\eta|=5$ , for the measurement of the transverse energy in the event.

### 3.4.2 CMS Pixel Detector and Readouts

Since the LHC operation from 2009, CMS pixel detector uses planar-type sensors only, even-though 3D sensors were the strong candidates. LHC upgrade and the associated R&D activities are still considering the 3D Si sensors as the promising candidate for future HL-LHC CMS upgrades. Hereby, CMS tracker is beholding a limited scope with this thesis interest and the following sections will comprise the most prominent ROCs information, which are relevant to the ongoing FBK 3D sensor production.

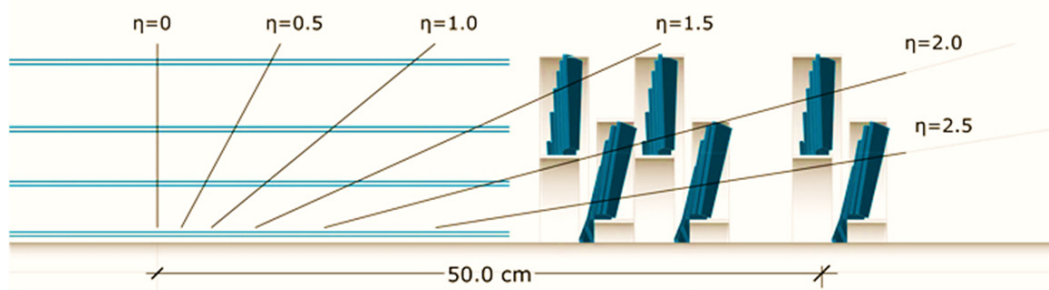


**Figure 3.18:** Schematic of Si pixel position from interaction point.

CMS trackers consists of four cylindrical barrel layers (BPIX) and three disks on either end of the barrel (FPIX). It is expected that the improved design enhances

tracking efficiency by up to 20%, while the fake rate is decreased by almost 20% at high pseudo-rapidity. Even though the inclusion of an extra layer (figure 3.18) adds ~50% more pixels, the total amount of material is decreased by using ultra-light mechanical support structures, and by relocating electrical patch panels outside of the sensitive volume. At the latest, Layer 1 is holding PROC600 readout and the upper 2-3-4 layers are upgraded with PSI46dig since the winter shutdown of 2016-2017.

### **PSI46 Compliant Si Pixel Detector**

The silicon sensors will keep the n<sup>+</sup>-in-n design of the present detector with 100×150 μm<sup>2</sup> pixel size, processed on 285 μm active thick diffusion oxygenated float zone silicon. The pixels on the n-side are isolated with either moderated p-spray (BPIX) or p-stop (FPIX). The pixel size is larger on contact edges between two sections, to allow sufficient mechanical tolerance on readout chip dicing. The size of the edge pixels is twice the normal pixel size (2×(150×100μm<sup>2</sup>)), while the corner pixels are four times.

### **PSI46 Front End**

PSI46dig is the state of art Front End readout chip for CMS pixel sensors. ROC amplifies and shapes the signal, compares it with an adjustable threshold, and stores it in a buffer, where it awaits for the trigger decision. Additionally, every hit is attributed a time stamp and an address of the hit pixel. In case of a positive L1 (Level 1) trigger decision, the information containing the signal height and the pixel address is transferred to the periphery. The PSI46dig readout chip is of 180 μm thick and is produced as radiation hard in 250 nm CMOS process. It holds an array of 52×80 pixel unit cells (PUCs), corresponding to the sensor pixels, a double column periphery for 26 double columns, each responsible for 2×80 PUCs, and a controller and interface block including an analog-to-digital converter (ADC), a central readout buffer and the data serializer. The chip is additionally equipped with several programmable digital-to-analog converters (DACs) used along the analog readout chain. The function of some DACs, relevant for this work, will be explained in the following. Each ROC also has 35 wire bond pads, which are used for powering and input/output signal transmission.

The charge deposited in the sensor enters the analog part of the PUC via bump-bond. The signal is then processed by a charge sensitive preamplifier and a shaper. The ROC also possesses an internal charge injection mechanism, which is used for calibration. The calibration signal can be injected either directly to the amplifier input or over an air capacitance gap into the sensor. The height of the calibration signal can be adjusted with an 8-bit DAC  $V_{Cal}$ . Two ranges of the  $V_{Cal}$  exist and can be selected by the CtrlReg DAC. The low range corresponds to about 65 injected electrons per DAC unit, while the high range corresponds to about 450 electrons per DAC unit. The injected charge can be delayed with respect to the clock cycle with another DAC, the CalDel. Analog processing unit of PSI46dig is shown in figure 3.19. After the

amplification, the signal is compared to an adjustable global threshold in the comparator using ROC register,  $V_{thrComp}$ . Adjusting 4 trim bits individual pixels can be adjusted. If the signal exceeds the threshold, it is temporarily stored in a sample and hold circuit whose sampling time can be adjusted by the  $V_{hdDel}$  DAC. Every double column (DC) of  $2 \times 80$  pixels has its own double column periphery. If a hit is detected in any of the pixels in the DC, the column drain mechanism starts. In the first step the time stamp is recorded. This is the current value of an 8-bit counter, which enables to match an event with a certain bunch crossing. The time stamp operates at 40 MHz, hence a maximum 11 trigger latency of  $255 \times 25 \text{ ns} = 6,375 \text{ ns}$  is allowed before another event uses the same time stamp.

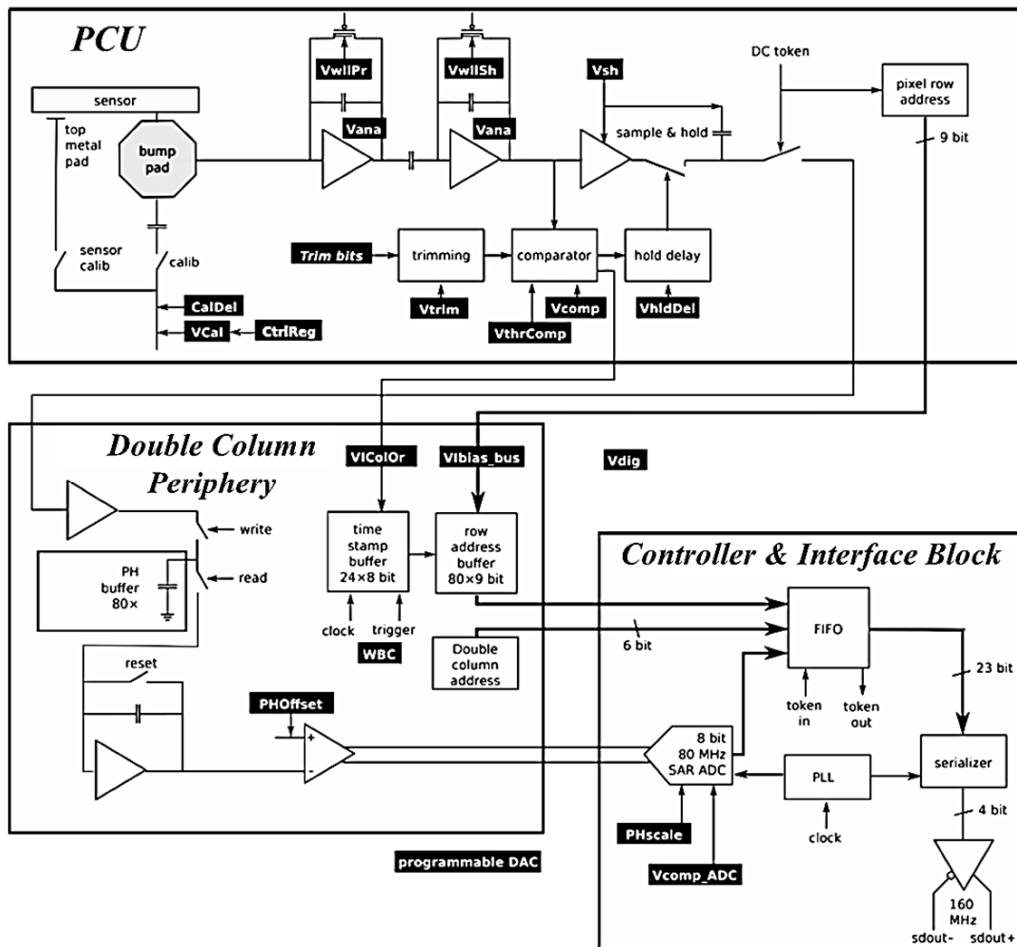


**Figure 3.19:** Schematic of PSI46dig analog processing unit.

In case of a positive 11 trigger decision for a certain event, all double columns with the corresponding time stamp stop their normal operation to preserve data. The pixel address and the pulse height are then passed from the double column periphery to the controller and interface block. The analog pulse height information is at this point digitized by an 8-bit ADC. For every hit, the column number (6 bits), the row number (9 bits) and the pulse height (8 bit) are written as a 23 bit word in the central readout buffer. The readout buffer is designed as a FIFO (First In First Out) with a storage capacity of 64 23-bit words. When the ROC is read out, the output data format is

generated by an event builder and passed to a serializer, which transfers the data out of the ROC.

## **PROC600**

PROC600 is based on the same 250 nm CMOS technology as the PSI46dig chip. The analog pixel front end and most of the chip periphery are the same as in PSI46dig while the digital part of the double column and the pulse height readout are entirely new. The ROC size is  $7.86 \times 10.5 \text{ mm}^2$  and it consists of three parts. The first one is a 4160 pixel array arranged in 52 columns and 80 rows with the conventional pixel size of  $150 \times 100 \mu\text{m}^2$ . The second part is composed of an interface of 26 double columns, each containing a data buffer with 56 buffer cells (each cell stores a  $2 \times 2$  pixel cluster address and the four analog pulse heights) and one 40 cell deep time stamp buffer. The third part is a control interface block where readout logic, DACs, I2C interface, ROC readout buffer, 8 bit ADC etc. are located.

Several new features are implemented in the new ROC. The main ones are: i) a checkout mechanism that allows the column drain to run continuously and does not require a buffer reset; ii) a different communication logic design between the pixel unit cell and the periphery that allows for 7 pending column drains instead of 3 and iii) a new 40MHz Dynamic Cluster Column Drain (DCCD) mechanism, which improves the 2.4 times higher in readout speed comparing to PSI46dig. PROC600 even demonstrated very high hit efficiency 99.4% for  $300 \text{ MHz/cm}^2$  X-ray exposer after having irradiated with 23 MeV proton (KIT Zyklotron AG) at accumulated 1.2MGy TID (Si) [113].

## **ROC4Sens**

The design of this prototype readout ROC4Sens was released at the same time of PROC600 but with bump-pad position of  $50 \mu\text{m}$  by  $50 \mu\text{m}$  in staggered style, which enables to test the HL-LHC compliant small pitch and thin sensors. It followed the same IBM 250nm CMOS processing technology. Bump pad opening remains  $15 \mu\text{m}$ . The entire ROC size is about  $8 \times 8 \text{ mm}^2$  and it consists  $160 \times 160$  active pixels. Radiation tolerance of this ROC is expected up to 5 MGy.

### **3.4.3 CMS Si Strip Tracker**

The Silicon Strip Tracker (SST) consists of four main subsystems: the four-layer Tracker Inner Barrel (TIB), the six-layer Tracker Outer Barrel (TOB) and, on each side of the barrel region, the three-disk Tracker Inner Disks (TID), and the nine-disk Tracker End Caps (TEC). Each TID disk is made of three rings of modules, while the TEC disks have seven rings. Overall, the tracker cylinder is 5.5 m long and 2.4 m in diameter, with a total active area of  $198 \text{ m}^2$ , consisting of 15,148 detector modules and comprising 9.3 million detector channels. Each detector module consists of a carbon or graphite fiber frame, which supports the silicon sensor and the associated front-end

readout electronics. Four barrel layers and three rings in the end cap disks are equipped with double-sided modules, each of which is constructed from two single-sided modules mounted back-to-back with a stereo angle of 100 Mrad between the strips. The silicon sensors are made up of single-sided p<sup>+</sup> strips on n-bulk sensors with two different thicknesses: 320μm and 500μm in the inner four and outer six layers of the barrel, respectively; 320μm in the inner disks; and 320μm and 500μm in the inner four and outer three rings of the end cap disks, respectively. There are a total of fifteen different types of sensors in the SST, which vary in terms of strip length and pitch to ensure that the single strip occupancy is low even at full LHC luminosity.

### **APV25 SST Readout**

IBM processed APV25 readout chip in 250 nm CMOS. The chip samples, amplifies, buffers, and processes signals from 128 detector channels at a frequency of 40 MHz. Thus fast pulse shaping is required for providing the bunch crossing identification and minimizing pileup. This is hard to achieve with low noise and power levels, so the APV25 chip uses pre-amplifier and shaper stages to produce a CR-RC pulse shape with a relatively slow rise-time of 50 ns in an operating mode, known as peak. As an alternative, deconvolution performs additional signal processing to constrain the signal to a single bunch crossing (at the expense of a reduced SNR). In the absence of a trigger, no data frames are output by the APV25 chip, but tick marks are produced in every 70 clock cycles [114].

Taking into account the forthcoming HL-LHC requirements, several improvements will be made within both sides of SST and corresponding readout chip. Detector shall follow the n<sup>+</sup>-in-p type sensor but they will be thinned down to the backside (p<sup>+</sup>-substrate) for Float Zone Si wafer. Active thickness of the detectors will be 200-300μm that shall bring the greater opportunity of having lower reverse bias voltage, for achieving lower full depletion voltage and lower leakage current than the present one. The readout chip shall use a more aggressive CMOS processing technology like 130 nm for CBC (CMS Binary Chip for SST) [115] and 65 nm for SSA (Strip Sensor ASIC) with several enhanced functionalities.

## Chapter IV

### Radiation Hardness of FBK 4-inch 3D DDTC Si Sensors

3D Silicon radiation sensors that had been introduced by S. Parker and collaborators at the Stanford Nanofabrication Facility (SNF) in 1997, are now grown with technological maturity and have been holding a pioneering place among all radiation hardness candidates, thus they should be a favorite choice the future High Luminosity upgrades at the LHC (HL-LHC) [116]. In 3D sensors, columnar or trench electrodes of both doping types, oriented perpendicularly to the wafer surface, penetrate the substrate. In this configuration the spacing between the electrodes can be engineered by layout and is independent of the substrate thickness extensively, keeping only in mind the maximum aspect ratio achievable for the etched electrodes. This has been the key feature inherently making 3D sensors radiation hard: the inter-electrode spacing can be made small enough to mitigate the effect of charge carrier trapping on the signal efficiency even for very large radiation fluences, as is also demonstrated by simple geometrical considerations [117].

The scope of this chapter shall be understanding more details on technicalities of radiation hardness of two generations of FBK productions in terms of bias operating range (after irradiation): state of art IBL design and modified junction column non-passing through technology. In general, it should also be noted that the breakdown voltage of 3D sensors is not as high as that of planar sensors, due to several process and design constraints. Before irradiation this is not a big concern, since the applied breakdown voltage generally remains much larger than the full depletion voltage. As an example, the typical breakdown voltage for 3D sensors fabricated at FBK for the IBL ranged from 40 V to 60 V before irradiation, while the full depletion voltage was lower than 10 V [32]. After irradiation, the situation becomes more complex and it is required thereby to be carefully analysed. Both the breakdown voltage and the full depletion voltage increase, but to different extents, depending on the structures, the irradiation scenarios, and the annealing conditions. The increase of the full depletion voltage depends on the bulk radiation damage and the related increase in the effective substrate doping concentration, as can be predicted analytically (i.e., by using the Hamburg model [118]). On the contrary, the increase of the breakdown voltage depends not only on the bulk damage but also on the surface damage and the related increase of oxide charge and interface state densities. As a result, the breakdown voltage of irradiated devices is not straight-forward to predict. An analytical model was proposed in [119], based on the properties of cylindrical (for columns) and spherical (for column tips, when applicable) junctions, but it does not account for surface effects, so it is not reliable either before or after irradiation. TCAD simulations could yield accurate results for non-irradiated sensors if properly tuned for specific technologies [53,120]. They remain yet less accurate for irradiated sensors, mainly due to the lack

of comprehensive radiation damage models incorporating both bulk damage and surface damage in aggregated way (in particular for the interface state parameters), which are still under development by several collaborators [121, 122].

**Table 4.1:** Summary of breakdown voltage values ( $V_{bd}$ ) measured on proton irradiated 3D sensors from different foundries. The proton fluences are converted to 1-MeV neutron equivalent ( $n_{eq}$ ) fluences by using the reported hardness factors in according to the NIEL hypothesis. The bias values required to saturate the signal amplitudes ( $V_{bias}$ ) are also reported, wherever applicable. For some devices (\*) exhibiting charge multiplication effects,  $V_{bias}$  values were estimated from the collected charge versus voltage curves, although no signal saturation is present.

Manufacturer	Sensor type	Proton energy	Hardness factor	Fluence ( $n_{eq}/cm^2$ )	$V_{bd}$ (V)	$V_{bias}$ (V)		
SNF	Full-3D, n-in-p	55 MeV	1.71	$1.7 \times 10^{14}$	~60	20		
				$1.7 \times 10^{15}$	>100	105		
		800 MeV	0.62	24 GeV/c	0.62	$3.2 \times 10^{14}$	~60	50
				0.71	$1.4 \times 10^{15}$	90	90	
					$3.5 \times 10^{15}$	170	110	
					$7 \times 10^{15}$	190	120	
CNM	3D-DDTC, p-in-n	25 MeV	2	$2 \times 10^{15}$	~260	~120*		
				$2 \times 10^{16}$	~350	~250*		
	3D-DDTC, n-in-p			$2 \times 10^{15}$	~250	~120*		
				$2 \times 10^{16}$	~400	~250*		
				$5 \times 10^{15}$	~200	160		
FBK	3D-DDTC, p-in-n	25 MeV	2	$1 \times 10^{15}$	~220	~80*		
				$2 \times 10^{15}$	~260	~120*		
	3D-DDTC, n-in-p	24 GeV/c	0.62	$2 \times 10^{15}$	90, 130	80, 120		
		25 MeV	2	$1 \times 10^{15}$	110, 150	60, 100		
	3D-DDTC+, n-in-p	25 MeV	2	$5 \times 10^{15}$	~160	150		
				$2 \times 10^{16}$	~200	>200		

The breakdown voltage values measured after irradiation on 3D sensors from different manufacturers remain mainly quite non-uniform, that depends on geometry and fabrication details as well. A summary of results present in the literature for proton irradiated 3D sensors is shown in table 4.1. In general, double-sided sensors with partially-through electrodes (referred to as 3D-DDTC) exhibit larger breakdown voltage values (e.g., those reported for CNM samples in [6,124]) than sensors with passing-through electrodes (both single-sided, namely Full-3D from SNF [35,123], and double-sided, namely 3D-DDTC+ from FBK) [64,78,124,125], but it is in fact a combination of different factors, among them the electrode depths, surface isolation layers (p-stop rather than p-spray), and other geometry details, that mostly affects the breakdown behavior. From the comparison between the breakdown voltage values and bias voltage values reported in Table 1, it is clear that the breakdown voltage is sometimes not high enough for optimal detector operation. This is particularly evident for FBK devices irradiated to very large fluences. As an example, during the IBL qualification phase, in order to achieve the target hit reconstruction efficiency of 97%, a bias voltage of at least 150 V was required for 3D pixel sensors irradiated with

protons at the benchmark fluence of  $5 \times 10^{15} \text{ n}_{\text{eq}}/\text{cm}^2$  [78]. Such a voltage value turned out to be very close to the breakdown voltage of sensors irradiated at that fluence, so that the operational margin has been quite narrow. In a later study, 3D strip sensors from the same batches of the IBL pixels fabricated at FBK were irradiated with protons up to  $2 \times 10^{16} \text{ n}_{\text{eq}}/\text{cm}^2$  and measured at the University of Freiburg [125]. In this case, the breakdown voltage increased to  $\sim 200 \text{ V}$ , but, as demonstrated by position resolved laser tests, it was lower than the full depletion voltage, so that the sensors could not be operated at the optimal bias voltage.

In foreseen applications at the HL-LHC, where the integrated radiation fluence will be as high as  $2 \times 10^{16} \text{ n}_{\text{eq}}/\text{cm}^2$  in the innermost tracking layers, the breakdown voltage of FBK 3D sensors could therefore become a limiting factor, although it is also expected that smaller inter-electrode spacing will be used, which will reduce the full depletion voltage [126]. Even below breakdown, biasing an irradiated 3D sensor at a relatively high voltage ( $\sim 200 \text{ V}$ ) could cause the leakage current to be higher than predicted by using the current damage constant  $\alpha^*$  [118] due to the onset of impact ionization effects caused by high electric fields [124]. Therefore, the leakage current of irradiated 3D sensors should also be carefully investigated. The thorough study of leakage current and breakdown voltage of irradiated 3D sensors from FBK allowed to gain deeper insight to improve both the design and the fabrication technology for future HL-LHC productions production.

#### **4.1 Two Prime Double-Sided 3D Sensors**

Optimal sensor design approach for HL-LHC 3D sensors has been investigated using the detailed study between two different FBK fabrication batches here. One of them is the ATLAS IBL production (ATLAS10) [section 2.2.3], and the second one (DTC5) is a modified R&D batch fabricated to improve the breakdown voltage of ATLAS10 through adopting some modified process steps and layout diversity. Both these batches were processed with the silicon substrates from the same ingot from TOPSIL, Denmark. These wafers were float zone, double-side polished, p-type, with 100 mm diameter,  $\langle 100 \rangle$  crystal orientation, 230  $\mu\text{m}$  thickness, and a very high resistivity, in the range from 10 to 30  $\text{k}\Omega \text{ cm}$ . As it is shown in the schematic cross sections of these batches (figure 4.1), the main difference is the depth of the junction ( $\text{n}^+$ ) columnar electrodes. The junction electrodes of IBL technology (figure 4.1 left) were etched all the way through the wafer thickness (passing-through). In this design p-spray was required on both wafer surfaces to isolate the  $\text{n}^+$  electrodes. In the later modified R&D batch (figure 4.1 right) the etching of the junction electrodes was stopped nominally  $\sim 25 \mu\text{m}$  from the opposite wafer surface (partially-through). This design relaxed the inclusion of p-spray on the back side (p side), that was uniformly doped with the same boron diffusion used for the ohmic ( $\text{p}^+$ ) columnar electrodes.

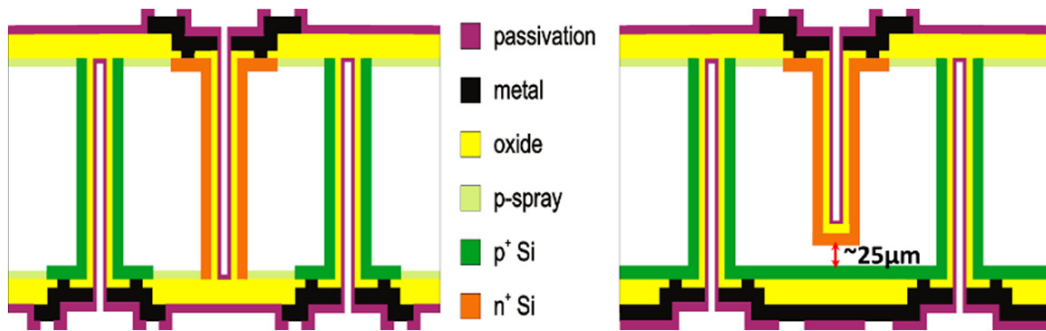


**Figure 4.1:** Schematic cross sections of the 3D sensors under study: (left) devices from the ATLAS10 batch of the IBL production, with passing-through junction electrodes; (right) devices from the DTC5 R&D batch, with partially-through junction electrodes. In both cases the ohmic electrodes are passing-through.

As it can be seen from figure 2.26 (b), the sensor of IBL Technology (ATLAS10) was limited to breakdown at 40V-60V reverse biasing before irradiation. Even though irradiation helps to improve the breakdown, such intrinsic breakdown range of non-irradiated devices gave a possible hint to experience the limited biasing operating range even after irradiation. A comparative data analysis reported for charge collection efficiency using  $^{90}\text{Sr}$  beta source (figure 4.2 (a)), made on the FE-I4 pixel sensors, fabricated at two different design approaches: full-passing through technology of FBK, Trento (figure 4.1 left) and non-passing through technology of CNM, Barcelona (figure 2.12(e)). In a careful observation, it can be noticed that FBK sensors of passing through technology was reaching to its charge collection limit (at the saturation plateau) earlier due to the anticipated full depletion obtained with full passing-through columns with respect to the CNM sensors of non-passing through technology at the same reference accumulated fluence. Since the CNM sensors owned higher breakdown limit, they collected more charge in comparison to FBK one for a higher applied reverse bias. This study gave clear motivation to review the FBK IBL design.

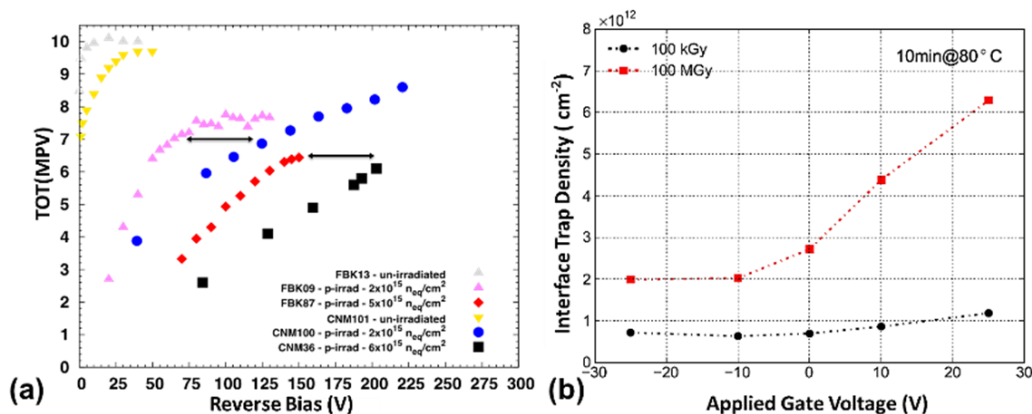


**Figure 4.2:** (a) Charge collection in FE-I4 pixel sensors with  $^{90}\text{Sr}$  beta source [78]. (b) Gate voltage dependence of the interface trap density for the MOS capacitors irradiated to 100 kGy and 100 MGy, annealed at 80°C for 10 minutes [141].

After a thorough TCAD simulation study, it was found that the electric field intensity throughout the  $n^+$ -column is not uniform. The inclusion of metal field-plate provided better voltage handling capability at the main  $n^+$  to p-spray junction on the

front side but the back side of  $n^+$ -column still remained a vulnerable point [33], where the highest electric field peak develops as the bias voltage is increased. Besides, in the IBL sensor operation, the reverse bias voltage is applied from the back of the sensor as planar sensors. For externally applied negative voltage, the direction of the electric field in the  $\text{SiO}_2$  at the back side goes from the  $\text{Si-SiO}_2$  interface to the aluminium gate. As a result, the radiation induced introduction of positive oxide charges close to the  $\text{Si-SiO}_2$  interface is smaller at the back of the sensors than at the front (similarly to what happens in MOS structures irradiated with X-rays, as shown in figure 4.2(b)). In the presence of the p-spray layer, the electric field intensity is attenuated with irradiation, but this effect is different on the two sensors sides. Thereby, higher electric field intensity remains larger at the back side of  $n^+$ -column of FBK IBL technology, possibly leading to earlier breakdown.

Keeping these facts in mind, FBK adopted a modified approach in the DTC5 batch, by shortening the  $n^+$ -column depth. In both technologies the ohmic columns remained passing-through. This feature was eminent in order to provide the proper ohmic fence termination surrounding the active area, thus yielding a slim edge with a size of  $200\mu\text{m}$  or below [73, 75].

The characterization of the sensor electrical behavior was carried out using small test structures, so-called 3D diodes. These devices consist of an array of junction columns all connected together by either a metal grid or an  $n^+$ -diffusion or both, so as to obtain a 2-electrode device. In this respect the testing can be performed without the need of complex bonding solutions. These 3D diodes reproduce the electrode configurations and layout details of their parent pixel or strip sensors. However, owing to their relatively small size (a few  $\text{mm}^2$ ), 3D diodes often remain free from process-related defects, making it possible to investigate the intrinsic properties of the different structures.

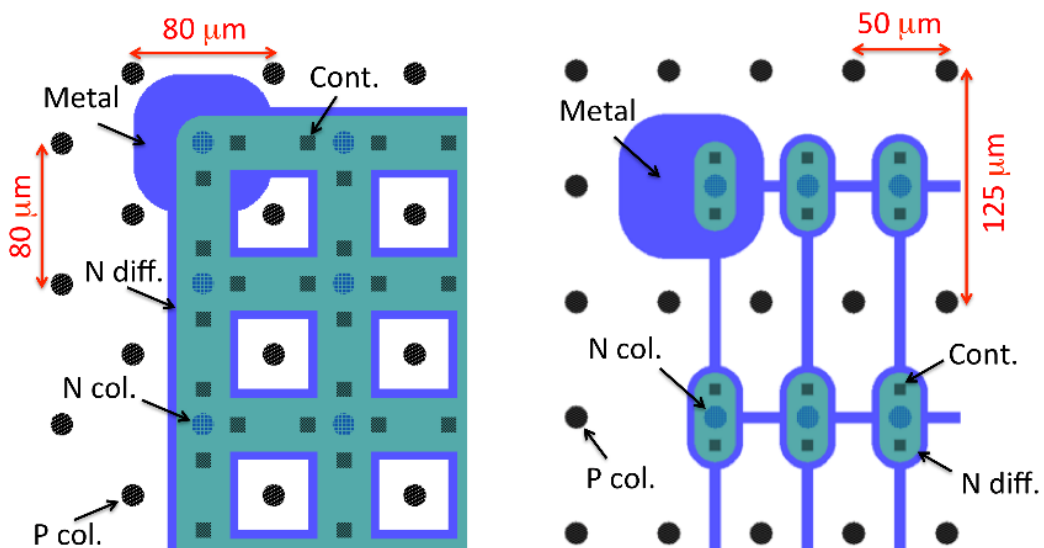
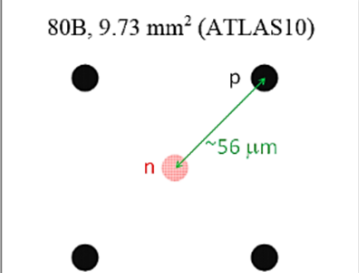
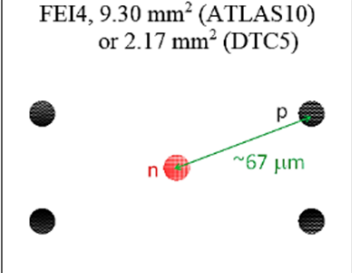
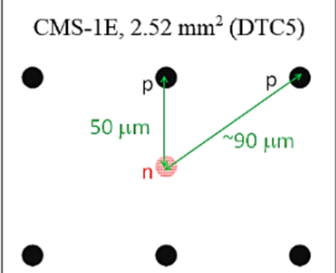
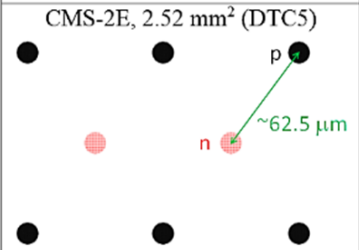
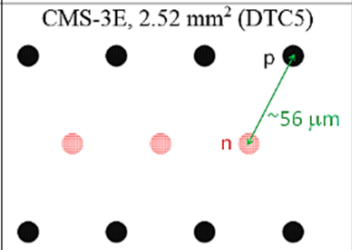
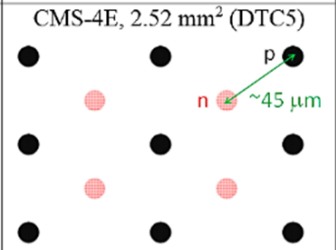


Figure 4.3: Layout of the corner regions of the 3D diodes examined, with indication of the main features: (left) the 80B diode, and (right) the FEI4 diode.

The layout details of two types of 3D diodes are shown in figure 4.3. On the left in figure 4.3 is the 80B diode, with a pitch of  $80\ \mu\text{m}$  between columnar electrodes of the same doping type, corresponding to a distance of  $\sim 56\ \mu\text{m}$  between columns of opposite type [13]. Junction columns are shorted by a grid of  $n^+$ -diffusion and metal. On the right in figure 4.3 is the FEI4 diode, with a pitch of  $50\ \mu\text{m}$  (in X) and  $125\ \mu\text{m}$  (in Y) between columnar electrodes of the same doping type, corresponding to a distance of  $\sim 67\ \mu\text{m}$  between columns of opposite type. Junction columns are surrounded by a small  $n^+$ -diffusion and shorted by a grid of metal. This layout matches that of ATLAS IBL 3D pixel sensors [73].

**Table 4.2:** Summary of the device geometries with sketches of the column configuration.

<p>80B, <math>9.73\ \text{mm}^2</math> (ATLAS10)</p> 	<p>FEI4, <math>9.30\ \text{mm}^2</math> (ATLAS10) or <math>2.17\ \text{mm}^2</math> (DTC5)</p> 	<p>CMS-1E, <math>2.52\ \text{mm}^2</math> (DTC5)</p> 
<p>CMS-2E, <math>2.52\ \text{mm}^2</math> (DTC5)</p> 	<p>CMS-3E, <math>2.52\ \text{mm}^2</math> (DTC5)</p> 	<p>CMS-4E, <math>2.52\ \text{mm}^2</math> (DTC5)</p> 

Other diodes from the DTC5 batch have a layout similar to the FEI4 one, but with different inter-electrode spacing, matching those of pixel sensors compatible with the CMS PSI46 read-out chips [126]. All diodes from the DTC5 batch have smaller active areas than those of the ATLAS10 batch. Geometrical details of different structures are summarized in Table 4.2.

## 4.2 Irradiation Campaigns

Several irradiations at different facilities have been made in order to study the radiation tolerance of these sensors.

- **X-ray irradiation:** This campaign was intended to study the impact of surface damage alone on the breakdown voltage. It was performed at the Semiconductor Irradiation Facility (Seifert RP-149) available at the INFN LNL (Legnaro, Italy), which features an X-ray tube with a tungsten anode having a continuous energy spectrum up to  $60\ \text{keV}$  (at the maximum voltage of  $60\ \text{kV}$ ) with a peak at  $10\ \text{keV}$ . Irradiation was carried out at room temperature on devices keeping both unbiased and reverse biased at  $20\ \text{V}$ . Dosimetry is accomplished by calibrated square silicon diodes with an active area of  $25\ \text{mm}^2$  and a thickness of  $300\ \mu\text{m}$ . The

dose rate and the area of irradiation with a dose rate uniformity within 10% depend on the X-ray tube operating condition ( $V$ ,  $I$ ) and on the distance between the X-ray tube and the DUT (e.g., a dose rate of  $\sim 500$  rad/s can be reached on an area of  $\sim 15 \times 10$  mm<sup>2</sup> at a distance,  $d = 10$  cm with a current,  $I = 50$  mA at  $V=50$  kV) [127].

- ***γ-ray irradiation*** was performed at the Sandia Gamma Irradiation Facility (Albuquerque, USA) by using a planar array of Cobalt-60 sources providing uniform exposure at a rate up to approximately 1 krad per second. Irradiation was carried out in a dry cell at room temperature with the devices unbiased. Dosimetry is accomplished by using thermoluminescent devices (TLDs) or ion chambers to measure the rate at the location of the device under test. The rate is then used to compute the total irradiation time required. The uncertainty on the measurement is  $\pm 5\%$ .

- ***Neutron irradiations*** were performed at the TRIGA Mark II reactor at the Jozef Stefan Institute – JSI (Ljubljana, Slovenia) and at the Sandia Annular Core Research Reactor (Albuquerque, USA). The former is a light-water reactor fuelled by solid elements with a maximum power of 250 kW. Several tubes in the reactor core can be used for irradiation purposes, and the reactor power can be varied to achieve fluxes up to  $4 \times 10^{12}$  n cm<sup>-2</sup> s<sup>-1</sup>. The neutron energy spectrum is broad, ranging from thermal neutrons up to 10 MeV. The hardness factor is 0.9 and the accuracy in the neutron fluence is given as 10% [128]. No deliberate cooling system is installed in usual condition.

The Sandia reactor is a pool-type reactor having a core formed of BeO-UO<sub>2</sub> fuel elements arranged around a 9-inch diameter dry central cavity. During irradiation, samples are placed in a lead-boron lined vessel producing a narrow filtered neutron spectrum centered on 1 MeV. The temperature of the cavity depends upon reactor power and thus rate of irradiation. Temperature can be maintained below 100°C during continuous operation up to applied fluence  $2 \times 10^{15}$  cm<sup>-2</sup>. Higher fluences can be achieved without exceeding this temperature by applying the dose in cycles of  $2 \times 10^{15}$  cm<sup>-2</sup> followed by cooling pauses. TLDs measure the absorbed dose or ionizing radiation exposure. To measure the total fluence, two types of dosimetry are applied: sulfur for fluences up to  $2 \times 10^{15}$  cm<sup>-2</sup>, and Ni-58 foils for fluences in the range  $1 \times 10^{13}$  cm<sup>-2</sup> to  $3 \times 10^{16}$  cm<sup>-2</sup>. The typical uncertainty for this combined method is below 3.7%.

- ***Proton irradiations*** were performed with 25 MeV protons at KIT (Karlsruhe, Germany) and 800 MeV protons at LANSCE (Los Alamos, USA).

At KIT protons are obtained from a cyclotron. Devices to be irradiated are mounted on an aluminium frame and placed in a box cooled by nitrogen to -30°C in order to prevent structures from annealing during the irradiation. The box is fixed to a moving table allowing the samples to be scanned by the proton beam both in X and Y for a homogenous irradiation. The fluence is estimated analytically from the beam properties and then verified by using nickel foils placed behind the structures for

dosimetry. The uncertainty of the irradiation fluence is estimated to be lower than 20% [129].

LANSCE utilizes the 800 MeV primary proton beam, which can deliver approximately  $8 \times 10^{15}$  p cm<sup>-2</sup> over a 24-hour period to a stack of devices oriented perpendicularly to a beam of diameter 1 to 3 cm. Devices were irradiated unbiased, at room temperature. The uncertainty on the proton fluence, as measured with gamma spectrometry on high purity aluminium foils, is 10%. There is an additional component to the uncertainty received by any particular device, and this derives from the location of the device in the beamspot. This uncertainty is conservatively 16%, so the total uncertainty on any received fluence should be a quadrature sum of these two terms [130]. No deliberate cooling system was installed in general condition. At LANSCE, some samples were irradiated twice: after the first irradiation they were tested, and then they were irradiated again to reach a higher total fluence. For these samples, the uncertainty in the fluence values is therefore even higher, up to ~20%.

Unless otherwise stated, devices were irradiated without bias (i.e., with floating terminals). Moreover, no high temperature annealing was performed. In fact, most of the 3D data from literature summarized in Table 1, with the only exception of those FBK sensors (3D-DDTC<sup>+</sup>) irradiated with 25MeV proton at  $5 \times 10^{15}$  n<sub>eq</sub>/cm<sup>2</sup>, were obtained without annealing, so it was chosen to perform our study in the same way to compare the breakdown voltage values, that were our primary concern. X-ray and  $\gamma$ -ray irradiated samples were stored at room temperature and measured either at room temperature or at slightly lower temperature, whereas all other irradiated samples were measured at low temperature and stored in a freezer to avoid the annealing effect. However, the detectors had to be kept at room temperature for a short time during handling and experimental setup. It is thereby likely they would have experienced a short term annealing (on the order of two hours).

### **4.3 Experimental Setups**

The devices were measured mainly at the University of Trento (UTN), but also the University of New Mexico (UNM) collaborated with these activity in extent.

For measurements at UNM a probe station with a thermal chuck was used. Measurements are performed at temperatures +10 °C, 0 °C, and -10 °C. Lowered temperature is necessary to control electrical breakdown in the most highly irradiated devices, and a cold thermal environment comparable to this is foreseen for tracking volumes at the HL-LHC. The relative humidity remained less than 5% for all measurements. To find the sensor depletion voltage, a 1064 nm laser was mounted on the top facet of a biased sensor surface. The sensor was kept upon a thermal chuck. The collimation of the laser was adjusted to allow the beam to flood the entire sensor active area. The signal stimulated in the sensor by the laser photon is read out through a Picoprobe-35, which is grounded through the chuck and transmitted to a

Tektronix TDS7254B digital oscilloscope. The oscilloscope and laser are triggered by a fast pulser whose repetition rate is adjusted to allow the signal to dissipate completely between pulses. In each applied bias reference to the sensor, the value of the signal peak is recorded and averaged over 1000 laser pulses. The bias is incremented in units of few 10s V from zero until the signal value reaches to a plateau. Since the drift velocity of sensing charge particle depends on the depleted width of the sensor in terms of applied electric field, the voltage at which the plateau is achieved indicates the saturation of drift velocity and this reference bias is the full depletion voltage,  $V_{\text{depl}}$ . The uncertainty had taken account the laser spot positioning error, measurement temperature, instruments' tolerance, which is to be 20%.

To measure the leakage current in dependence of the applied reverse bias voltage, a Keithley 237 source-measure unit was applied to the p-side of the sensor keeping in dark closure. Leakage current data are acquired by a Keithley 617 electrometer. The data are collected at a rate of one point per second. Dry nitrogen is applied continuously to the environment to prevent condensation. The measurement is confirmed for voltage ramped up and down, for magnitudes greater than 100 V to avoid artifacts arising from the intrinsic accuracy of the Keithley devices. Three measurements are made at each voltage point. Their average is used as the measurement value, and their standard deviation is assigned as the statistical uncertainty. The statistical uncertainty on any measured current is  $(3-9) \times 10^{-13}$  A. The systematic uncertainties on the bias voltage and leakage current derive from the manufacturer's accuracy specifications for the Keithley 237 and 617 are  $\pm(0.04\% + 240 \text{ mV})$  on the applied voltage and  $\pm(0.3\% + 100\text{fA})$  on the measured current, respectively.

For measurements at UTN facility, the irradiated samples are mounted on custom PCB's with gold plated pads for the wire bonding of the devices. Measurements of the assemblies are then performed in a climate chamber at temperatures varying over the range from +20 °C and -20 °C. Since the climate chamber does not allow for humidity control, 3D sensors measured here would have been quite sensitive to humidity effects at low temperatures [14]. Capacitance-voltage (C-V) tests are performed with a HP4284A LCR meter at frequencies of 1 kHz and 10 kHz with parallel plate capacitance model implemented with LabView integrated system. The bias voltage is systematically raised by 1 V increments from 0 V to around 250 V or until breakdown occurs. The uncertainty is estimated to be around 10%. Depletion voltage is determined from the capacitance versus voltage graph in log-log where knee appears. However, after heavy irradiation, due to the effects of, a sharp full depletion plateau cannot be expected as it is usually seen for nonirradiated device, due to frequency dependent C-V behavior. The carriers are trapped at the defect levels and their emission rates are not fast enough to follow the measuring signal. Aside, parallel plate capacitive model used for 3D sensors does not fully agree. Still it is possible to find the full depletion voltage by choosing the proper frequency (i.e., 1kHz

signal frequency follows better to these 3D sensors' bulk resistivity) and fitting data with two intersecting straight lines in the region of C-V curve knee. The uncertainty of this full depletion measurement include the regression linear fit error, as well as the choice of data range used for the fits. As recommended in [131], wherever applicable, the maximum bias voltage for the fit should be at least 100 V above the depletion voltage in order to improve the accuracy, but this is not always possible with 3D sensors. It should also be worth to mention that C-V curves of 3D sensors normally do not show a perfect saturation, even before irradiation, as a result of some side effects like p-spray depletion at the surface [120]. Thus, the full depletion voltage information reported here have a relatively large uncertainty, up to 30% in the worst case.

In case of the leakage current measurement versus bias voltage, high voltage is applied to the sensor from a Keithley 2410 source-measure unit. Leakage current data are acquired by a HP4145B semiconductor parameter analyzer using average integration time. The systematic uncertainties on the bias voltage and leakage current derive from the manufacturer's accuracy specifications for the Keithley 2410 and HP4145B, respectively. For the former, they are  $\pm(0.02\% + 100 \text{ mV})$  on the applied voltage. For the latter, they depend on the range of the measured current:  $\pm(1\% + 6\text{pA})$  up to 1nA,  $\pm(1\% + 15\text{pA})$  from 1nA to 10nA,  $\pm(0.5\% + 100\text{pA})$  from 10nA to 100nA,  $\pm(0.5\% + 1\text{nA})$  from 100nA to 1 $\mu\text{A}$ ,  $\pm(0.3\% + 10\text{nA})$  from 1 $\mu\text{A}$  to 10 $\mu\text{A}$ ,  $\pm(0.3\% + 100 \text{ nA})$  from 10 $\mu\text{A}$  to 100 $\mu\text{A}$ ,  $\pm(0.3\% + 1\mu\text{A})$  from 100 $\mu\text{A}$  to 1mA.

From the I-V curves measured both at UNM and UTN, the adimensional function  $k(I; V)$  was used, that represents the sensitivity of the current to the voltage, calculated as in equation (4.1),

$$k(I, V) = \frac{\Delta I}{\Delta V} \cdot \frac{V}{I} \quad (4.1).$$

The breakdown voltage is then extracted as the maximum voltage for which the value of  $k$  is lower than a limit value  $k_{bd}$ . This method, first introduced in [132], is suitable to deal with those cases where, due to defects, the current shows a smooth and continuous increase rather than an abrupt increase, since it allows this behavior to be disentangled from a real avalanche breakdown. Moreover, the method is independent from the depletion voltage reference, so the full depletion voltage,  $V_{fd}$  related uncertainty does not impact the I-V results. Taking into account that the adimensional 'k' values are normally between 0.2 and 0.6 in most of the measured I-V curves until a few Volts before breakdown, that a value of 1 corresponds to an ohmic behavior (sometimes observed in highly irradiated sensors), and a value much larger than 1 points to a real avalanche behavior, in our investigations we set  $k_{bd}$  to 4 to indicate the avalanche induced breakdown. Bearing in mind the instrumental accuracy, the high reproducibility of the I-V curves, as well as the dependence of the results on the data range used to calculate  $k(I, V)$ , the total uncertainty is estimated to

be below  $\pm 1V$  for those devices exhibiting an abrupt increase of the current at breakdown, and up to  $\pm 3V$  for those devices exhibiting a smooth rise.

**Table 4.3:** Summary of all samples considered with indication of the facility where they were irradiated and measured: University of New Mexico (UNM) and University of Trento (UTN).

Irradiation	ATLAS10		DTC5	
	80B	FEI4	FEI4	CMS
X-ray@Legnaro	7 (UTN)	6 (UTN)	4 (UTN)	—
$\gamma$ -ray@Sandia	—	—	5 (UNM)	—
Neutrons@JSI	12 (UTN)	9 (UTN)	4 (UTN)	—
Neutrons@Sandia	—	—	14 (UNM)	—
25 MeV protons@KIT	—	—	4 (UTN)	—
00 MeV protons@LANSCE	6 (UNM) +6 (UTN)	4 (UNM) +5 (UTN)	14 (UNM) +12 (UTN)	10 (UTN)

## 4.4 Comparative Experimental Studies

### 4.4.1 Before Irradiation

Comparative data relevant to the electrical characterization before irradiation of 3D diodes are from both of the ATLAS10 and DTC5, which have already been reported [32, 33, 120]. A brief summary of them is reported here to facilitate the comparison with the irradiated samples. All diodes have a very small depletion voltage, as measured with the C-V method. Values span from  $\sim 2$  V to  $\sim 10$  V, depending on the layout (i.e., inter-electrode spacing). The leakage currents at full depletion range from a few nA in the best samples (corresponding to about 1 pA/column) to  $\sim 20$  nA. Taking into account that diodes from the DTC5 batch have a smaller active area (see Table 4.2), their leakage current density is generally higher, up to a factor of 15 in some samples. This difference is likely due to the higher mechanical stress experienced by the DTC5 devices during processing, as a result of an asymmetric configuration of dielectric layers covering the silicon surface, which also caused a high bow at the end of the process [120].

In the case of intrinsic breakdown voltage, diodes from the ATLAS10 batch feature values in the range from 35 V to 65 V, whereas diodes from the DTC5 batch feature values in the range from 65 V to 130 V. This significant increase of the intrinsic breakdown voltage was possible by the modified process and layout changes implemented on purpose in the DTC5 batch. Stopping the  $n^+$  column etching  $\sim 25$   $\mu\text{m}$  from the opposite wafer surface avoids this critical region in the DTC5 (figure 4.1, right). By doing so, the maximum electric field peak remained to the front side only, where the enhanced layout design of using field plates around the junction column improved the intrinsic breakdown voltage of DTC5 in comparison to ATLAS10.

However, the presence of high electric fields at the  $n^+$  column tips of DTC5 devices should be considered (TCAD simulations show the related breakdown voltages are of the order of 250 V) [79, 132]. For its impact on the breakdown voltage, it is also useful to recall that the oxide charge density ( $N_{ox}$ ) measured through C-V measurements made on MOS capacitors is in the range  $(3-4)\times 10^{11} \text{ cm}^{-2}$  for the ATLAS10 batch [32], whereas for the DTC5 batch it is in the range  $(1-6)\times 10^{11} \text{ cm}^{-2}$ , with a much wider non-uniformity (likely due to the high mechanical stress problem mentioned above), which can explain the large variations observed in the breakdown voltage values.

#### 4.4.2 X-ray and Y-ray Irradiation

Several diodes from the ATLAS10 batch were irradiated with X-rays at a nominal dose of 2 Mrad(Si) to the front-side, along with MOS capacitors from the same wafers. During irradiation most devices were left floating, although a few of them were reverse biased at 20 V. Irradiation caused a sizable increase of the leakage current, due to increasing surface generation, as well as an increase of the breakdown voltage of at most  $\sim 50$  V. This is to be attributed to the higher oxide charge density (a value of the order of  $1\times 10^{12} \text{ cm}^{-2}$  was measured from C-V curves of MOS capacitors irradiated without bias). I-V curves of some 3D diodes of the FEI4 type are shown in figure 4.4. Current values are normalized to device active area in order to ease the comparisons between two batches. Samples W20-D5 and W20-D6 likely received a lower dose due to their peripheral position in the irradiated assembly, hence their lower leakage current. Diode W15-D27 is the only device in this group irradiated under bias; in spite of the much larger oxide charge density extracted from the MOS capacitor in this condition ( $N_{ox}\sim 4\times 10^{12} \text{ cm}^{-2}$ ), the leakage current and the breakdown voltage are comparable to those of the other samples. Similar results were obtained from diodes of the 80B type from the same batch.

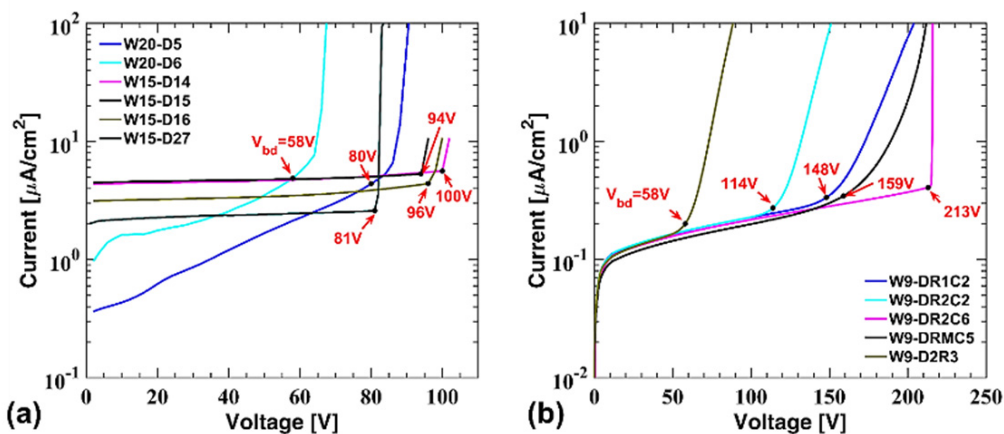


**Figure 4.4:** I-V Curves of FE-I4 3D diodes: (a) ATLAS10 batch irradiated with X-rays at a dose of 2 Mrad(Si), measured at 20°C in UTN and (b) DTC5 batch irradiated with Y-rays at a dose of 100 Mrad(Si), measured at -10°C in UNM.

Table 4.4 summarizes the most important data for all these samples: the leakage current density at full depletion ( $J_{lk}$ ), the depletion voltage ( $V_{depl}$ ), the

breakdown voltage ( $V_{bd}$ ), and the breakdown voltage difference with respect to the pre-irradiation value ( $\Delta V_{bd}$ ). Minor differences are observed in the  $J_{lk}$  and  $V_{bd}$  with different layouts. Moreover, the depletion voltage remained almost unaffected by X-ray irradiation. A few FEI4 type diodes from the DTC5 batch were irradiated with X-rays at front side at a nominal dose of 1 Mrad(Si), along with some MOS capacitors from the same wafer. The oxide charge density yielded,  $N_{ox} \sim 3 \times 10^{12} \text{ cm}^{-2}$ . During irradiation devices were reverse biased at 20 V.

**Table 4.4:** Summary of the electrical characteristics of 3D diodes from the ATLAS10 batch irradiated with X-rays at a nominal dose of 2 Mrad(Si). All diodes were left floating during irradiation except those indicated by ( $\perp$ ), which were reverse biased at 20V.

Device ID	Diode type	$J_{lk}$ (nA/cm <sup>2</sup> )	$V_{depl}$ (V)	$V_{bd}$ (V)	$\Delta V_{bd}$ (V)
W15-D9	80B	719.4±4.6	6±1	76±1	33±2
W15-D10 ( $\perp$ )		1438.8±17.5	6±1	82±1	28±2
W15-D11		4111.0±30.8	6±1	94±1	33±2
W15-D28		3288.8±26.7	6±1	66±1	17±2
W20-D9		2857.1±24.5	6±1	86±1	39±2
W20-D10		3463.5±27.6	6±1	90±1	44±2
W20-D29		801.6±5.0	6±1	82±1	37±2
W15-D14	FEI4	4301.1±32.3	7±1	100±1	37±2
W15-D15		4602.1±33.8	7±1	94±1	30±2
W15-D16		3225.8±26.9	7±1	96±1	35±2
W15-D27 ( $\perp$ )		2258.1±22.0	7±1	81±1	43±2
W20-D5		623.7±4.2	7±1	80±3	35±4
W20-D6		1763.4±19.6	7±1	58±3	8±4

Data extracted from these devices are summarized in Table 5 and it can be seen that  $V_{bd}$  is generally higher compared to the ATLAS10 batch.  $V_{bd}$  values reported are in fact strongly not uniform, with one device was showing even  $V_{bd}$  degradation, probably due to a defect. As is shown in figure 4.4 (b) and Table 5, similar behavior was observed on other diodes irradiated with  $\gamma$  -rays at a much higher dose of 100 Mrad(Si). All devices in both campaigns were left floating during irradiation. After irradiation measurements were taken at -10°C, hence the relatively low leakage currents. One device (D2R3) shows a significant  $V_{bd}$  degradation, due to a mechanical defect. It is worth noticing that  $V_{depl}$  was slightly increased by  $\gamma$ -ray irradiation, because of the bulk- type defects induced by  $\gamma$ -rays at large doses [133].

**Table 4.5:** Summary of the electrical measurements of 3D diodes of the FEI4 type from the DTC5 batch irradiated with: X-rays at a nominal dose of 1 Mrad(Si) under 20 V reverse bias and measured at room temperature (up), and b)  $\gamma$ -rays at a nominal dose of 100 Mrad(Si) keeping terminal floating, measured at  $-10^\circ\text{C}$  after irradiation.

Irradiation/Dose	Device ID	$J_{lk}$ (nA/cm <sup>2</sup> )	$V_{depl}$ (V)	$V_{bd}$ (V)	$\Delta V_{bd}$ (V)
X-rays 1 Mrad(Si)	W9-D4	921.7 $\pm$ 9.2	6 $\pm$ 1	68 $\pm$ 3	-15 $\pm$ 4
	W9-D8	921.7 $\pm$ 9.2	6 $\pm$ 1	196 $\pm$ 3	101 $\pm$ 4
	W9-D4R1C2	645.2 $\pm$ 7.8	7 $\pm$ 1	129 $\pm$ 3	55 $\pm$ 4
	W9-D8R1C2	645.7 $\pm$ 7.8	7 $\pm$ 1	116 $\pm$ 3	41 $\pm$ 4
$\gamma$ -rays 100 mrad(Si)	W9-DR1C2	124.4 $\pm$ 1.9	12 $\pm$ 1	148 $\pm$ 3	74 $\pm$ 4
	W9-DR2C2	124.4 $\pm$ 1.9	10 $\pm$ 1	114 $\pm$ 3	14 $\pm$ 4
	W9-DR2C6	119.8 $\pm$ 1.9	10 $\pm$ 1	213 $\pm$ 1	163 $\pm$ 2
	W9-DRMC5	110.6 $\pm$ 1.8	12 $\pm$ 1	159 $\pm$ 3	78 $\pm$ 4
	W9-D2R3	119.8 $\pm$ 1.9	14 $\pm$ 1	58 $\pm$ 3	-49 $\pm$ 4

#### 4.4.3 Neutron Irradiation

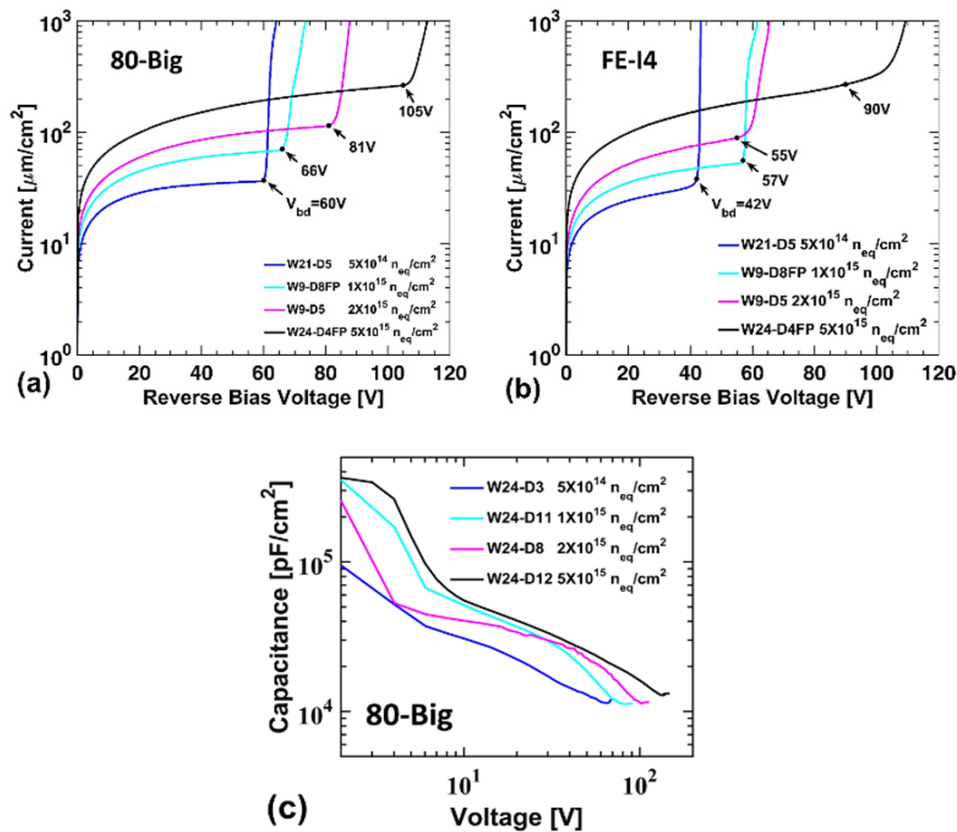


**Figure 4.5:** (a) I-V curves of four 3D diodes of the 80-Big type from the ATLAS10 batch irradiated with neutrons at JSI at four different fluences, (b) I-V curves of four 3D diodes of the FE-I4 type from the ATLAS10 batch irradiated with neutrons at JSI at four different fluences, and (c) C-V curves of four 3D diodes of the 80B type from the ATLAS10 batch irradiated with neutrons at JSI at four different fluences and measured at UTN at  $-10^\circ\text{C}$  and 1 kHz frequency.

Several diodes from the ATLAS10 batch were irradiated with neutrons at JSI in the fluence range from  $5 \times 10^{14}$  to  $5 \times 10^{15}$   $n_{eq}/cm^2$  and were then measured at UTN. As shown in figure 4.5 (a), reporting the I-V curves of four 80-Big type 3D diodes irradiated at the four different fluences and measured at  $-10^\circ C$ , irradiation induced a significant increase of the leakage current. It had less contribution to the breakdown voltage,  $V_{bd}$  which reached up to 100 V at the largest fluence. The same phenomenon was also observed for the FE-I4 type ATLAS10 3D diodes irradiated at JSI facility, as can be seen from figure 4.5(b). These voltage values are eminently not high enough to allow for observing the full depletion voltage through C-V measurements. The C-V curves as reported in figure 4.5(c) for ATLAS10 80-Big type 3D diodes stop being meaningful, due to the onset breakdown, before the capacitance values reach to a saturation plateau.

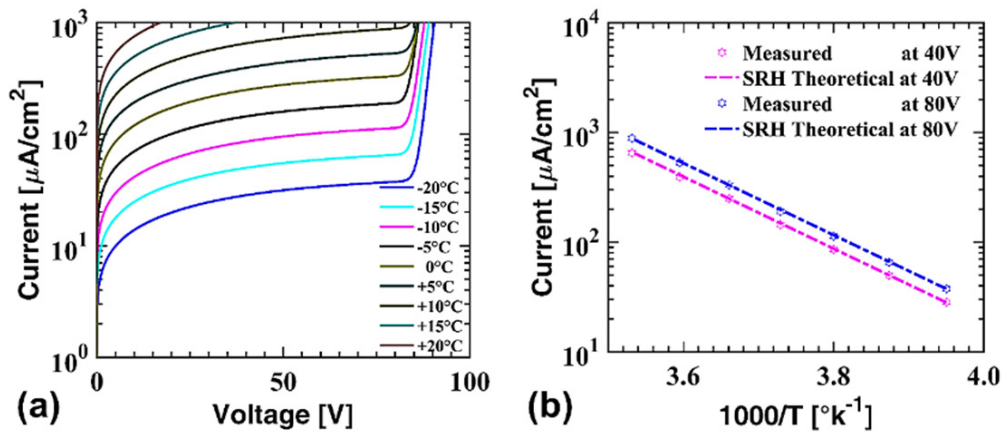


**Figure 4.6:** (a) I-V curves of a 3D diode of the 80B type from ATLAS10 batch irradiated with neutrons at JSI at a fluence of  $2 \times 10^{15}$   $n_{eq}/cm^2$  and measured at UTN at different temperatures and (b) Arrhenius plot comparing measured and calculated values of leakage current at 40 V and 80 V and their evolution with temperature for the same diode of left.

**Table 4.6:** Summary of the electrical characteristics of 3D diodes of the 80B type from the ATLAS10 batch irradiated with neutrons at JSI and measured at UTN.

Fluence ( $n_{eq}/cm^2$ )	TID (Mrad(Si))	Device ID	$J_{lk}$ at $-20^\circ C$ ( $\mu A/cm^2$ )	$\alpha^*$ ( $10^{-17} A/cm$ )	$V_{bd}$ (V)	$\Delta V_{bd}$ (V)
$5 \times 10^{14}$	0.56	W24-D3	$12.0 \pm 0.1 @ 55$ V	$5.98 \pm 0.61$	$60 \pm 1$	$14 \pm 2$
		W24-D5	$11.3 \pm 0.1 @ 42$ V	$5.76 \pm 0.58$	$48 \pm 1$	$2 \pm 2$
		W24-D10	$10.1 \pm 0.1 @ 55$ V	$5.12 \pm 0.52$	$61 \pm 1$	$15 \pm 2$
$1 \times 10^{15}$	1.11	W9-D2	$23.2 \pm 0.2 @ 60$ V	$5.72 \pm 0.59$	$67 \pm 3$	$18 \pm 4$
		W21-D3	$23.2 \pm 0.2 @ 57$ V	$5.63 \pm 0.58$	$60 \pm 1$	$13 \pm 2$
		W24-D11	$22.3 \pm 0.2 @ 60$ V	$5.57 \pm 0.56$	$66 \pm 1$	$18 \pm 2$
$2 \times 10^{15}$	2.22	W21-D2	$42.7 \pm 0.2 @ 70$ V	$4.71 \pm 0.70$	$74 \pm 1$	$28 \pm 2$
		W21-D6	$43.5 \pm 0.2 @ 70$ V	$4.73 \pm 0.68$	$72 \pm 1$	$26 \pm 2$
		W24-D8	$36.5 \pm 0.2 @ 75$ V	$4.61 \pm 0.47$	$81 \pm 1$	$34 \pm 2$
$5 \times 10^{15}$	5.56	W9-D5	$86.1 \pm 0.4 @ 80$ V	$4.18 \pm 0.49$	$82 \pm 3$	$29 \pm 4$
		W24-D7	$76.7 \pm 0.3 @ 85$ V	$4.05 \pm 0.42$	$90 \pm 1$	$40 \pm 2$
		W24-D12	$101.8 \pm 0.4 @ 90$ V	$4.33 \pm 0.67$	$105 \pm 1$	$55 \pm 2$

I-V measurements were performed at different temperatures in the range from  $-20^{\circ}\text{C}$  to  $20^{\circ}\text{C}$ . As an example, figure 4.6 (a) shows the I-V curves of a diode irradiated at  $2 \times 10^{15} \text{ n}_{\text{eq}}/\text{cm}^2$ . The current increases with temperature as expected. The temperature dependence can be better appreciated from the Arrhenius plots of figure 4.6 (b), where the current density values measured at different temperatures and at two bias voltages (40 V and 80 V) are compared to those obtained by scaling the values measured at  $0^{\circ}\text{C}$  ( $T_{\text{R}}=273.15 \text{ K}$ ) to different temperatures according to the SRH model of equation 2.16, taking into account an effective bandgap,  $E=1.21\text{eV}$  [134]. The agreement between measurements and calculations is very good, that anticipates the evidence of a dominant current contribution from thermal generation in the depleted bulk even at high voltage, close to breakdown. Conversely, it had been reported that impact ionization effects caused a significant deviation from the SRH model before irradiation even at applied bias well below breakdown [120].

**Table 4.7:** Summary of the electrical characteristics of 3D diodes of the FEI4 type from the ATLAS10 batch irradiated with neutrons at JSI and measured at UTN.

Fluence ( $\text{n}_{\text{eq}}/\text{cm}^2$ )	TID (Mrad(Si))	Device ID	$J_{\text{lk}}$ at $-20^{\circ}\text{C}$ ( $\mu\text{A}/\text{cm}^2$ )	$\alpha^*$ ( $10^{-17} \text{ A/cm}$ )	$V_{\text{bd}}$ (V)	$\Delta V_{\text{bd}}$ (V)
$5 \times 10^{14}$	0.56	W9-D1	$9.3 \pm 0.1 @ 42 \text{ V}$	$4.59 \pm 0.47$	$44 \pm 1$	$3 \pm 2$
		W21-D1	$10.6 \pm 0.1 @ 38 \text{ V}$	$5.12 \pm 0.52$	$41 \pm 1$	$2 \pm 2$
		W21-D5	$10.9 \pm 0.1 @ 39 \text{ V}$	$4.93 \pm 0.54$	$41 \pm 1$	$2 \pm 2$
$1 \times 10^{15}$	1.11	W9-D3	$19.6 \pm 0.2 @ 50 \text{ V}$	$4.68 \pm 0.47$	$51 \pm 1$	$11 \pm 2$
		W9-D8FP	$17.3 \pm 0.2 @ 55 \text{ V}$	$4.28 \pm 0.46$	$56 \pm 3$	$10 \pm 4$
		W21-D9FP	$18.4 \pm 0.2 @ 50 \text{ V}$	$4.54 \pm 0.47$	$51 \pm 1$	$5 \pm 2$
$2 \times 10^{15}$	2.22	W9-D5	$29.5 \pm 0.2 @ 53 \text{ V}$	$3.73 \pm 0.40$	$54 \pm 1$	$10 \pm 2$
		W19-D8FP	$41.6 \pm 0.2 @ 53 \text{ V}$	$4.69 \pm 0.66$	$56 \pm 1$	$6 \pm 2$
$5 \times 10^{15}$	5.56	W24-D4FP	$104.5 \pm 0.4 @ 85 \text{ V}$	$4.21 \pm 0.65$	$90 \pm 1$	$40 \pm 2$

Tables 4.6 and 4.7 summarize the most important data for the neutron irradiated samples of the 80B and FEI4 type from the ATLAS10 batch at different neutron irradiation fluences. Only minor differences were observed between samples of different geometries. The values of the current density ( $J_{\text{lk}}$ ) are referred to a bias voltage close to the breakdown voltage although full depletion was not clearly achieved. This fact along with the lack of a high temperature annealing and other non-idealities, such as, the uncertainties in the irradiation fluences, the self-heating effects experienced by the devices during irradiation, and possible humidity effects (measurements made at low temperatures with the UTN setup), made the extraction of the current damage constant ( $\alpha$ ) less significant. However, as reported, a wide range of fluences were investigated in this study, so the leakage current density alone would not give an immediate idea of the order of magnitude. Thereby, it was more appropriate to report the geometric current related damage rate ( $\alpha^*$ ), which is defined as the current increase with increasing fluence. This parameter depends on the sensor geometric volume rather than on the depleted one, so its values could differ from the standard  $\alpha$ , in particular at the largest fluences where the full depletion arrives at very

large bias. It has been reported that in undepleted depth the electric field still remains but weak. Hereby,  $\alpha^*$  defines more appropriately the damage constant for the neutron irradiated samples reported here, although for any fully depleted device, the standard  $\alpha$  and  $\alpha^*$  will be numerically same. The  $\alpha^*$  values in Tables 4.6 and 4.7 represent the average and total uncertainty. These values are in reasonable agreement with those observed in irradiated devices, not subjected to a high temperature annealing [14,135] within the above mentioned uncertainties. The decreasing trend of  $\alpha^*$  with fluence is probably to be ascribed to the smaller volume depleted at higher fluences before breakdown occurs. The increasing trend of  $V_{bd}$  with fluence is likely due to the surface damage effects from the increasing  $\gamma$ -ray background (the Total Ionizing Dose (TID) values quoted in Tables 4.6 and 4.7 are estimated from [135]).

Some diodes of the FEI4 type from the DTC5 batch were irradiated with neutrons at JSI at two different fluences ( $8 \times 10^{15}$  and  $1 \times 10^{16}$  neq/cm<sup>2</sup>), and were then measured at UTN. As an example, figure 4.7 shows the I-V curves of two samples measured at -10°C. One sees both the expected large increase in leakage current and the breakdown voltage sizable increase up to ~200V. Due to the very large fluences, full depletion was not reached, as can be observed from the C-V graphs reported in figure 4.7(b). Measurements stop being meaningful due to the onset of breakdown before the capacitance curves show any sign of saturation.

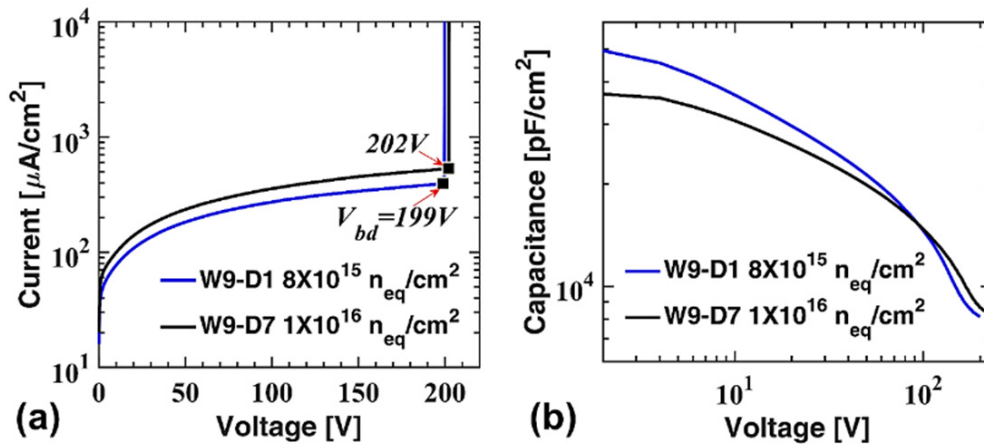


**Figure 4.7:** (a) I-V curves of two 3D diodes of the FEI4 type from the DTC5 batch irradiated with neutrons at JSI at two different fluences and measured at UTN at -10°C and (b) C-V curves of the same two 3D diodes measured at UTN at -10°C and 1 kHz frequency.

In order to study if the leakage current is mainly dominated by thermal generation, I-V measurements were performed at different temperatures in the range from -20° C to 20° C for the samples of DTC5 as well. Figure 4.8(a) and 4.8(b) show the I-V curves of a FE-I4 type diode irradiated at  $1 \times 10^{16}$  neq/cm<sup>2</sup> and the corresponding Arrhenius plots at three bias voltages (40, 100, and 200 V). The greater agreement between measurements and SRH-based calculations confirmed the leakage current

dependence mainly dominated by thermal generation in the depleted bulk, even at higher bias reference, close to breakdown.

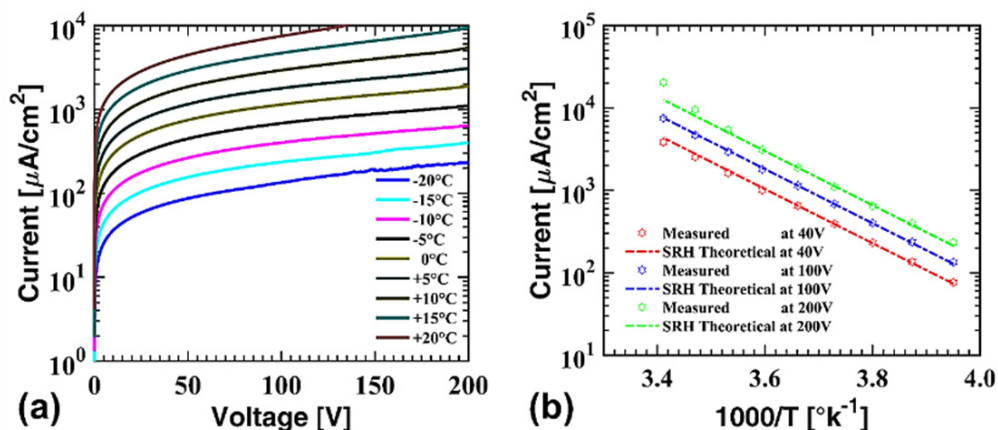


**Figure 4.8:** (a) I-V curves of a 3D diode of the FEI4 type (W9-D7) from the DTC5 batch irradiated with neutrons at JSI at a fluence of  $1 \times 10^{16} \text{ n}_{\text{eq}}/\text{cm}^2$  and measured at UTN at different temperatures, and (b) Arrhenius plot comparing measured and calculated values of leakage current at three bias voltages (40, 100, and 200 V) and their evolution with temperature for the same diode.

Table 4.8 summarizes the most important data for all the samples from the DTC5 batch irradiated with neutrons at JSI. Likewise tables 4.6 and 4.7, table 4.8 reported the damage constant rate with respect to  $\alpha^*$  values and their decreasing trend with fluence. The breakdown voltage,  $V_{\text{bd}}$  of DTC5 were larger with respect to the ATLAS10 and this is likely by the larger TID obtained at the larger irradiation fluences considered. The different geometries of the sensors also played a major role in  $V_{\text{bd}}$  that will be discussed in Section 4.4.5.

**Table 4.8:** Summary of the electrical characteristics of 3D diodes of the FEI4 type from the DTC5 batch irradiated with neutrons at JSI and measured at UTN.

Fluence ( $\text{n}_{\text{eq}}/\text{cm}^2$ )	TID (Mrad(Si))	Device ID	$J_{\text{lk}}$ at $-20^\circ\text{C}$ ( $\mu\text{A}/\text{cm}^2$ )	$\alpha^*$ ( $10^{-17} \text{ A}/\text{cm}$ )	$V_{\text{bd}}$ (V)	$\Delta V_{\text{bd}}$ (V)
$8 \times 10^{15}$	8.90	W9-D1	$153.9 \pm 0.9 @ 180 \text{ V}$	$6.02 \pm 0.90$	$199 \pm 1$	$80 \pm 2$
		W9-D2	$202.8 \pm 1.1 @ 180 \text{ V}$	$6.69 \pm 0.81$	$194 \pm 1$	$90 \pm 2$
$1 \times 10^{16}$	11.12	W9-D3	$181.1 \pm 1.0 @ 180 \text{ V}$	$4.95 \pm 0.63$	$193 \pm 1$	$88 \pm 2$
		W9-D7	$214.8 \pm 1.1 @ 180 \text{ V}$	$5.06 \pm 0.57$	$202 \pm 1$	$83 \pm 2$

Another larger set of FEI4 diodes from the DTC5 batch was irradiated with neutrons at Sandia at three different fluences ( $1 \times 10^{15}$ ,  $5 \times 10^{15}$  and  $1 \times 10^{16} \text{ n}_{\text{eq}}/\text{cm}^2$ ), and were then measured at UNM. As an example, I-V curves of all samples irradiated at  $5 \times 10^{15} \text{ n}_{\text{eq}}/\text{cm}^2$  and measured at  $-10^\circ\text{C}$  are reported in figure 4.9(a). As it is seen, DTC5 reported comparatively high breakdown voltage, and it is possible to observe full depletion from laser test. The output signal from laser excitation as a function of reverse bias in the same samples is shown in figure 4.9(b), measured at  $0^\circ\text{C}$ . A clear

saturation of the curves can be observed at reverse voltage of the order of 100 V, an evidence of full depletion.

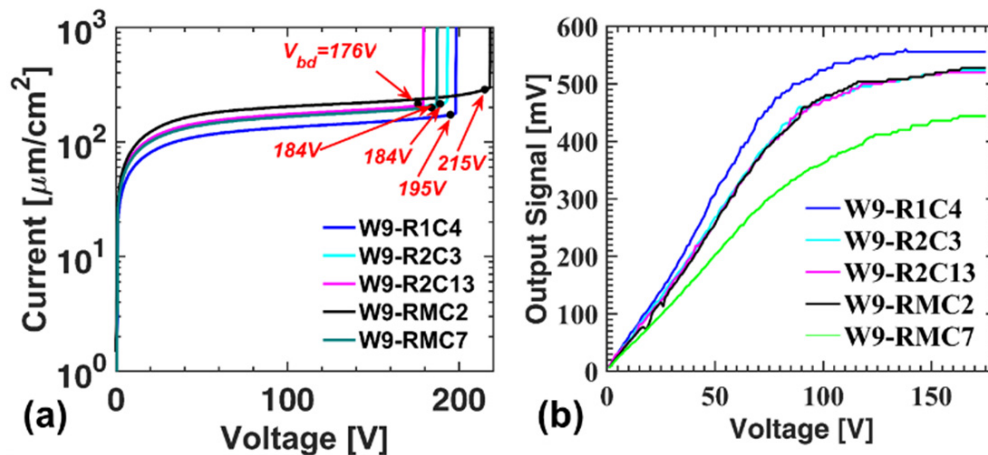


**Figure 4.9:** (a) I-V curves of five 3D diodes of the FEI4 type from the DTC5 batch irradiated with neutrons at Sandia at  $5 \times 10^{15} n_{eq}/\text{cm}^2$  and measured at UNM at  $-10^\circ\text{C}$ , and (b) Output signal in response to laser stimulation as a function of reverse bias in the same 3D diodes measured at UNM at  $0^\circ\text{C}$ .

**Table 4.9:** Summary of the electrical characteristics of 3D diodes of the FEI4 type from the DTC5 batch irradiated with neutrons at Sandia and measured at UNM. In some devices,  $V_{depl}$  could not be measured (n.a.) due to earlier breakdown.

Fluence ( $n_{eq}/\text{cm}^2$ )	TID (Mrad(Si))	Device ID	$J_{lk}$ at $-10^\circ\text{C}$ ( $\mu\text{A}/\text{cm}^2$ )	$\alpha^*$ ( $10^{-17} \text{A}/\text{cm}$ )	$V_{depl}$ (V)	$V_{bd}$ (V)	$\Delta V_{bd}$ (V)
$1 \times 10^{15}$	0.6	W9-R1C3	$87.1 \pm 0.3 @ 100 \text{ V}$	$6.88 \pm 1.14$	$60 \pm 12$	$189 \pm 1$	$101 \pm 2$
		W9-R2C7	$92.7 \pm 0.3 @ 100 \text{ V}$	$7.19 \pm 1.25$	$68 \pm 14$	$201 \pm 1$	$128 \pm 2$
		W9-RMC1	$104.6 \pm 0.3 @ 100 \text{ V}$	$7.46 \pm 1.56$	$65 \pm 13$	$217 \pm 3$	$106 \pm 4$
		W9-RMC6	$105.5 \pm 0.3 @ 100 \text{ V}$	$7.59 \pm 1.61$	$66 \pm 13$	$223 \pm 3$	$150 \pm 4$
$5 \times 10^{15}$	3.0	W9-R1C4	$148.8 \pm 0.4 @ 150 \text{ V}$	$2.33 \pm 0.14$	$94 \pm 19$	$195 \pm 1$	$103 \pm 2$
		W9-R2C3	$187.6 \pm 0.6 @ 150 \text{ V}$	$2.74 \pm 0.32$	$104 \pm 21$	$189 \pm 1$	$102 \pm 2$
		W9-R2C13	$192.6 \pm 0.6 @ 150 \text{ V}$	$2.69 \pm 0.50$	$105 \pm 21$	$176 \pm 1$	$97 \pm 2$
		W9-RMC2	$222.1 \pm 0.7 @ 150 \text{ V}$	$2.99 \pm 0.73$	$103 \pm 21$	$215 \pm 1$	$125 \pm 2$
		W9-RMC7	$183.4 \pm 0.5 @ 150 \text{ V}$	$2.63 \pm 0.42$	$109 \pm 22$	$184 \pm 1$	$102 \pm 2$
$1 \times 10^{16}$	6.0	W9-RMC4	$612.9 \pm 1.8 @ 200 \text{ V}$	$4.50 \pm 0.54$	n.a.	$199 \pm 1$	$99 \pm 2$
		W9-RMC3	$562.2 \pm 1.7 @ 195 \text{ V}$	$4.13 \pm 0.51$	n.a.	$196 \pm 1$	$94 \pm 2$
		W9-R2C12	$334.6 \pm 1.0 @ 155 \text{ V}$	$2.60 \pm 0.37$	n.a.	$157 \pm 1$	$86 \pm 2$
		W9-R2C10	$520.7 \pm 1.6 @ 190 \text{ V}$	$4.19 \pm 0.37$	n.a.	$193 \pm 3$	$112 \pm 4$
		W9-R1C7	$427.6 \pm 1.3 @ 175 \text{ V}$	$2.92 \pm 0.81$	n.a.	$177 \pm 1$	$92 \pm 2$

Table 4.9 summarizes the most important data for all samples irradiated with neutrons at Sandia. All samples exhibit a large increase of  $V_{bd}$  as a result of the TID received ( $\sim 0.6 \text{ Mrad(Si)}$  for  $1 \times 10^{15} n_{eq}/\text{cm}^2$  fluence [136]) and of the sensor geometry. The relatively low values of  $\alpha^*$  measured at high fluences in comparison to  $1 \times 10^{15} n_{eq}/\text{cm}^2$  are likely due to the high temperature experienced by the samples during irradiation. As a result, non-negligible annealing effects are present, which are of course more pronounced at larger fluences due to the much longer irradiation time.

#### 4.4.4 Proton Irradiation

Several diodes from the ATLAS10 batch were irradiated with 800 MeV protons at LANSCE at different fluences in the range from  $\sim 5 \times 10^{14}$  to  $\sim 5 \times 10^{15}$   $n_{eq}/cm^2$ . Irradiated devices were measured at both facilities of UNM and UTN. The uncertainty involved in these investigations has already been briefly discussed in section 4.2. Figure 4.10 (a) and (b) show the I-V and C-V curves made on two 3D diodes of the 80B type irradiated at two different fluences and measured at UTN at  $-10^\circ C$ . The leakage current increase is similar to that observed in the devices irradiated with neutrons at similar fluences (see figure 4.5 (a)). The increase of the breakdown voltage within these proton irradiated devices is more pronounced, which could be anticipated from the much larger TID associated with proton irradiation [176]. Owing to the larger breakdown voltage, full depletion could be reached in these samples (as reported in C-V curves of figure 4.10(b)).

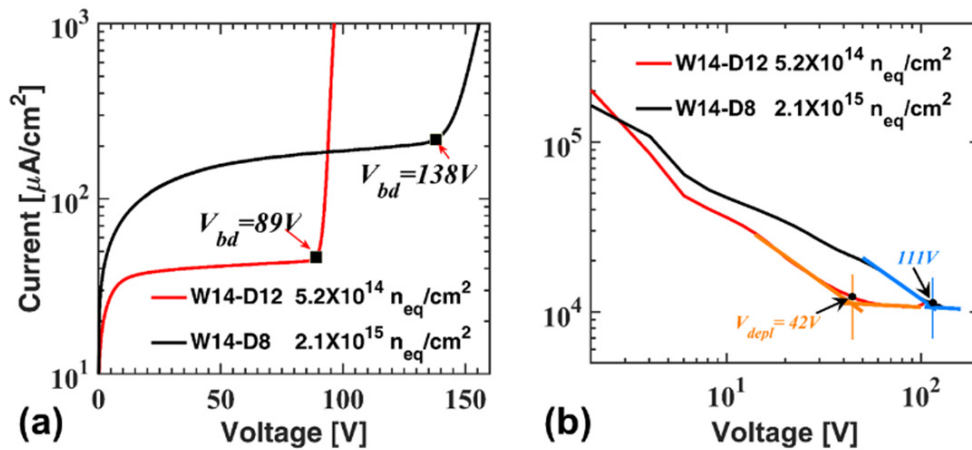


**Figure 4.10:** (a) I-V curves of two 3D diodes of the 80B type from the ATLAS10 batch irradiated with protons at LANSCE at two different fluences and measured at UTN at  $-10^\circ C$ , and (b) C-V curves of the same 3D diodes as in Fig. 15 measured at UTN at  $-10^\circ C$  and 1 kHz frequency. The depletion voltages are taken at the intercepts of two straight lines fitting the curves near the kinks.

Tables 4.10 and 4.11 summarize the most important data for all samples from the ATLAS10 batch irradiated with protons at LANSCE. The  $\alpha^*$  values are generally larger than for neutron irradiation, because the lower temperature experienced during irradiation reduces self-annealing effects. They still hold a wider dispersion because of the larger uncertainty in the fluences. As expected,  $V_{bd}$  values reported here are relatively large and increase with fluence, because of the increased TID involved. Four diodes of the FEI4 type from the DTC5 batch were irradiated with 25 MeV protons at KIT at two different fluences ( $5 \times 10^{15}$  and  $1 \times 10^{16}$   $n_{eq}/cm^2$ ), and were then measured at UTN [138]. Several other diodes from the DTC5 batch, of both the FEI4 and CMS types, were irradiated with 800 MeV protons at LANSCE at different fluences (in the range from  $\sim 7 \times 10^{14}$  to  $\sim 1 \times 10^{16}$   $n_{eq}/cm^2$ ), and were then measured at UNM and UTN. As an example, Figure 4.11(a) and (b) reported the I-V and C-V curves respectively of three 3D diodes of the FEI4 type irradiated at different fluences and measured at UTN

at  $-10^{\circ}\text{C}$ . Since the breakdown voltages were high enough, depletion voltages could be estimated from the C-V curves.

**Table 4.10:** Summary of the electrical characteristics of 3D diodes of the 80B type from the ATLAS10 batch irradiated with protons at LANSCE and measured at UNM and UTN. Some devices (#) reached the reported fluence after being irradiated a second time.

Fluence ( $n_{eq}/\text{cm}^2$ )	TID (Mrad(Si))	Device ID/Facility	$J_{fk}$ at $-10^{\circ}\text{C}$ ( $\mu\text{A}/\text{cm}^2$ )	$\alpha^*$ ( $10^{-17}$ A/cm)	$V_{depl}$ (V)	$V_{bd}$ (V)	$\Delta V_{bd}$ (V)
$5.2 \times 10^{14}$	22	W12-D1/UNM	$68.9 \pm 0.2 @ 70 \text{ V}$	$8.46 \pm 2.20$	$36 \pm 7$	$75 \pm 1$	$30 \pm 2$
		W12-D2/UNM	$78.5 \pm 0.2 @ 70 \text{ V}$	$9.82 \pm 2.82$	$38 \pm 8$	$107 \pm 1$	$61 \pm 2$
		W12-D3/UNM	$53.5 \pm 0.2 @ 70 \text{ V}$	$6.64 \pm 1.65$	$52 \pm 10$	$122 \pm 3$	$76 \pm 4$
		W14-D10/UTN	$31.1 \pm 0.2 @ 70 \text{ V}$	$4.64 \pm 0.82$	$49 \pm 15$	$73 \pm 1$	$43 \pm 2$
		W14-D11/UTN	$47.4 \pm 0.2 @ 70 \text{ V}$	$7.18 \pm 1.27$	$46 \pm 14$	$86 \pm 1$	$32 \pm 2$
		W14-D12/UTN	$42.7 \pm 0.2 @ 70 \text{ V}$	$6.95 \pm 1.14$	$44 \pm 13$	$89 \pm 1$	$33 \pm 2$
$1.3 \times 10^{15}$	55	W12-D1/UNM (#)	$91.3 \pm 0.3 @ 70 \text{ V}$	$4.66 \pm 1.25$	$40 \pm 8$	$75 \pm 1$	$30 \pm 2$
		W12-D2/UNM (#)	$96.8 \pm 0.3 @ 70 \text{ V}$	$5.10 \pm 1.44$	$38 \pm 8$	$142 \pm 1$	$96 \pm 2$
		W12-D3/UNM (#)	$73.4 \pm 0.2 @ 70 \text{ V}$	$3.79 \pm 1.00$	$45 \pm 9$	$147 \pm 1$	$101 \pm 2$
$2.1 \times 10^{15}$	89	W12-D4/UNM	$344.2 \pm 1.0 @ 100 \text{ V}$	$10.53 \pm 2.94$	$82 \pm 16$	$189 \pm 1$	$142 \pm 2$
		W12-D5/UNM	$334.0 \pm 1.0 @ 100 \text{ V}$	$10.31 \pm 2.81$	$98 \pm 20$	$178 \pm 3$	$130 \pm 4$
		W12-D6/UNM	$207.9 \pm 0.6 @ 100 \text{ V}$	$6.46 \pm 1.72$	$85 \pm 17$	$182 \pm 1$	$137 \pm 2$
		W14-D7/UTN	$169.4 \pm 1.5 @ 105 \text{ V}$	$6.44 \pm 1.12$	$81 \pm 24$	$160 \pm 1$	$101 \pm 2$
		W14-D8/UTN	$189.9 \pm 1.6 @ 105 \text{ V}$	$7.66 \pm 1.25$	$111 \pm 32$	$138 \pm 3$	$79 \pm 4$
		W14-D9/UTN	$140.7 \pm 1.4 @ 105 \text{ V}$	$5.67 \pm 0.92$	$81 \pm 24$	$113 \pm 1$	$63 \pm 2$
$5.5 \times 10^{15}$	232	W12-D4/UNM (#)	$404.9 \pm 1.2 @ 140 \text{ V}$	$4.37 \pm 1.11$	$118 \pm 24$	$236 \pm 3$	$189 \pm 4$
		W12-D5/UNM (#)	$411.9 \pm 1.2 @ 140 \text{ V}$	$4.40 \pm 1.09$	$123 \pm 25$	$244 \pm 3$	$196 \pm 4$
		W12-D6/UNM (#)	$364.5 \pm 1.1 @ 140 \text{ V}$	$3.78 \pm 0.91$	$115 \pm 23$	$204 \pm 3$	$159 \pm 4$

**Table 4.11:** Summary of the electrical characteristics of 3D diodes of the FEI4 type from the ATLAS10 batch irradiated with protons at LANSCE and measured at UNM and UTN. Some devices (#) reached the reported fluence after being irradiated a second time.

Fluence ( $n_{eq}/\text{cm}^2$ )	TID (Mrad(Si))	Device ID/Facility	$J_{fk}$ at $-10^{\circ}\text{C}$ ( $\mu\text{A}/\text{cm}^2$ )	$\alpha^*$ ( $10^{-17}$ A/cm)	$V_{depl}$ (V)	$V_{bd}$ (V)	$\Delta V_{bd}$ (V)
$2.1 \times 10^{15}$	89	W14-D1/UNM	$254.2 \pm 0.8 @ 60 \text{ V}$	$7.22 \pm 2.15$	n.a.	$70 \pm 1$	$31 \pm 2$
		W14-D2FP/UNM	$366.7 \pm 1.1 @ 80 \text{ V}$	$10.39 \pm 3.05$	$74 \pm 15$	$151 \pm 3$	$98 \pm 4$
		W14-D3/UNM	$332.9 \pm 1.0 @ 80 \text{ V}$	$10.10 \pm 2.55$	n.a.	$89 \pm 1$	$45 \pm 2$
		W14-D4FP/UNM	$255.3 \pm 0.8 @ 80 \text{ V}$	$7.68 \pm 1.89$	$76 \pm 15$	$103 \pm 1$	$55 \pm 2$
		W12-D1/UTN	$167.2 \pm 1.6 @ 110 \text{ V}$	$6.69 \pm 1.12$	n.a.	$112 \pm 1$	$65 \pm 2$
		W12-D10/UTN	$154.8 \pm 1.5 @ 105 \text{ V}$	$6.59 \pm 1.28$	n.a.	$109 \pm 1$	$76 \pm 2$
		W12-D2FP/UTN	$164.9 \pm 1.6 @ 110 \text{ V}$	$6.66 \pm 1.09$	$95 \pm 29$	$111 \pm 1$	$75 \pm 2$
		W12-D8FP/UTN	$103.4 \pm 0.4 @ 100 \text{ V}$	$4.40 \pm 0.72$	$75 \pm 23$	$106 \pm 1$	$65 \pm 2$
		W12-D9FP/UTN	$152.6 \pm 1.5 @ 115 \text{ V}$	$6.37 \pm 1.06$	$81 \pm 24$	$122 \pm 1$	$80 \pm 2$
$5.5 \times 10^{15}$	232	W14-D1/UNM (#)	$304.5 \pm 0.9 @ 135 \text{ V}$	$3.72 \pm 1.22$	n.a.	$140 \pm 1$	$101 \pm 2$
		W14-D2FP/UNM (#)	$562.5 \pm 1.7 @ 160 \text{ V}$	$6.32 \pm 2.27$	$141 \pm 28$	$224 \pm 3$	$171 \pm 4$
		W14-D3/UNM (#)	$631.4 \pm 1.9 @ 100 \text{ V}$	$5.96 \pm 2.54$	n.a.	$125 \pm 1$	$81 \pm 2$
		W14-D4FP/UNM (#)	$417.8 \pm 1.2 @ 160 \text{ V}$	$5.90 \pm 1.49$	$126 \pm 25$	$207 \pm 1$	$159 \pm 1$

I-V measurements were performed at different temperatures in the range from  $-20^{\circ}\text{C}$  to  $20^{\circ}\text{C}$ . As an example, figure 4.12 (a) and (b) show the I-V curves of a diode of the FEI4 type irradiated at  $4 \times 10^{15} n_{eq}/\text{cm}^2$  and the corresponding Arrhenius plots at two bias voltages (100 and 175 V). The good agreement between measurements and SRH-based calculations, confirmed the leakage current dependence on thermal generation only.

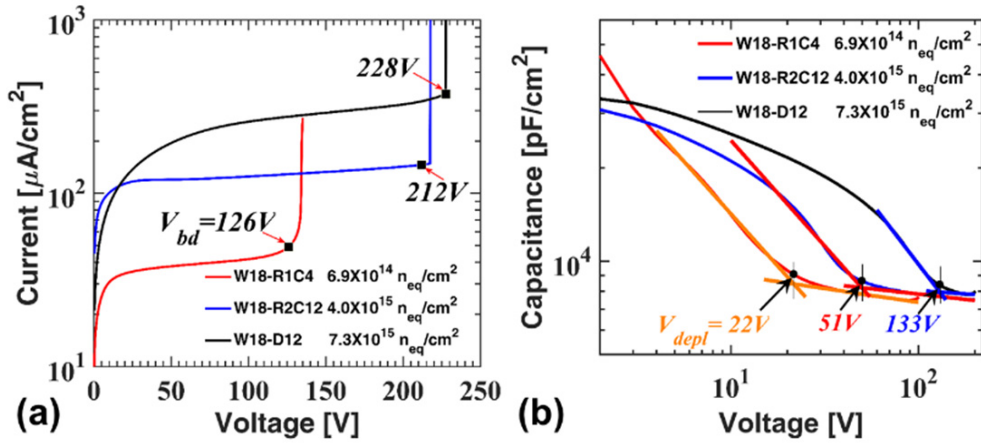


**Figure 4.11:** (a) I-V curves of three 3D diodes of the FEI4 type from the DTC5 batch irradiated with protons at LANSCE at three different fluences and measured at UTN at  $-10^\circ\text{C}$ , and (b) C-V curves of the same 3D diodes measured at UTN at  $-10^\circ\text{C}$  and 1 kHz frequency. The depletion voltages are taken at the intercepts of two straight lines fitting the curves near the kinks.

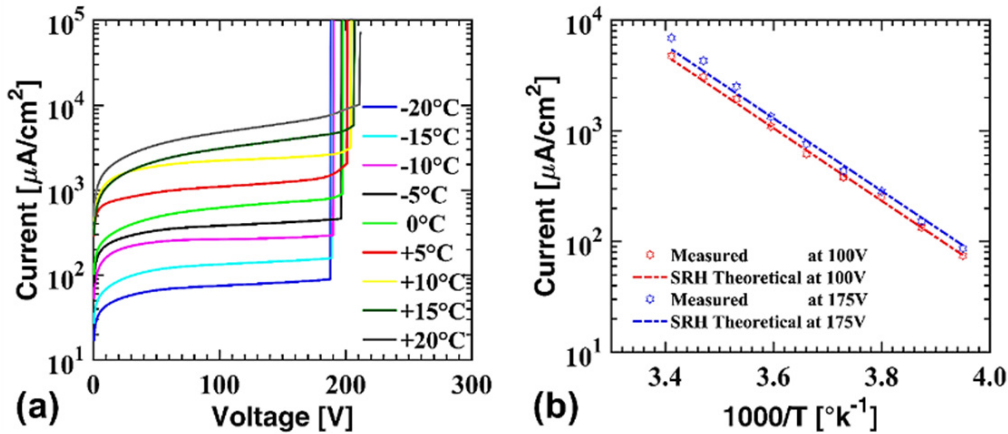


**Figure 4.12:** (a) I-V curves of a 3D diode of the FEI4 type (W18-R2C10) from the DTC5 batch irradiated with protons at LANSCE at a fluence of  $4 \times 10^{15} \text{ n}_{eq}/\text{cm}^2$  and measured at UTN at different temperatures, and (b) Arrhenius plot comparing measured and calculated values of leakage current at two bias voltages (100 and 175 V) and their evolution with temperature for the same 3D diode.

**Table 4.12:** Summary of the electrical characteristics of 3D diodes of the FEI4 type from the DTC5 batch irradiated with protons at KIT and measured at UTN.

Fluence ( $\text{n}_{eq}/\text{cm}^2$ )	TID (Mrad(Si))	Device ID	$J_{lk}$ at $-10^\circ\text{C}$ ( $\mu\text{A}/\text{cm}^2$ )	$\alpha^*$ ( $10^{-17} \text{ A/cm}$ )	$V_{depl}$ (V)	$V_{bd}$ (V)	$\Delta V_{bd}$ (V)
$5.0 \times 10^{15}$	750	W9-D6/UTN	$404.6 \pm 1.7 @ 150 \text{ V}$	$6.68 \pm 1.47$	$141 \pm 42$	$205 \pm 1$	$93 \pm 2$
		W9-D13/UTN	$457.6 \pm 1.8 @ 150 \text{ V}$	$7.55 \pm 1.67$	$131 \pm 39$	$207 \pm 1$	$96 \pm 2$
$1.0 \times 10^{16}$	1500	W9-D14/UTN	$781.6 \pm 6.9 @ 200 \text{ V}$	$6.45 \pm 1.39$	n.a.	$211 \pm 1$	$105 \pm 2$
		W9-D15/UTN	$904.1 \pm 7.3 @ 200 \text{ V}$	$7.47 \pm 1.56$	n.a.	$217 \pm 1$	$101 \pm 2$

Tables 4.12, 4.13 and 4.14 summarize the most important data for all samples from the DTC5 batch irradiated with protons. Geometrical damage constant rate,  $\alpha^*$ , was adopted within these table, as it was considered for tables 4.10 and 4.11. Compared to proton irradiated samples from the ATLAS10 batch,  $V_{bd}$  values are generally larger at lower fluences, but they are similar at large fluences.

**Table 4.13:** Summary of the electrical characteristics of 3D diodes of the FEI4 type from the DTC5 batch irradiated with protons at LANSCE and measured at UNM and UTN. Some devices (#) were re-irradiated to reach the reported fluence.

Fluence ( $n_{eq}/cm^2$ )	TID (Mrad(Si))	Device ID/Facility	$J_{fk}$ at $-10^\circ C$ ( $\mu A/cm^2$ )	$\alpha^*$ ( $10^{-17} A/cm$ )	$V_{depl}$ (V)	$V_{bd}$ (V)	$\Delta V_{bd}$ (V)
$6.9 \times 10^{14}$	29	W18-R1C1/UNM	43.3±0.1@100 V	4.98±0.93	29±6	160±1	70±2
		W18-R1C2/UNM	37.3±0.1@100 V	4.37±0.74	25±5	222±1	127±2
		W18-R1C3/UTN	37.8±0.2@100 V	4.32±0.70	21±6	125±1	45±2
		W18-R1C4/UTN	41.9±0.3@100 V	5.26±0.87	22±7	126±3	41±4
$4.0 \times 10^{15}$	169	W18-D1/UNM	322.1±1.0@150 V	6.23±1.10	100±20	215±1	115±2
		W18-D2/UNM	462.7±1.4@150 V	8.73±1.66	110±22	231±3	138±4
		W18-D4/UNM	298.6±0.9@150 V	5.11±1.56	105±21	218±1	129±2
		W18-R2C2/UNM	240.5±0.7@150 V	4.52±0.90	105±21	209±1	124±2
		W18-R2C5/UNM	367.7±1.1@150 V	6.89±1.39	105±21	246±3	149±4
		W18-RMC1/UNM	180.6±0.5@150 V	3.52±0.59	90±18	212±1	132±2
		W18-R2C4/UTN	181.1±1.0@100 V	3.51±0.68	n.a	115±1	20±2
		W18-R2C9/UTN	298.6±1.4@150 V	6.43±1.27	117±35	190±1	80±2
		W18-R2C10/UTN	274.2±1.3@150 V	5.70±1.12	97±29	187±1	81±2
		W18-R2C12/UTN	132.7±0.9@150 V	3.10±1.39	51±16	212±1	97±2
		W18-D3/UTN	294.0±1.3@150 V	5.11±1.53	138±41	200±1	85±2
W18-D7/UTN	346.1±1.5@150 V	6.87±1.12	124±37	202±1	91±2		
$7.3 \times 10^{15}$	308	W18-D10/UNM	310.1±0.9@200 V	3.34±0.59	95±19	246±3	146±4
		W18-D15/UNM	920.8±2.8@200 V	8.99±2.31	160±32	232±3	132±4
		W18-RMC3/UNM	711.5±2.1@200 V	6.11±2.77	100±20	228±1	148±2
		W18-RMC4/UNM	381.1±1.1@200 V	3.94±0.77	105±21	212±1	117±2
		W18-2R3/UNM	425.8±1.3@100 V	4.41±0.86	n.a.	115±1	25±2
		W18-2R2/UNM	511.5±1.5@100 V	5.24±1.07	107±21	131±1	51±2
		W18-RMC5/UTN	681.6±6.6@200 V	7.63±1.28	152±46	237±3	123±4
		W18-D9/UTN	306.9±1.4@200 V	3.79±0.85	129±39	202±1	89±2
		W18-D11/UTN	545.2±6.2@200 V	6.04±1.16	145±44	202±1	88±2
		W18-D12/UTN	353.5±1.5@220 V	4.29±1.99	133±40	228±1	113±2
$1.1 \times 10^{16}$	456	W18-D10/UNM (#)	1237.3±3.7@250 V	8.97±1.81	230±46	261±3	161±4
		W18-RMC3/UNM (#)	1391.7±4.2@240 V	9.65±2.14	230±46	250±3	170±4
		W18-RMC4/UNM (#)	1307.4±3.9@240 V	9.25±1.95	220±44	240±3	145±4
		W18-2R3/UNM (#)	743.8±2.2@125 V	5.26±1.11	n.a.	140±1	50±2
		W18-2R2/UNM (#)	682.0±2.0@145 V	4.88±1.05	n.a.	148±1	68±2

**Table 4.14:** Summary of the electrical characteristics of 3D diodes of the CMS type from the DTC5 batch irradiated with protons at LANSCE and measured at UTN.

Fluence ( $n_{eq}/cm^2$ )	TID (Mrad(Si))	Device ID	$J_{fk}$ at $-10^\circ C$ ( $\mu A/cm^2$ )	$\alpha^*$ ( $10^{-17} A/cm$ )	$V_{depl}$ (V)	$V_{bd}$ (V)	$\Delta V_{bd}$ (V)
$6.9 \times 10^{14}$	29	W18-1E1	38.49±0.23@100 V	4.49±1.07	63±19	140±1	35±2
		W18-1E2	26.19±0.17@100 V	3.62±0.68	53±16	113±1	2±2
		W18-1EN1	25.00±0.16@100 V	3.48±0.56	60±18	192±3	77±4
		W18-1EN2	34.13±0.21@100 V	5.15±0.99	62±19	205±1	90±2
$4.0 \times 10^{15}$	169	W18-2E1	98.81±0.69@150 V	3.00±1.17	110±33	256±3	140±4
		W18-2E2	248.81±1.14@150 V	5.78±0.97	112±34	216±3	104±4
		W18-2EN2	137.70±0.81@150 V	3.57±0.79	75±23	195±1	87±2
		W18-3E2	224.60±1.07@150 V	4.92±1.11	51±15	181±1	80±2
		W18-3EN1	380.56±1.54@150 V	7.07±2.26	54±16	193±3	93±4
W18-4E1	239.68±1.12@150 V	3.86±0.70	46±14	170±1	64±2		

#### 4.4.5 Annealing Campaign

A study of annealing effects had followed in order to cross-check if the relatively high values of leakage current exhibited by some devices were determined by the lack of a high-temperature annealing step. The systematic annealing study also confirms the sensors effective state, how they would behave after a long maintenance periods in LHC upgrades. Both beneficial annealing and reverse annealing could be involved at this stage. In our investigations, few selected samples from both the ATLAS10 and DTC5 batches were annealed at 80°C for 60 minutes. Afterwards, I-V characteristics were measured again at different temperatures (from -20°C to 20°C whenever applicable).

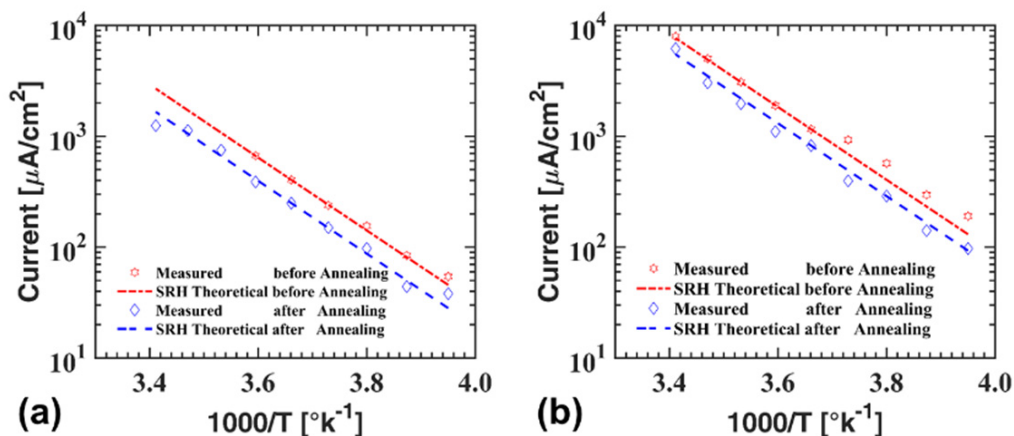


**Figure 4.13:** (a) Arrhenius plot comparing measured and calculated values of leakage current at 70 V bias voltage and their evolution with temperature in a 3D diode of the 80B type (W14-D8) from the ATLAS10 batch irradiated with protons at LANSCE at a fluence of  $2.1 \times 10^{15} \text{ n}_{\text{eq}}/\text{cm}^2$  and measured at UTN at different temperatures before and after annealing at 80°C for 60 minutes, and (b) Arrhenius plot comparing measured and calculated values of leakage current at 150 V bias voltage and their evolution with temperature in a 3D diode of the FEI4 type (W18-RMC5) from the DTC5 batch irradiated with protons at LANSCE at a fluence of  $7.3 \times 10^{15} \text{ n}_{\text{eq}}/\text{cm}^2$  and measured at UTN at different temperatures before and after annealing at 80°C for 60 minutes.

Above the figures 4.14 (a) and (b) both show the Arrhenius plots at a bias reference for two diodes from the ATLAS10 and DTC5 batches, irradiated with 800 MeV protons at LANSCE at  $2.1 \times 10^{15} \text{ n}_{\text{eq}}/\text{cm}^2$  and  $7.3 \times 10^{15} \text{ n}_{\text{eq}}/\text{cm}^2$ , respectively. In both cases, the leakage current is significantly lower after the annealing. Moreover, the agreement between measurements and SRH-based calculations remained good even after the annealing, again confirming that the leakage current in these devices is primarily affected by thermal generation.

Table 15 summarizes the relevant data extracted from the I-V curves of all annealed samples, in comparison to the values before annealing. It can be seen that the  $\alpha^*$  values are reduced by about a factor of two, which is in quite good agreement with the exponential-logarithmic model of leakage current introduced in [14] within the uncertainties here present. It should be noted that the annealing step also caused a decrease of the breakdown voltage, which in some cases forced the choice to extract

the  $\alpha^*$  values at voltages lower than those used for the considered samples in the previous Tables (the values before annealing are shown at these same lower voltages in Table 14 for a direct comparison). This effect is likely due to the impact of the annealing step on the oxide charge and interface state densities, which are decreased, as well as in the effective substrate doping concentration, which is increased [14].

**Table 4.15:** Summary of the electrical characteristics of a few 3D diodes from the ATLAS10 and DTC5 batches irradiated with neutrons or protons and re-measured at UTN after annealing at 80°C for 60 minutes.

Batch	Irradiation and Fluence ( $n_{eq}/cm^2$ )	Device ID/Type	$\alpha^*$ PRE ( $10^{-17}$ A/cm)	$\alpha^*$ POST ( $10^{-17}$ A/cm)	$V_{bd}$ PRE (V)	$V_{bd}$ POST (V)
ATLAS10	Neutrons@JSI $2.0 \times 10^{15}$	W21-D6/80B	$4.60 \pm 0.66$ @65 V	$2.93 \pm 1.20$ @65 V	$72 \pm 1$	$71 \pm 1$
		W24-D8/80B	$4.50 \pm 0.46$ @70 V	$2.39 \pm 1.09$ @70 V	$81 \pm 1$	$77 \pm 1$
	Protons@LANSCE $2.1 \times 10^{15}$	W14-D8/80B	$7.66 \pm 1.25$ @105 V	$4.66 \pm 0.88$ @105 V	$138 \pm 3$	$120 \pm 3$
		W12-D9FP/FEI4	$6.15 \pm 1.02$ @100 V	$4.17 \pm 1.22$ @100 V	$22 \pm 1$	$105 \pm 1$
DTC5	Neutrons@JSI $8.0 \times 10^{15}$	W9-D1/FEI4	$6.02 \pm 0.90$ @180 V	$2.64 \pm 0.73$ @180 V	$199 \pm 1$	$193 \pm 1$
		W9-D2/FEI4	$6.69 \pm 0.81$ @180 V	$2.93 \pm 0.45$ @180 V	$194 \pm 1$	$185 \pm 1$
	Protons@LANSCE $4.0 \times 10^{15}$	W18-3EN1/CMS	$7.07 \pm 2.26$ @150 V	$5.55 \pm 1.11$ @150 V	$193 \pm 3$	$182 \pm 3$
	Protons@LANSCE $7.3 \times 10^{15}$	W18-RMC5/FEI4	$7.63 \pm 1.28$ @200 V	$4.42 \pm 0.84$ @200 V	$237 \pm 3$	$224 \pm 3$

## 4.5 Summary Insight

In spite of the several uncertainties affecting the results, among them primarily those in the irradiation fluences, depleted volumes, and annealing conditions, which induce quite large non-uniformities in the measured values, the leakage current behavior of the reported samples does not show anomalous effects leading to sizable deviations from the theoretical expectations. As it can be seen in the summary plot of figure 4.14(a), the range of  $\alpha^*$  values is comparable to the one generally accepted in case of devices subjected to negligible annealing [14, 135]. Moreover, for a subset of samples representative of the two different technologies and of both neutron and proton irradiations, it has been shown in Section 4.4 that the  $\alpha^*$  values significantly decrease after a high-temperature annealing step, making them comparable to those normally observed in annealed samples [14].

The current measurements at different temperatures were found to be in good agreement with the SRH-based theoretical model. This supports the conclusion that the leakage current after irradiation is dominated by thermal generation in the depleted bulk. In most cases, with the exception of a few samples probably suffering from process defects, this holds true up to high bias voltages just below breakdown. As a

result, it can be inferred that FBK 3D irradiated sensors can be safely operated at bias voltages up to a few volts from breakdown without significant increase of the leakage current. This was in fact the case for 3D pixel prototypes tested for ATLAS IBL qualification [78].

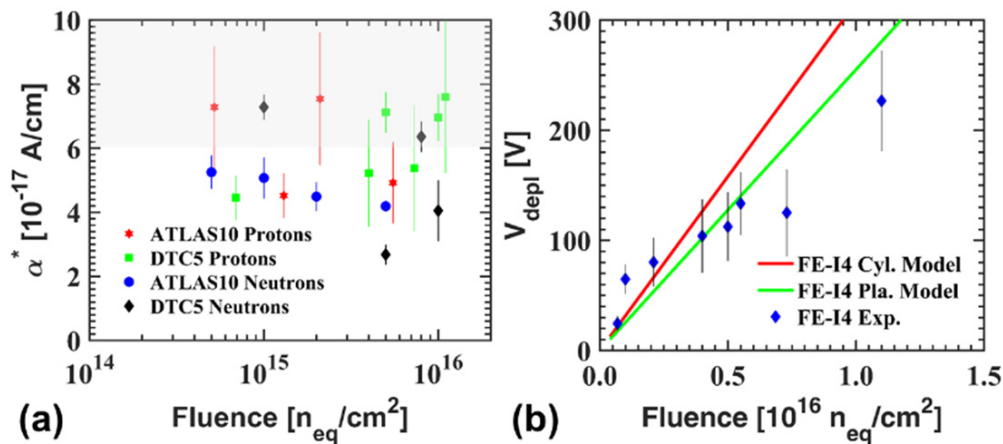


**Figure 4.14:** (a) Summary plot of the geometric current related damage rate ( $\alpha^*$ ) at different fluences. Symbols represent the average values and error bars the total uncertainties. The shaded region represents the range of  $\alpha$  values observed in irradiated samples not subjected to annealing, and (b) Summary plot of the depletion voltage ( $V_{depl}$ ) of all 3D diodes of the FEI4 type at different fluences. Symbols represent the average values and error bars the total uncertainties. Analytical estimates according to planar (pla) and cylindrical (cyl) junction models of  $V_{depl}$  are also shown.

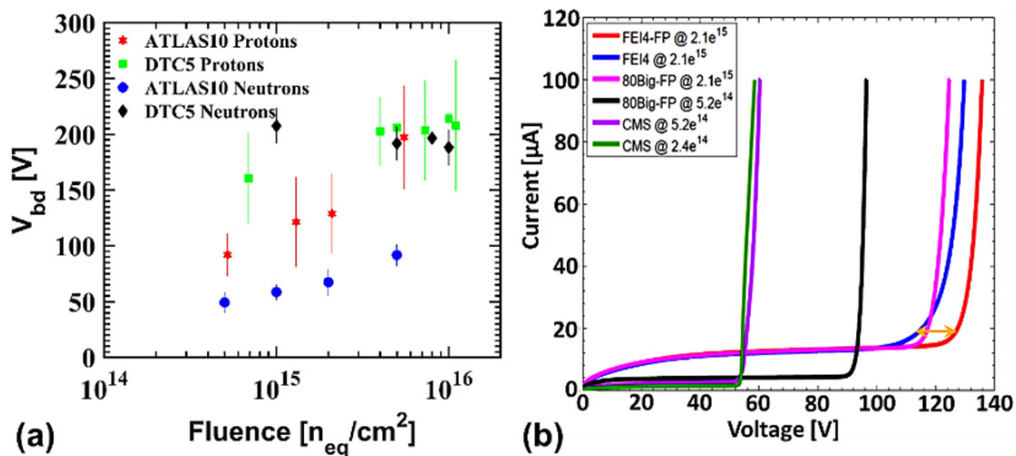


**Figure 4.15:** (a) Summary plot of the breakdown voltage at different fluences. Symbols represent the average values and error bars the total uncertainties, (b) Comparative I-V characteristics plot of sensors of different geometries of ATLAS10 batch, irradiated at different proton fluences in LANCSE facility and measured in UTN at  $-10^\circ C$ . FP denotes inset defined the sensors with field plate.

As far as the depletion voltage is concerned, within the relatively large uncertainty affecting the C-V based extraction method, up to fluences of the order of  $5 \times 10^{15} n_{eq}/cm^2$  the measured values are in reasonable agreement with theoretical

expectations based on the linear increase of the effective substrate doping concentration with fluence due to acceptor-like defects [139], whereas at very large fluences the measured values underestimate the theoretical ones. As an example, figure 4.14(b) shows the  $V_{\text{depl}}$  values for all devices of the FEI4 type at different fluences, in comparison to analytical estimates based on both planar and cylindrical junction models, keeping into account the electrode radius and spacing, and assuming the introduction rate of the effective space charge concentration to be  $0.017 \text{ cm}^{-1}$  [119]. It can be seen that up to  $5.5 \times 10^{15} \text{ n}_{\text{eq}}/\text{cm}^2$  the agreement between experimental data and models is acceptable, whereas at the two largest fluences the difference is increased. Similar discrepancies were previously observed for depletion voltage values measured from C-V curves in 3D sensors from CNM irradiated to  $1 \times 10^{16} \text{ n}_{\text{eq}}/\text{cm}^2$ , as a result of the very high bulk resistivity at large fluences and of the presence of a low electric field throughout the bulk already at low voltage [69].

The breakdown voltage behavior does not lend itself to a straightforward interpretation, because it strongly depends on the sensor geometry as well as on the irradiation condition applied to the samples referred here. Figure 4.15 (a) summarizes all data for neutron and proton irradiated samples. Similarly to the pre-irradiation case, most devices from the ATLAS10 batch have sizably lower breakdown voltages than devices from the DTC5 batch, and sometimes the breakdown voltage is not high enough to allow full depletion to be reached. However, when the TID associated with the irradiation is very high (i.e., for proton irradiation at  $5.5 \times 10^{15} \text{ n}_{\text{eq}}/\text{cm}^2$ ), such as to significantly increase the oxide charge and interface state densities, the breakdown voltage of ATLAS10 devices is comparable to those of the best DTC5 devices. For X- and  $\gamma$ -ray irradiations, results confirm the superior performance of DTC5 devices in terms of breakdown voltage.

In order to gain greater insight into the breakdown voltage behavior of both batches in different irradiation scenarios, the following features and assumptions should be taken in account.

- The ATLAS10 and DTC5 sensors are very similar as far as the front-side is concerned (viz. figure 4.1). The oxide thickness remained the same in both batches, so as the same p-spray dose, and field plates of the same width are present in all considered layouts. It would be worth noting that CMS type sensors of ATLAS10 batch did not include field plate on the front side, which made these devices more vulnerable to breakdown than 80B and FE-I4 type sensors. That has also been the motivation leaving the electrical analysis of CMS type sensors of ATLAS10 within this chapter so far. From figure 4.15 (b), it is remarkable to point out that the sensors without Field Plate (FP) had much lower breakdown voltage than the sensor with field plate, as the electric field optimization was not possible in either side of the sensors.

- The ohmic columns are passing-through in both FBK batches, so that the bias voltage applied to the back side is transmitted to the p-spray layer on the front side in a similar way.
- In ATLAS10 sensors, due to both types of column passing through structure, the initial (process dependent) values of oxide charge and interface state densities could be assumed to be the same on both sensor sides, during neutron and proton irradiation. The increase of oxide charge and interface state densities with increasing TID can also be assumed to be the same on both sensor sides as devices were irradiated without a bias. On the contrary, during X-ray irradiation from the front side the TID on the back side should be comparatively much smaller in scale (in particular for the few devices irradiated under bias). Hence, the oxide charge and interface state densities on the sensor's back side remained different than the front side for ATLAS10 batch.
- in DTC5 sensors, due to the partially-through junction columns and to the high doping of the uniform p<sup>+</sup> layer on the back side, surface damage effects are not relevant for the back side.

These considerations suggest a possible explanation for the observed breakdown voltage trends. Similarly to the pre-irradiation case, the most critical region for breakdown in ATLAS10 devices is likely on the back side at the junction between the n<sup>+</sup>-column and the p-spray. In fact, the increase of oxide charge and interface state densities with TID lowers the electric field peaks on both the front side and the back side, thus improving the breakdown voltage [16]. Similar trend was observed in 3D sensors with passing-through junction columns fabricated at SNF (viz. Table 4.1). Owing to the field plates, the electric field peak on the front side is split in two sub-peaks of lower amplitude, so that the highest electric field peak is on the back side [16, 120]. In ATLAS10 devices, the breakdown voltage values are therefore mainly determined by the amount of surface damage on the back side. For irradiation with 10-keV X-rays, the TID on the back side is a small fraction of that on the front side (~15% can be estimated for a 230 μm sensor thickness, corresponding to ~300 krad). As a result, the increase of oxide charge and interface state densities is limited [140, 141], and correspondingly the breakdown voltage increase is only a few tens of volts (from Table 4,  $\Delta V_{bd} = 32.8 \pm 8.9$  V). For neutron irradiation, an increase of  $V_{bd}$  is observed as the fluence is increased, because of the increasingly larger TID involved on both sensor sides. Despite the fact that the TID on the back side is larger than with X-rays, its effects on the oxide charge and interface state densities are likely attenuated by the lower fractional hole yield [142] and the self-annealing effects due to the temperature increase during irradiation, so that the increase of  $V_{bd}$  is slightly higher than with X-rays only at the maximum fluence (from Tables 4.6 and 4.7,  $\Delta V_{bd} = 40.8 \pm 10.2$  V at  $5 \times 10^{15}$  n<sub>eq</sub>/cm<sup>2</sup>). For proton irradiation, the increase of  $V_{bd}$  is instead

more pronounced already at the lowest fluence because of the much larger TID, which results in larger oxide charge and interface state densities. At the largest proton fluence,  $5.5 \times 10^{15} \text{ n}_{\text{eq}}/\text{cm}^2$ , the TID is about 230 Mrad(Si), so that the surface damage effects are likely saturated [140, 141]. In this case, the increase of  $V_{\text{bd}}$  is indeed very large (from Tables 4.10 and 4.11,  $\Delta V_{\text{bd}} = 147.3 \pm 44.5 \text{ V}$ ), bringing the breakdown voltage to values of the order of 200 V. These values are similar to those measured on 3D strip sensors from the same batch irradiated with protons to  $2.0 \times 10^{16} \text{ n}_{\text{eq}}/\text{cm}^2$  [125], thus confirming a saturation effect on the breakdown voltage values for the considered technology.

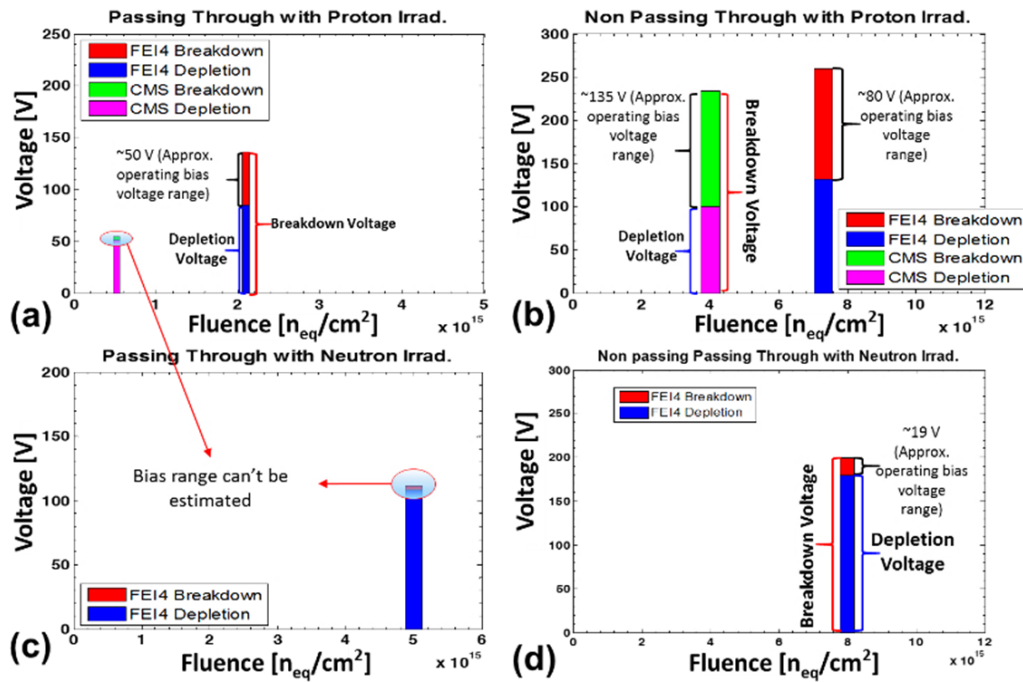


**Figure 4.16:** Bias range,  $\Delta V_{\text{bd}}$ , reported for irradiated sensors of geometrical diversity vs. fluence: **(a)** CMS and FE-I4 type sensor of ATLAS10, irradiated with protons at LANCSE, measured in UTN at  $-10^\circ\text{C}$ , **(b)** CMS and FE-I4 type sensor of DTC5, irradiated with protons at LANCSE, measured in UTN at  $-10^\circ\text{C}$ , **(c)** FE-I4 type sensor of ATLAS10, irradiated with neutrons at JSI, measured in UTN at  $-10^\circ\text{C}$ , and **(d)** FE-I4 type sensor of DTC5, irradiated with neutrons at JSI, measured in UTN at  $-10^\circ\text{C}$ .

In DTC5 devices, due to their different geometry, the breakdown can occur either at the front side or at the junction column tips, depending on the irradiation scenario. Before irradiation, when the oxide charge and interface state densities are relatively low, the largest electric field peaks are on the front side [33]. As a result,  $V_{\text{bd}}$  is larger than in ATLAS10 devices owing to the beneficial effects of the field plates. After irradiation, when the involved TID causes the oxide charge and interface state densities to increase,  $V_{\text{bd}}$  is sizably increased. From figure 4.14(b), it can be seen that the  $V_{\text{bd}}$  values at the largest fluences of both protons and neutrons are all of the order of 200 V on average. For protons, due to the huge TID values involved, one possible explanation could be the saturation of oxide charge and interface state densities. However, a slightly larger  $V_{\text{bd}}$  is measured for neutron irradiation at the lowest fluence,

$1 \times 10^{15} \text{ n}_{\text{eq}}/\text{cm}^2$ , for which the TID is only  $\sim 0.6 \text{ Mrad}(\text{Si})$ , not high enough to saturate the oxide charge and interface state densities. This suggests that a different mechanism, independent of surface damage, limits the breakdown voltage in DTC5 devices at values in the range (200-250) V. At these high voltage values, the electric field at the junction column tips is indeed very large [58, 124], and it might further increase with fluence due to the larger effective substrate doping concentration caused by bulk damage [14]. Compared to other double-sided 3D sensors from CNM [124], this effect is here more pronounced and limits the breakdown voltage to lower values. The reason for this difference is most likely due to the  $p^+$  uniform layer on the sensor back side (see figure 4.1 right). While the presence of this layer lowers the depletion voltage of regions below the junction column tips, it also increases the electric field peaks at the junction column tips as compared to a back side without a p-doped region typical of CNM sensors [78].

As reported through a comparative bar plot diagram in figure 4.16, the partial passing through technology of DTC5 batch showed a significant improvement on bias operating range ( $\Delta V_{\text{bd}}$ ) over the full passing through technology of ATLAS10 batch for both irradiation campaigns made with protons and neutrons. The improvement of  $\Delta V_{\text{bd}}$  is clearly noticeable in different sensor pitch-geometries (CMS-type and FE-I4 type, as shown in figure 4.16 (a) and (b)) for irradiation campaign made at LANCSE and measured in UTN at  $-10^\circ\text{C}$ . Even it has already been discussed that the full depletion voltage is almost impossible to follow due to the limited breakdown voltage present in most cases for JSI neutron irradiated sensors (of both batches), it is still possible to see in figure 4.16 (d) that shortening the junction column depth in DTC5 showed a glimpse of  $\Delta V_{\text{bd}}$  improvement, especially for FE-I4 type sensors. 3D diodes with partially-through junction columns (DTC5) reported much higher breakdown voltages even at relatively low TID values ( $\sim 1 \text{ Mrad}$ ). In fact, in these devices the critical point for breakdown is initially at the front side, at the junction between  $n^+$  column and p-spray, where the presence of a field plate strongly attenuates the electric field peaks. As a result, very large breakdown voltage values ( $>300 \text{ V}$ ) could be predicted by projecting this trend to irradiations involving very large TID ( $\sim 100 \text{ Mrad}$ ), but this is not confirmed experimentally. The breakdown voltage values of the best samples reach at most  $\sim 250 \text{ V}$ , and this can be explained by the presence of a different limiting mechanism, i.e., the high electric fields at the junction column tips.

3D sensors with partially-through junction columns could therefore be effectively operated in a wider range of irradiation scenarios than their counterparts with passing-through junction columns. Both types of sensors are certainly suitable for proton fluences of the order of  $5 \times 10^{15} \text{ n}_{\text{eq}}/\text{cm}^2$ , but they are not favoured for fluences of the order of  $1 \times 10^{16} \text{ n}_{\text{eq}}/\text{cm}^2$ , because the breakdown voltage could prevent them from being operated at the optimal bias voltage, unless the inter-electrode spacing is reduced. Future applications of 3D sensors at the HL-LHC will involve radiation fluences up to  $2 \times 10^{16} \text{ n}_{\text{eq}}/\text{cm}^2$  and, for low occupancy, small pitch pixels (e.g.,  $50 \times 50$

$\mu\text{m}^2$  or  $25 \times 100 \mu\text{m}^2$ ). As a result, the inter-electrode spacing will be decreased to values of 30-40  $\mu\text{m}$ . This will significantly reduce the depletion voltages and also make future 3D sensors more robust against charge trapping, but it could also cause higher electric fields and risk of breakdown voltage reduction driven by avalanche effects.

## Chapter V

### FBK 1st 6-inch Pilot Production of Modified 3D DDTC Si Sensor

Following their application to the ATLAS Insertable B-Layer (IBL) [73, 78] over the last years, 3D sensors have become one of the ultimate choices of future High Luminosity LHC (HL-LHC) upgrades [116]. FBK upgraded its fabrication line from 4-inch (100-mm) to 6-inch (150-mm) diameter wafers since 2014. The first pilot production of modified DDTC 3D Si sensors shall be reported in the following discussion, which will be denoted as DTC6. The typical standard thickness for 6-inch wafers for microelectronics is 675  $\mu\text{m}$  [143], whereas the recommended wafer thickness for 3D sensors for High Energy Physics (HEP) experimentation is of the order of 200  $\mu\text{m}$ . Thus the usual fabrication process of double-sided 3D sensors on relatively thin 6-inch substrates without a support wafer had become more challenging because of mechanical issues (compatibility with processing equipment, fragility) even though the increased area available on wafer ( $\sim 2\times$ ) brought an advantageous feature for the foreseen mass productions of HL-LHC.

By the end of 2014, this DTC6 test batch was fabricated at FBK with the aim to qualify the possible issues involved on such upgrade on process line. While maintaining a double-sided fabrication approach, this batch adopted DTC5 complaint design with additional modifications, in order to start exploring their effectiveness for future productions. The use of improved DRIE with self-edge protection and the partial filling of all columns with poly-Si were the key features attained within this batch for the first time. Other process and layout improvements were also implemented to enhance the breakdown voltage capability of 3D sensors, based on the results obtained from the last test batch made on 4-inch wafers, as reported in chapters 2 and 4.

#### 5.1 *Fabrication*

Due to the procurement related issues of finding 6-inch wafers at thinner active thickness as per interest of HEP, it had been quite hard to find the suitable one within the limited production timeline. Finally, wafers having 275  $\mu\text{m}$  thickness were chosen, which were relatively thicker in comparison to the active thickness (230 $\mu\text{m}$ ) of the sensors' production of ATLAS10 and DTC5. Such constraint came with additional costs of processing complexities and yield challenges. Chosen wafers of DTC6 were Float Zone, p-type having a nominal resistivity greater than 5  $\text{k}\Omega\text{ cm}$ .

### 5.1.1 Process Design

The schematic cross-section of the sensors is reported in figure 5.1. Similar to the last 3D sensors made on 4-inch wafers [33,138], the ohmic ( $p^+$ ) columns, etched from the back side, extend through the full wafer thickness, to allow for slim edge terminations by using the approach proposed in [75]. On the contrary, the junction ( $n^+$ ) columns, etched from the front side, are not etched through the full wafer thickness, but rather stop a short distance from the opposite surface of back side. By doing so, the most critical region for breakdown, i.e., the  $n^+$  column/ $p$ -spray junction on the back side, was avoided [33, 138].

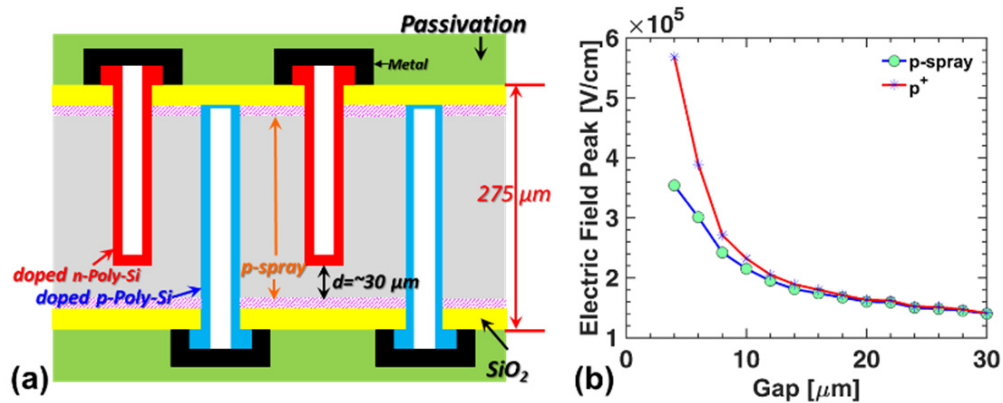


**Figure 5.1:** (a) Schematic cross-section of double-sided 3D sensors of DTC6, and (b) Simulated electric field peak at n-column tip as a function of the gap at 76 V reverse bias.

P-spray layers were kept at both sides of the wafers to prevent from the inversion of the surface. Two different Boron doses were used for the p-spray implantation, thus there had been two different process splits ( $1.5 \times 10^{12}$  and  $2 \times 10^{12}$  cm<sup>-2</sup>). While p-spray on the front side was strictly necessary to ensure isolation between  $n^+$  columns, its presence on the back side was aimed to avoid the high electric field peaks at the interface close to the  $p^+$  columns. As already discussed in details in chapter 4, high electric field would otherwise be induced by the increased concentration of electrons in the inversion layer after irradiation. Note that in the last sensors made on 4-inch wafers a  $p^+$  layer was used for this purpose (as it reported in figure 4.1 right) and was realised with the same thermal diffusion of boron used for  $p^+$  column doping by removing the oxide layer from the back side [33]. With p-spray, since the oxide layer was not removed, a better symmetry between the front side and the back side (hence lower mechanical stress) was maintained. Hence, the risk of the wafer bowing was strongly reduced with this production.

The distance between the  $n^+$  column tip and the back surface is referred to as gap. It is a critical parameter and should be chosen as a trade-off between the breakdown voltage and the charge collection efficiency. The charge collection efficiency at a given voltage obviously improves as the gap decreases, thus the overlap between the junction and ohmic columns increases. On the contrary, as it can

be seen from TCAD simulation results of figure 5.1(b), the peak electric field at the column tip increases as the gap is decreased in the presence of a p-spray or a p<sup>+</sup> layer on the back side. This phenomenon could lead the device into the early breakdown if the gap is too small. Simulations in the same figure also endorsed the process modification of using the p-spray instead of p<sup>+</sup> in terms of reducing the high electric field peak, although minor differences are observed for the initial target gap of 20 μm.

A relatively safe design value of 245 μm was finally chosen for the n<sup>+</sup> column depth, corresponding to a gap of 30 μm. FBK had previously demonstrated the feasibility of 260 μm column depth by Deep Reactive Ion Etching (DRIE) with 12 μm wide hole openings. This same 12 μm wide hole openings was also used for the state of art IBL production, that corresponds to a depth-width aspect ratio around 22:1 [144]. Witnessing the greater yield within IBL production, such depth-width aspect ratio was chosen for this batch as well. In order to use it for the 245 μm deep n<sup>+</sup> columns, 12 μm design width was applied. On the other side, the design width increased to 13 μm for the p<sup>+</sup> columns in aim to achieve a greater depth up to 275 μm active thickness while minimizing the column dead area. It should be mentioned that the upgrade of the DRIE equipment to 6-inch wafers also includes a mechanical protection of the wafer edges that brought an additional ease in production line. The sacrificial layers previously used for edge protection during the etching steps have been omitted.

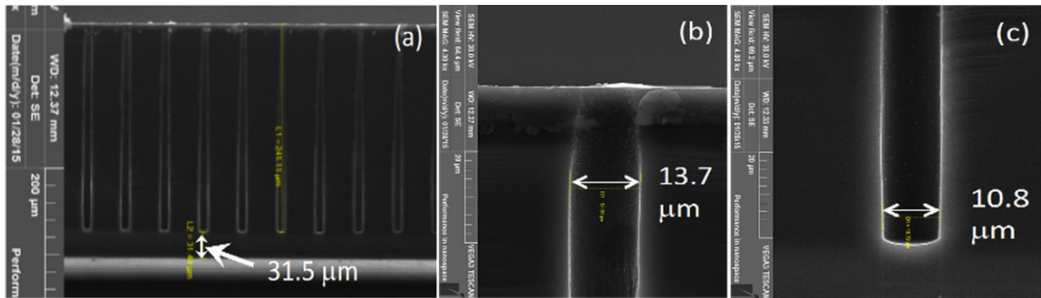
Several interesting modifications were made within this production. The columns were partially filled with poly-Si and selectively doped by thermal diffusion from POCl<sub>3</sub> (n<sup>+</sup>) and BBr<sub>3</sub> (p<sup>+</sup>) gas sources. An important advantage of using poly-Si partial filling is that columns can be contacted by metal directly placing over the poly-Si, without employing any additional dedicated masks, i.e., lithography and etching steps, for the contacts. Moreover, highly doped surface layers around the openings of the columns have been avoided within this DTC6 production that were known to affect the electrical characteristics of sensors from previous batches [120]. A passivation layer is finally deposited over the metal layer on both wafer sides, and patterned to expose metal pads for probing and bonding.

### 5.1.2 Process Characterization

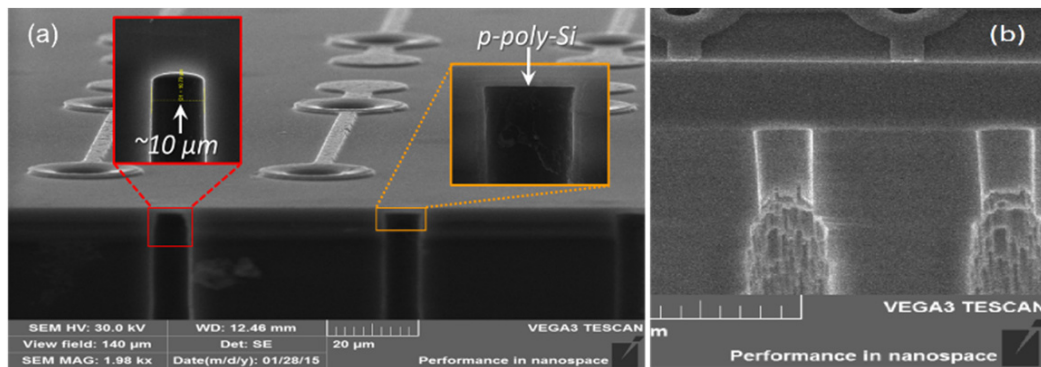
As expected, the modified process implementation was faster than the IBL one. It was around 30% lower in number of steps. Like every 3D sensor fabrication, the most delicate steps were the column etchings by DRIE. In this batch, the etching of n<sup>+</sup> columns was performed smoothly, whereas some problems were encountered while etching was made for p<sup>+</sup> columns.

Figure 5.2 shows Scanning Electron Microscope (SEM) micrographs of n<sup>+</sup> columns. From figure 5.2 (a), it can be seen that the distance from the column tips to the opposite surface is 31.5 μm, close to the design value targeted. The column depth uniformity also remained pretty good. In the figure, the column width seems to increase

with depth, but this artifact is due to the effect of sample cleaving. More accurate values of the column width can be estimated from the figure 5.2 (b) and 5.2 (c), which were taken from different samples. As expected, the column width was larger close to the column opening ( $13.7\ \mu\text{m}$ ) than close to the column tip ( $10.8\ \mu\text{m}$ ). Nevertheless, both values were close to the design value ( $12\ \mu\text{m}$ ), and the width uniformity is in fact better than that obtained in the IBL batches. In IBL production, the column width had the same design value but its effective size decreased from  $11\ \mu\text{m}$  at the opening to  $7\ \mu\text{m}$  at the end of the columns [32].



**Figure 5.2:** SEM micrographs of  $n^+$  columns: (a) view of some entire columns, and column details (b) close to the opening, and (c) close to the tip.



**Figure 5.3:** SEM micrographs of  $p^+$  columns: (a) details of columns close to the end, also showing partial poly-Si filling, and (b) defects due to the long etching time.

The etching of passing-through  $p^+$  columns was more complicated due to their greater depth required within this production, in spite of the increased design column width. The risk involved within this etching process was led by a long etching time. In fact, the modified etching recipe used to improve the column width uniformity here turned out to yield a slightly lower etching rate than previously achieved. Figure 5.3 shows SEM micrographs of  $p^+$  columns, where figure 5.3(a) shows the details of the end of two columns, that were effectively etched all-through the substrate stopping at the dielectric layer on the front side and with similar width shrink as observed for the  $n^+$  columns. The successful deposition of a thin layer of poly-Si into the columns can also be observed. However, the long etching time caused some defects due to the local collapse of the photoresist mask and/or of the protective polymer used in DRIE process (an example of a major defect close to the column end can be observed in figure 5.3 (b)). These defects caused a low mechanical yield of the process (several

wafers were in fact broken after the etching), and are also believed to be the cause of the poor electrical yield, as will be discussed in section 5.4. Clearly, this experience suggest that in case of future productions with this double-sided approach, thinner wafers and/or larger p<sup>+</sup> columns should be used.

## 5.2 Wafer Layout

The large area available on 6-inch wafers allows a large variety of sensors to be accomodated on the wafer layout as it could be found in figure 5.4. A wide safety margin (>1cm) was kept from the wafer edge. The four large dashed areas at the wafer periphery were designed to connect the sensor bias from the back side for ease of testing on an automatic probe station.

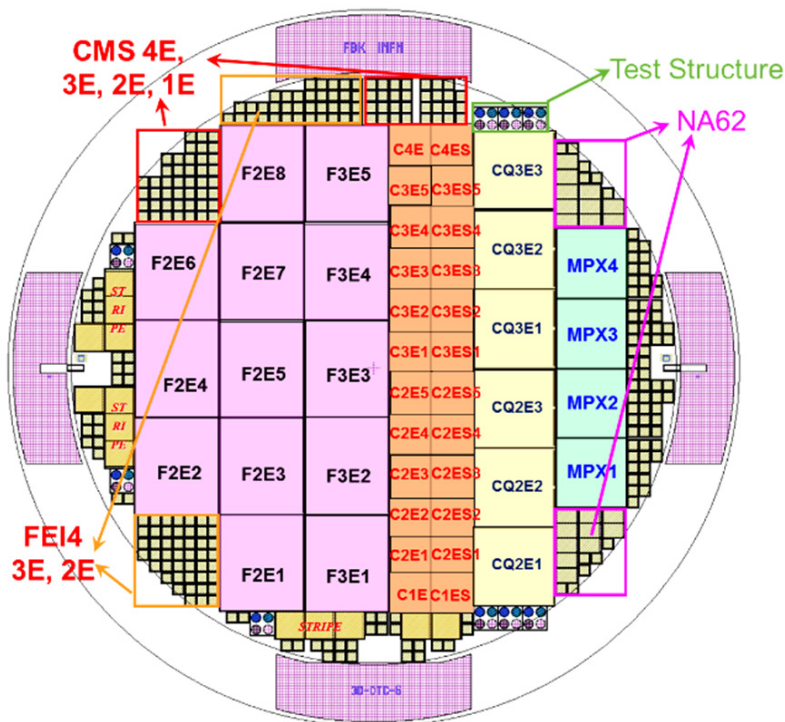


**Figure 5.4:** Wafer layout of the 3D-DTC-6 batch, with indication of the many different sensors.

The core of the wafer layout contains pixel sensors compatible with the ATLAS FE-I4 [74] and the CMS PSI46 [126] read-out chips. Layout included 13 “FE-I4” single tiles: 8 of them had pixels with 2 n<sup>+</sup> columns (F2E), like the IBL ones, whereas the other 5 had pixels with 3 n<sup>+</sup> columns (F3E). There were 24 “PSI46” single tiles, differing in the number of n<sup>+</sup> columns (1, 2, 3, and 4) per pixel (C1E, C2E, C3E, and C4E in figure 5.4 respectively), as well as 6 quad tiles (2×2 arrays) of sensors C2E and C3E (CQ2E and CQ3E in figure 5.3). On the right side of the wafer layout held other pixel sensors compatible with the MEDIPIX2 (MPX) and small NA62 read-out chips. All FE-I4 and PSI46 pixel sensors featured 150- $\mu$ m wide slim edges [75]. A more aggressive 100- $\mu$ m wide edge design was implemented on one side of these sensors in order to study them as the requirement of the forward physics experiments [84]. The periphery of the wafer layout hosted several smaller sensors (3D strips, 3D diodes) and test

structures (i.e., MOS capacitors). In particular, 3D diodes ( $\sim 2 \text{ mm}^2$  area) reproduced the basic 3D cell layouts of all types of large pixel and strip sensors, but with all columns of the same type shorted together by a metal grid to obtain a 2-electrode device [32]. It is worth to stress that it was not possible to fabricate planar test structures with this process due to the absence of highly doped surface regions in this modified technology.

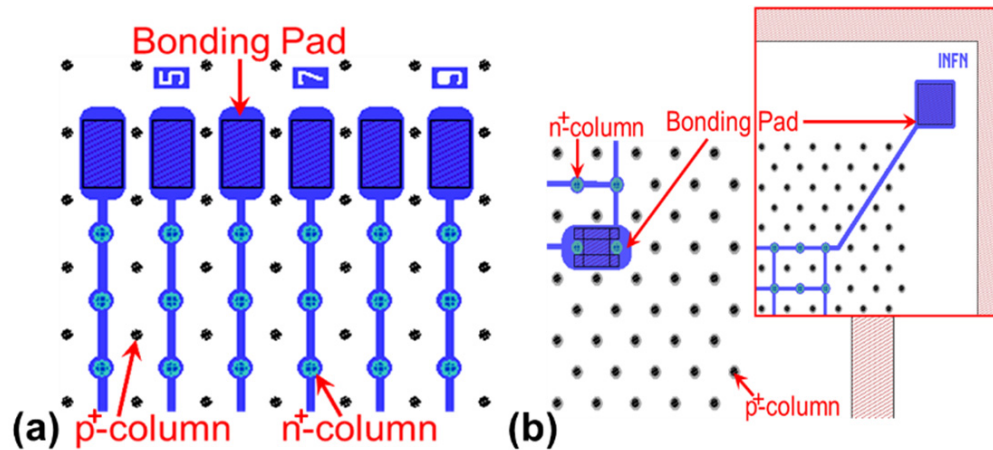


**Figure 5.5:** Layout details of: (a) 3D strip sensor, and (b) 3D diode (with inset, it shows a larger bonding pad outside the ohmic fence, due to limited pitch area within active region).

For realizing their impact on the electrical characteristics, some layout details of strip and diode sensors and bond-pad arrangement are shown in figure 5.5. In strip sensors (figure 5.5 (a)), bonding pads were placed at the ends of the strips (one per side), without overlapping the ohmic column fence that surrounds the active area [75]. This was easily achieved due to the relatively large pitch between columns ( $80 \mu\text{m}$ ). Conversely, in 3D diodes, bonding pads were either embedded within the active area (if the pitch between columns was large enough to avoid overlaps) or placed outside the ohmic fence: both solutions, with different sizes, were implemented in the diode layout shown in figure 5.5 (b). However, in some other diodes where the column density was higher, pads were only placed outside the ohmic fence in order not to overlap the ohmic columns in the active area that could otherwise be critical for breakdown.

## 5.3 *Electrical Characterization*

### 5.3.1 Before Irradiation

The current-voltage (I-V) curves of all sensors were initially measured on an automatic probe station up to 100 V reverse bias by using a temporary metal layer. In the 13 FE-I4 pixel sensors the temporary metal was patterned in 80 rows shorting 336 pixels each, that were individually measured, like for the IBL sensors [32, 73]. The measurements were entirely made in UTN facility following the same experimental setup, as described in section 4.3. All other sensors were covered by a large

unpatterned temporary metal layer, and only the total current was measured. These tests highlighted the good intrinsic properties of the small sensors but also a non-negligible density of defects, which make the yield of large area sensors very low.

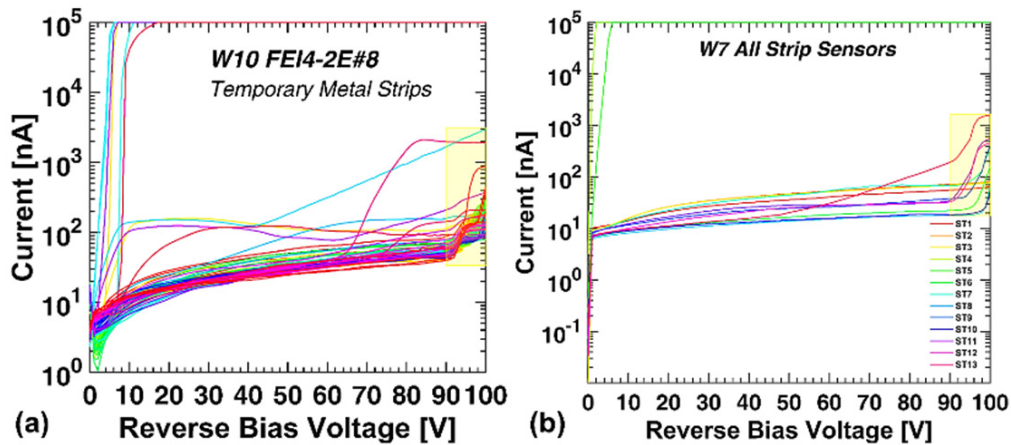


**Figure 5.6:** Electrical tests with temporary metal on automatic probe-station: (a) I-V curves of 80 rows of 336 pixels in a F2E ('FE-I4 2E Pixel') sensor of wafer 10, and (b) total I-V curves of all strip sensors from wafer 7. In both figures, transparent yellow rectangular inset shows the RAF ('Rise and Flatten') behavior, discussed later.

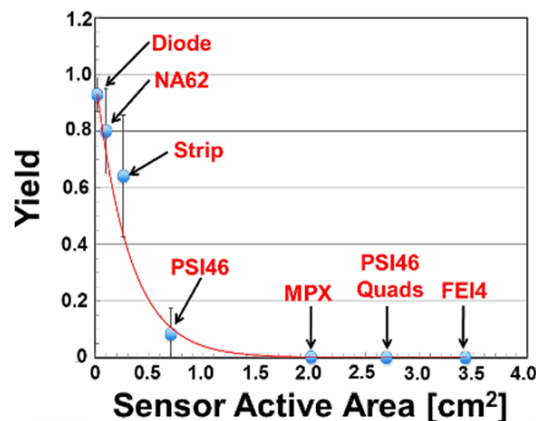


**Figure 5.7:** Yield from electrical tests in sensors of different area from all wafers: symbols indicate the average values, and error bars represent the standard deviation. Data are fitted with Poisson model,  $Y = \exp(-cA)$  [145].

As an example, Figure 5.6 (a) represented the I-V curves from the 80 rows of pixels in a F2E sensor: most curves reach 100 V without breakdown, but a few curves show early breakdown at low voltage (<10 V). This behavior is typical of all the FE-I4 sensors. Since one row of pixels with early breakdown is enough to cause the failure of an entire sensor, the yield for these large devices is almost zero. This is also the case for the PSI46 quads and for the MPX sensors, whereas a few PSI46 single chips are working. On the contrary, most diodes (~2 mm<sup>2</sup>) do not show sign of breakdown up to 100 V. The yield is also high for other small sensors, like NA62 pixels, and still acceptable for medium size sensors like strips. As an example, figure 5.6(b) shows the total currents of all strip sensors from wafer 7, where only two sensors out of eleven show early breakdown.

Figure 5.7 clearly demonstrates that the yield depends on the sensor area. Data are fitted with Poisson model,  $Y=\exp(-cA)$ , where  $Y$  is the yield,  $A$  is the sensor active area, and  $c$  is a fitting parameter. This equation is normally used to statistically estimate the production yield for a device of a given area assuming a uniform distribution of killer defects on wafer with a known density [145]. Notably, the value of the fitting parameter,  $c=3.203\text{ cm}^{-2}$  is in very good agreement with the value of the defect density derived from the average yield of diodes ( $3.195\text{ cm}^{-2}$ ). In other words, the small but non negligible number of defects observed on diodes is a reasonable explanation for the lower yield on sensors of increasing area as well as the zero yield on the larger ones. These defects were probably caused by the etching step of  $p^+$  columns, as described in Section 5.1.2, that could indeed explain the abrupt increase of the current as the depletion region reaches the  $p^+$  columns. It is to be noted that the depletion voltage, as measured from C-V curves, is lower than 5 V.

In order to try to use some large pixel sensors for functional tests anyway, the best wafer (i.e., the one with lower defect density) was chosen and a special bump bonding mask was designed to remove the few rows of pixels with defects from the FE-I4 sensors. The bump bonding attempt of these samples at Selex was not successful, anyway.

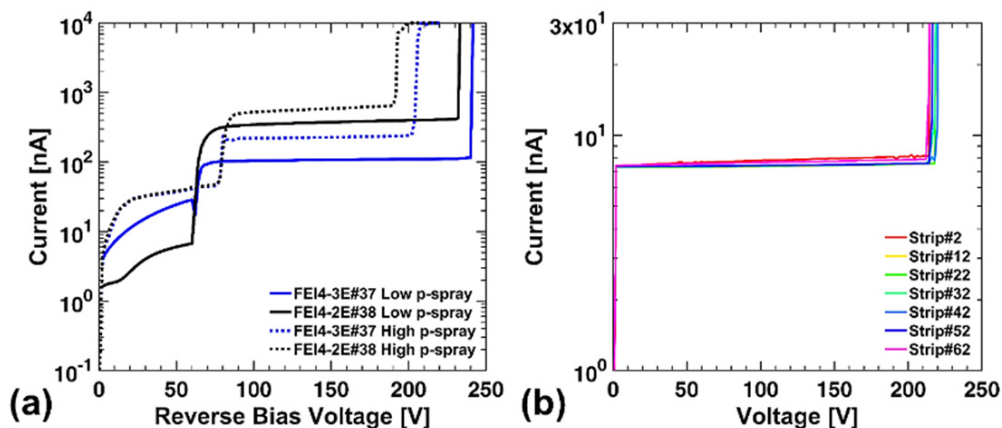


**Figure 5.8:** I-V curves measured after temporary metal removal: (a) FE-I4 diodes from two wafers with different p-spray doses and (b) single strips of a strip sensor from wafer 7 (low p-spray).

Further electrical tests were performed after temporary metal removal up to large bias voltages in order to gain deeper insight into the sensor characteristics. In particular, in temporary metal tests, all sensors exhibited a peculiar shape of the I-V curves, featuring a sharp rise of the current at a voltage ranging from  $\sim 60$  V to  $\sim 90$  V, depending on the p-spray dose and on the layout, followed by saturation. This behavior that will be referred to as RAF (“Rise and Flatten”) was observed in all diodes after temporary metal removal, as this can be seen in figure 5.8 (a). This phenomenon instead was absent in other types of sensors. As an example figure 5.8 (b) shows the I-V curves for strips. Manual probing made on singular pitch of pixelated sensors yielded similar results. However, it is worth noting that, in all sensors, the breakdown voltage was remarkably high (from  $\sim 200$  to  $\sim 240$  V, depending on the p-spray dose),

much more than in previous productions. This large improvement could be attributed to the several design and technological modification implemented in this batch that has been an encouraging R&D step at FBK in view of future productions oriented to the HL-LHC.

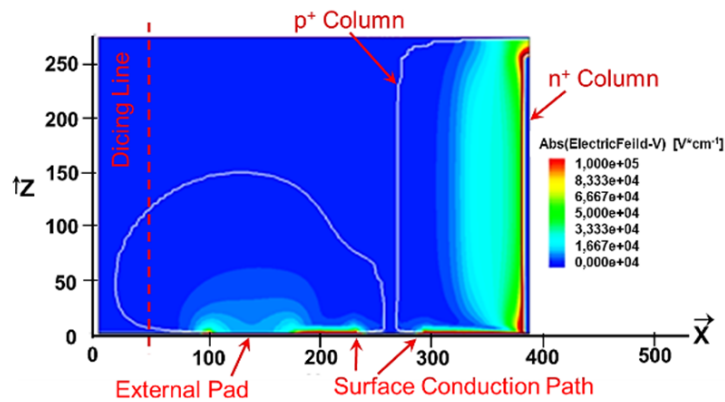


**Figure 5.9:** 2D cut of the simulated electric field distribution at 100 V bias in a 3D diode close to the edge.

As far as RAF is concerned, the differences observed between diodes and other devices after temporary metal removal suggested it could be due to a layout effect. As shown in figure 5.5(b), a specific feature of diodes, not common to other structures, is the presence of bonding pads outside the ohmic column fence and close to the dicing line. A similar approach was used for the layout of the temporary metal pads placing them beyond the ohmic fence in all sensors. As a result, a surface conduction path is formed underneath the metal connections to the pads when the threshold voltage of the related parasitic MOS structures is reached. In this context, the current from the diode periphery suddenly adds up to the one from the active volume. To support this explanation, 3D TCAD simulations were performed incorporating the geometries and technological parameters of the devices (e.g., the p-spray profiles extracted from SIMS measurements; the oxide thickness,  $t_{ox} \sim 1.1 \mu\text{m}$ , and fixed charge density,  $N_{ox} \sim 3 \times 10^{11} \text{ cm}^{-2}$  extracted from the C-V curves of MOS capacitors). Figure 5.9 shows a 2D cut of the simulated electric field distribution in the device (upside down) at 100 V (i.e., beyond the threshold voltage): a relatively wide depletion region outside the active area can be observed, which causes an additional current to be drawn by the diode.

The impact of this current on the noise would hinder the diode performance as a radiation detector, especially after dicing, when the additional current is further increased by the defects at the saw cut. Therefore, on all diodes having other pads available within the active area, the problem was fixed by reprocessing the wafers with a specially designed lithographic mask, allowing the metal connections between the active area and the external pads to be removed. As it can be seen in figure 5.10, showing the I-V curves of a diode at different stages, this remedy was effective. The

RAF behavior disappeared and the current remained relatively low both before and after dicing until breakdown.

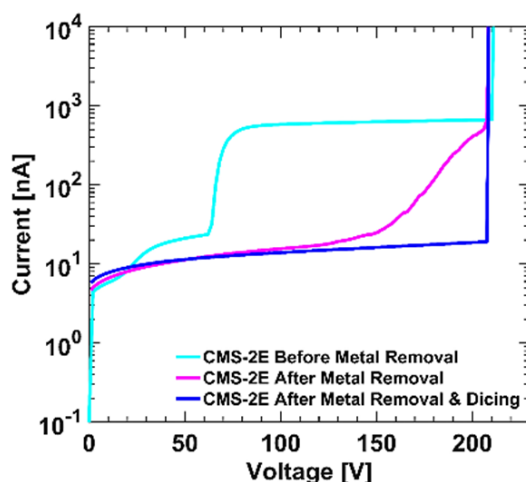


**Figure 5.10:** I-V curves of a CMS-2E diode measured before and after disconnecting the external metal pads.

### 5.3.2 After $\gamma$ -ray Irradiation

A few MOS test structures from the DTC6 batch were irradiated with  $\gamma$ -rays at the Sandia Gamma Irradiation Facility (Albuquerque, USA) to four different doses (Si): 10 Mrad, 50Mrad, 100 Mrad and 500Mrad. More information on irradiation condition of this  $\gamma$ -campaign can be found in section 4.3. Oxide charge density was extracted from C-V characteristics measured at UTN with the experimental setup mentioned in section 4.2. As an example, figure 5.11 reports the MOS capacitance measured before and after 10Mrad Gamma irradiation with 10 kHz signal frequency at room temperature. There has been no significant change in capacitance values except for a shift of flatband voltage,  $V_{fb}$ , to the right. The oxide charge and interface state densities were enhanced from the irradiation campaign causing such a trend (see figure 5.11).

**Table 5.1:** Summary of oxide charge density of Gamma irradiated devices.

Irradiation Dose	Device ID	Oxide Charge Density, $N_{ox}$ [ $cm^{-2}$ ]
10 Mrad (Si)	W7-MOS6	1.36879E+12
50 Mrad (Si)	W7-MOS2	1.07375E+12
100 Mrad (Si)	W7-MOS9	9.04055E+11

Oxide charge densities extracted from the devices irradiated to different TIDs are summarized in Table 5.1. It can be seen that surface damage contribution from Gamma irradiation increased the fixed oxide charge ( $\sim 3$ - $4$ X higher than the non-irradiated condition). There has been a little decreasing trend with increasing TID, as could be witnessed from table 5.1. This can be anticipated from the time and temperature dependant self-annealing effect made on the devices at higher TIDs.

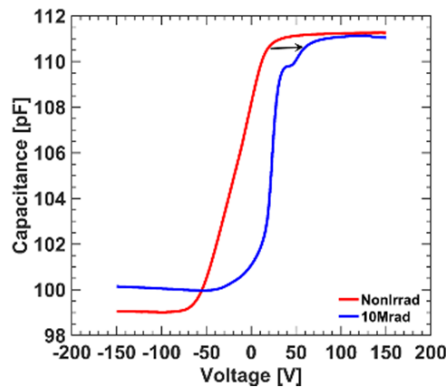


**Figure 5.11:** MOS C-V of W7-MOS6 test structure before and after  $\gamma$ -rays (10 Mrad [Si]) irradiation, measured at UTN at room temperature.

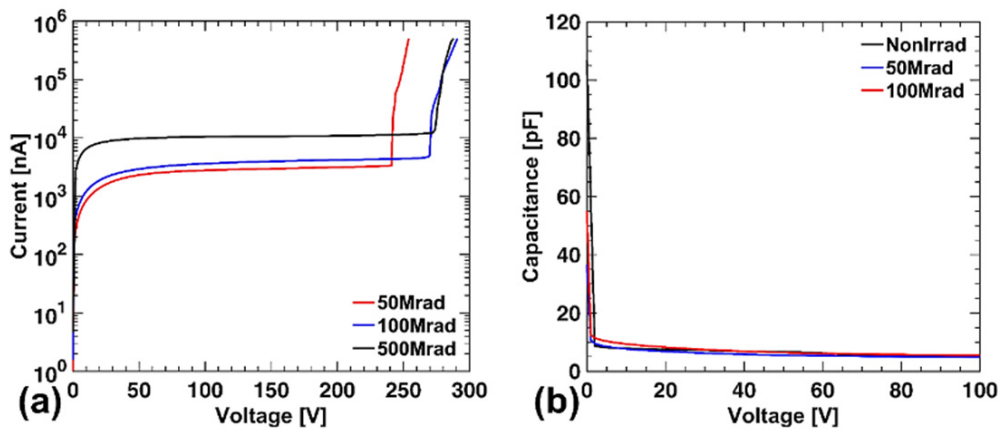


**Figure 5.12: (a)** I-V measurement of single strip of strip sensors: W7-ST12, W7-ST8 and W7-ST6, irradiated with  $\gamma$ -rays (50 Mrad(Si), 100Mrad(Si) and 500Mrad(Si) respectively), measured in UTN at room temperature. **(b)** C-V measurement of single strip of strip sensors: W7-ST1, W7-ST12 and W7-ST8, measured in UTN at 10 kHz and at room temperature. During the measurement, neighboring strip were grounded to avoid parasitic effects.

As an example figure 5.12 (a) is representing the gamma irradiated strip samples at three different TIDs, measured at UTN at room temperature. During measurements, neighbouring strips were biased at the same potential as it was applied to strip under experimentation, so the probing leakage current quantity holds only the intrinsic current contribution from the strip area targeted. As it was expected, the leakage current increased with higher TIDs, so as the breakdown voltage increased. In all TID cases, background gamma effect at bulk played the role in device breakdown voltage,  $V_{bd}$ , whereas leakage current enhancement was probably influenced from the aggregation of both surface and bulk damage. Figure 5.12(b) reports here the C-V measurement made on strip sensors irradiated at 50Mrad and 100Mrad TIDs at UTN at 10 kHz at room temperature. The depletion saturation plateau arrived at less than 10 V for higher TIDs alike in nonirradiated devices. Such phenomenon confirmed that there might be a moderately low bulk gamma contribution into substrate damage even for the highest TID and no significant deterioration has been observed in full-depletion.

The results on the first double-sided 3D sensors fabricated at FBK on 6-inch wafers here reported were limited to Gamma irradiation campaign only since a high density of process defects was observed, most likely to be ascribed to the long p+ column etching step caused by the non-optimal wafer thickness. For future productions with this technology, it gave a clear indication that thinner wafers should be chosen. The intrinsic electrical characteristics measured in small sensors in both non-irradiated and gamma irradiated conditions are in fact quite good, in agreement with TCAD simulation expectations. In particular, owing to the modified design and technology, the breakdown voltage exceeds 250 V at 500 Mrad. Since such a TID is similar to the one that will be encountered at future applications at HL-LHC upgrades, this result confirm that modified junction column partial passing through design is capable to ensure better radiation tolerance after large radiation fluences.

## Chapter VI

### New Small-Pitch and Thin 3D Si Sensors for HL-LHC

The upgrades of the major experiments (ATLAS and CMS) at the High-Luminosity LHC (HL-LHC) aim at the complete replacement of their tracking detectors to cope with the predicted higher event pile-up (140 events/bunch-crossing) and integrated luminosity of 3000 fb<sup>-1</sup>. The innermost tracking layers will have to withstand very large radiation fluencies up to  $2 \times 10^{16}$  1-MeV equivalent neutrons per square centimeter ( $n_{\text{eq.cm}^{-2}}$ ) [116]. Owing to their intrinsic (geometry dependent) radiation tolerance [117], 3D sensors are very promising candidates for this application. However, despite their remarkable performance, existing 3D pixel sensors, e.g., those currently installed in the ATLAS IBL [73,76], cannot fulfil the challenging demands of HL-LHC, calling for the development of a new generation of these devices which should feature: very dense pixel granularity ( $50 \times 50$  or  $25 \times 100 \mu\text{m}^2$ ), thinner active region ( $\sim 100 \mu\text{m}$ ), narrower columnar electrodes ( $\sim 5 \mu\text{m}$  diameter) with reduced inter-electrode spacing ( $\sim 30 \mu\text{m}$ ), and very slim edges ( $\sim 100 \mu\text{m}$ ).

Fondazione Bruno Kessler (FBK) of Trento, Italy, was one of the two fabrication facilities, together with CNM-IMB of Barcelona, Spain, involved in the 3D pixel sensor production for the ATLAS IBL [73]. Since then, the fabrication line at FBK was upgraded to process 6-inch diameter silicon wafers [146]. While the increased area available on wafer (about a factor of two as compared to 4-inch diameter) can offer a significant advantage in case of volume productions, maintaining the double-sided fabrication process [32] for thin 6-inch substrates is not the best choice because of several mechanical issues involved (compatibility with processing equipment, fragility etc.). Therefore, a different technological approach has been conceived, that uses Si-Si direct wafer bonded (DWB) substrates with a single-sided process [147]. The fabrication of a first batch of these new, small-pitch 3D sensors was completed at FBK at the beginning of 2016, and extensive electrical measurements were carried out with encouraging results.

The fabrication technology and the design of these new 3D sensors, as well as selected results from the characterization of different sensors (diodes, strips, pixels), also in comparison to TCAD simulation predictions are summarized here. Preliminary results will also be reported about the electrical characterization of different test-structures irradiated with X-rays,  $\gamma$ -rays, neutrons and protons to understand both the surface and bulk damage effects and the suitability of these devices to be operated in the HL-LHC.

## 6.1 Fabrication

The devices are the first small-pitch 3D sensors with thin active layer ever fabricated. A single-sided process on Si-Si DWB substrates from IceMOS Technology Ltd. was used. These substrates consist of a Float Zone high-resistivity layer of the desired thickness (namely 100  $\mu\text{m}$  and 130  $\mu\text{m}$  in the first production) directly bonded (i.e., without an oxide layer in between) to a 500- $\mu\text{m}$  thick low-resistivity handle wafer, thus ensuring sufficient mechanical robustness. The quality of this kind of raw material, which was previously unexplored for detector applications, was assessed by a preliminary batch of planar sensors [148]: from leakage current measurements, the bulk generation lifetimes were proved to be quite good, of the order of a few ms. Moreover, from capacitance-voltage curves of test diodes, it was possible to extract the substrate doping profiles, which revealed a significant back-diffusion of boron dopant from the handle wafer into the active layer with a depth of about 10  $\mu\text{m}$ . This makes the effective thickness of the active layer 10  $\mu\text{m}$  smaller, a fact that should be kept in account for the etching of the columnar electrodes.

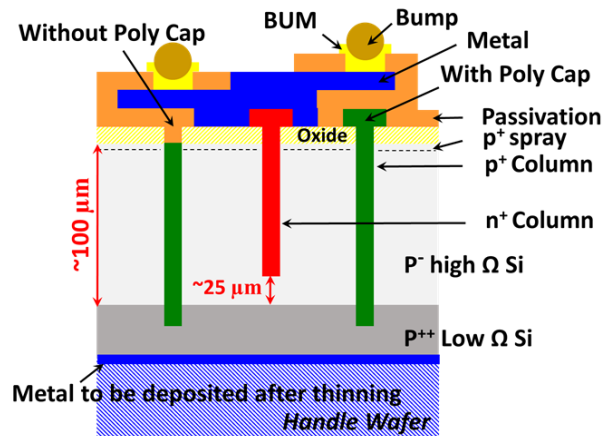


**Figure 6.1:** Schematic cross-section of the proposed single-sided 3D sensors on Si-Si DWB substrates. BUM denotes bump underneath metal.

### 6.1.1 Process Design

The schematic cross-section of the proposed sensors is shown in figure 6.1. The direct bonding of the high  $\Omega$ -Si (active) layer ( $\langle 100 \rangle$  crystal orientation, resistivity higher than  $3\text{k}\Omega\cdot\text{cm}$ ) to the low  $\Omega$ -Si handle wafer dictates the choice of different column depths for the junction ( $n^+$ ) and the ohmic ( $p^+$ ) electrodes. The  $p$ -columns are etched first by Deep Reactive Ion Etching (DRIE) through the whole high  $\Omega$ -Si layer thickness and penetrate by a few  $\mu\text{m}$  into the low  $\Omega$ -Si layer. By doing so, a good ohmic contact is made on the handle wafer, which can eventually be partially removed with a post processing and coated with a metal layer to allow for sensor bias from the back-side. Lessons learned from the ATLAS IBL experience suggest this is essential to ensure 3D sensor installation within a pixel module [73,76]. On the contrary, the  $n$ -columns do not penetrate through the entire active layer, but rather stop at a short distance ( $\sim 25\ \mu\text{m}$ ) away from the low  $\Omega$ -Si layer, in order to avoid the early

breakdown. A p-spray layer obtained with a low dose Boron implantation is present at the front side, to prevent the inversion of surface, thus isolating the n-columns [146].

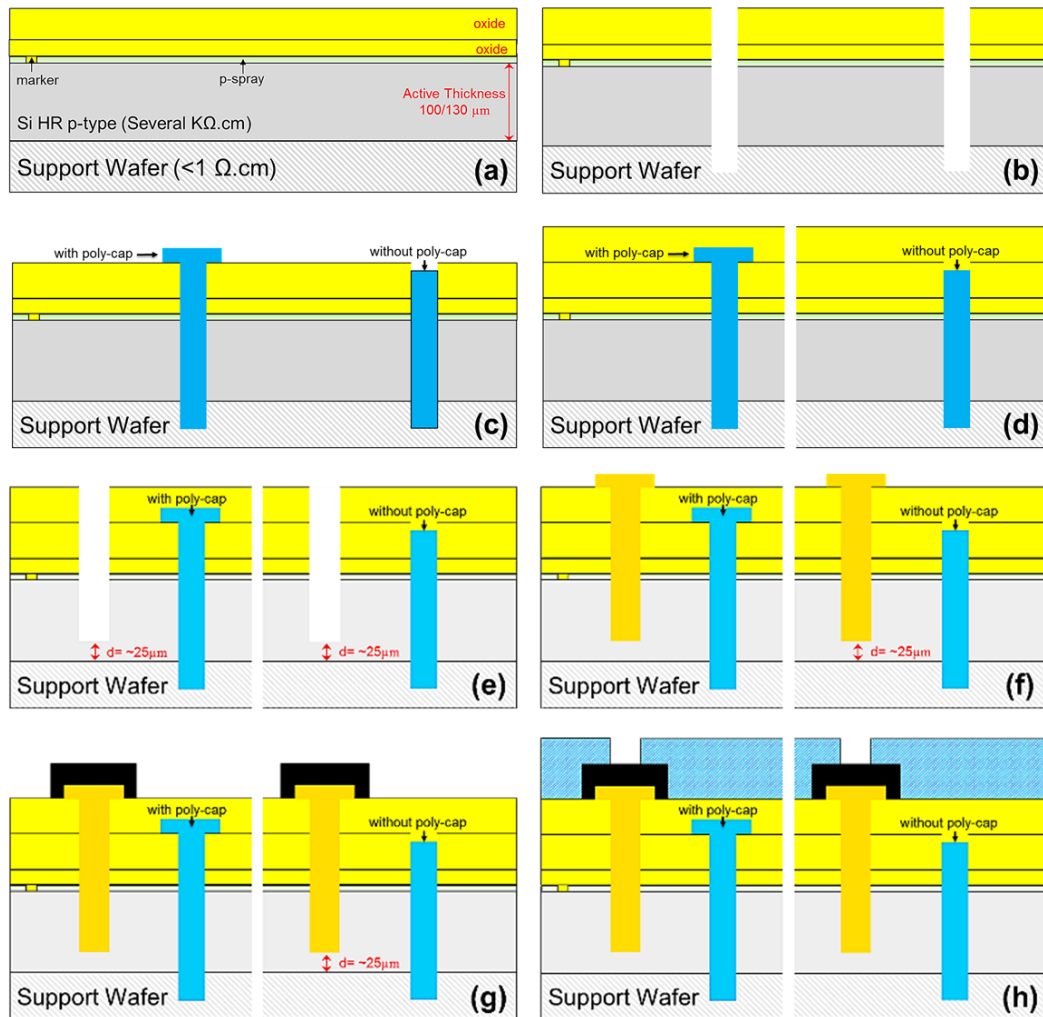


**Fig. 6.2:** Key steps of new thin 3D Si sensor processing: (a) Oxidation and p-spray implant, (b) p-column definition and etching, (c) p-hole poly-Si filling, (d) Re-oxidation, (e) n-column etching, (f) n-hole poly-Si filling, (g) Deposition and definition of metal, and (h) Deposition and definition of passivation.

The fabrication process sequence is reported in Fig. 6.2 and explained in the following:

#### a) Oxidation & Marker association:

Initially a thin oxidation layer was grown on bare Si wafer from the front side. Using RIE process, a marker was induced as the reference for device processing and filled with silicide. Afterward, boron implantation is done to create the p-spray isolation layer. Thereby, non-pyrophoric and noncorrosive Tetra-Ethyl-Ortho-Silicate (TEOS) technology was adopted to grow the state of art conformal thick oxide layer of several 100nm.

#### b) p-column etching:

In this sequential stage, a mask was printed and patterned through a lithographic process. DRIE was then applied to form a p-column hole that reached

beyond high resistive active layers to low resistive substrate. The recipe of DRIE was optimized with respect to column depth (for the two different active layer thicknesses) rather than to uniformity in this case.

**c) p-type poly-Si filling:**

During this step, p-hole was partially filled with poly-Si at the range of few 100nm thickness and doped with  $\text{BBr}_3$  ( $\text{p}^+$ ) with the thermal diffusion process. Afterward, the hole was filled again with poly-Si with larger thickness ( $\sim 2 \mu\text{m}$ ), that eventually caused almost complete filling of the holes and the formation of a thick layer of poly-Si also at the surface. Such a poly-Si layer was later etched, either with a mask, hence forming the poly-cap at the top of the column hole (Figure 2(c) left), or uniformly without a mask (Figure 2(c) right).

**d) Re-oxidation:**

In this stage, a TEOS film was deposited again for growing another step of the thick oxide layer to prepare the front side for forming the n-type hole.

**e) n-column etching:**

At this step, the n-column mask was printed and patterned with the lithographic process and afterwards, the n-hole was formed with DRIE process. The recipe of DRIE within this stage was optimized for the column-depth aspect ratio-uniformity by varying temperature and time. The gap size of an n-column tip from the low  $\Omega$ -Si layer still kept the nominal value of  $25 \mu\text{m}$ .

**f) n-hole poly-Si filling:**

Likewise step 'b', a thin poly-Si layer (few 100nm) was deposited in the n-hole. Then the entire hole was doped with the  $\text{POCl}_3$  ( $\text{n}^+$ ) gas source by a thermal diffusion process and consequently filled with a thicker poly-Si layer ( $\sim 1 \mu\text{m}$ ), which, after etching with a mask, eventually formed the poly-cap at the top of the n-column.

**g) Deposition and definition of metal:**

At this stage, Aluminum metal ( $\sim 1 \mu\text{m}$ ) was deposited through the sputtering process, and a mask was applied using the lithographic process to define the pattern of metal, connecting the n-columns.

**h) Deposition and definition of Passivation:**

The protecting passivation layer (nitride enhanced dielectric oxide material) was deposited in this step, and opened locally with lithography to expose metal pads for probing and bump-bonding.

Table 6.1 summarizes the process splits used in the first batch. Among the 10 processed wafers, note that W82 was broken at the end of the process before temporary metal deposition (following the passivation opening, not shown in Fig. 6.2).

**Table 6.1:** Schematic of processed wafer with different options.

	Wafer ID									
	W36	W41	W48	W50	W54	W70	W76	W77	W78	W82
Poly-cap presence	yes			no			yes			no
Nominal Active Wafer thickness [ $\mu\text{m}$ ]	100 $\mu\text{m}$					130 $\mu\text{m}$				

### 6.1.2 Process Characterization

The process ascribed above come with the reduction of the almost 30% less processing steps than the IBL technology. However, this process steps lead to the newer challenges relevant to the single-sided process of both types of columns while adopting the small-pitch design. Figure 6.3(a) shows the layouts of the two most important pixels cells, featuring  $50 \times 50 \mu\text{m}^2$  and  $25 \times 100 \mu\text{m}^2$  sizes. The  $50 \times 50 \mu\text{m}^2$  small pitch has one n+ column (1E) at the center, with an inter-electrode spacing  $L \sim 36 \mu\text{m}$ . This layout is pretty safe since the distances between the different structures are large enough (at least several  $\mu\text{m}$ ). In particular, the bump-bonding pad can be placed on either side of the n-column while remaining far enough ( $>15 \mu\text{m}$ ) from the p-columns. On the contrary, the  $25 \times 100 \mu\text{m}^2$  layout can either be made with one n-column (1E), with an inter-electrode spacing  $L \sim 51 \mu\text{m}$ , or, for higher radiation hardness, with two n-columns (2E), with an inter-electrode spacing  $L \sim 28 \mu\text{m}$ . In the latter case (as shown  $25 \times 100 \mu\text{m}^2$ -2E pitch in figure 6.3(a)), the layout is really dense and the bump-bonding pad is very near to both n+ and p+ columns, so that misalignment problems could cause the pad to overlap the columns, thus leading to high electric fields with the risk of microdischarges. In this respect, the p-column finishing option “without poly-cap” would add a safety margin of a few  $\mu\text{m}$ , but it should be proved not to worsen the sensor electrical characteristics.

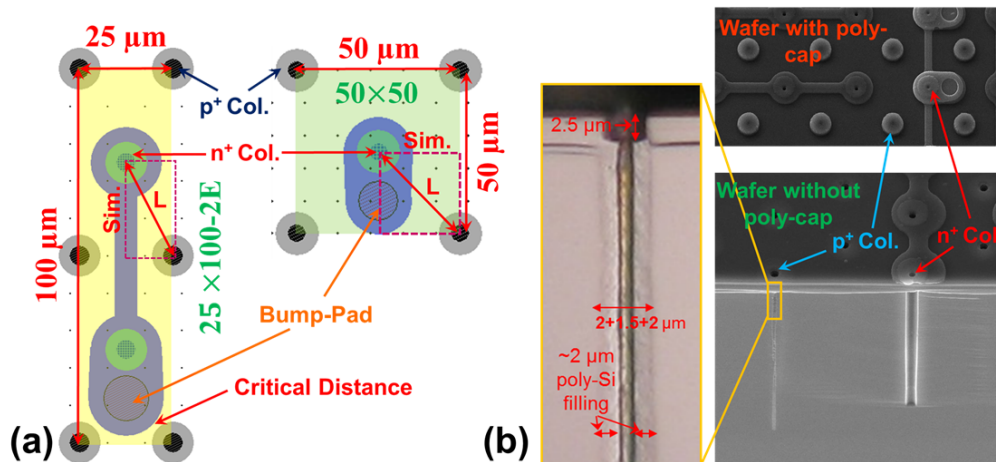


**Figure 6.3:** (a) Layout-view of the  $25 \times 100$ -2E (yellowish rectangle) and  $50 \times 50$  (greenish square) pixels; (b) SEM images: n+ column and p+ column with representation of both “with poly-cap” and “without poly-cap” options.

Likewise, every other 3D sensor productions, the most delicate steps has remained the column etchings by DRIE. The etching recipes had been previously optimized with dedicated tests [32], so that results were good. Figure 6.3(b) shows a few pictures from Scanning Electron Microscope (SEM). It can be seen that the column widths are pretty uniform along their depths, where it is also evident that the poly-Si etching step “without cap” shows not to have damaged the p-columns’ openings.

## 6.2 Wafer Layout

The large area available on 6-inch wafers allows accommodating a huge variety of sensors on the wafer layout (called 3DSS-6, see figure 6.4(a)) while ensuring a wide safety margin ( $>1$  cm) from the wafer edge. In this batch, the wafers hold the RD53A fine pitch recommendations with existing state of art pixelated sensors compatible with ATLAS FE-I4 and the CMS PSI46 read-out chips (ROCs). There have been 13 “FE-I4” single tiles: some of them have the same column configuration as the IBL pixels [73], with or without guard ring. There are 38 “PSI46” single tiles, differing in the number of n-columns (2 and 3) per pixel of conventional geometries, along with the new small-pitch designs, with or without guard ring. There are also 9 “FE-I3” compliant sensors with a combination of new pixel sizes. Some other sensors are instead oriented to the new ROCs being developed by the RD53 Collaboration [149]. There are 11 big ( $0.9\text{ cm}^2$ ) and 18 small ( $0.36\text{ cm}^2$ ) prototype sensors of these kinds. All the big sensors have pixel cell size of  $50\times 50\ \mu\text{m}^2$ , whereas the small kinds comprise the geometrical diversity of  $50\times 50$ , or  $25\times 100$ -2E, or  $25\times 100$ -1E  $\mu\text{m}^2$  fine pitches.

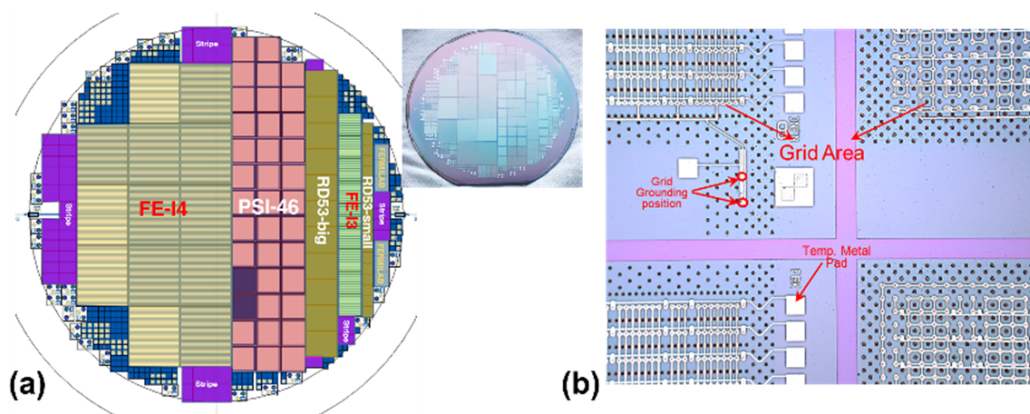


**Figure 6.4:** (a) Wafer layout of the 3DSS-6 batch, with an indication of the many different sensors. The top right inset shows an image of fabricated 3DSS-6 wafer at FBK. (b) Micrograph of pixel sensors, showing the metal grid shorting non-read-out pixels and the temporary metal.

We would like to stress here that all the pixelated sensors are designed with slim edges [75]. Compared to the  $200\text{-}\mu\text{m}$  design used for the ATLAS IBL pixels, the possibility to use a reduced pitch for the columns here allows for more aggressive designs, down to  $75\text{-}\mu\text{m}$  size [150]. The periphery of the wafer layout hosts several smaller sensors (3D strips, 3D diodes) and test structures. In particular, 3D diodes ( $\sim 2\text{ mm}^2$  area) reproduce the basic 3D cell layouts of all types of large pixel and strip

sensors, but all columns of the same type are shorted together by a metal grid to obtain a 2-electrode device [32].

One of the biggest challenges of the layout design for this batch was to make the new, small-pitch pixels compatible to the existing ROCs that have larger pixel pitches. To this purpose, in the sensor layouts,  $n^+$ - and  $p^+$ -columns are placed on either  $25 \times 100 \mu\text{m}^2$  or  $50 \times 50 \mu\text{m}^2$  grids, corresponding to the elementary cells. One or more cells are then connected to the ROC bonding pads, whereas the remaining  $n$ -columns are all shorted by a metal grid and connected to the extra bonding pads that are grounded in ROC (see figure 6.4(b)). This solution allows as many small pixels as possible to be tested, avoiding problems in ROC tuning, since all read-out channels have the same input capacitance, and ensuring proper boundary conditions, since all columns are uniformly biased. However, it should be noted that the geometrical efficiency is small (as an example, it is 20% in an FE-I4 based design, where the ROC pixel cells are  $50 \times 250 \mu\text{m}^2$ ), making data analysis more difficult. Finally, Figure 6.3(b) also shows the temporary metal grid that is used for on-wafer electrical tests of pixel sensors [32].

### **6.3 Simulation**

Two-dimensional and three-dimensional finite-element Synopsis TCAD software have been used to investigate the electrical and charge collection properties of small pitch and thin 3D sensors. In order to predict and optimize the performance of these new 3D sensors, numerical device simulations have been performed on two different shapes of pixel geometries proposed by RD53A collaboration [149]:  $50 \times 50 \mu\text{m}^2$  (square) or  $25 \times 100 \mu\text{m}^2$  (rectangular) 3D pixels, compatible with the new 65 nm CMOS chips under development for the ATLAS and CMS pixel detectors at the High-Luminosity LHC (HL-LHC). This choice was made in order for the sensors to be more radiation tolerant. In fact, in the “ $25 \times 100$ ” pixel with only one read out electrode, the inter-electrode distance ( $L$ ) would be more than  $50 \mu\text{m}$ , that is too large to counteract charge trapping at the maximum expected fluence of  $2 \times 10^{16} n_{\text{eq}}/\text{cm}^2$ . In view of HL-LHC application, a design with smaller columnar diameter and inter-electrode spacing must be implemented with respect to existing 3D pixels of LHC (i.e. ATLAS10). The column aspect ratio, thinner sensors have to be used within this respect of design constraints. The electrical and charge collection properties of these downscaled devices is demonstrated in the following sections, including investigation of the possibility to increase the charge collection efficiency (CCE) by means of charge multiplication.

Simulation of optimal termination structures around the sensor perimeter to achieve active or very-slim edges must also be performed. Because of symmetry considerations, minimum size cells were considered as simulation domains (see red regions in figure 6.3(a)), while values of all parameters are representative of FBK

technology. Full 3D simulations were performed, also incorporating detailed information about the dielectric layers, the metal layers, and the surface insulating layer (p-spray). The column diameters have chosen  $5\ \mu\text{m}$  and the active layer thickness have taken account as of  $150\ \mu\text{m}$ , where the  $n^+$ -column depth remains  $130\ \mu\text{m}$ . The simulation domains have denoted for  $25\times 100\ \mu\text{m}^2$  fine pitch as red rectangular inset in figure 6.3(a) (left) and for  $50\times 50\ \mu\text{m}^2$  pixel has as red square inset in figure 6.3(a) (right).

### 6.3.1 Simulation for Non-irradiated devices

This first set of simulations was aimed at predicting the impact of technology and layout choices on the electrical properties of new sensors made at FBK, in accordance to the approach described in figure 6.1. In particular, AC small-signal simulations were performed to predict the pixel capacitance, and quasi-static simulations were performed to predict the breakdown voltage values. For these simulations, a full 3D domain was used, also incorporating the dielectric layers, the metal layers, the surface insulating layers (p-spray). As also indicated in figure 6.3 (a), the simulated structures exploit the 3D pixel symmetry to minimize the number of grid points and therefore the simulation time. They consist of a  $1/4$  of a pixel in case of the  $50\times 50$ -1E pixel, and of  $1/8$  of a pixel in case of the  $25\times 100$ -2E pixel. Simulated full 3D domains presents in figure 6.5(a).

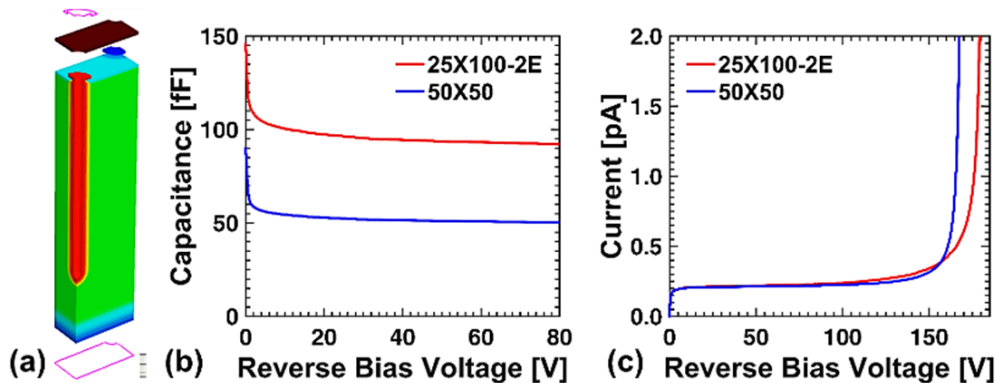


**Figure 6.5:** (a) Simulated full 3D domain and electrical characteristics for  $50\times 50$  and  $25\times 100$ -2E pixels (b) I-V curves, (c) C-V curves.

The active layer considered in simulations has low doping,  $7\times 10^{11}\ \text{cm}^{-3}$  and is  $150\ \mu\text{m}$  thick (as a worst case for capacitance). This active layer is assumed to be directly in contact with the first few micrometers of the handle wafer of high doping ( $5\times 10^{19}\ \text{cm}^{-3}$ ). The read-out electrode ( $n^+$  column, shown in red in figure 6.5(a)) was stopping  $20\ \mu\text{m}$  from the high doping region, whereas the bias electrode ( $p^+$  column, shown in blue at a corner in figure 6.5(a)) is passing through the active layer. Both columns have uniform, high doping ( $5\times 10^{19}\ \text{cm}^{-3}$  of Phosphorous and Boron, respectively), with  $2.5\ \mu\text{m}$  lateral diffusion. The tip of the read-out column is rounded with the same vertical radius as the lateral one. A p-spray layer, presented in cyan at the top in figure 6.5(a) with boron (B) profile representative of FBK process, is used

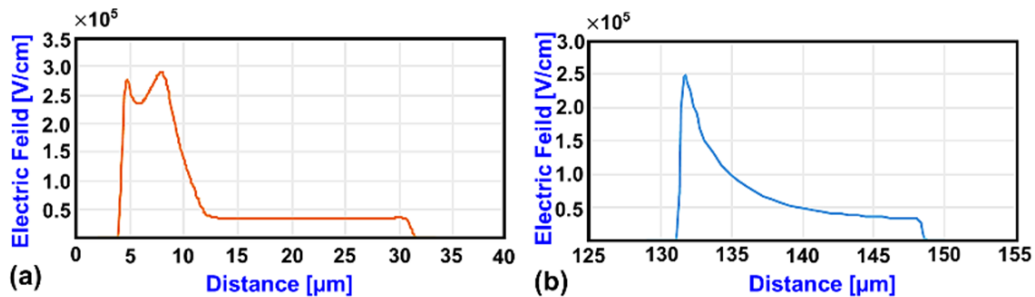
for surface isolation, and is covered by a 1  $\mu\text{m}$  thick silicon oxide layer (shown in brown in figure 6.5(a)). The shape of the metal layers (shown in fuchsia in figure 6.5(a)) matches that of the pixel layout; in particular, for the front-side, it is slightly larger than the readout electrode that is representing the inclusion a field plate at simulation domain.

### Accounted TCAD models for Simulation

The simulations with Synopsys TCAD used typical models (e.g., effective intrinsic density, doping dependent Shockley-Read-Hall generation/recombination and mobility, high field saturation, etc.) and default values for most parameters. For other parameters values typical of the FBK technology were used: among them, the lifetimes of minority carriers in the bulk ( $\sim\text{ms}$ ), as well as the oxide charge density ( $3 \times 10^{11} \text{ cm}^{-2}$ ) and surface generation velocity (10 cm/s) to model the Si/SiO<sub>2</sub> interface. In order to predict avalanche breakdown, impact ionization effects were incorporated in the quasi-static simulation according to the avalanche model by Van Ovestraeten/De Man with electron/hole driving force.

### Electrical Characterization

Figure 6.5 (b) shows the simulated capacitance versus voltage (C-V) curves, normalized to the full pixel size. It can be seen that, owing to the small value of L, full depletion is achieved at very low voltage. The capacitance values are about 50 fF for the 50 $\times$ 50-1E pixel and about 100 fF for the 25 $\times$ 100-2E pixel: this is mainly due to the 1E configuration of the former and the 2E configuration of the latter. Both values include all contributions intrinsic to the 3D sensor, but not that from the bumps that might add a few tens of fF more. Therefore, the 25 $\times$ 100-2E pixel is critically close to the 100 fF limit set by the RD53 Collaboration for the total capacitance.



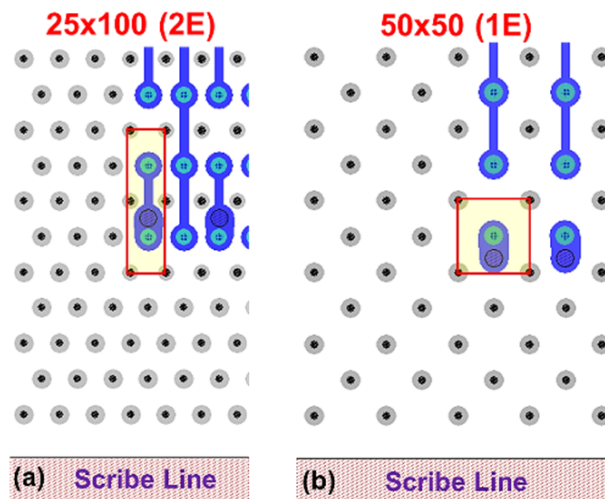
**Figure 6.6:** Simulated electric field profiles at 160V (close to breakdown) in a 50x50 pixel along 1D cuts taken: (a) at the surface along a diagonal line connecting the centers of the two columns, and (b) at the read-out column tip along a vertical line connecting the column tip to the back-side.

Figure 6.5(c) shows the simulated current versus voltage (I-V) curves, normalized to the full pixel sizes. As expected, the currents are very low. Most notably, the breakdown voltage is very high, in the order of 150V. Minor differences are observed between the two structures, likely due to the different discretization grid accounted in the simulation rather than to physical reasons. Inspection of the electric

field profiles suggests that breakdown is initially localized at the junction between the read-out column and the p-spray layer on the front-side. As an example, figure 6.6 shows the simulated electric field profiles at 160 V (close to breakdown) in a  $50 \times 50$  pixel along 1D cuts taken at the surface and at the read-out column tip. It can be seen that the electric field peak is larger at the surface. However, also the peak at the column tip is relatively large, and, in fact, it could even be higher considering the real scenario where the shape of the tip will not as uniform as the rounded one considered in simulation domain. Hereby, it leads to an uncertain conclusion on where the breakdown occurs in real devices.

### Slim Edge

Additional simulations of non-irradiated devices were intended to assess the effectiveness of a slim edge termination. For the ATLAS IBL, a slim edge concept based on a fence of ohmic columns was introduced, which made the structure able to confine the depletion region spreading from the outermost junction columns, ensuring not reaching the highly damaged cut region [75]. Compared to the  $200 \mu\text{m}$  design used for the ATLAS IBL pixels, the possibility of using a reduced pitch (higher density) for the columns makes their blocking action even more effective. So, the depletion region is confined within a very short distance from the junction columns. This allows for more compact designs, edge down-sized to  $75\text{-}\mu\text{m}$  size [150]. The aim of this set of simulations is actually to predict the maximum extension of the depletion region at the edge, so as to validate the slim edge designs. The very same models as in electrical characterization in full 3D domain were used this study, as mentioned earlier. The simulation domains accounted here to two dimensions only and so, the Si/SiO<sub>2</sub> interface parameters are not included.



**Figure 6.7:** Layout schematics of edge corner regions of RD53A recommendation of thin and small pitch adapted to FE-I4 pixel sensors: (a)  $25 \times 100 \mu\text{m}^2$  and (b)  $50 \times 50 \mu\text{m}^2$ . The outermost fine pitches of respected geometries are indicated by red rectangle/square.

Figure 6.8 shows the simulated electric field distribution at 200 V reverse bias to the edge corners of the  $25 \times 100 \mu\text{m}^2$  and  $50 \times 50 \mu\text{m}^2$  HL-LHC compliant small pitch for simulated domain denoted in figure 6.7. This applied bias voltage is much larger than the required scale for a non-irradiated device and it is clearly visible that the depletion region does not reach the scribe-line. This indicates that the dead area, i.e., the distance from the outermost pixel and the scribe-line is very small and it could be further decreased down to  $\sim 50 \mu\text{m}$  by imposing more aggressive designs (i.e., the higher density of ohmic columns). Alternative designs featuring a 3D guard ring are also feasible while maintaining the same dead area.

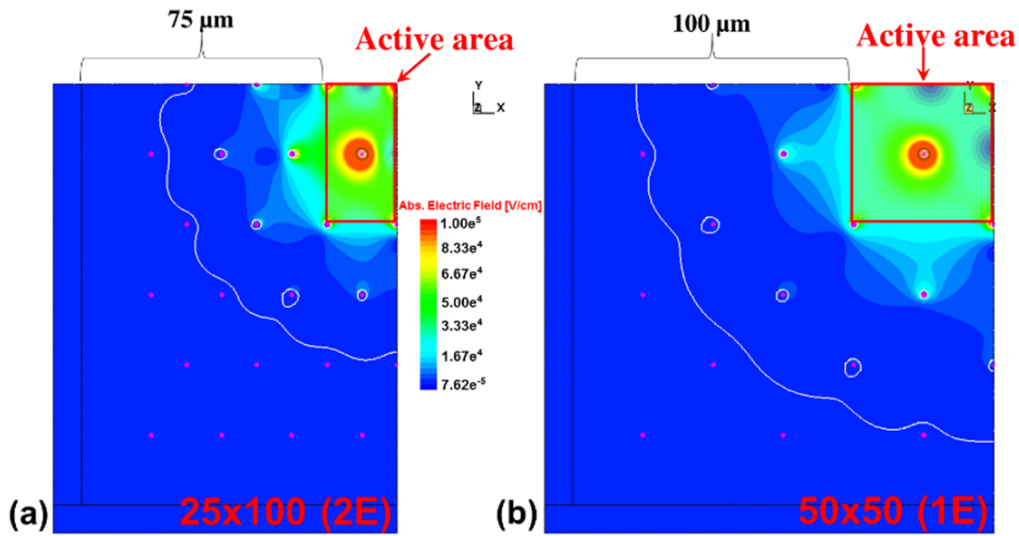


**Figure 6.8:** Simulated two dimensional electric field distribution at 200V reverse bias to the edge corner of RD53A recommended small pitches: (a)  $25 \times 100 \mu\text{m}^2$  and (b)  $50 \times 50 \mu\text{m}^2$ . Depletion boundary is denoted here with white line.

### 6.3.2 Simulation for Irradiated Devices

Owing to the short inter-electrode distance, new fine-pitch 3D sensors are expected to be very radiation tolerant up to the very large fluences foreseen at the HL-LHC. These simulations are intended to estimate the charge collection performance. In particular, the signal efficiency (charge collection efficiency) will be evaluated, that is defined as the ratio of the collected charge after irradiation and before irradiation. For these simulations, a simplified quasi-2D domain was used. It consists of a sensor slice,  $1\text{-}\mu\text{m}$  thick, taken at half the depth of the structures considered for full 3D domain (figure 6.5(a)).

Simulations consider the hit of a minimum ionizing particle at different points uniformly distributed within the 3D pixel cells, as shown in figure 6.9. In case of the  $50 \times 50 \mu\text{m}^2$  pixel, the pixel symmetry allows considering half of the cell area. Two additional models are considered for this simulation to understand the irradiated sensors. The first one is the “Heavy Ion” model, which allows the release of charge packets at different positions within the simulation domain with a uniform distribution

along the vertical axis and a Gaussian distribution across the horizontal plane. The second one is the deep-level trap model that accounts for radiation damage effects in the silicon bulk. Simulations were carried out using the 3-level “new Perugia” trap model for p-type silicon, which is summarized in Table 6.2 [151].

**Table 6.2:** New Perugia bulk damage model for p-type silicon.

Defect	E [eV]	$\sigma_e$ [cm <sup>2</sup> ]	$\sigma_h$ [cm <sup>2</sup> ]	$\eta$ [cm <sup>2</sup> ]
Donor	$E_v+0.36$	$3.23 \times 10^{-13}$	$3.23 \times 10^{-14}$	0.9
Acceptor	$E_c-0.42$	$1.0 \times 10^{-15}$	$1.0 \times 10^{-14}$	1.6
Acceptor ( $f \leq 7 \times 10^{15} \text{ cm}^{-2}$ )	$E_c-0.46$	$7.0 \times 10^{-15}$	$7.0 \times 10^{-14}$	0.9
Acceptor ( $7 \times 10^{15} \text{ cm}^{-2} \leq f \leq 1.5 \times 10^{16} \text{ cm}^{-2}$ )	$E_c-0.46$	$3.0 \times 10^{-15}$	$3.0 \times 10^{-14}$	0.9
Acceptor ( $1.6 \times 10^{16} \text{ cm}^{-2} \leq f \leq 2.2 \times 10^{16} \text{ cm}^{-2}$ )	$E_c-0.46$	$1.5 \times 10^{-15}$	$1.5 \times 10^{-14}$	0.9

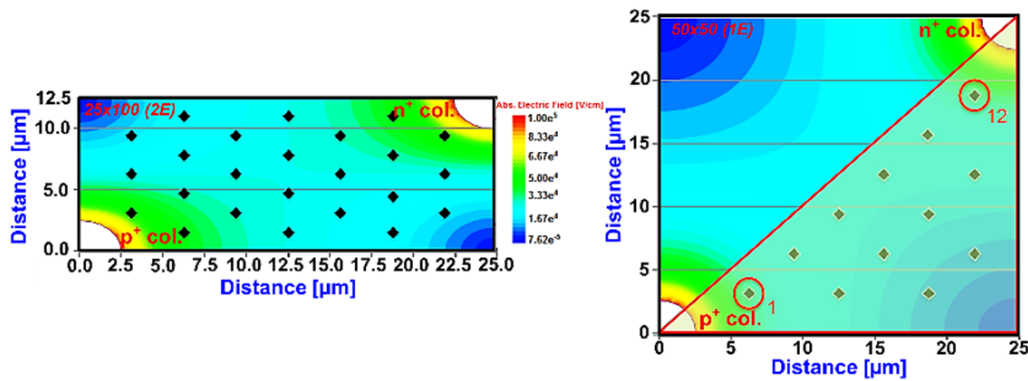


**Figure 6.9:** Simulated 2D slices showing the particle hit points for the  $25 \times 100 \mu\text{m}^2$  (LEFT) and the  $50 \times 50 \mu\text{m}^2$  (RIGHT) 3D pixels. Different black dotted hit points have set to the different electric field values. The hit points closest to the ohmic column (1) and to the read-out column (12) are indicated by red circles in the  $50 \times 50 \mu\text{m}^2$  pixel.

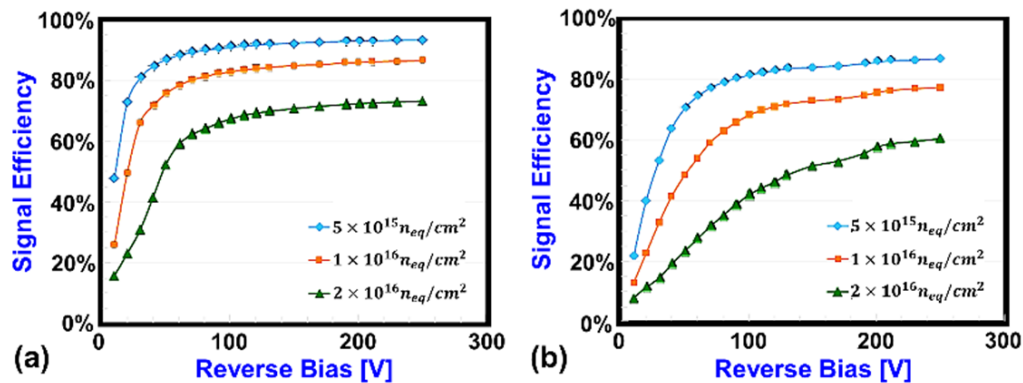


**Figure 6.10:** Simulated average signal efficiency as a function of bias voltage at different irradiation fluences for the two pixel layouts: (a)  $25 \times 100 \mu\text{m}^2$ , and (b)  $50 \times 50 \mu\text{m}^2$ .

These simulations require to start with a quasi-static analysis in order to save the different bias voltage conditions that are later fed as initial conditions for the transient analysis of the charge collection process. Three irradiation fluences were considered, namely  $5 \times 10^{15}$ ,  $1 \times 10^{16}$ , and  $2 \times 10^{16} \text{ neq/cm}^2$  and the trap model parameters were set according to the values shown in Table 6.2. The output of transient simulations provides current pulses at the read-out electrode as a function of time. A data post-processing is then required, that: (i) subtracts the leakage current

from the current pulse; (ii) performs a numerical integration in the time domain over 20 ns (compatible with LHC bunch-crossing); (iii) averages over all the hit positions at a given bias voltage. Results relevant to the two pixel geometries at different irradiation fluences are shown in Fig. 6.10, which shows the average values over all the charge release points of figure 6.9. Remarkably good values of signal efficiency are obtained with both geometries (note that also the 60% obtained in the worst-case is much higher than experimentally observed from 3D sensors of previous generation with larger  $L \sim 56 \mu\text{m}$ ). In particular, owing to the smaller value of  $L$ , the superior performance of the  $25 \times 100 \mu\text{m}^2$  pixel is evident in many respects: signal efficiency reaches higher values with a clear saturation trend at lower voltage as compared to the  $50 \times 50 \mu\text{m}^2$ .

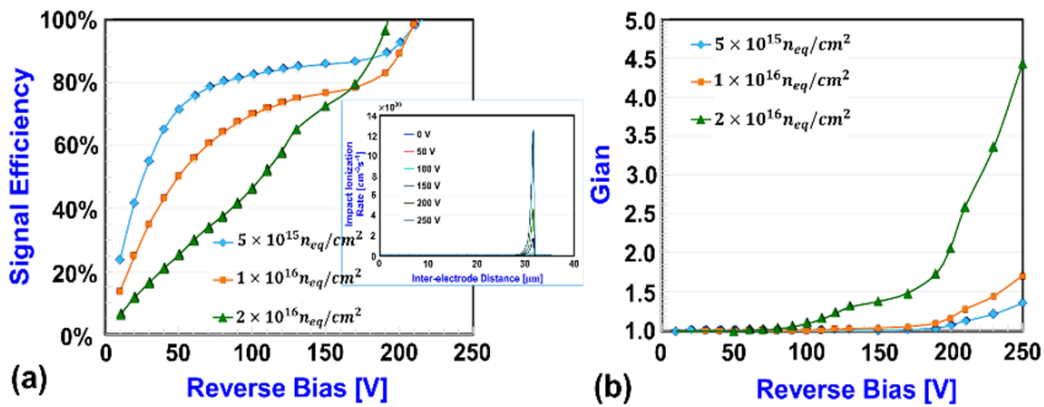


**Figure 6.11:**  $50 \times 50 \mu\text{m}^2$  pixel irradiated at  $2 \times 10^{16} \text{ neq/cm}^2$ : (a) simulated average signal efficiency and (b) average gain, at different reverse bias.

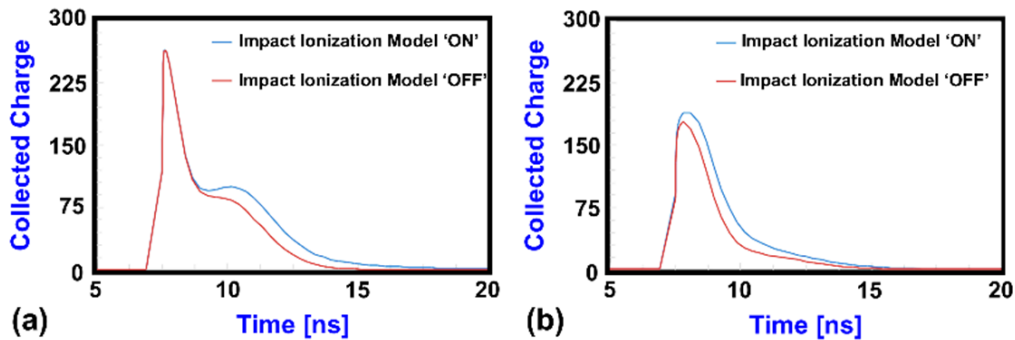


**Figure 6.12:** Simulated current signals in the  $50 \times 50 \mu\text{m}^2$  pixel irradiated at  $2 \times 10^{16} \text{ neq/cm}^2$  at 250 V bias, with and without avalanche multiplication: (a) hit point 1, close to the ohmic column, and (b) hit point 12, close to the read-out column.

The onset of charge multiplication effect could be predicted by simulations as a result of the fine inter-electrode distance at large bias. With increasing bias, the electric field peak at the read-out electrode is increased and could reach the critical value eventually. This leads devices into impact ionization effects, which are more pronounced in the  $50 \times 50 \mu\text{m}^2$  pixel at the largest irradiation fluence. Figure 6.6 (a) has already shown the 1D profiles of the electric field of same pitch at 160V (close to breakdown), that is almost reaching the critical value of  $3 \times 10^5 \text{ V/cm}$ , but the impact ionization effects start acting even at lower voltages. The corresponding impact

ionization rate along a diagonal connecting the centers of the ohmic column and of the readout column at different bias voltages is reported in the inset of figure 6.11(a). As a result, the average signal efficiency reported exhibits values in excess of 100% because of charge multiplication near 200V bias voltage, as it can be seen in figure 6.11(a). The corresponding gain, the ratio of the collected charge with avalanche multiplication and without avalanche multiplication, can be found in figure 6.11(b) as a function of bias voltage. At lower fluences, the gain starts deviating from unity only at a very large voltage (near breakdown). On the contrary, the deviation is clearly visible for the largest fluence considered in simulation ( $2 \times 10^{16} \text{ n}_{\text{eq}}/\text{cm}^2$ ) at a lower voltage and it actually explodes at the very large bias.

Figure 6.12 illustrates the different signal dynamics in the two “extreme” hit positions of the simulation domain (points 1 and 12, as it could be found in figure 6.9). The signals with and without avalanche multiplication are compared at the maximum value of the applied bias reference (250 V) to highlight the differences. In reference of Ramo’s Theorem, for hit points close to the read-out electrode (like point 12), signals increase already at low voltage since the weighting field is high, depletion is obtained soon, and trapping of electrons is very small. Therefore, the electron contribution to the signal is achieved soon with minor losses, whereas no contribution from holes is possible due to trapping. At this point, electrons give a prompt contribution to the signal, so that their multiplication peak gets mixed with the main one, as could be seen in figure 6.12 (b). Conversely, for hit points close to the ohmic electrode, like point 1, signals increase at the larger voltages necessary to spread the depletion layer farther from the read-out electrode and can reach higher values because of a concurrent hole-electron contribution. For this reason, hole contribution showed the prompt peak to the collected signal at beginning, followed by a delayed peak caused by electrons. With the case of impact ionization activation, the delayed signal peak enhanced as reported in figure 6.12 (a).

## **6.4 Experimental Results**

### **6.4.1 Before Irradiation**

#### **Electrical Characterization**

The fabrication of the first batch of these new thin, fine-pitch 3D sensors was completed at FBK in March 2016. Extensive characterization of sensors and test structures has been carried out since then. Since the electrical characterization of pixel sensors is not easy, for the comparison to simulation results, 3D diodes are particularly useful. These devices reproduce the basic 3D cell layouts of pixel sensors, but all columns of the same type are shorted together by a metal grid to obtain a 2-electrode device. Owing to their relatively small size (a few  $\text{mm}^2$ ), 3D diodes are often free from process-related defects, making it possible to investigate the intrinsic properties of the different structures. We have implemented 3D diodes both with and without a guard

ring. An example of 3D diode layout with a guard ring is shown in figure 6.13(a). They were probed with the experimental setup for electrical characterization at room temperature, using the required combination of HP4284A LCR meter at the frequency of 1/10 kHz, HP4145B semiconductor parameter analyzer with average integration time and Keithley 2410 voltage source.

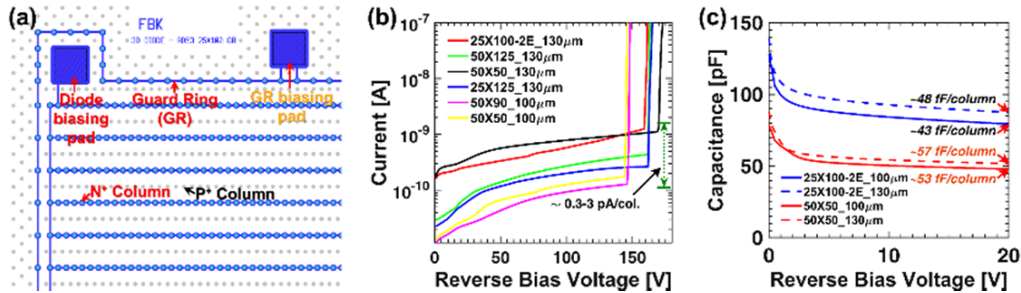
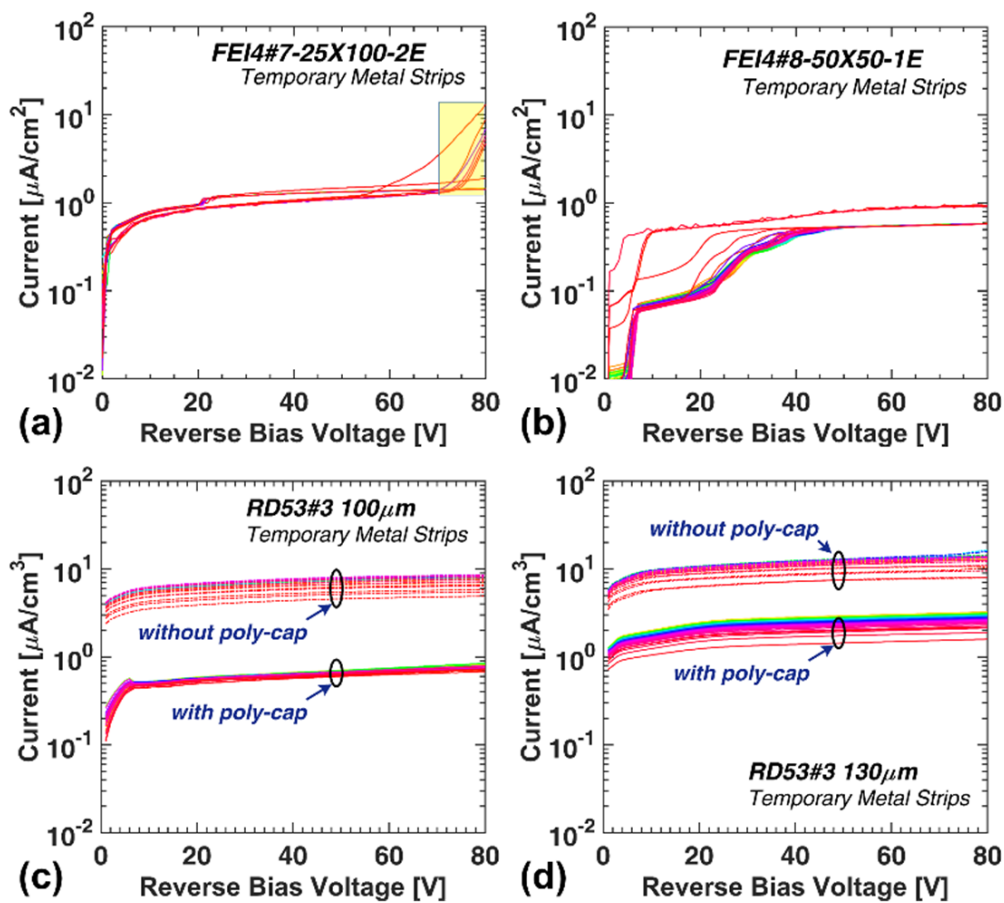


**Figure 6.13:** (a) Layout of a 3D diode with guard ring; (b) I-V curves of diodes of different active thickness and unit cell geometries; (c) C-V curves of diodes of different active thickness and unit cell geometries.

Figure 6.13(b) shows the leakage currents of several diodes of different active thicknesses and unit cell geometries. The measured leakage current values are very good: if normalized to the number of columns, they are in the range from 0.3 to 3 pA, comparable to the simulated values. The relatively wide spread of the measured current values is likely to be ascribed to the different quality of the active layer material for 100 μm and 130 μm thick wafers in terms of carrier lifetimes, as also observed in a preliminary test batch of planar devices [148]. It can also be observed that the breakdown voltage is large (~150 V), very close to the simulated values. Figure 6.13(b) also shows data relevant to unit cell layouts having a larger inter-electrode distance (e.g., 50×90, 50×125 μm<sup>2</sup>). It is worth to note that both leakage current and breakdown voltage are similar to those of fine-pitch devices, proving that the latter are not intrinsically more critical. Figure 6.13(c) shows the C-V curves of 3D diodes of different thicknesses and featuring the two most important cell layouts. The curve shapes are in good agreement with the simulated ones, and they confirm the very low depletion voltage of these sensors. After normalizing the capacitance values to the respective number of columns present in the diodes, results are found to be of the order of 50 fF per column, very close to the simulated values, and with slight differences (4-5 fF per column) between the two different active layer thicknesses.

I-V curves of all pixel sensors were initially measured on wafer with an automatic probe station making use of a temporary metal layer patterned in strips that short-circuit rows of pixels together [32]. This probing approach made it possible to monitor the quality of pixel sensors before bump bonding by means of statistically significant distributions of the main parameters. As an example, current-voltage curves of FE-14 type pixel sensors of 25×100 μm<sup>2</sup> and 50×50 μm<sup>2</sup> fine pitches of the wafer 76 are reported in figure 6.14 (a) and (b). Later they are used for bump-bonding in order to study them within test-beam. Figure 6.14 also shows results relevant to the

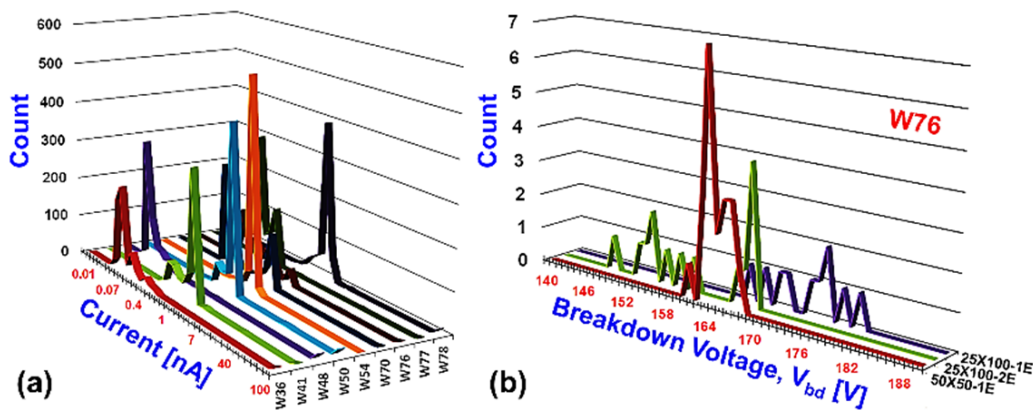
so called “RD53-big” sensors, which feature an array of  $200 \times 168$  pixels of  $50 \times 50 \mu\text{m}^2$  size. Sensor from wafers with both  $100 \mu\text{m}$  and  $130 \mu\text{m}$  active layer thickness are considered, also evaluating the impact of the poly-cap option. Figure 6.14(c) and (d) show I-V curves for the metal strips of selected sensors, belong to different wafers. Each strip shorts 3 rows of 200 pixels each. Similarly to diode measurements, it is confirmed that leakage currents are lower for substrates with  $100 \mu\text{m}$  thick active layer. The observed difference in the currents is in fact much larger ( $\sim 3.5\text{x}$ ) than expected from the different thickness alone. Most notably, for both  $100 \mu\text{m}$  and  $130 \mu\text{m}$  thick active layers, the option “without poly-cap” exhibits much larger leakage currents ( $\sim 10\text{x}$ ). This difference seems to indicate that the removal of the poly-Si layer from the wafer front-side without a mask actually induces some damage at the p-column openings, although this was not evident from SEM micrographs.



**Figure 6.14:** I-V curves of strips of FE-I4 type pixel sensors of W76 with poly cap having each one short-circuiting 336 pixels: (a) of  $25 \times 100\text{-}2\text{E} \mu\text{m}^2$  pitch; yellow inset shows ‘RAF’ behavior as discussed in chapter 5, and (b) of  $50 \times 50\text{-}1\text{E} \mu\text{m}^2$  pitch. Leakage current measurements through temporary metal strips of “RD53-big” pixel sensors of  $50 \times 50 \mu\text{m}^2$  pitch having each one short-circuiting 3 rows of 200 pixels: (c) I-V curves of strips with  $100\text{-}\mu\text{m}$  active thickness with poly-cap (W36) and without poly-cap (W54); (d) I-V curves of strips with  $130\text{-}\mu\text{m}$  active thickness with poly-cap (W76) and without poly-cap (W78).

The distribution of leakage current values measured at 20 V reverse bias (at full depletion) in all RD53-big sensors (11 per wafer, from 9 wafers) is reported the wide

dispersion of leakage current values [152]. However, it should note that even the largest values, if normalized to the number of columns, correspond to just a few pA, which is remarkably low for the 3D sensor technology, and comparable to the best results obtained from the ATLAS IBL production [32]. As an example, figure 6.15(a) shows the distribution RD53-big sensors of current per wafer at reverse bias 20V (full depletion). Per wafer dispersion of leakage current values is small, that indicates the process uniformity over the entire wafer area statistically significant. The variation of leakage current distributions from wafer to wafer can be anticipated from the non-uniformity of wafer surface quality made during production. From the same figure it is also possible to observe that the total number of strips with defects causing high leakage current ( $\sim 100$  nA) is small in number. Only 81 strip of 5544 strips of all 9 wafers are causing such high current, corresponding to  $\sim 1.46\%$ , demonstrates the good process quality even for relatively big devices with high column density, and is promising in view for future productions.



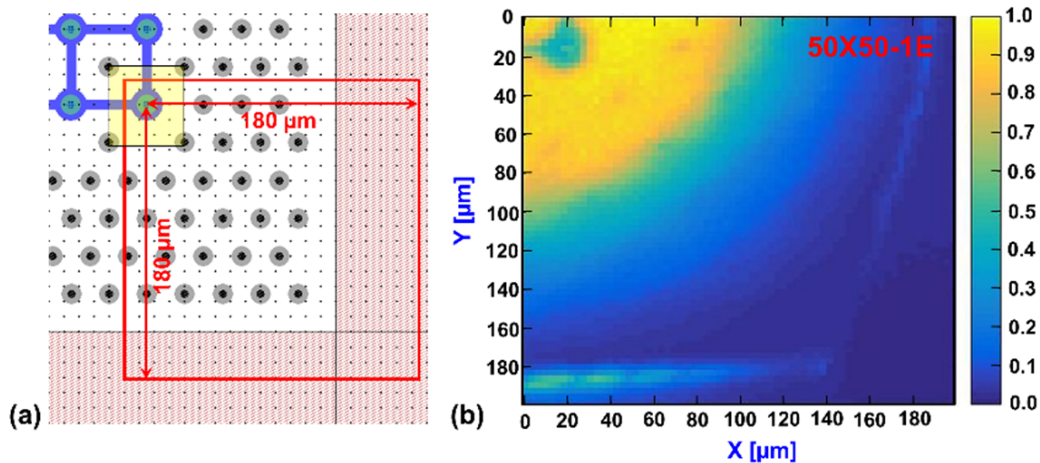
**Figure 6.15:** (a) Distribution of the currents at full depletion (20 V) of all strips from all RD53-big sensors (11 per wafer) on 9 wafers, (b) Distribution of the Breakdown Voltage ( $V_{bd}$ ) of the Diode of W76 of different fine pitches, as measured manually on probe station:  $50 \times 50\text{-}1\text{E } \mu\text{m}^2$  (20 of them),  $50 \times 50\text{-}2\text{E } \mu\text{m}^2$  (15 of them), and  $50 \times 50\text{-}2\text{E } \mu\text{m}^2$  (10 of them).

Figure 6.15(b) shows the distribution of the breakdown voltage ( $V_{bd}$ ) of diodes of thin 3D diodes of different geometries of W76: 20 of  $50 \times 50\text{-}1\text{E } \mu\text{m}^2$ , 15 of  $25 \times 100\text{-}2\text{E } \mu\text{m}^2$  and 10 of  $25 \times 100\text{-}1\text{E } \mu\text{m}^2$ . As it can be seen, variations in the breakdown voltage are slightly dispersed in all kind small-pitch sensors as shown in the figure 6.15(b). However a good uniformity in the breakdown voltage can be remarked with values of ranging from 145 to 185 V, a greater agreement with the simulated value of  $V_{bd}$ . Another interesting point to observe is that all such small sensors ( $\sim 3 \text{ mm}^2$ ) did not show any sign of early breakdown (yield is  $\sim 100\%$ ) again anticipating the good process quality.

### Laser Enhanced Space Resolved Characterization

An interesting functional test made on 3D diodes after dicing and mounting on a PCB, using a read-out circuit made of a charge amplifier and a fast shaper to verify the slim-edge simulation result. Fast shaper was used to suppress any diffusion-

related charge collection. Such experimental investigation made it possible to monitor the lateral spread of the depletion region. As an example, figure 6.16 (b) shows the map of the signal measured with a position resolved 1055 nm laser beam (FWHM  $\sim 5 \mu\text{m}$ ) in a diode biased at 70 V, i.e., well beyond full depletion. The layout of the corner region investigated with this method is also reported in figure 6.16 (a). The outermost n-column is recognizable in the signal map as the low signal region at the top-left corner, due to the light reflection from the metal layer. The high signal region spreads from around the n-column and it extends within the slim edge region by about  $80 \mu\text{m}$ , is still in a good agreement with simulated expectations reported earlier.



**Figure 6.16:** (a) Layout Schematic of  $50 \times 50 \mu\text{m}^2$  3D diode slim-edge corner; (b) 2D signal map of results from position resolved laser scan on the slim-edge region of  $50 \times 50 \mu\text{m}^2$  geometry at reverse bias 70 V.

### Charge Collection with $\beta$ -Source

Although 3D pixel sensors are main interest for the HL-LHC upgrades, charge collection measurements with  $\beta$ -Source were performed with strip detector. Testing of strip detectors requires less effort and is less expensive, as no bump bonding for the connection of the sensor and the read out chip is required. Measurements were performed using a beta source setup in combination with the ALIBAVA readout system [153], which is based on the Beetle ASIC [154]. The setup remains at University of Freiburg, Germany. Due to the technological constraint of FBK 3D detectors processing, it is not even possible to adapt the AC fan-in within these strip design; a RC coupled adapter is used instead to integrate each strip to a channel of the Beetle chip. The Beetle employs analogue read-out, has a shaping time of approximately 25 ns and is synchronized to a 40 MHz system clock. The signal pulse heights are converted into digital counts and can be further processed for the data analysis. The ALIBAVA system measures the phase of incoming trigger signals with respect to a 10 MHz internal clock. From these data, the pulse shape of the Beetle chip can be reconstructed. To assure that the pulse is always sampled close to its maximum, only events within a 10 ns wide time window around the peak are accepted [153].

The cooling of the detectors is based on liquid nitrogen. Nitrogen is evaporated and blown on the back sides of the devices under test. Sensor temperatures between  $-15^{\circ}\text{C}$  and  $-60^{\circ}\text{C}$  can be achieved. A temperature sensor is glued on the board next to the detector to monitor the temperature with a precision of  $\pm 1^{\circ}\text{C}$ . The stability of the cooling environment during a measurement was approximately  $\pm 1.5^{\circ}\text{C}$ . To obtain a conversion from ADC counts into charge, the setup is calibrated using a planar reference detector. A temperature dependent calibration was performed to account for the temperature dependence of the gain of the Beetle chip with an uncertainty of  $\sim 6\%$  [154].

Charge collection measurements were performed using fast electrons emitted by a  $^{90}\text{Sr}$  source. The readout is triggered by coincident signals of two scintillators, which are located behind the device under test. Almost all electrons emitted by the beta decay of  $^{90}\text{Sr}$  to  $^{90}\text{Y}$  are absorbed in the sensor or the first scintillator, which has a thickness of 4 mm. Hence, practically all coincidence signals are caused by fast electrons emitted in the beta decay of  $^{90}\text{Y}$  to  $^{90}\text{Zr}$ . These have a maximum energy of 2.3 MeV and can be regarded as minimum ionizing particles. Therefore, the deposited energy is approximately equal to the energy deposited by particles usually considered for tracking and reconstruction in high-energy physics detectors.

For the analysis of the beta source measurements a clustering algorithm is applied incorporating the strip capacitance, interstrip capacitance and the capacitance of RC Fan-in. First, the channel having the highest signal to noise ratio in each event is determined. This channel is accepted if the signal-to-noise ratio is higher than a seed cut, which was usually varied between three and four for the signal-to-noise ratio. The signals of neighboring channels are added as long as the ratio between their signal and their noise exceeds a given threshold. This threshold was typically varied between two and three for the signal-to-noise ratio. The cuts were slightly varied to improve the separation of the signal peak from the noise distribution in cases where the signal-to-noise ratio was low. The resulting spectrum was fitted by a convolution of a Landau function and a Gaussian. Signal values quoted below reflect the most probable value of the Landau distribution which was extracted from the fit.

As an example figure 6.17 (a) shows the signal of non-irradiated strip sensors of  $50 \times 50 \mu\text{m}^2$  small pitch as a function of the applied bias voltage. The measurements were performed at two different temperatures:  $-15^{\circ}\text{C}$  and  $-35^{\circ}\text{C}$ . The signal of the non-irradiated detector reaches a plateau at 2V as expected from the full depletion point of device. The expected signal corresponds to MIP ( $\sim 73 \text{ e-h}^+$  generation per  $\mu\text{m}$ ) over the effective thickness of around  $120 \mu\text{m}$  Si is  $\sim 8.7 \text{ Ke}^-$  [155]. It would be worth to mention that the active layer thickness of this DUT is  $130 \mu\text{m}$  but due to the Boron diffusion from the highly doped handle-wafer at the back side, the active thickness was reduced by  $\sim 10 \mu\text{m}$  [148]. It is evident from figure 6.17 (a) that lower temperature enhanced the charge collection, which can be anticipated from the carrier mobility (drift velocity) dependence upon temperature. Through the mobility, drift velocity has a very

complex temperature dependence, defined by the interplay of the following four scattering parameters: phonon scattering  $\mu_{ph}$ , surface roughness scattering  $\mu_{sr}$ , bulk charge Coulombic scattering  $\mu_{cb}$ , and interface charge Coulombic scattering  $\mu_{int}$  [156]. Each of these scattering parameters is related to the temperature of the material and the effective transverse electric field,  $E_{eff}$ , present in the device [157]. The combined scattering effect on the effective mobility,  $\mu_{eff}$ , in dependence of temperature,  $T$ , can be formulated using Mathieson's rule [156]:

$$\frac{1}{\mu_{eff}(T, E_{eff})} \propto \frac{1}{\mu_{ph}(T, E_{eff})} + \frac{1}{\mu_{sr}(T, E_{eff})} + \frac{1}{\mu_{cb}(T, E_{eff})} + \frac{1}{\mu_{int}(T, E_{eff})} \quad (6.1).$$

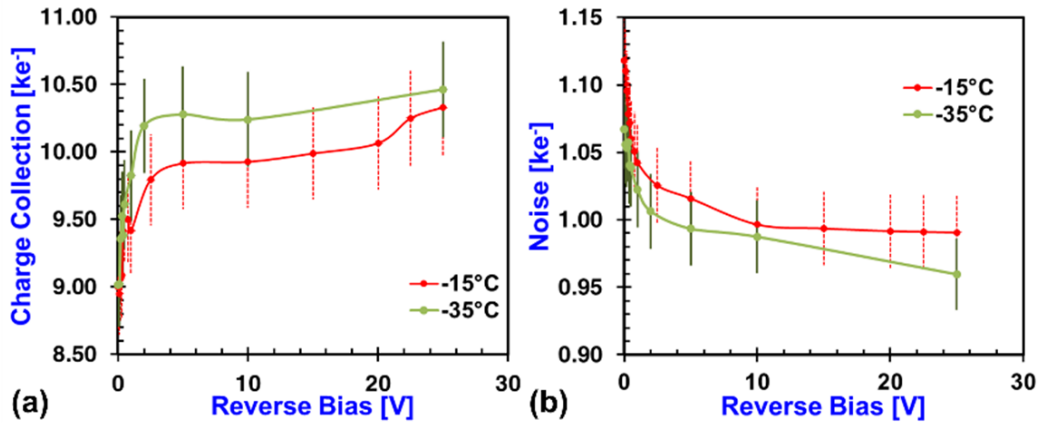


**Figure 6.17:** Non-Irradiated strip sensor of  $50 \times 50 \mu\text{m}^2$  fine pitch placed under  $^{90}\text{Sr}$  source and read with ALIBAVA system at University of Freiburg, Germany facility: **(a)** Signal as function of reverse bias voltage at different temperature, and **(b)** Noise at different temperature. Only statistical errors are considered, the systematic error due to the calibration uncertainty is not taken into account. Dead or extremely noisy channels were excluded.

For the considered devices, where the density of charge carriers is relatively small and the transport is mainly horizontal within the bulk, phonon scattering plays the major role for mobility, and the reduced thermal vibrations attained at lower temperature make mobility increase, helping to boost the signal at low voltage. However, within the error bar limit reported in figure 6.17(a), signal saturation for both temperatures at higher bias is in fact of good agreement.

Noise measurement in  $\text{ke}^-$  as a function of the reverse bias at two different temperatures can be observed in figure 6.17 (b). Consistently with the trend in the capacitance vs voltage curves, a sharp drop of noise is observed as the reverse bias reaches the full depletion value around 2V, eventually arriving to a saturation plateau. The plateau is in fact maintaining a slightly decreasing trend at higher bias references, which can be understood from the 3D sensor capacitance dependence upon voltage. As expected, the noise is lower at  $-35^\circ\text{C}$ , consistently with series noise direct dependence on  $T$ .

Impact ionization effects in charge collection and noise at higher bias voltage (close to breakdown) should be interesting investigations in future.

## Test-beam Campaign

One wafer (W76) was chosen for bump-bonding to be performed at Leonardo S.P.A. (former Selex-ES) in Rome, Italy, in July 2016. Soon after the FE-I4 pixel sensors of W76 were bump-bonded and assembled in modules, extensive electrical and functional tests were performed in the laboratory facility of INFN-Genova. The best two candidates of small pitch of different geometry:  $50 \times 50 \mu\text{m}^2$  and  $25 \times 100 \mu\text{m}^2$  along conventional  $50 \times 250 \mu\text{m}^2$  pitch were chosen for test-beam campaign in August 2016. A high resolution pixel telescope ACONITE, developed by the EUDET and AIDA projects was used for data taking at CERN SPS beam line during the campaign. The telescope consists of two arms, each containing three pixel planes. The DUT are placed between the arms, on a high precision  $XY_\phi$  table, that can be controlled from outside the beam line. The six telescope planes are sensors of the type Mimosas26 [167]. These are monolithic active pixel sensors (MAPS) with a  $18.4 \mu\text{m}$  pitch. MAPS are silicon pixel devices with amplifiers integrated directly in each pixel. The resolution of the sensors depends on threshold settings in the electronics, but it is approximately  $4\text{-}5 \mu\text{m}$ . The sensors consist of  $576 \times 1152$  pixels, covering an area of  $224 \text{mm}^2$ . The readout is binary, meaning no information about the amount of deposited charge is stored, except that it went above threshold. Approximately 10,000 frames can be read out per second. A schematic of test beam setup is shown in figure 6.18. All sensors were placed in the orthogonal direction of beam line. INFN-Genova took the leading role in data reconstruction of test-beam campaign.

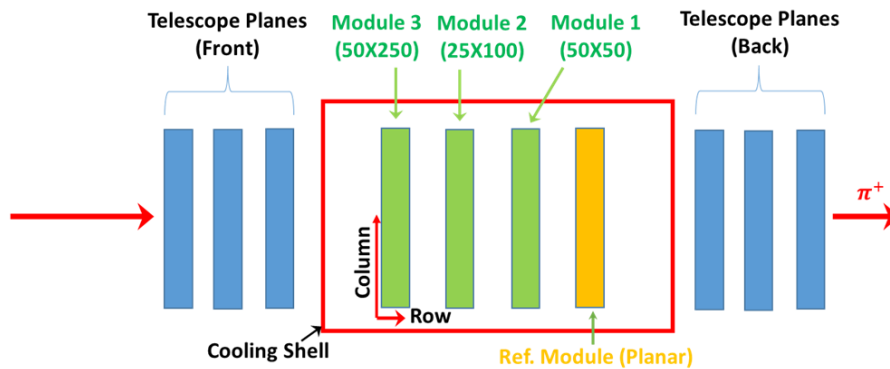


**Figure 6.18:** Schematic overview of the ACONITE telescope with FE-I4 type pixel sensors.

The test-beam data collected by the data acquisition systems are normally stored in a packed binary format in order to reduce bandwidth and storage requirements. The first step in the reconstruction of the particle tracks is therefore to decode these data and to translate them into a more accessible format. The devices that have been used in the experiments produce zero-suppressed data, meaning only information about channels going above threshold is retained. A large amount of noise hits per readout trigger can multiply the amount of data the detector generates by a large factor. This can have an adverse effect on both the time needed to perform the reconstruction and the quality of the reconstructed tracks. The position of the particle passing through the detector is estimated from clusters, not from the individual hits. A

cluster is a group of one or more neighbouring hits that are assumed to have been caused by the same particle. Another physical challenge of cluster finding for small pitch pixelated sensors was the presence of grids, adapted around the active small-pitch pixel area to be compliant with FE-I4 readout. Charge leaking around the inactive-area, made it quite complex to make straight forward comparison between small-pitch pixel sensors to  $50 \times 250 \mu\text{m}^2$  pixel design. Tuning parameters on readout device have clear effect on hit efficiency since the lower threshold increase the signal detection probability but it also needs to be adjusted with combination of the proper threshold and ToT (Time of threshold, a parameter to define the accumulated charge collected over time) with a considerable noise level.

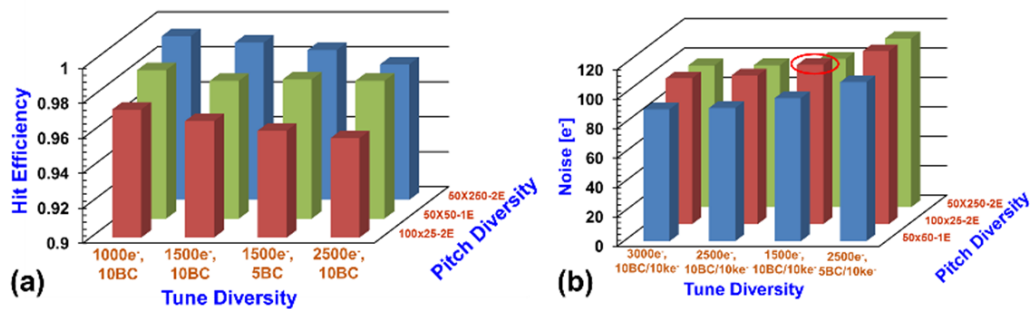


**Figure 6.19:** (a) Hit efficiency plot in dependence of FE-I4 tuning parameters. (b) Noise level as a function of combination tuning parameters.

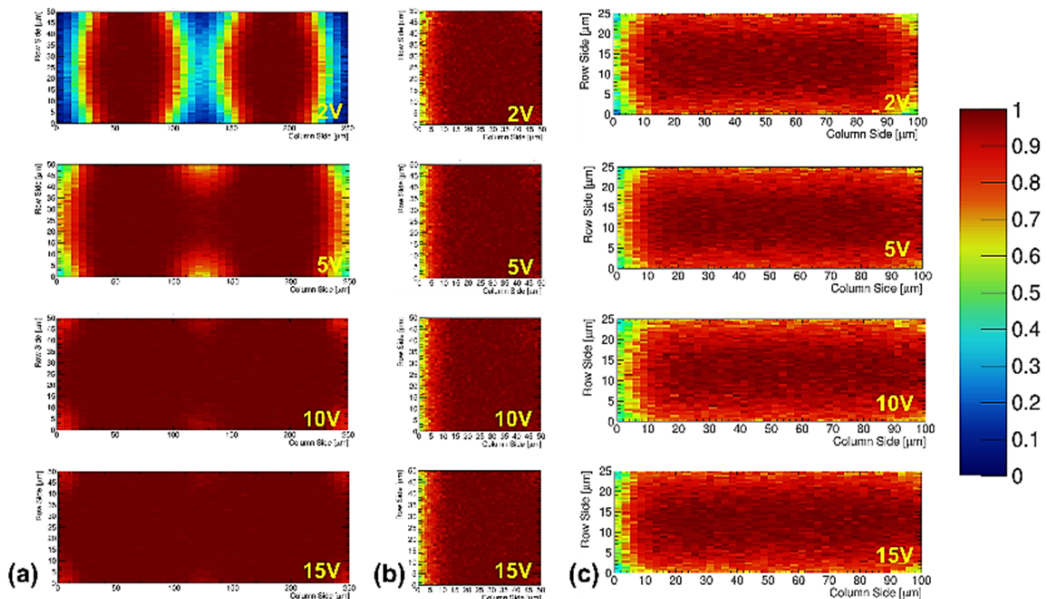


**Figure 6.20:** 2D Hit efficiency map for different pitches plotted as a function of applied reverse bias with tuning parameters: threshold 1.5ke<sup>-</sup>, TOT=10BC/10 ke<sup>-</sup>: (a)  $50 \times 250 \mu\text{m}^2$ , (b)  $50 \times 50 \mu\text{m}^2$ , and (c)  $25 \times 100 \mu\text{m}^2$ .

As example figure 6.19 (a) shows the hit efficiency probability of different fine pitches as function of FE-I4 tuning parameter. Lower level threshold increases the signal probability but it would also come in enhancing the noise. Figure 6.19(b) shows the noise level moderately lower up to 100e<sup>-</sup> only for the combination of threshold level 1500e<sup>-</sup> with ToT 10BC (10Ke<sup>-</sup>). As it was expected, the large capacitance contribution

from  $25 \times 100 \mu\text{m}^2$  pixel to larger noise input into readout system, denoted in red circle in figure 6.19(b).

In order to investigate the spatial dependence of the hit efficiency, 2D hit efficiency maps of the pixels were built. 2D hit efficiency map of all the candidates is reported in figure 6.20. As it could be seen at small-pitch sensors were fully depleted at 2V reverse bias, whereas  $50 \times 250 \mu\text{m}^2$  sensors required around 10V to have 100% hit efficiency. As figure 6.18 already demonstrates the modules were placed as orthogonal to beam plane, the charge introduced had to pass through columnar dead region, needed to diffuse first from the column to depleted zone, that would require stronger electric field at larger bias. For this reason, the sensor with  $50 \times 250 \mu\text{m}^2$  pitch that remains partially depleted condition at lower voltage  $\sim 2\text{V}$ , showed lower charge collection. A  $\pm 10\text{-}25^\circ$   $\epsilon$  rotation to conventional  $50 \times 250 \mu\text{m}^2$  IBL pixel sensors would help to overcome the charge particle passing through columnar dead region and increase the hit efficiency in smaller reverse bias [158], which should be an interesting study in future test beam campaign. That's instead confirms that the newer small and thin pixel sensors is less susceptible to  $\epsilon$  rotation.

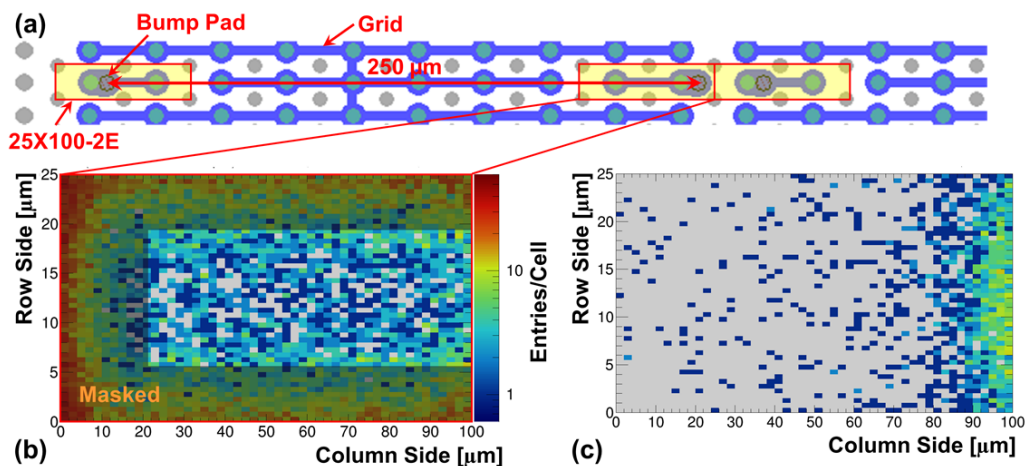


**Figure 6.21:** (a) layout schematic of  $25 \times 100\text{-}2\text{E} \mu\text{m}^2$  adopted to FE-I4 compliant pixel design. (b) 2D Hit efficiency map for  $25 \times 100\text{-}2\text{E} \mu\text{m}^2$  pitch at 10V reverse bias with tuning parameters: threshold  $1.5\text{ke}^-$ ,  $\text{TOT}=10\text{BC}/10 \text{ke}^-$ . Grey zone is the applied mask to evaluate the real charge hit in active pixel without leaking convolution from neighbouring grids, (c) The charge sharing within neighbouring  $25 \times 100\text{-}2\text{E} \mu\text{m}^2$  fine pitches only after the mask applied.

It is also worth to note that figure 6.20 (b) and (c) show inefficient edge hits at the edges for the small pitch of  $25 \times 100 \mu\text{m}^2$ , which could be anticipated from a complex cluster definition due to the presence of grid (figure 6.20(a)) in neighbouring cells. Charge sharing is important feature of pixel detector as it is directly related to tracking resolution and radiation hardness. The generated signal of a track going through a sensor can be shared between neighbouring cells. High charge sharing results in better tracking resolution as the track position can be more precisely determined. On the other hand, less signal will be available to each of the hit pixel cells, decreasing the probability to go above the comparator threshold and therefore

being registered. It is well known that charge collection efficiency decreases under radiation exposure. Hence it is desirable to minimize the charge sharing for detectors running in a high radiation environment, such as ATLAS, in order to maintain the high efficiency. Soon as the mask applied to the known leaking boundary, the charge sharing was reduced to a significant order, as it could be seen from figure 6.21(c).

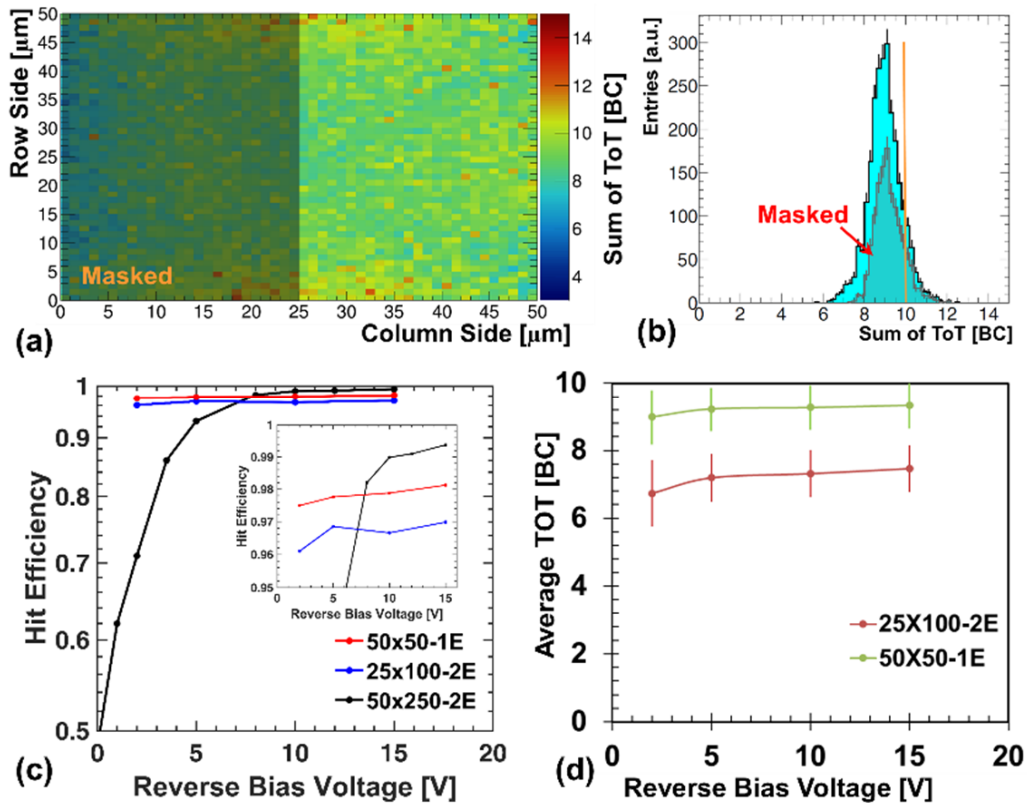


**Figure 6.22:** (a) 2D hit map of  $25 \times 100$ -2E  $\mu\text{m}^2$  pitch adopted to FE-I4 compliant pixel design at 10V reverse bias. Grey inset shows the mask applied for hit efficiency calculation to avoid the charge leaking. (b) Landau distribution of same pitch with tuning parameters: threshold  $1.5\text{ke}^-$ ,  $\text{TOT}=10\text{BC}/10\text{ke}^-$ . (c) Comparative hit efficiency plot with pitch diversity as a function of reverse bias voltage. (d) Detector charge response in term of TOT as a function of reverse bias voltage, calibrated in  $10\text{ke}^-$ .

Similar conditions are valid in the FE-I4 pixel sensors of  $50 \times 50\ \mu\text{m}^2$  fine pitch. The overall hit efficiency is needed to calculate from tracks passing through the device, excluding tracks passing grid. Considering the FE-I4 pixel design of  $50 \times 50$ -1E  $\mu\text{m}^2$  fine pitch adopted in 3DSS-6 layout another mask is applied, as could be found in figure 6.22 (a). The corresponding Landau charge distribution is reported in figure 6.22(b). As expected small-pitch design act to collect cent percent charge soon as they become fully depleted at around 2V (figure 6.22(c)). Noisy pixels are flagged and eliminated from this important study for 3D devices of the charge response. The sum of charge build up on the capacitors of preamplifiers in the channels of a cluster should be proportional to the energy loss of particle. The distribution of the sum of the time-over-threshold values should roughly show the distribution of energy losses in the sensitive area of detector. In 3D devices, this distribution differs from the distribution

in a planar device due to tracks passing through the electrodes, which are not fully sensitive due to the columnar dead area. As an example figure 6.22 (d) is showing the detector response as a function of reverse bias applied. The expected  $\sim 8.7 \text{ ke}^-$  is clearly achieved for  $50 \times 50\text{-}1\text{E} \mu\text{m}^2$  fine pitch since the fully depleted volume achieved for 2V reverse bias. The pixel  $25 \times 100\text{-}2\text{E} \mu\text{m}^2$  fine pitch instead shows relatively lower charge collection that can be anticipated from error of masked resolved extrapolated Landau distribution of deposited energy in the sensor and alignment error among modules placed physically during campaign.

### 6.4.2 After Irradiation

Different irradiation campaigns were made on test structures as well as in strip sensors of 3DSS-6 production to get the clear understanding of sensor performance to be operated in highly irradiative environment. The relevant primary results are discussed in the following sections.

#### X-ray Irradiation

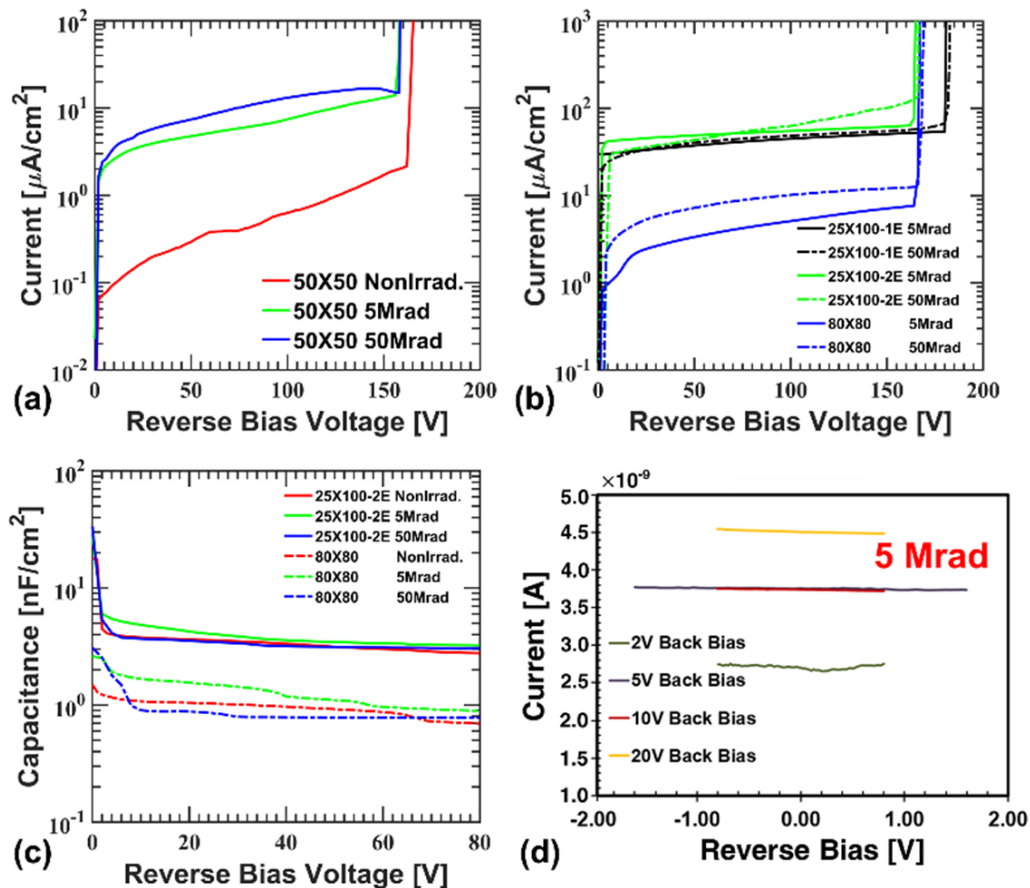


**Figure 6.23:** Electrical characteristics of strip sensors of  $130\text{-}\mu\text{m}$  active thickness without poly-cap (W82): (a) I-V curves of  $50 \times 50 \mu\text{m}^2$  pixel size before and after irradiation at different TIDs (b) I-V curves of different pixel geometries at different TIDs, and (c) C-V curves of different pixel geometries before and after irradiation at different TIDs. (d) Interstrip current measured as a function different back bias reference for a strip sensor of  $50 \times 50 \mu\text{m}^2$  pitch.

In 3D sensors from previous productions at FBK, carried out with the double-sided process approach, the breakdown voltage values were found to be largely dependent on the properties of the Si/SiO<sub>2</sub> interface, and particularly the oxide charge and interface state densities. In order to assess this aspect for the new technology, two sets of strip sensors including three different small-pitch designs, i.e., 50×50 μm<sup>2</sup>, 25×100-1E μm<sup>2</sup>, and 25×100-2E μm<sup>2</sup>, and one large pitch design (80×80), were irradiated with 50-keV X-rays at the Rutherford Appleton Laboratory (UK) to two Total Ionizing Doses (TIDs): 5 Mrad(Si) and 50 Mrad(Si). RAL owns Seifert RP149 X-ray system with tungsten source that could emit 3000W (up to 50mA and 60kV) accelerating electron. During irradiation, devices were not biased. Since, there has also been no deliberate cooling system, the sensors irradiated at higher TID would have experienced self-annealing effect.

Electrical tests were performed on a significant fraction of strips in each sensor. Figure 6.23(a) shows the I-V curves of one strip in a 50×50 μm<sup>2</sup> sensor from W82 (130-μm active thickness, without poly-cap) in different conditions: before irradiation, after 5 Mrad(Si), and after 50 Mrad(Si). It can be seen that X-ray irradiation caused a sizable increase of the leakage current, due to surface generation, but only minor changes in the breakdown voltage. Figure 6.23(b) shows the I-V curves for different designs at different TIDs. Also in this case, negligible differences in the breakdown voltage are observed. However, it is possible to appreciate the much higher impact of X-ray irradiation on the leakage current in case of designs with higher densities of columns.

The leakage current dependence on the column density can be explained by the surface generation contribution that originates from the depleted regions at the n<sup>+</sup>-column/p-spray junctions on the front side: the higher the number of columns, the larger the effective depleted perimeter, the larger the current. On the contrary, the weak dependence of the breakdown voltage on the irradiation is less obvious. Although direct measurements could not be performed, X-ray irradiation is expected to have caused a significant increase of oxide charge and interface state densities as compared to the pre-irradiation values. As a result, the breakdown voltage value should be increased if breakdown occurs at the surface on the front side. Conversely, the minor changes observed in the breakdown voltage after irradiation suggest this is not the case, and that a different mechanism, independent of surface damage, limits the breakdown voltage, most likely due to the high electric field at the n-column tips. Figure 2.23 (c) shows the C-V curves for different designs at different TIDs. As expected, the capacitance is much higher for the design with higher column density. Moreover, X-ray irradiation seem to have a minor impact on the capacitance that is compatible with a prevalent contribution from the columnar electrodes rather than from the surface.

Finally, interstrip resistance measurements were performed to understand the stand of surface isolation property at such higher TID (Si). As an example figure 2.23

(d) shows the interstrip current measured for a strip sensor of  $50 \times 50 \mu\text{m}^2$  fine pitch. The important outcome of these tests is that the interstrip resistance remains very large (at least a few  $\text{G}\Omega$ ) even for the largest TID regardless of the specific design, as the summary of these investigations reports in table 6.3. This confirms the effectiveness of the p-spray layer in isolating the n-columns also in the presence of severe surface damage.

**Table 6.3:** Inter strip resistance as a function back bias, measured in UTN, for 3D strip sensors irradiated at RAL, UK with 50 keV X-rays. Reported interstrip resistance holds the error limit  $\pm 6.5\%$  in account of data fitting tolerance, measurement system inaccuracy, X-ray beam non-uniformity and the TID uncertainty involved in campaign. Here, device '1E' represents  $25 \times 100$ -1E  $\mu\text{m}^2$  fine pitch, '2E' represents  $25 \times 100$ -2E  $\mu\text{m}^2$  fine pitch, '50' represents  $50 \times 50 \mu\text{m}^2$  fine pitch and '80' represents  $80 \times 80 \mu\text{m}^2$  fine pitch.

Device ID	Back Bias [V]	TID (Si) [Mrad]	Inter Strip Resistance [ $\text{G}\Omega$ ]
ST25_1E	2	5	$100.00 \pm 6.50$
	5		$50.00 \pm 0.33$
	10		$10.00 \pm 0.65$
	20		$3.33 \pm 0.22$
ST24_2E	2		$5.00 \pm 0.33$
	5		$1.00 \pm 0.07$
	10		$0.25 \pm 0.02$
	20		$2.50 \pm 0.16$
ST9_50	2		$33.33 \pm 2.17$
	5		$100.00 \pm 6.50$
	10		$50.00 \pm 3.25$
	20		$25.00 \pm 1.63$
ST17_80	5		$100.00 \pm 6.50$
	10		$11.11 \pm 0.72$
	20		$50.00 \pm 3.25$
ST3_1E	2		50
	5	$5.00 \pm 0.33$	
	10	$3.33 \pm 0.22$	
	20	$3.33 \pm 0.22$	
ST12_2E	2	$3.33 \pm 0.22$	
	10	$2.50 \pm 0.16$	
	20	$2.50 \pm 0.16$	
ST21_50	2	$1.00 \pm 0.07$	
	5	$0.16 \pm 0.01$	
	10	$5.00 \pm 0.33$	
	20	$14.29 \pm 0.93$	
ST5_80	2	$0.03 \pm 0.01$	
	5	$0.33 \pm 0.02$	
	10	$5.00 \pm 0.33$	
	20	$10.00 \pm 0.65$	

### Y-ray Irradiation

A Few FE14 type diodes from this new thin and small pitch batch, 3DSS-6 were irradiated with  $\gamma$ -rays at front side at a nominal dose of 5 and 50 Mrad(Si), along with some MOS capacitors from the same wafer. Irradiation was performed at the Sandia Gamma Irradiation Facility (Albuquerque, USA) by using a planar array of Cobalt-60 sources providing uniform exposure at a rate up to approximately 1000 rad per second.

The uncertainty on the measurement would  $\pm 5\%$ . During irradiation all type of devices were unbiased. The oxide charge density yielded from C-V measurement on planar like MOS test structures,  $N_{ox} \sim 6.4 \times 10^{11} \text{ cm}^{-2}$  for 5 Mrad(Si) and  $N_{ox} \sim 6.7 \times 10^{11} \text{ cm}^{-2}$  for 50 Mrad(Si). Considering the non-irradiation condition of W82 (the oxide charge density is  $N_{ox} \sim 1.2 \times 10^{10} \text{ cm}^{-2}$ )  $N_{ox}$  has enhanced almost 50 times higher for both doses.

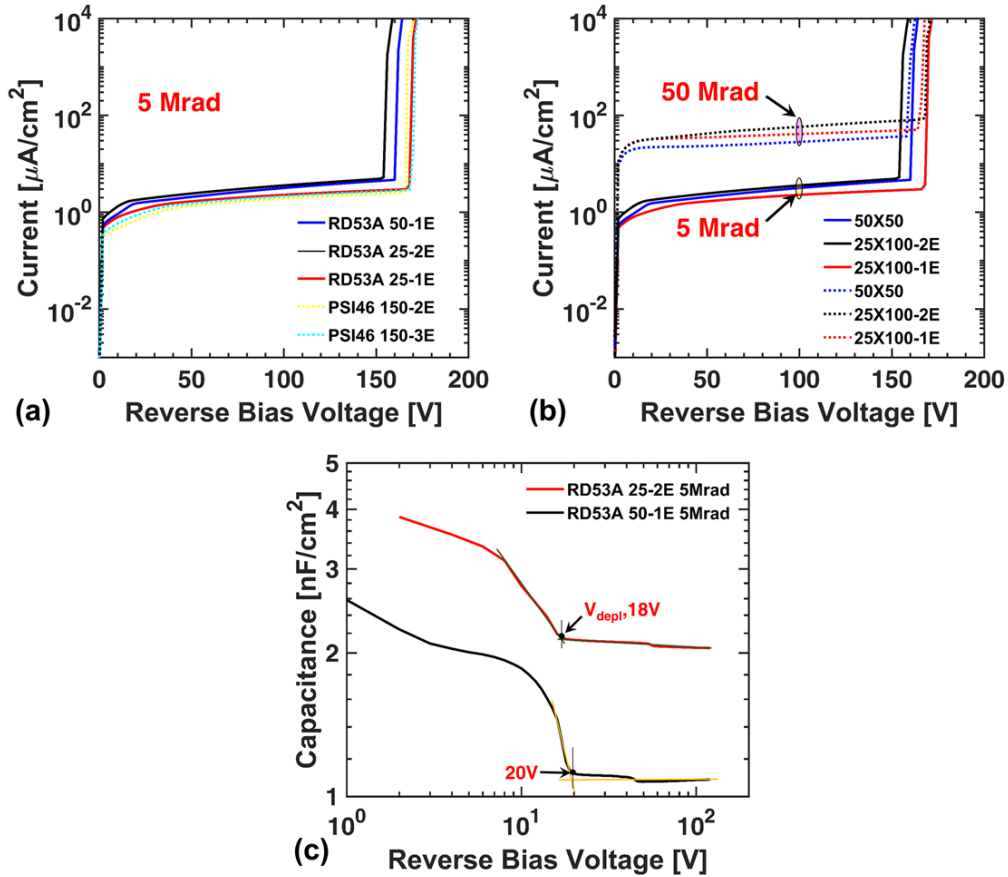


**Figure 6.24:** Electrical characteristics of thin 3D diodes of 130- $\mu\text{m}$  active thickness without poly-cap (W82) and with poly-cap (W76) measured in UTN at room temperature: **(a)** I-V curves of 3D diodes of different geometries irradiated with 5 Mrad(Si) Gamma **(b)** I-V curves of small-pitch 3D diodes irradiated with 5 and 50 Mrad(Si) Gamma, **(c)** C-V curves of small-pitch 3D diodes with 5 Mrad(Si) Gamma and measured with 1 KHz signal (100mV).

Data were measured in both UTN and UNM facility. In UTN, the measurement were performed using the suitable combination of Keithley 2410 source-measure unit, HP4145B semiconductor parameter analyzer and HP4284A LCR meter and the results are discussed here still hold the same system error margin mentioned in section 4.3. As an example figure 6.24(a) shows the I-V curves shows the measurement made at UTN at room temperature of 3D diode of different inter-electrode distances, irradiated with 5 Mrad(Si). The leakage current is increased almost 10 times higher than non-irradiated condition, which could be anticipated from the surface damage made from campaign. The breakdown voltage,  $V_{bd}$  remains in around 160V as it was in non-irradiated condition, which indicates the device breakdown is mostly dominated by the high electric field present at the junction column

tip than at the surface [146]. Figure 6.24(b) shows the I-V curves of fine pitches, irradiated at 5 and 50 Mrad(Si). The leakage current shows logarithmic linear dependence on TIDs. Even though the oxide charge remained almost constant for both TID campaigns, bulk type damage made from  $\gamma$ -rays should be higher for higher TID. This helps to understand the increasing leakage current. C-V measurements made in UTN is showing the clear dependence of bulk damage effect on the irradiated devices. Figure 6.24 (c) reports the full depletion,  $V_{\text{depl}}$ , arrival for fine pitches at around 20V for 5 Mrad (Si) Gamma campaign, a later arrival in comparison to the relevant candidates of X-ray campaign. Smaller inter-electrode distance in  $25 \times 100 \mu\text{m}^2$  pitch diode helps to achieve the full depletion voltage,  $V_{\text{depl}}$ , earlier than  $50 \times 50 \mu\text{m}^2$  pitch as it could found from the same figure.

Table 6.4 summarizes the most important data for all these samples: the leakage current density at full depletion ( $J_{\text{lk}}$ ) condition was taken at 50V reverse bias, the depletion voltage ( $V_{\text{depl}}$ ), and the breakdown voltage ( $V_{\text{bd}}$ ) with associating the error limit. As already described, due to the lower effect of surface induced damage, there has been no significant improvement on breakdown voltage to any device reported here after  $\gamma$ -rays irradiation.

**Table 6.4:** Summary of the electrical measurements of 3D diodes irradiated with  $\gamma$ -rays at a nominal dose of 5 and 50 Mrad(Si), measured at UTN at  $-$ room temperature. Here 50-1E means  $50 \times 50 \mu\text{m}^2$  pitch, 25-2E means  $25 \times 100$  -2E  $\mu\text{m}^2$  pitch, CMS-2E denotes  $150 \times 100$  -2E  $\mu\text{m}^2$  pitch and CMS-3E denotes  $150 \times 100$  -3E  $\mu\text{m}^2$  pitch.

Irradiation/Dose	Device ID	$J_{\text{lk}}$ at -50V [ $\mu\text{A}/\text{cm}^2$ ]	$V_{\text{depl}}$ [V]	$V_{\text{bd}}$ [V]
5 Mrad (Si)	W76-D210-CMS-2E	1.35 $\pm$ 0.39	47 $\pm$ 1	166 $\pm$ 2
	W76-D211-25-1E	1.68 $\pm$ 0.39	34 $\pm$ 2	166 $\pm$ 2
	W76-D25-50-1E	2.08 $\pm$ 0.39	20 $\pm$ 2	162 $\pm$ 2
	W76-D40-25-2E	2.44 $\pm$ 0.39	18 $\pm$ 2	154 $\pm$ 2
	W76-D204-CMS-3E	1.51 $\pm$ 0.39	34 $\pm$ 2	170 $\pm$ 2
	W76-D502-50-1E	1.89 $\pm$ 0.39	20 $\pm$ 2	162 $\pm$ 2
	W76-D194-25-2E	2.53 $\pm$ 0.39	16 $\pm$ 2	154 $\pm$ 2
50 Mrad (Si)	W76-D26-50-1E	23.36 $\pm$ 0.45	82 $\pm$ 2	160 $\pm$ 2
	W76-D196-25-2E	42.17 $\pm$ 0.51	64 $\pm$ 2	168 $\pm$ 2
	W76-D195-50-1E	35.11 $\pm$ 0.49	86 $\pm$ 2	166 $\pm$ 2
	W76-D205-CMS-2E	37.22 $\pm$ 0.50	96 $\pm$ 2	170 $\pm$ 2
	W76-D60-25-2E	15.47 $\pm$ 0.43	68 $\pm$ 2	158 $\pm$ 2
	W76-D208-25-1E	33.79 $\pm$ 0.49	76 $\pm$ 2	180 $\pm$ 2
	W76-D198-CMS-3E	37.04 $\pm$ 0.50	88 $\pm$ 2	174 $\pm$ 2
	W76-D501-50-1E	27.81 $\pm$ 0.47	76 $\pm$ 2	164 $\pm$ 2

In UNM facility, both I-V and C-V measurements were made with dry nitrogen to avoid the humidity effects. More details on setup can be found in section 4.3. I-V measurements were performed at different temperatures: 20°C, 5°C to -10°C. As an example, figure 6.25 (a) shows the temperature dependent Arrhenius plots of  $50 \times 50 \mu\text{m}^2$  pitch like 3D diodes at different TIDs where the current density values measured

at different temperatures at 50 V bias (fully depleted) are shown. They are compared to those obtained by scaling the values measured at 5°C ( $T_R=278.15$  K), the current operating temperature of LHC according to the SRH model of equation 2.16. The agreement between measurements and calculations is very good for the sample irradiated with 5 Mrad (Si) that anticipates the evidence of a dominant current contribution from thermal excitation even at high voltage, close to breakdown. Contrary, it is showing the measurement data of 50 Mrad(Si) campaign outlying from the SRH prediction (red-circled insets in figure 6.25(a)) that indicates the leakage current is dominating by bulk doping modification made at such higher TID.

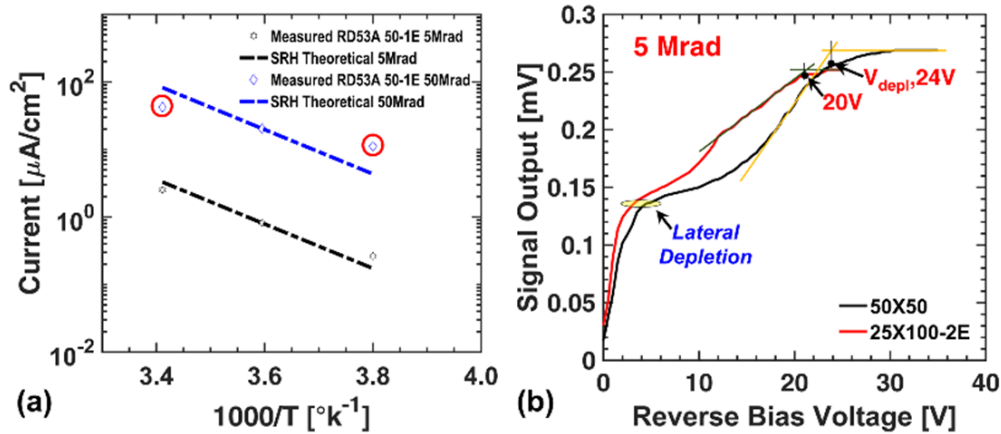


**Figure 6.25:** UNM measurements: (a) Arrhenius plot comparing measured and calculated values of leakage current at 50 V and their evolution with temperature of  $50 \times 50 \mu\text{m}^2$  pitch 3D diodes. (b) Output signal in response to laser stimulation as a function of reverse bias of small-pitch 3D diodes of different geometries, irradiated with 5 Mrad(Si) TID, measured at  $-10^{\circ}\text{C}$ .

**Table 6.5:** Summary of the electrical measurements of 3D diodes irradiated with Y-rays at a nominal dose of 5 Mrad(Si) and measured at UNM at  $-10^{\circ}\text{C}$ . Here 50-1E means  $50 \times 50 \mu\text{m}^2$  pitch, and 25-2E means  $25 \times 100$  -2E  $\mu\text{m}^2$  pitch.  $V_{bd}^*$  is denoting breakdown voltage before irradiation.

Irradiation/Dose	Device ID	$J_{lk}$ at -50V [ $\mu\text{A}/\text{cm}^2$ ]	$V_{depl}$ [V]	$V_{bd}$ [V]	$V_{bd}^*$ [V]
5 Mrad (Si)	W76-D36-50-1E	$0.26 \pm 0.39$	$24 \pm 1$	$148 \pm 1$	$148 \pm 1$
	W76-D86-50-1E	$0.19 \pm 0.39$	$21 \pm 1$	$165 \pm 1$	$150 \pm 1$
	W76-D50-25-2E	$0.25 \pm 0.39$	$25 \pm 1$	$153 \pm 1$	$160 \pm 1$
50 Mrad (Si)	W76-D37-50-1E	$11.14 \pm 0.42$	n.a.	$150 \pm 1$	$150 \pm 1$
	W76-D90-50-1E	$10.67 \pm 0.42$	n.a.	$150 \pm 1$	$150 \pm 1$
	W76-D206-25-2E	$5.94 \pm 0.40$	n.a.	$156 \pm 1$	$157 \pm 1$

The output signal from laser excitation as a function of reverse bias in the 3D diodes of two different small pitch dimensions in figure 6.25(b), measured at UNM at  $-10^{\circ}\text{C}$ . A clear saturation of the curves can be observed at reverse voltage 20V order of 20 V, an evidence of full depletion,  $V_{depl}$ . Interesting two stages of the depletions are there: laterally inter-column depletion and the depletion from junction column tip to back side [32]. In both kinds of depletion for  $25 \times 100 \mu\text{m}^2$  pitch sensors arrived earlier for having the lower inter-electrode distances. Table 6.5 summarizes the most important data for all small pitch sensors measured in UNM at  $-10^{\circ}\text{C}$ . For the gamma

irradiated devices at 50 Mrad (Si), spatial resolved LASER test was made at reverse bias up to 40V, which was yet too short to reach the saturation plateau. So, the full depletion voltage,  $V_{\text{depl}}$ , was not possible to estimate (denoted as 'n.a.' in table 6.5). However, it is still worth to find that the breakdown voltage remains almost unchanged at this larger TID, which is again implicating the fact that the  $V_{\text{bd}}$  is actually less affected through the surface damage.

One interesting observation here is also that  $V_{\text{depl}}$  is  $\sim 20\text{V}$  for the devices that are irradiated at 5 Mrad (Si) Gamma dose. This value is way too high in comparison to the campaign made for the old double-sided modified technology (DTC5) at 100 Mrad (Si) ( $V_{\text{depl}}$  arrived only at  $\sim 10\text{V}$  only, although the inter-electrode distance was much larger) [viz., Chapter 4]. To understand this issue qualitatively, it would be worth to relook at the device structure in these two batches. In DTC5, the wafer is of highly resistive float zone wafer only, whereas this thin sensor is of highly resistive float zone (FZ) wafer (later thinned to  $\sim 100\ \mu\text{m}$ ) directly bonded with  $500\ \mu\text{m}$  thick low resistive Czocharski (CZ) handle wafer. Intrinsically, Czocharski wafer is enriched with oxygen that could have diffused to FZ wafer after several high thermal treatments made during the wafer fabrication and device processing, and thus can change FZ impurity level in comparison to DTC5 batch. Gamma rays can introduce defects at the SiSi interface and bulk damage in addition to the conventional surface damage at the upper surface. These defects can influence the quantum tunneling process of charges from handle layer to active layer and modulate the effective doping concentration. Aside this, oxygen enriched Si substrate will host vacancy-oxygen (VO) and interstitial-carbon-interstitial oxygen ( $\text{C}_i\text{O}_i$ ) complexes during bulk damage process, which should act differently than the irradiated intrinsic FZ Si. Moreover, uncontrolled temperature profile during gamma campaign could have added even more vacancy-oxygen complexes with elevated temperature scale [168]. A combined effect of all these facts have hindered the expectations. Further investigations with appropriate techniques, e.g., Deep Level Transient Spectroscopy (DLTS), could be made to quantify the traps and interface states in this thin batch production. Thinning the handle wafer and metal deposition at later stage, as aimed for HL-LHC final production, should improve the device performance.

### Neutron Irradiation

Several diodes from this first thin 3D batch production were irradiated with neutrons at JSI in the range from  $5 \times 10^{15}$  to  $2 \times 10^{16}$   $n_{\text{eq}}/\text{cm}^2$  and were then measured at UTN. The oxide charge density,  $N_{\text{ox}}$ , yielded from C-V measurement on planar like MOS test structures and the summary are reported in table 6.6. As it could be found from the table,  $N_{\text{ox}}$  increased 10 times higher for the nominal TID of 5.56 Mrad (Si) in comparison to non-irradiated condition. For the highest fluence,  $N_{\text{ox}}$  was even increased up to around 20 times more.

**Table 6.6:** Summary of the oxide charge density,  $N_{ox}$ , extracted from planar MOS capacitors, that were neutron irradiated in JSI and measured in UTN at different temperature reference.

Fluence [ $n_{eq}/cm^2$ ]	TID [Mrad (Si)]	Device ID	MOS Type	Applied Temperature	Oxide Charge [ $cm^2$ ]
$5 \times 10^{15}$	5.56	W82-TP30	Metal MOS	20°C	1.24E+12
				5°C	1.08E+12
				-10°C	1.41E+12
			Metal n-poly MOS	20°C	1.03E+12
				5°C	1.12E+12
$2 \times 10^{16}$	22.24	W82-TP31	Metal MOS	20°C	3.23E+12
				5°C	2.49E+12
				-10°C	1.53E+12
			Metal n-poly MOS	20°C	1.57E+12
				5°C	2.52E+12

Due to the unfortunate mechanical stress made during wire bonding of these test samples, required for experimental setup, all diodes irradiated at  $2 \times 10^{16} n_{eq}/cm^2$  fluence and the maximum quantity of  $1 \times 10^{16} n_{eq}/cm^2$  fluence become non-functional. From the I-V curves measured at  $-10^\circ C$  of small-pitch thin 3D diodes irradiated at  $5 \times 10^{15} n_{eq}/cm^2$  fluence, shown in figure 6.26 (a), it can be seen that irradiation induced a significant increase of the leakage current in comparison to non-irradiated condition (6.23(a)), as well as an increase of the breakdown voltage,  $V_{bd}$ , which reached up to 200 V. In UTN facility no dry air is available in the environmental chamber that would have an effect on the determination of breakdown voltage and the leakage current due to the high humidity (>80%) present at low temperature. Charges from the external sensor environment, including negative charges associated with humid air, travel along electric field lines that loop outside the sensor between the  $n^+$ - and  $p^+$ -electrodes to the  $SiO_2$  layer, until groups of charges aggregate around electrodes of opposite sign [123]. This can increase the magnitude of the electric field around the electrodes and potentially cause localized breakdown to occur [165]. The silicon oxide layer on the sensor can also induce a thin accumulation layer of negative charges from the environment which compensates for some of the positive charges within the  $SiO_2$ . Continuing to increase negative charges along the oxide surface can cause instabilities in the leakage current and eventually lead to surface depletion, thereby increasing the total leakage current of the sensor [165].

Bulk traps made during this high fluence irradiation entrap the charge carriers and consequently lead to act on impact ionizing breakdown to be delayed. The same phenomenon was also observed at the largest fluence that could be tested ( $1 \times 10^{16} n_{eq}/cm^2$ ) as it could be seen in figure 6.23 (b), where the leakage current density and breakdown voltage for  $25 \times 100 \mu m^2$  small-pitch diodes increased. A relatively large damage constant rate ( $\alpha$ ) for same small pitch irradiated with  $5 \times 10^{15} n_{eq}/cm^2$  fluence reports  $(5.19 \pm 0.68) \times 10^{-17} A/cm$  at 120V reverse bias reference, which anticipates a possible occurrence of impact ionization effect at lower bias voltage. The estimated  $\alpha$  at the same bias of small pitch devices irradiated at  $1 \times 10^{16} n_{eq}/cm^2$  fluence is

$(4.51 \pm 0.74) \times 10^{-17}$  A/cm, which indicates the device possibly experienced the onset of impact ionization at larger voltage because of larger  $V_{bd}$ .

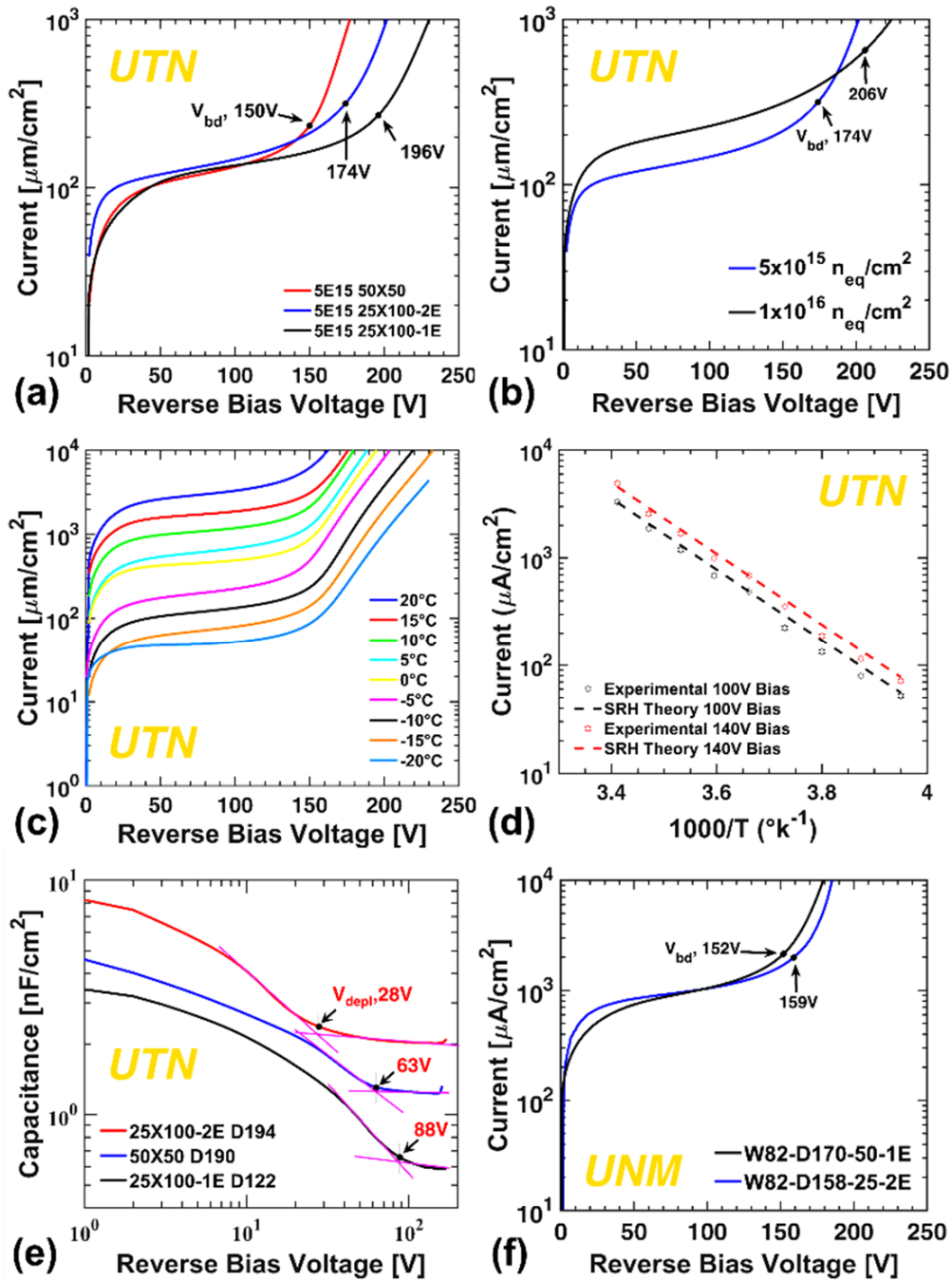


**Figure 6.26:** Ljubljana neutron irradiated samples measured at UTN: (a) I-V curves of 3D diodes of different small-pitch dimensions as a function of applied bias irradiated with  $5 \times 10^{15}$   $\text{n}_{\text{eq}}/\text{cm}^2$ , measured at  $-10^\circ\text{C}$  (b) I-V curves of  $25 \times 100$ -2E  $\mu\text{m}^2$  pitch 3D diodes as a function of applied bias irradiated with  $5 \times 10^{15}$  and  $1 \times 10^{16}$   $\text{n}_{\text{eq}}/\text{cm}^2$ , measured at  $-10^\circ\text{C}$ , (c) I-V curves of  $50 \times 50$ -1E  $\mu\text{m}^2$  pitch 3D diodes as a function of applied bias at different temperatures, irradiated at  $5 \times 10^{15}$   $\text{n}_{\text{eq}}/\text{cm}^2$ , (d) Arrhenius plot comparing measured and calculated values of leakage current at two bias voltages (100, and 140 V) and their evolution with temperature for the same diode of (c), and (e) C-V curves of 3D diodes of different small pitches, irradiated with  $5 \times 10^{15}$   $\text{n}_{\text{eq}}/\text{cm}^2$  in unbiased condition, measured at UTN at  $-10^\circ\text{C}$  and 1 kHz frequency. (f) I-V curves of  $50 \times 50$ -1E

and 25×100-2E pitch 3D diodes irradiated with neutrons at Sandia at  $5 \times 10^{15}$   $n_{eq}/cm^2$  and measured at UNM at  $-10^\circ C$ .

The current increases with temperature as expected for the 25×100  $\mu m^2$  small-pitch irradiated at  $1 \times 10^{16}$   $n_{eq}/cm^2$  fluence (figure 6.26(c)). The temperature dependence can be better appreciated from the Arrhenius plots of figure 6.26(d), where the current density values measured at different temperatures and at two bias voltages (100V and 140V) are compared to those obtained by scaling the values measured at  $0^\circ C$  ( $T_R=273.15$  K) to different temperatures according to the SRH model of equation 2.16, taking an account of effective bandgap,  $E=1.21$ eV [134]. The agreement between measurements and calculations is good, that anticipates the evidence of a dominant current contribution from thermal generation in the depleted bulk even at high voltage, close to breakdown.

Owing to the larger breakdown voltage, it was possible to reach full depletion within these devices: this can be seen from the C-V curves of figure 6.26(e), that also highlight the impact of the inter-electrode distance on the depletion voltage (the lowest value of  $\sim 28$ V is found for the 25×100-2E  $\mu m^2$  pitch device which has  $L \sim 28$   $\mu m$ ). Table 6.7 summarizes the most important data for all samples irradiated at JSI with at  $5 \times 10^{15}$   $n_{eq}/cm^2$  fluence. Both the leakage current density at full depletion ( $J_{lk}$ ) condition and the damage constant rate ( $\alpha$ ) is calculated at 140V reverse bias reference.

Interestingly, few alive 3D diodes irradiated at  $1 \times 10^{16}$   $n_{eq}/cm^2$  fluence show a smaller damage constant rate ( $\alpha$ ), less than  $4 \times 10^{-17}$  A/cm, than the samples reported in table 6.7 at same bias reference, which could be anticipated from either the smaller depletion volume at 140V or the self-annealing effect involved during the campaign at targeted larger irradiation fluence.

**Table 6.7:** Summary of the electrical measurements of 3D diodes irradiated with Neutron at JSI facility and measured at UTN at  $-10^\circ C$ . Here 50-1E means  $50 \times 50$   $\mu m^2$ , 25-1E means  $25 \times 100$  - 1E  $\mu m^2$  and 25-2E means  $25 \times 100$  -2E  $\mu m^2$  fine pitches.

Fluence [ $n_{eq}/cm^2$ ]	TID [Mrad(Si)]	Device ID	$J_{lk}$ at $-10^\circ C$ [ $\mu A/cm^2$ ]	$\alpha$ [ $10^{-17}$ A/cm]	$V_{depl}$ [V]	$V_{bd}$ [V]
$5 \times 10^{15}$	5.56	W82-D122-25-1E	218.93±0.97	5.65±1.84	88±1	196±2
		W82-D194-25-2E	256.84±1.08	6.64±0.98	28±1	174±2
		W82-D190-50-1E	189.98±0.88	6.90±0.95	63±1	150±2

It is not straightforward to understand the mechanisms leading to increased breakdown voltage in neutron irradiated samples. Although the considered fluences are large enough to cause a non-negligible increase of the oxide charge density, results obtained with  $\gamma$ -rays suggest the reason might be rather a bulk damage effect than a surface one. Bulk modification from neutron irradiation comes with two additional concurrent effects. One of them is bulk traps that entrap the charge carriers causing a sort of quenching effect increasing the breakdown voltage,  $V_{bd}$ . At the same time, the increased effective doping concentration in the bulk generates higher electric field, that might lead to early breakdown. The larger inter-electrode distance present

( $L \sim 51 \mu\text{m}$ ) in  $25 \times 100\text{-}1\text{E} \mu\text{m}^2$  pitch sensor experiences the higher breakdown driven by the bulk trap effect whereas  $50 \times 50 \mu\text{m}^2$  pitch and  $25 \times 100\text{-}2\text{E} \mu\text{m}^2$  pitch sensors experience the compromising effect upon geometrical dependence. However, the charge collection in  $25 \times 100\text{-}1\text{E} \mu\text{m}^2$  pitch will not be great because the generated charges will have to travel larger mean free path.

Another set of 3D diodes were neutron irradiated at pool-type reactor (hardness factor 0.73) of Sandia at  $5 \times 10^{15} \text{ n}_{\text{eq}}/\text{cm}^2$  (corresponding TID  $\sim 3 \text{ Mrad (Si)}$ ) and measured in UNM at  $-10^\circ\text{C}$ . Some of them were already re-irradiated at cumulative  $1 \times 10^{16} \text{ n}_{\text{eq}}/\text{cm}^2$  fluence (6 Mrad (Si)). As an example, figure 6.26 (f) reports I-V curves of  $25 \times 100\text{-}2\text{E} \mu\text{m}^2$  small-pitch 3D diodes. The leakage current density at reference bias voltage is larger than measured from the campaign made at JSI at same level fluences, an effect that is still under investigation.

**Table 6.8:** Summary of the electrical measurements of 3D diodes of  $50 \times 90 \mu\text{m}^2$  irradiated with Neutron at SANDIA facility and measured at UTN. Damage constant rate ( $\alpha$ ) is calculated at 140V bias reference.

Fluence [ $\text{n}_{\text{eq}}/\text{cm}^2$ ]	TID [Mrad (Si)]	Device ID	$J_{\text{lk}}$ [ $\mu\text{A}/\text{cm}^2$ ]	$\alpha$ [ $10^{-17} \text{ A}/\text{cm}$ ]	$V_{\text{depl}}$ [V]	$V_{\text{bd}}$ [V]
$5 \times 10^{15}$	3	W82-D153-50 $\times$ 90	120.09 $\pm$ 0.67	3.98 $\pm$ 0.98	56 $\pm$ 2	152 $\pm$ 2
		W82-D154-50 $\times$ 90	131.69 $\pm$ 0.71	4.14 $\pm$ 1.01	46 $\pm$ 2	152 $\pm$ 2
		W82-D155-50 $\times$ 90	132.02 $\pm$ 0.71	4.12 $\pm$ 0.91	50 $\pm$ 2	150 $\pm$ 2
		W82-D188-50 $\times$ 90	106.11 $\pm$ 0.63	4.24 $\pm$ 0.65	52 $\pm$ 2	138 $\pm$ 2
		W82-D503-50 $\times$ 90	137.45 $\pm$ 0.72	3.81 $\pm$ 1.72	44 $\pm$ 2	138 $\pm$ 2

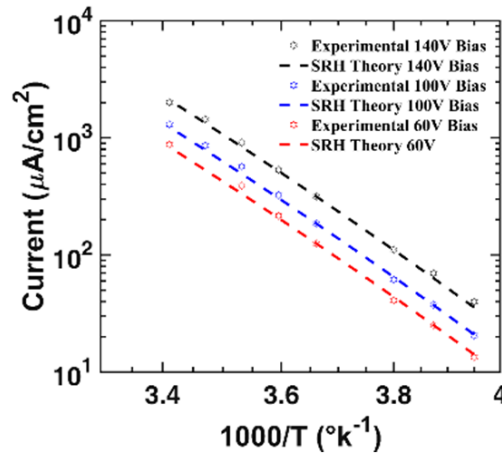


**Figure 6.27:** Arrhenius plot comparing measured at UTN at  $-10^\circ\text{C}$  and calculated values of leakage current at three depleted bias references (60V, 100V, and 140 V) and their evolution with temperature for the W82-D153-50 $\times$ 90 diode of  $50 \times 90 \mu\text{m}^2$  geometry of wafer 82.

A set of diodes of larger pitch of  $50 \times 90 \mu\text{m}^2$  was irradiated in the SANDIA neutron facility and measured in UTN facility at different temperatures varying from  $20^\circ\text{C}$  to  $-20^\circ\text{C}$ . The measurements summary is presented in table 6.8. Reported leakage current density ( $J_{\text{lk}}$ ), breakdown voltage ( $V_{\text{bd}}$ ) and full depletion voltage ( $V_{\text{depl}}$ ) in the table quoted from the measurements at  $-10^\circ\text{C}$ . The error limit reported here have considered all accountabilities: the error in instrumentation, beam non-uniformity, statistical inaccuracy. It worth to find that damage constant rate ( $\alpha$ ) is remained as it

was expected, well below  $4 \times 10^{-17} \text{A/cm}$ , showing the substrate damage as linearly proportional upon fluence.

As an example of the temperature dependence, figure 6.27 shows the Arrhenius behavior of diode W82-D153 of  $50 \times 90 \mu\text{m}^2$  pitch irradiated in Sandia with neutrons and measured in UTN facility. The good leakage current agreement on SRH prediction supports the fact these diodes are still experiencing the thermal generated carrier as the primary source. But it should stress that these diodes have inter-electrode distance almost twice than RD53A recommended small-pitch ( $50 \times 50\text{-}1\text{E}$  or  $25 \times 100\text{-}2\text{E} \mu\text{m}^2$ ), so they are less prone to impact ionization effects.

### Proton Irradiation

Few strip sensors were irradiated with 24 GeV/c protons in CERN Proton Synchrotron (PS) beam at  $1.72 \times 10^{16} \text{p/cm}^2$  and  $3.2 \times 10^{16} \text{p/cm}^2$  fluences. The theoretical relative hardness of the 24 GeV/c protons, which is the ratio of the NIEL factors of the 24 GeV/c protons to that of 1 MeV neutrons is approximately 0.6, that results in 1-MeV neutron equivalent fluences of  $1.02 \times 10^{16} \text{n}_{\text{eq}}/\text{cm}^2$  and  $1.92 \times 10^{16} \text{n}_{\text{eq}}/\text{cm}^2$ , respectively. Fluence measurement was made using aluminum foil having the same area as the strip geometry. The error of the fluence measurement could be estimated  $\pm 7\%$ .

Interstrip measurement was made on these irradiated sensors as a function of back bias voltage. The measurement was performed at room temperature. Table 6.9 reports the measurement summary for  $25 \times 100\text{-}2\text{E} \mu\text{m}^2$  and  $80 \times 80\text{-}1\text{E} \mu\text{m}^2$  small-pitch strip sensors made at  $\sim 1 \times 10^{16} \text{n}_{\text{eq}}/\text{cm}^2$  and  $\sim 2 \times 10^{16} \text{n}_{\text{eq}}/\text{cm}^2$ . The reported interstrip resistance values were found to be in range of  $\text{M}\Omega$  only. Although this value is pretty small, it should not be interpreted as a loss of isolation at the surface. In fact, despite the huge TID involved with these proton irradiations, as high as 504 Mrad(Si) and 938 Mrad (Si) at the two fluences, respectively, the surface damage alone does not justify the measured values, that are rather due to the very large leakage current originating at bulk affecting the measurement at room temperature.

**Table 6.9:** Summary on inter-strip resistance measurement made on CERN 24 GeV/c Proton at room temperature.

Strip-pixel Geometry w.r.t. Fluence type and Quantity	Back bias						$R_{\text{int}}$ [ $\text{M}\Omega$ ]
	-5V	-10V	-20V	-40V	-80V	-90V	
25X100_2E 1e16 Proton	0.20	0.20	0.50	2.00	2.50	3.33	
25X100_2E 2e16 Proton	0.10	0.11	0.25	1.00	-	-	
80um 1e16 Proton	0.33	0.50	0.33	-	-	2.50	
80um 2e16 Proton	0.50	0.50	0.50	-	-	2.50	

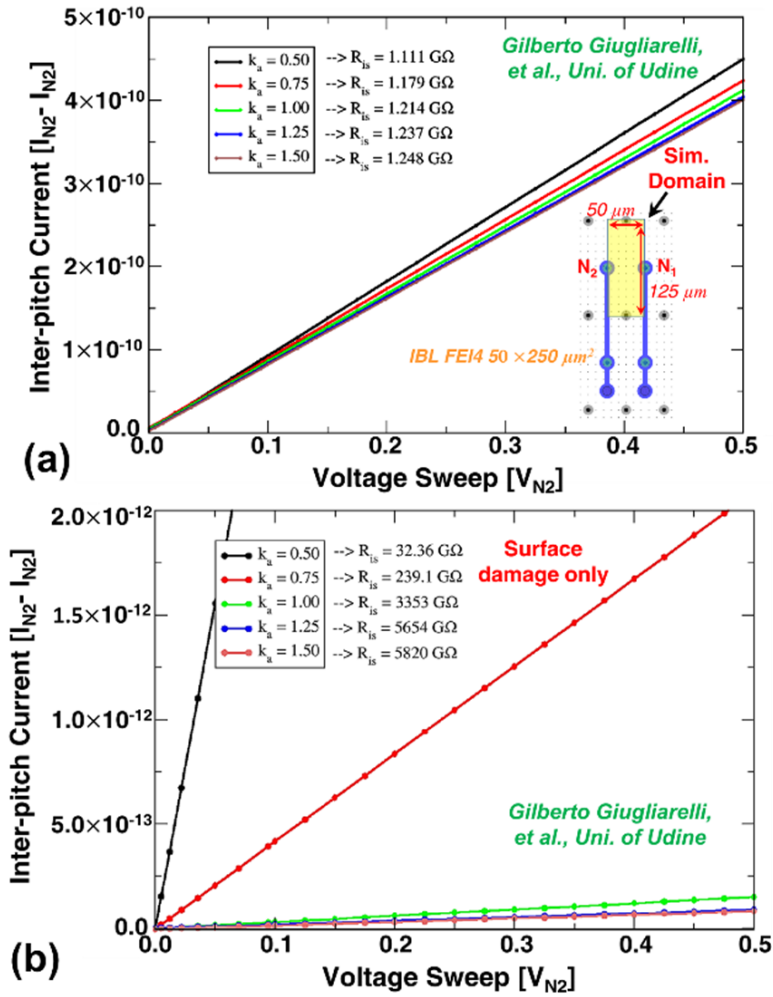


**Figure 6.28:** TCAD simulation for inter-strip resistance study made on IBL type FE14 50×250-2E μm<sup>2</sup> pitch in account of: **(a)** surface and bulk damage model, and **(b)** surface damage only. Simulation domain is highlighted in inset as yellow marked region.

A relevant surface isolation study with TCAD simulation was made considering both Perugia surface model and bulk damage associated models described in section 6.3.1 at  $5 \times 10^{15}$  n<sub>eq</sub>/cm<sup>2</sup> fluence. The study was performed at the University of Udine with reference to an IBL FE-14 pixel, biased at 200 V, but it is of more general validity. As it could be seen in figure 6.28(a), the simulated results suggest that after normalization to a full strip area, the inter-strip resistance would be in the range of a few MΩ only. Considering that the simulated fluence is one half of the smaller experimental one, the agreement is good enough. At the same time, when repeating the simulation without bulk damage, the result due to the surface damage alone is much larger, as can be seen in figure 6.28(b).

Several strips of each sensor were electrically characterized in University of Freiburg facility at -10°C. As an example, figure 6.29(a) shows the I-V curves measured in single strip keeping the neighbouring the strips floating. For both pitches of geometrical diversity the figure shows qualitatively higher leakage current for the higher irradiating fluence. Overall the breakdown voltage increased by ~100-150 V

with respect to the non-irradiated condition. The leakage current density is even higher than the results shown from neutron irradiation campaign, but a comparison cannot be made since with the neighbouring strips left floating. In this condition, the depletion volume is not well confined to the geometrical size of the strip. It is interesting to find that the breakdown voltage at the larger fluence ( $2 \times 10^{16} \text{ n}_{\text{eq}}/\text{cm}^2$ ) for both types of small pitches remains smaller than the lower one ( $1 \times 10^{16} \text{ n}_{\text{eq}}/\text{cm}^2$ ). It could be happening that irradiation at  $2 \times 10^{16} \text{ n}_{\text{eq}}/\text{cm}^2$  have made significant change in the effective doping concentration and the consequently leading them to have larger electric field at higher bias. The phenomenon would make those devices into earlier breakdown driven by onset impact ionization effects. As expected, the full depletion of the device irradiated at higher fluence requires higher bias due to the increased effective doping of the bulk. Figure 6.29(b) reports the C-V curves for the single strip of  $25 \times 100\text{-}2\text{E} \mu\text{m}^2$  fine pitch at two different fluences as a function of reverse bias, where it is evident that the sample irradiated at higher fluence requires larger voltage applied to be fully depleted.

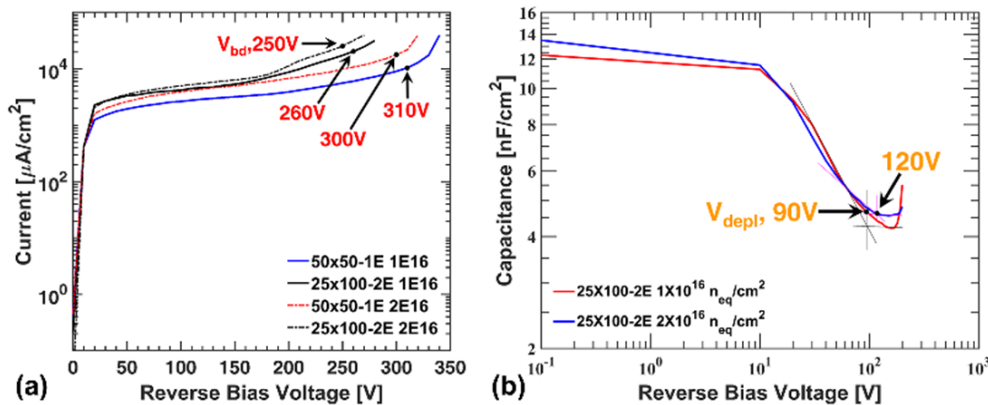


**Figure 6.29:** Electrical characterization of CERN 24GeV/c Proton irradiated strip sensors measured in University of Freiburg Germany: (a) I-V curves of single strip of  $50 \times 50\text{-}1\text{E} \mu\text{m}^2$  and  $25 \times 100\text{-}2\text{E} \mu\text{m}^2$  fine pitches as a function of bias at  $-10^\circ\text{C}$  at different fluencies, (b) C-V curves of single strip of  $25 \times 100\text{-}2\text{E} \mu\text{m}^2$  fine pitch as a function of bias at  $-10^\circ\text{C}$  at different fluencies, with 1kHz frequency. Full depletion voltage is evaluated using logC-logV domain at intersecting point of two fitted straight lines.

A set of 3D diodes and other test structures were irradiated with 800 MeV protons at LANCSE facility. A brief note on this facility and the corresponding proton irradiation uncertainty has been already discussed in section 4.3. Two target fluences were taken in account into this campaign:  $5 \times 10^{15} \text{ n}_{\text{eq}}/\text{cm}^2$  and  $1 \times 10^{16} \text{ n}_{\text{eq}}/\text{cm}^2$  but due to an unexpected non-uniform beam condition, the devices instead received  $1.3 \times 10^{16} \text{ n}_{\text{eq}}/\text{cm}^2$  (550 Mrad (Si)) and  $3.5 \times 10^{16} \text{ n}_{\text{eq}}/\text{cm}^2$  (1481 Mrad (Si)) fluence (equivalent dose) at the end. As an example, figure 6.30 shows the I-V behavior of 3D diodes of  $50 \times 50\text{-}1\text{E} \mu\text{m}^2$  dimension irradiated at both fluences and measured in UNM at  $-10^\circ\text{C}$ . This preliminary result corroborates the  $V_{\text{bd}}$  characteristics of the strip devices irradiated with 24 GeV/c proton at CERN. For the sample irradiated at  $1.3 \times 10^{16}$

$n_{eq}/cm^2$  fluence the improvement of the breakdown voltage up to  $\sim 80V$ . On the contrary, the  $V_{bd}$  for the device irradiated at  $3.5 \times 10^{16} n_{eq}/cm^2$  is smaller, and might be due to the significant increase of the effective doping concentration in the bulk, high electric field at the column tip.

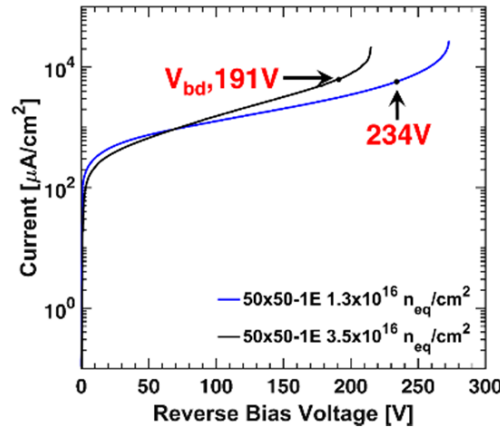


**Figure 6.30:** I-V curves of 3D diodes of  $50 \times 50\text{-}1E \mu m^2$  fine pitch irradiated with protons at  $1.3 \times 10^{16} n_{eq}/cm^2$  and  $3.5 \times 10^{16} n_{eq}/cm^2$ . Measurements were taken in UNM at  $-10^\circ C$

Calculated damage constant rate  $\alpha$  for diode irradiated at  $3.5 \times 10^{16} n_{eq}/cm^2$  is  $(15.63 \pm 3.05) \times 10^{-17} A/cm$  at applied 140 V, quite similar to the one estimated for the device of same fine pitch but irradiated at  $1.3 \times 10^{16} n_{eq}/cm^2$  fluence, that is  $(15.46 \pm 11.00) \times 10^{-17} A/cm$ . A possible explanation for this large values is the early onset of impact ionization effects. More insight into these phenomena should be gained by measuring a statistically significant sample and studying the temperature dependence of current.

HL-LHC compliant 3DSS first production at FBK came with good electrical yield, as it has been reported in this chapter so far. Measurements reported here for sensors show good agreement with TCAD simulation predictions in respect to both electrical and functional point of view. Even at the largest fluence taken into account for either neutron or proton irradiation campaign, the per column capacitance remains few 10s of fF and the leakage current density remains below 100nA at full depletion, that satisfies the target values set from the RD53 collaboration.

Although there are still several measurements to be performed, in particular charge collection efficiency tests for irradiated samples and annealing studies, it is still worth to affirm that the single-sided, small-pitch and thin 3D sensors are experimentally showing their design robustness to take the challenges at extreme irradiation environment of HL-LHC.

## 6.5 2<sup>nd</sup> Production of Small-pitch, Thin 3D Radiation Sensors at FBK

Increased luminosity requirements at foreseen HL-LHC come into play with the higher hit-rate capability, increased granularity, high irradiation tolerance, and reduced material budget. Most of these requirements benefit from having thinner active layers. Among the possible substrate options suitable for the fabrication of thin pixels like, SOI, epitaxial, or local thinning [159]. FBK first production of this 3D sensors came to choose the fabrication making on Si–Si Direct Wafer Bonded (DWB) wafers, which are obtained bonding together two different wafers: a high-resistivity (HR) Float Zone sensor wafer and a low-resistivity (LR) Czochralski handle wafer.

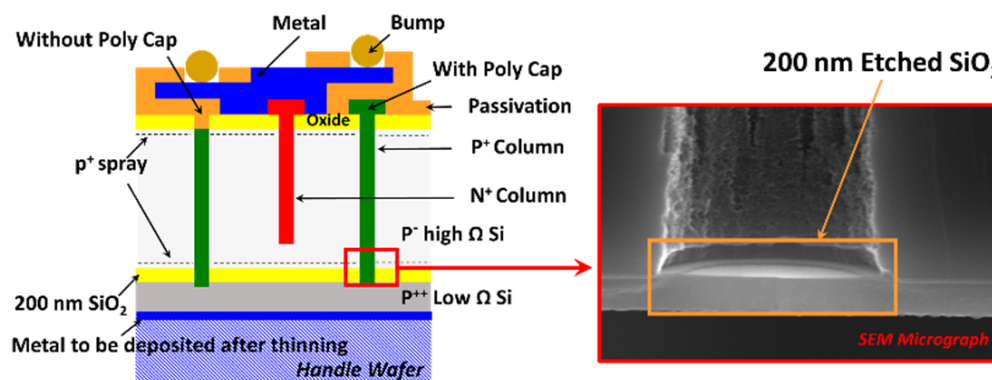


**Figure 6.31:** Schematic cross-section of the proposed thin 3D on SOI substrate. SEM micrograph of the bottom of a column etched by DRIE down, made at FBK.

Another alternative to be studied in the 2<sup>nd</sup> production will be SOI wafers, which differ from the Si–Si DWB one for the presence of a 200-nm thick buried SiO<sub>2</sub> layer in between the two silicon layers. One additional requirement for fabricating the 3D sensors on SOI based wafer is to etch columns (3D) through the bonding SiO<sub>2</sub> layer, so as to reach the low resistive handle wafer as it could be seen in figure 6.31. This step is not trivial, and dedicated tests have been performed at FBK to prove its feasibility. The inset SEM micrograph shows the sketch of the performed test, which consisted in etching columns all the way through active highly resistive layer. As it has already reported Boron diffusion made on the first production at FBK Si–Si DWB wafer from the back, resulted the effective active thickness reduced to ~10μm, the processing on SOI wafer would prevent the phenomenon.

The 2<sup>nd</sup> batch has the goal to confirm and improve the fabrication technology and to test new sensor designs. Therefore, a new layout was designed, that has already been submitted to FBK for production. A full wafer layout of this upcoming production is reported in figure 6.32 (a). The large area available on 6-inch wafers allowed accommodating a huge variety of sensors on the wafer layout while maintaining a wide safety margin around 1 cm from the wafer edge. The core of the wafer layout contains 5 pixel sensors compatible with the ATLAS FE-I4 and 26 pixel sensors compatible with the CMS PSI46 read-out chips (ROCs). Both these kinds

adopted new small pitch geometries aside the conventional pixel geometry:  $50 \times 250 \mu\text{m}^2$  of FE-14 and  $150 \times 100 \mu\text{m}^2$  of PSI46. The FE-14 and PSI46 compatible sensors with small pitches have the large inactive pixels within consecutive bump pads and they have been gridded and terminated to extra pads [150].

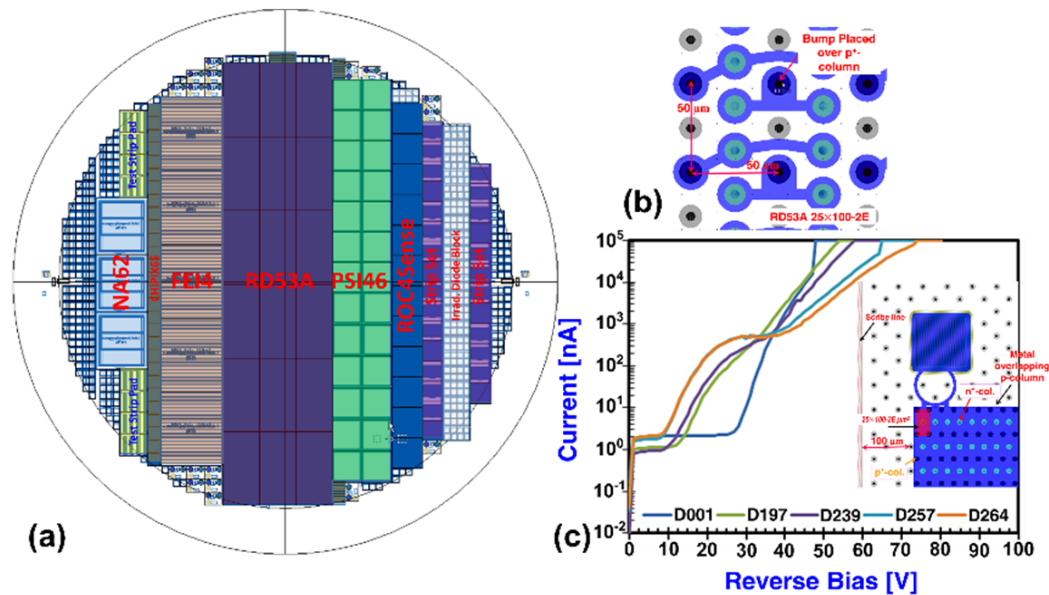


**Figure 6.32:** (a) Full wafer layout of upcoming 2<sup>nd</sup> batch production of small-pitch, thin 3D sensor at FBK. (b) Layout schematic of CHIPIX65 RD53A sensors of  $25 \times 100\text{-}2\text{E} \mu\text{m}^2$  fine pitch fabricated in 3DSS-6 batch placing bump over p<sup>+</sup>-column. (c) I-V curves of all W82 3D diodes of  $25 \times 100\text{-}2\text{E} \mu\text{m}^2$  fine pitch placing metal coverage over the entire diode active area, a mimic test structure of RD53A sensors of  $25 \times 100\text{-}2\text{E} \mu\text{m}^2$  fine pitch.

The batch is focused mainly accommodating the newer small pitch RD53A readout compatible design, that included 18 pixelated sensors of them having  $50 \times 50$ ,  $25 \times 100\text{-}2\text{E}$ , and  $25 \times 100\text{-}1\text{E} \mu\text{m}^2$  pitch diversity. RD53A readout is based on 65nm CMOS technology having  $192 \times 400$  pixels ( $2.36 \text{ cm}^2$ ) [108]. One of the biggest challenge was to adapt to the bump pad into the pixel sensor  $25 \times 100\text{-}2\text{E} \mu\text{m}^2$  pitch (figure 6.3(a)) for  $50 \mu\text{m}$  by  $50 \mu\text{m}$  square bump array. The space constraint led to adapt the placement of the bump pad and pixel interconnecting metal being overlapped with p<sup>+</sup>-column. In fact, this solution was already tried in the first 3D Si-Si DWB production on the CHIPIX65 [160] compatible pixel sensors that consist  $64 \times 64$  pixels ( $0.12 \text{ cm}^2$ ) having  $50 \mu\text{m}$  by  $50 \mu\text{m}$  square bump array, as it can be found in figure 6.32 (b). Actually, none of the sensors of this type having  $25 \times 100\text{-}2\text{E} \mu\text{m}^2$  pitch dimension were found to be working in all wafers processed at 3DSS-6 batch at FBK. Initial measurements were made shorting the pixel with temporary metal [32]. Any process induced point defect dependent on sensor area could lead the entire device to be nonfunctional [145]. To gain better insight into this issue all 3D diodes of W82 that have  $25 \times 100\text{-}2\text{E} \mu\text{m}^2$  fine pitch but covered with metal over the entire area (viz. figure 6.32 (c) inset) were measured, showing the same results. Since the probability of having defects for small area devices like 3D diodes is small [146], the phenomenon

of early breakdown ( $<10\text{V}$ , see figure 6.32 (c)) might have been instead caused from micro-discharge effects, as also suggested by the fact that these devices experienced irreversible dielectric burn-out at large voltage [7]. Due to the placement of the bump over the  $p^+$ -columns, the entire applied bias voltage has to drop across insulating layer in between. Such a dielectric layer was not optimized in the first batch, both in terms of composition and of thickness. An improved process recipe and a modified design were adopted for the 2<sup>nd</sup> batch production at FBK by optimally placing the bump inside the sub-pixel domain of  $25\times 100\text{-}2\text{E } \mu\text{m}^2$  fine pitch, as it is seen in figure 6.33(a). Even though this design kept the challenge of having the critical distance between bump pad to  $p^+$ -column while maintaining the state of art mask-alignment limit at FBK.

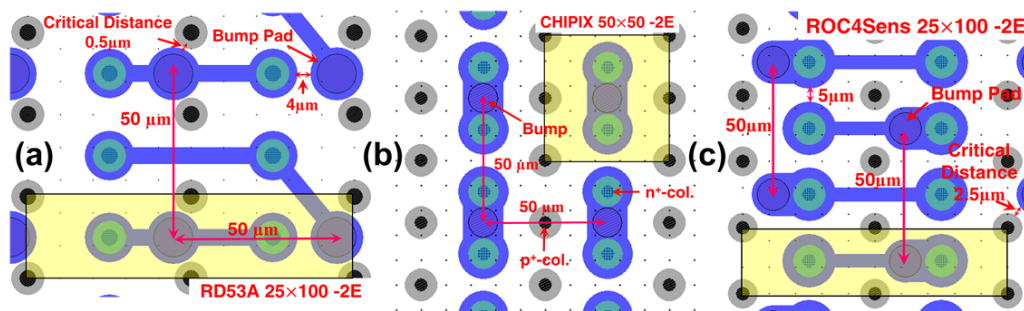


**Figure 6.33:** (a) Improved design of RD53A sensors of  $25\times 100\text{-}2\text{E } \mu\text{m}^2$  fine pitch. (b) Layout of CHIPIX65 sensors with  $25\times 100\text{-}2\text{E } \mu\text{m}^2$  fine pitch. (c) Layout of ROC4Sens sensors with  $25\times 100\text{-}2\text{E } \mu\text{m}^2$  fine pitch having  $50 \mu\text{m}$  by  $50 \mu\text{m}$  staggered bump pad.

A total of 28 CHIPIX65 readout compatible sensors were also included in this layout with all relevant small pitch dimensions:  $50\times 50$ ,  $25\times 100\text{-}2\text{E}$ , and  $25\times 100\text{-}1\text{E } \mu\text{m}^2$ . One additional design  $50\times 50\text{-}2\text{E}$  fine pitch which is comparable to sub pixel domain,  $25\times 50 \mu\text{m}^2$  of  $25\times 100\text{-}2\text{E}$  fine pitch is included. This design relaxes adopting the critical bump-pad positioning as it can be seen from figure 6.33(b). Aside, the direct comparison that could be made between  $50\times 50\text{-}2\text{E}$  and  $25\times 100\text{-}2\text{E}$  from geometrical dependence point of view,  $50\times 50\text{-}2\text{E}$  should come with lower capacitance because of having the shorter interconnecting metal used within the pixel's junction columns. There are also 12 tiles of R4S (ROC4Sens) readout (see, section 3.4.2) compatible sensors which keeps  $50 \mu\text{m}$  by  $50 \mu\text{m}$  staggered bump pad positioning. These sensors include all small-pitch pixel dimensions recommended from RD53A collaboration. As an example the most critical design of  $25\times 100\text{-}2\text{E } \mu\text{m}^2$  small pitch shown in figure 6.33(c) owns the distance between bump-pad and  $p^+$ -column largely safe at  $2.5 \mu\text{m}$ .

There are three NA62 readout compliant large sensors included within this layout with different inter-electrode distances:  $30 \mu\text{m}$ ,  $40 \mu\text{m}$  and  $50 \mu\text{m}$ . The motivation of these sensors' inclusion is to exploit ultra-fast silicon detector (UFSD) which establish a new paradigm for space-time particle tracking point. One possible use of timing resolution, if it could be made fast enough, would be in small-angle, far-forward detectors at colliders where relative timing of the two scattered particles could locate their vertex position among several possible vertices. The arrangement would

be more like that at fixed-target experiments than at colliders and could allow for multiple, small-area detectors run at a lower temperature than that of the central detectors. Giga-tracker readout [161] using in NA62 experiment is of 250nm CMOS technology having 10fC/pitch limit with time response <200ps. The state of art 3D silicon sensors aimed to be used in time resolution field reported the time response at 31ps owing hexagonal pitch of inter-electrode distance (L) 50  $\mu\text{m}$  only [162]. The electrostatic characteristics of two trench-electrode pitches (figure 6.34 (a)) having trench to electrode distance 50  $\mu\text{m}$  were studied using quasi-stationary TCAD simulation: hexagonal (left) and square (right). A 2D cut of electric field distribution of the simulation domain, indicated (insets of figure 6.34 (a)) reports that the electric field distribution to the corner edge of p-type trench for hexagonal pitch is relatively more uniform than square one, as they can be seen in figure 6.34(b). This has been the motivation to include the cluster alike NA62 compliant 3D sensor design at upcoming 2<sup>nd</sup> production at FBK. As an example, a NA62 compliant 3D sensor having inter-electrode distance 30  $\mu\text{m}$  could be seen in figure 6.32(c). 100  $\mu\text{m}$  wide slim edge was kept for pixelated sensors. The release of this production is expected to be in July 2017.

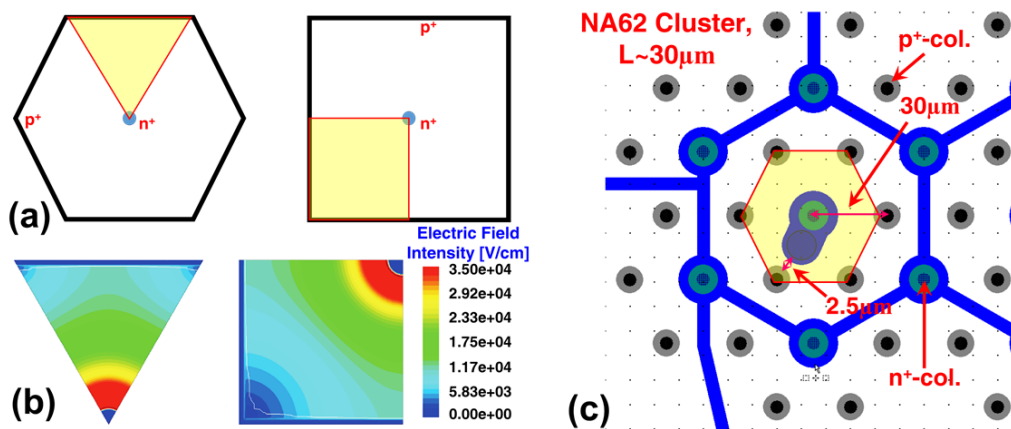


**Figure 6.34:** (a) Trench-electrode pitch geometries: hexagonal (left) and square (right). Simulation domain for quasi-electrostatic characteristics is notified with yellow marked regions. (b) 2D cut of electric field distribution on simulation domain.

A sufficient quantity of strip sensors of small pitch design:  $50 \times 50$ ,  $25 \times 100$ -2E, and  $25 \times 100$ -1E  $\mu\text{m}^2$  aside the conventional  $80 \times 80$ -1E  $\mu\text{m}^2$  pitch were included into this layout but with an inclusion of DC Fan-in. First production of 3D Si-Si DWB at FBK probing pad integrated inside the slim-edge, that restricted to keep the  $80 \mu\text{m} \times 40 \mu\text{m}$  pad with passivation opening of  $70 \mu\text{m} \times 30 \mu\text{m}$  while the inter-pad distance were limited to 10  $\mu\text{m}$  for all small pitch strips. Such design constraint made the yield of consecutive wire bonding on pads very challenging since the least wedge needle width remained 50  $\mu\text{m}$  available within the collaborators. A DC Fan-in design included within the batch to relax such constraint while it will certainly bring a larger capacitance because of having longer metal used to connect the Fan-in pads to strip at active region. Figure 6.35 (a) shows the layout schematic of this design, where the pad size

was enlarged to  $120\mu\text{m}\times 60\mu\text{m}$  pad with passivation opening of  $110\mu\text{m}\times 55\mu\text{m}$  keeping the inter-pad distance as of  $20\mu\text{m}$ . Several kinds of 3D test diodes were included representing each diverse pixelated sensor included within this layout. Conventional MOS planar test structures are there as well to estimate the oxide charge density in order to qualitatively quantify the surface condition of the sensor.

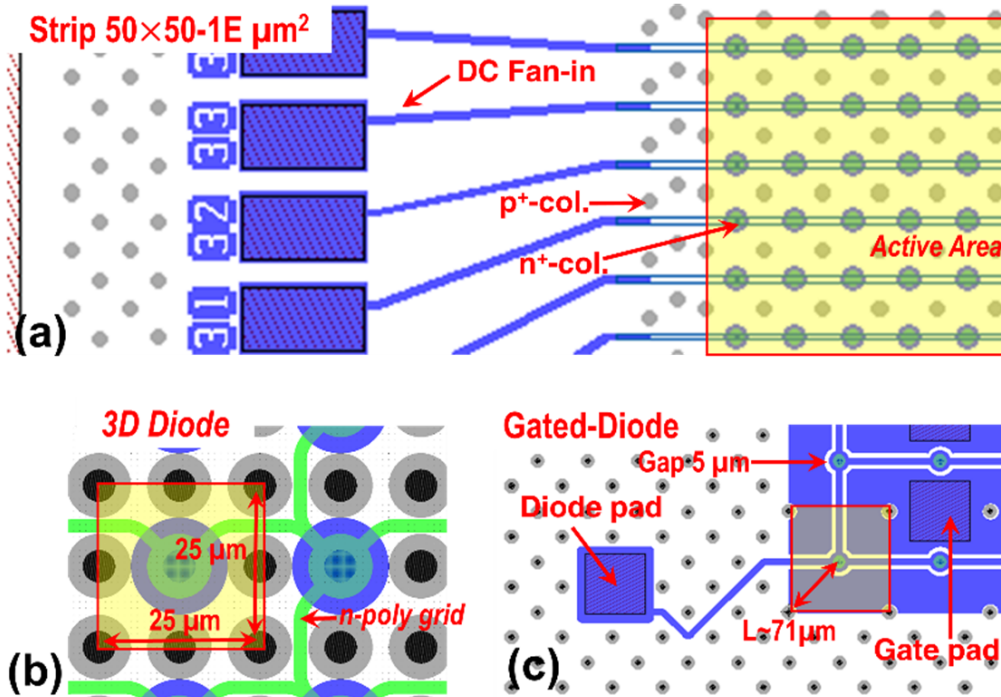


**Figure 6.35:** (a) Layout schematic of  $50\times 50\ \mu\text{m}^2$  fine pitch strip sensor. (b) 3D diode of multiplication of  $25\times 25\ \mu\text{m}^2$  pixel having n-poly grid within the active area. (c) Layout schematic of a full 3D gated diode of  $100\times 100\ \mu\text{m}^2$  pixel.

Several 3D diode types also came with n-poly grid diversity instead of the conventional metal grid. This choice can allow for very dense column designs like the one shown in figure 6.35(b). Moreover, LASER induced position resolved measurement made on small-pitch 3D diodes suggested that many photon reflects back while they are incident on metal, as the shadow image of metal shown in figure 6.16(b), whereas with poly-Si a larger portion of the devices could be explored. A full 3D gated-diode test structure of inter-electrode distance of  $\sim 71\ \mu\text{m}$  was included to estimate the surface generation current as it is shown in figure 6.35(c). Though the oxide charge density through C-V measurements made on MOS like test structure provide the rough estimation on the process induced surface quality of the devices (as it was  $\sim 10^{10}\ \text{cm}^2$  in 3DSS-6 production), the gated diode is another classical test structure where the gate MOS remains enclosed by circumfered diode area. This allows the surface generation velocity,  $S_0$ , to be evaluated from DC measurements on this structure where the diode lateral boundary conditions can be defined externally through voltage sweeping in the gate. A first FBK thin planar production on Si-Si DWB wafer was completed at the end 2014 [163], where the  $S_0$  measured on planar gated diodes was  $4\pm 0.5\ \text{cm/s}$ . Since the adopted 3D technology does not allow

for planar implanted regions to be implemented, a “semi 3D” gated diode structure was conceived and included in the first batch. Basically, the diode is made by junction columns, whereas the gate is made with a metal pad in between. A detail of the layout is shown in Fig. 6.36(b). The structure was shown to be qualitatively functional: as can be seen from Fig. 6.36(a), the three-regions gated diode I-V behavior is indeed observed.

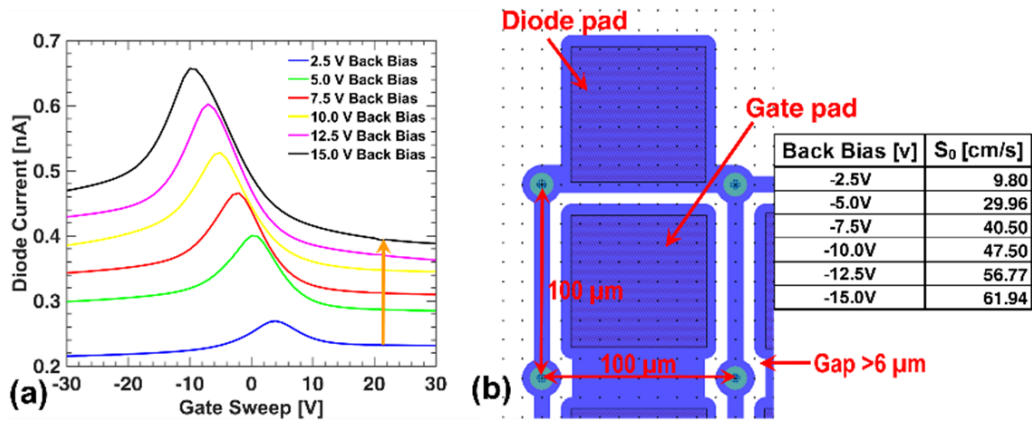


**Figure 6.36:** (a) Diode current as a function of gate voltage at different reverse bias conditions. (b) Layout schematic of a “semi 3D” gated diode. Upper right inset is showing the calculated surface generation rate,  $S_0$ .

In accumulation condition of the MOS gate, the leakage current of the diode metallurgical junction ( $I_j$ ) is collected mainly. At this stage the sweeping of the gate voltage toward depletion introduce a sharp increase in diode current ( $I_d$ ). The bulk ( $I_g$ ) and surface ( $I_s$ ) generation currents start originating from underneath the gate and are being added up to the diode current. A further decrement of the gate voltage results in a small increase of diode current ( $I_d$ ) because the depletion volume under the gate increases. Eventually there will be a sharp drop in diode current as soon as the inversion condition appears. This can be anticipated through the screening of the surface states made at the inversion layer. Beyond the strong-inversion threshold, the gated-diode current remains almost constant since the gate depletion region width reaches its maximum value. In this condition, the current difference between the peak current of depletion condition and the steady current of strong inversion region defines the quantity of surface generation current only [164].

However, it should be mentioned that having available only one metal layer, a gap ( $\sim 5 \mu\text{m}$ , see Fig. 6.36(b)) exists between the gate region and the junction column, making the collection of the surface generated current by the diode not straightforward. In the considered technology, the presence of the p-spray layer at the surface further hinders the gated diode operation, making the electron transport to the gate only possible by diffusion and punch-through rather than by drift in a surface channel. This is the reason why the values of the surface generation velocity extracted from the semi 3D gated diode show a strong reverse bias dependence. In addition, the values are

not so accurate because no guard ring shields the active area from collecting charge from the device periphery.

For these reasons, an improved design of gated diodes, both semi 3D and fully 3D, was conceived and implemented in the second batch, with reduced gaps, different gate widths and proper guard fences.

# Chapter VII

## Conclusions

This Ph.D. dissertation has reported on the development of small-pitch and thin 3D radiation sensors in an aim to be deployed into the foreseen Inner Tracker (ITk) upgrade of the ATLAS Experiment at the High Luminosity LHC (HL-LHC). This research work spans characterizing the state of art IBL 3D sensors to the development of this newer design and its post experimental validation from the simulated predictions with critical analysis through necessary irradiation campaigns. The University of New Mexico, USA, INFN-Genova, Italy and the University of Freiburg, Germany have been the main collaborators to the scope of this thesis activities.

As far as the design constraints of the newer 3D radiation sensors are concerned, the devices have to be radiation hard up to an integrated luminosity of 3000 fb<sup>-1</sup> in the foreseen upgrades at HL-LHC by 2024. Taking into account all possible challenges, the sensors' design is restricted to very dense pixel granularity (50×50 or 25×100 μm<sup>2</sup>), thin active region (~100 μm), narrower columnar electrodes (~5μm diameter) with reduced inter-electrode spacing (~30 μm), and very slim edges (~100 μm).

At the very beginning of this thesis work, FBK offered two different approaches of double-side processed sensor designs: state of art IBL design and modified junction column non-passing-through technology. The typical breakdown voltage for 3D sensors fabricated at FBK for the IBL ranged from 40 V to 60 V before irradiation and the full depletion voltage was limited to 10 V only. Considering the non-irradiated condition, the bias operating seemed quite sufficient for the long run whereas the situation becomes more complex after irradiation. Both the breakdown voltage and the full depletion voltage increase but of course, they remain dependent upon several aspects: structure diversity, irradiation scenarios, and annealing conditions. Such 3D sensors were irradiated up to the foreseen HL-LHC integrated fluences,  $2 \times 10^{16}$  1-MeV n<sub>eq</sub>.cm<sup>-2</sup> where the full depletion voltage was not even possible to be observed till its increased breakdown voltage around 200V. The radiation-induced oxide charge build-up within this design is not symmetric on both sensor sides of the sensors, that led devices to experience higher electric field intensity at the junction columns at back side because of having lower oxide charge density there and the consequent earlier onset of breakdown. In order to cope with these issues, FBK adopted a modified approach in the DTC5 batch, by shortening the n<sup>+</sup>-column depth but maintaining the ohmic columns passing through. Of course, this choice came with an expense of a slightly larger full depletion voltage due to the n<sup>+</sup>-column tip to back side vertical depletion. However, sensors from DTC5 batch reported intrinsic breakdown voltage up to 130 V. Several irradiations at different facilities were performed in order to study the radiation

tolerance of both these designs: X-ray irradiation was made in INFN LNL, Italy,  $\gamma$ -ray campaign was made in Sandia Gamma Irradiation Facility, USA, Neutron irradiations were performed at Jozef Stefan Institute, Slovenia, and Sandia BeO-UO<sub>2</sub> based reactor, USA and dedicated proton campaigns were made in KIT, Germany and LANSCE, USA. From the surface damage study, as it could be retrieved from X-ray and  $\gamma$ -ray results, IBL generations sensors showed clear enhancement on the breakdown from the increasing oxide charge density and the consequent p-spray depletion. Modified DTC5 instead were deviating the trend since the junction column tip effect became more pronounced as the cause of device breakdown. For neutron irradiation of the sensors of IBL generation, minor increase of  $V_{bd}$  as around  $\sim 10V$  is observed as the fluence is increased in comparison to X-ray campaign: in fact, in spite of the relatively larger TID involved on both sensor sides, the lower fractional hole yield and the self-annealing effects due to the temperature increase during irradiation caused this smaller breakdown shift. For proton irradiation campaign made on the IBL generation sensors, the breakdown voltage was reported to be  $\sim 200 V$  for the highest fluence  $5.5 \times 10^{15} \text{ n}_{eq}/\text{cm}^2$ . Irrespectively from surface damage, the breakdown voltage in DTC5 devices was reported in the range (200-250) V for both proton and neutron irradiated samples up to  $1 \times 10^{16} \text{ n}_{eq}/\text{cm}^2$ , which had been still higher in comparative investigations. Such findings gave a clear inset choice to adopt the modified junction column non-passing through technology for the future design by optimizing the inter-electrode distance in the range of 30-40  $\mu\text{m}$ .

FBK upgraded its fabrication line from 4-inch (100-mm) to 6-inch (150-mm) diameter wafers since 2014 and thus, a pilot production of modified DDTC 3D Si sensors was made in order to check possible process problems for 3D sensors. Double-sided processing technique conventionally used at FBK for 3D sensors production on relatively thin 6-inch substrates (without a support wafer) became a challenging constraint in this batch because of several mechanical issues (compatibility with processing equipment, fragility) involved even though the increased area available on wafer ( $\sim 2\times$ ) brought an advantageous feature for the foreseen production for HL-LHC. Due to the limiting options available during wafers procurement, a relatively thick (275  $\mu\text{m}$ ) substrate had been chosen. Several optimization studies were required in the processing line while keeping the junction column depth-width aspect ratio the same as in the IBL generation. A little increase in ohmic column opening, 13  $\mu\text{m}$ , was considered in an aim to etch down the entire substrate thickness. An enhanced mechanical protection of the wafer edges used into this pilot production simplified the process complexity by not using additional sacrificial layer alike earlier 4-inch production. Poly-Si partial filling in columns was adopted in this batch enabling the metal contacts to be directly placed over the poly-Si, without employing any additional dedicated masks. However, considering a first attempt on 6-inch 3D production, this batch faced several anomalies. A modified DRIE process recipe used in this batch came with a longer etching time (required for deeper ohmic

column formation) that created defects due to the local collapse of photoresist mask and/or of protective polymer. The probability of such a failure have a strong dependence of sensor size that made almost all the large-size pixelated sensors non-functional. Interestingly, the functional sensors of this production reported an intrinsic breakdown voltage of  $\sim 200\text{V}$  and the full depletion voltage at less than  $10\text{ V}$ . After  $\gamma$ -ray campaign made at Sandia, the breakdown voltage was shown to exceed  $250\text{ V}$  at  $500\text{ Mrad}$ , a dose similar to that expected at HL-LHC upgrades. This result confirmed that the modified junction column partial passing through design is capable of ensuring better radiation tolerance after large radiation fluences.

The fabrication of the first batch of the ultimate new thin, fine-pitch 3D sensors was completed at FBK in early 2016 through single-sided processing. Extensive characterizations of sensors and test structures have been made. As expected from TCAD simulation, thin and small-pitch sensors show an intrinsic breakdown voltage around  $160\text{V}$  while the full depletion remains at  $\sim 2\text{V}$  only. The very short inter-electrode distance ( $\sim 30\ \mu\text{m}$ ) allows charge trapping effects to be mitigated, making these sensors radiation hard and possibly getting benefit from the onset of impact ionization to boost the signal. But charge multiplication effects could also lead instead to increased leakage current and premature electrical breakdown. Incorporating advanced radiation damage models into TCAD simulation, a mean signal efficiency (as an average over different particle hit points over pixelated sensors) of up to  $70\%$  was obtained at the target fluence of  $2 \times 10^{16}\text{ n}_{\text{eq. cm}^{-2}}$ . To validate these expectations, a thorough experimental study is obviously required on the highly irradiated devices. In this context, several strip sensors, 3D diodes of RD53A recommended fine pitches, alike smaller arrays of basic 3D cells with all columns of the same doping type shorted together so as to obtain 2-electrode device were used. Dedicated campaigns were made with different irradiating particles at different facilities to get a clear picture of the device performance driven by the effect of both surface and bulk damage: i) X-ray at the Rutherford Appleton Laboratory, UK; ii)  $\gamma$ -ray irradiation at the Sandia Gamma Irradiation Facility (Albuquerque, USA); iii) Neutron irradiations at TRIGA Mark II reactor at JSI (Ljubljana, Slovenia) and at the Sandia Annular Core Research Reactor (Albuquerque, USA); iv)  $800\text{ MeV}$  protons at LANSCE (Los Alamos, USA) and  $24\text{ GeV/c}$  Proton in CERN Proton Synchrotron (PS) beam. Several strip sensors of different fine pitches were X-ray irradiated with  $5\text{ Mrad(Si)}$  and  $50\text{ Mrad(Si)}$ . In both cases, surface generated current from introduced interface traps increases the leakage proportionally to the TIDs applied while keeping the breakdown voltage similar to the pre-irradiation condition. This confirmed the breakdown being mainly controlled by the junction column tip's electric field intensity. It was also found that the inter-strip resistance at the largest TID remained in the range of  $\text{G}\Omega$ , which confirms the effectiveness of the p-spray layer in ensuring surface isolation even for extreme surface damage. These results were also confirmed by testing several 3D diodes and planar test structures irradiated with  $\gamma$ -rays. Samples irradiated with neutrons from JSI

facility reported the breakdown voltage enhancement in dependence of higher fluence up to  $1 \times 10^{16} \text{ n}_{\text{eq}} \text{ cm}^{-2}$  and so as of the inter-electrode distances present on geometry diversities. The corresponding increase in full depletion voltage from non-irradiated condition has been observed in dependence of the irradiation fluence and geometrical diversity of fine pitches. At the highest fluences, the devices experience the onset of impact ionization effects as estimated from the higher current damage rate  $\alpha$ , (greater than  $(4-5) \times 10^{16} \text{ A/cm}$ ) by having a precise temperature dependant leakage current density measurement. Proton irradiation campaigns were made at two different facilities with several 3D diodes, strip sensors, and planar test structures. Strip sensors irradiated with 24GeV proton at CERN facility exhibit a significant breakdown voltage improvement up to  $\sim 350\text{V}$  at  $1 \times 10^{16} \text{ n}_{\text{eq}} \text{ cm}^{-2}$  fluence. However, the samples irradiated at  $2 \times 10^{16} \text{ n}_{\text{eq}} \text{ cm}^{-2}$  show larger impact ionization effects, which have been estimated from the larger leakage current density reported and would have led to an earlier breakdown ( $\sim 150 \text{ V}$ ) by the large electric field induced by the increased effective doping concentration. Some test structures were proton irradiated in LANCSE up to an extreme  $3.5 \times 10^{16} \text{ n}_{\text{eq}}/\text{cm}^2$  fluence (corresponding to  $\sim 1.5 \text{ Grad (Si)}$  equivalent dose), showing a breakdown voltage of  $\sim 200\text{V}$ . More insight into these phenomena should be gained by measuring a statistically significant sample and studying the temperature dependence of the current. Although there are still several measurements to be performed, in particular, charge collection efficiency tests for irradiated samples and annealing studies, HL-LHC compliant 3DSS first production at FBK came with good electrical yield. Charge collection efficiency measured for non-irradiated  $25 \times 100 \mu\text{m}^2$  fine sensors through test-beam and  $\beta$ -source demonstrate that they reach the expected charge saturation limit ( $\sim 8.7 \text{ ke}^-$ ) at full depletion condition of 2V only.

Having summarized the main results, it can be concluded that this thesis got the scope in acute but systematic analysis upon the FBK sensors productions of state of art IBL generation, modified junction column non-passing-through design at both 4-inch and 6-inch double-sided process and as the entitled, newer small-pitch and thin 3D sensors of single sided process within the limited time constraint. Measurements reported here for sensors show good agreement with TCAD simulation predictions in respect to both electrical and functional point of view. Even at the largest fluence taken into account for either neutron or proton irradiation campaign for the newer design, the per column capacitance reports few 10s of fF only and the leakage current density remains well below 10nA at full depletion, that satisfies the target values set from the RD53 collaboration.

Hereby, I would like to take the opportunity to make the special mentions of Prof. Sally Seidel and Dr. Martin Hoferkamp, UNM, USA for taking care of all relevant  $\gamma$ -ray, neutron and proton irradiation campaigns at SANDIA and LANSCE, Prof. Vladimir Cindro, JSI, Slovenia for his warmth dedication on neutron irradiation, Dr. Federico Ravotti for his generosity at CERN 24GeV/c proton campaign and Dr. John Matheson, RAL, UK for his overwhelming help to X-ray irradiation campaign.

Nevertheless, I would like to acknowledge the funding bodies without whom this project would possibly remain as yet to resume. European Union's Horizon 2020 Research and Innovation program under Grant Agreement no. 654168 supported this work. The Ph.D. grant also received financial assistance from Autonomous Province of Trento through the Project MEMS3, and by the Italian National Institute for Nuclear Physics (INFN) through Projects ATLAS, CMS, and RD-FASE2 (CSN1).

## *References*

- [1] G.F. Knoll, *Radiation Detection and Measurement*, 3rd Edition, J. Wiley & Sons, New York, 2000.
- [2] G. Lutz, *Semiconductor radiation detectors – Device Physics*, Springer-Verlag Berlin Heidelberg, 2007.
- [3] J. Kemmer, *Fabrication of Low Noise Silicon Radiation Detectors by the Planar Process*, Nuclear Instruments and Methods in Physics Research A, 1980, 169 (499–502).
- [4] S. I. Parker, et al., *3D - A proposed new architecture for solid-state silicon detectors*, Nuclear Instruments and Methods in Physics Research A, 1997, 395(328-343).
- [5] A. H. Seidel, *Handbook of Radiation Effect*, Oxford University Press 2002.
- [6] F. Hartmann, "Evolution of Silicon Sensor Technology in Particle Physics", Springer Tracts in Modern Physics, Springer-Verlag Berlin Heidelberg, 2009, Volume 231
- [7] H. Spieler, "Semiconductor Detector Systems", Oxford University Press 2005.
- [8] P. P. Altermatt, et al., *The influence of a new band gap narrowing model on measurements of the intrinsic carrier density in crystalline silicon*, International Photovoltaic Science and Engineering Conference, Sapporo, 1999.
- [9] L. Rossi, et al., *Pixel Detectors From Fundamentals to Applications*, Springer, 2006.
- [10] L. Landau, *On the energy loss of fast particles by ionization*, Journal of Physics, 1944, 8(201-205).
- [11] R. Wunstorf, *Radiation Damage in Silicon Detectors Caused by Hadronic and Electromagnetic Irradiation*, Nuclear Instruments and Methods in Physics Research A, 1996, 377(290-297).
- [12] E. Fretwurst, *Radiation damage in silicon detectors*, Nuclear Instruments and Methods in Physics Research A, 2003, 512(30-43).
- [13] M. Huhtinen, *Simulation of non-ionising energy loss and defect formation in silicon*, Nuclear Instruments and Methods in Physics Research A, 2002, 491(194-215).

- [14] M. Moll, *Radiation Damage in Silicon Particle Detectors - microscopic defects and macroscopic properties*, PhD thesis, DESY-THESIS-1999-040, Universität Hamburg, 1999.
- [15] G. Aad, et al., *ATLAS Pixel Detector Electronics and Sensors*, Journal of Instrumentation, 2008, 3(P07007).
- [16] C. Piemonte, *Device simulations of isolation techniques for silicon microstrip detectors made on p-type substrates*, IEEE Transactions on Nuclear Science, 2006, 53 (3).
- [17] G. Lutz, et al., *Stripping detector*, Patent Application Laws OS 19620081 A1 21.11.97, Germany, 1997.
- [18] G. Lindström, et al., *Radiation hard silicon detectors - developments by the RD48 (ROSE) collaboration*, Nuclear Instruments and Methods In Physics Research A, 2001, 466(308-326).
- [19] V. A. Wright, et al., *3-D Medipix: A new generation of X-ray detectors*, Nuclear Instruments and Methods In Physics Research A, 2005, 546(319-323).
- [20] M. Da Rold, et al., *Study of breakdown effects in silicon multiguard structures*, IEEE Transaction of Nuclear Science, 1999, 46(1215-1223).
- [21] S. I. Parker, et al., *Results from 3-D silicon sensors with wall electrodes: near-cell-edge sensitivity measurements as a preview of active-edge sensors*, IEEE Transaction of Nuclear Science, 2001, 48(2405-2410).
- [22] G.F. Dalla Betta, et al., *Development of Active and Slim Edge Terminations for 3D and Planar Detectors*, Nuclear Science Symposium Conference Record, 2011, N25-4.
- [23] A. A. Ayón, et al., *Deep reactive ion etching: a promising technology for micro- and nanosatellites*, Smart Materials and Structures, 2001, 10 (1135-1144).
- [24] C.J. Kenney, et al., *Silicon detectors with 3-D electrode arrays: fabrication and initial test results*, IEEE Transaction of Nuclear Science, 1999, 46 (1224-1236).
- [25] C. Piemonte, et al., *Development of 3D detectors featuring columnar electrodes of the same doping type*, Nuclear Instruments and Methods in Physics Research A, 2005, 541(441-448).
- [26] S. Eränen, et al., *Silicon semi 3D radiation detectors*, IEEE Nuclear Science Symposium Conference Record, 2004, N28-3.

- [27] Z. Li, et al., *Development, simulation and processing of new 3D Si detectors*, Nuclear Instruments and Methods in Physics Research A, 2007, 583(139-148).
- [28] T. Grönlund, et al., *Full 3D simulations of BNL one-sided silicon 3D detectors and comparisons with other types of 3D detectors*, Nuclear Instruments and Methods in Physics Research A, 2008, 586(180-189).
- [29] G. F. Dalla Betta, et al., *New developments on 3D detectors at IRST*, IEEE Nuclear Science Symposium Conference Record, 2007, Conference Record, N18-3.
- [30] C. Fleta, et al., *Simulation and test of novel 3D silicon radiation detectors*, Nuclear Instruments and Methods in Physics Research A, 2007, 579(642-647).
- [31] Z. Li, et al., *Development of new 3D Si detectors at BNL and CNM*, IEEE Nuclear Science Symposium Conference Record, 2006, N34-5.
- [32] A. Zoboli, et al., *Double-Sided, Double-Type-Column 3D detectors at FBK: Design, Fabrication and Technology Evaluation*, IEEE Transaction of Nuclear Science, 2008, 55(2775-2784).
- [32] G. Giacomini, et al., *Development of double-sided full-passing-column 3D Sensors at FBK*, IEEE Transaction of Nuclear Science, 2013, 60(2357-2366).
- [33] M. Povoli, et al., *Layout and Process Improvements to Double-Sided Silicon 3D Detectors Fabricated at FBK*, IEEE Nuclear Science Symposium Conference Record, 2012, N14-204.
- [34] C.J. Kenney, et al., *Observation of Beta and X rays with 3-D architecture silicon microstrip detectors*, IEEE Transaction of Nuclear Science, 2001, 48(189-193).
- [35] S. I. Parker, C. J. Kenney, *Performance of 3-D architecture silicon sensors after intense proton irradiation*, IEEE Transaction of Nuclear Science, 2001, 48(1629-1638).
- [36] J.E. Metcalfe, et al., *Capacitance simulations and measurements of 3D pixel sensors under 55 MeV proton exposure*, IEEE Transaction of Nuclear Science, 2008, 55(2679-2684).
- [37] C. J. Kenney, et al., *Use of active-edge silicon detectors as X-ray microbeam monitors*, Nuclear Instruments and Methods in Physics Research A, 2007, 582(178-181).
- [38] C. Da Via, et al., *Advances in silicon detectors for particle tracking in extreme radiation environments*, Nuclear Instruments and Methods in Physics Research A, 2003, 509(86-91).

- [39] J. Morse, et al., *The spatial and energy response of a 3d architecture silicon detector measured with a synchrotron X-ray microbeam*, Nuclear Instruments and Methods in Physics Research A, 2004, 524(236-244).
- [40] A. Kok, et al., *3D detector – State of the art*, 13th International Workshop on Vertex Detectors (VERTEX), Italy, 2004.
- [41] C. Da Viá, et al., *Radiation hardness properties of full-3D active edge silicon sensors*, Nuclear Instruments and Methods in Physics Research A, 2008, 587(243-249).
- [42] C. Da Viá, et al., *3D active edge silicon sensors with different electrode configurations: radiation hardness and noise performance*, Nuclear Instruments and Methods in Physics Research A, 2009, 604(505-511).
- [43] M. Mathes, et al., *Test beam characterization of 3-D silicon pixel detectors*, IEEE Transaction of Nuclear Science, 2008, 55(3731-3735).
- [44] O. M. Røhne, *Edge characterization of 3D silicon sensors after bump-bonding with the ATLAS pixel readout chip*, IEEE Nuclear Science Symposium Conference Record, Germany, 2008, N27-8.
- [45] A. Pozza, et al., *First electrical characterisation of 3D detectors with electrodes of the same doping type*, Nuclear Instruments and Methods in Physics Research A, 2007, 560(317-321).
- [46] C. Piemonte, et al., *Study of the signal formation in single-type-column 3D silicon detectors*, Nuclear Instruments and Methods in Physics Research A, 2007, 579(633-637).
- [47] G.-F. Dalla Betta, et al., *Development of 3D detectors at FBK-irst*, 16th Workshop on Vertex Detectors (Vertex), 2008.
- [48] S. Ronchin, et al., *Fabrication of 3D detectors with columnar electrodes of the same doping type*, Nuclear Instruments and Methods in Physics Research A, 2007, 573(224-227).
- [49] M. Zavrtanik, et al., *Position sensitive TCT evaluation of irradiated 3D-STC detectors*, IEEE Nuclear Science Symposium Conference Record, 2007, N24-150.
- [50] S. Eckert, et al., *Signal and charge collection efficiency of a p-type STC 3D-detector irradiated to sLHC-fluences, read out with 40MHz*, Nuclear Instruments and Methods in Physics Research A, 2007, 581(322-325).

- [51] S. Eränen, et al., *Silicon semi 3D radiation detectors*, IEEE Nuclear Science Symposium Conference Record, 2004, N28-3.
- [52] L. Tlustos, et al., *Characterisation of a semi 3-D sensor coupled to Medipix2*, Nuclear Instruments and Methods in Physics Research A, 2007, 580(897-901).
- [53] D. Pennicard, et al., *Simulation results from double-sided 3-D detectors*, IEEE Transaction of Nuclear Science, 2007, 54(1435-1443).
- [54] A. Zoboli, et al., *Laser and Beta Source setup characterization of p-on-n 3D-DDTC detectors fabricated at FBK-IRST*, Nuclear Instruments and Methods in Physics Research A, 2008, 604(238-241).
- [55] M. Koehler, et al., *Beam Test Measurements with Double-Sided 3D Silicon Strip Detectors on n-type Substrate*, IEEE Transaction of Nuclear Science, 2010, 57(2987-2994).
- [56] A. Zoboli, et al., *Functional characterization of 3D-DDTC detectors fabricated at FBK-irst*, IEEE Nuclear Science Symposium Conference Record, 2008, N34-4.
- [57] G. Kramberger, et al., *Annealing study of effective trapping times in silicon detectors*, Nuclear Instruments and Methods in Physics Research A, 2007, 571(608-611).
- [58] G. Giacomini, et al., *Simulations of 3D detectors*, 20th Workshop on Vertex Detectors (Vertex), 2012.
- [59] A. Zoboli, et al., *Initial results from 3D-DDTC detectors on p-type substrates*, Nuclear Instruments and Methods in Physics Research A, 2010, 612(521-524).
- [60] G.-F. Dalla Betta, et al., *Performance evaluation of 3D-DDTC detectors on p-type substrates*, Nuclear Instruments and Methods in Physics Research A, 2010, 624(459-464).
- [61] A. Zoboli, et al., *Characterization and modeling of signal dynamics in 3D-DDTC detectors*, Nuclear Instruments and Methods in Physics Research A, 2010, 617(605-607).
- [62] G.-F. Dalla Betta, et al., *Development of 3D-DDTC pixel detectors for the ATLAS upgrade*, Nuclear Instruments and Methods in Physics Research A, 2011, 638(15-23).
- [63] P. Grenier, et al., *Test beam results of 3D silicon pixel sensors for the ATLAS upgrade*, Nuclear Instruments and Methods in Physics Research A, 2011, 638(33-40).

- [64] La Rosa, et. al., *Characterization of proton irradiated 3D-DDTC pixel sensor prototypes fabricated at FBK*, Nuclear Instruments and Methods in Physics Research A, 2012, 681(25-33).
- [65] A. Micelli, et. al., *3D-FBK Pixel sensors: recent beam tests results with irradiated devices*, Nuclear Instruments and Methods in Physics Research A, 2011, 650(150-157).
- [66] G. Pellegrini, et al., *First double sided 3-D detectors fabricated at CNM-IMB*, Nuclear Instruments and Methods in Physics Research A, 2011, 592(38-43).
- [67] D. Pennicard, et al., *Design, simulation, production and initial characterisation of 3D silicon detectors*, Nuclear Instruments and Methods in Physics Research A, 2009, 598(67-70).
- [68] D. Pennicard, et al., *Charge sharing in double-sided 3D Medipix2 detectors*, Nuclear Instruments and Methods in Physics Research A, 2009, 604(412-415).
- [69] R. L. Bates, et al., *Charge collection studies and electrical measurements of heavily irradiated 3D double-sided sensors and comparison to planar strip detectors*, IEEE Transaction of Nuclear Science, 2011, 58(3370-3383).
- [70] M. Koehler, et al., *Comparative measurements of highly irradiated n-in-p and p-in-n 3D silicon strip detectors*, Nuclear Instruments and Methods in Physics Research A, 2011, 659(272-281).
- [71] C. Da Vià, et al., *Development, Testing and Industrialization of Full-3D Active-Edge and Modified-3D Silicon Radiation Pixel Sensors with Extreme Radiation Hardness. Results, Plans*, ATLAS Upgrade Document, 2007 (<http://cern.ch/atlas-highlumi-3dsensor>)
- [72] M. Capeans, et al., *ATLAS Insertable B-Layer Technical Design Report*, CERN LHCC-2010-013.
- [73] C. Da Via, et al., *3D Silicon Sensors: Design, Large area production and Quality Assurance for the ATLAS IBL Pixel Detector Upgrade*, Nuclear Instruments and Methods in Physics Research A, 2012, 694(321-330).
- [74] M. Garcia-Sciveres, et al., *The FE-I4 Pixel Readout Integrated Circuit*, Nuclear Instruments and Methods in Physics Research A, 2011, 636(155-159).
- [75] M. Povoli, et al., *Slim edges in double-sided silicon 3D detectors*, Journal of Instrumentation, 2012, 7(C01015).

- [76] J. Albert, et al. (The ATLAS IBL Collaboration), *Prototype ATLAS IBL modules using the FE-I4A front-end readout chip*, Journal of Instrumentation, 2012, 7(P11010).
- [77] C. Gemme, et al., *3D sensors for tracking detectors: present and future applications*, 22nd Workshop on Vertex Detectors (Vertex), 2014.
- [78] B. Mandelli, et al. (The ATLAS IBL Collaboration), *The Pixel Detector of the ATLAS Experiment for the Run 2 at the Large Hadron Collider*, Nuclear Instruments and Methods in Physics Research A, 2016, 273(1166-1172).
- [78] G.-F. Dalla Betta, et al., *3D silicon sensors: irradiation results*, 21st Workshop on Vertex Detectors (Vertex), 2013.
- [79] C. Da Via, et al., *3D active edge silicon sensors: device processing, yield and QA for the ATLAS-IBL production*, Nuclear Instruments and Methods in Physics Research A, 2013, 699(18-21).
- [81] M. Petasecca, et al., *Numerical Simulation of Radiation Damage Effects in p-Type and n-Type FZ Silicon Detectors*, IEEE Transaction of Nuclear Science, 2006, 53(2971-2976).
- [82] D. Pennicard, et al., *Simulation of radiation-damaged 3D detectors for the Super-LHC*, Nuclear Instruments and Methods in Physics Research A, 2008, 592(16-25).
- [83] ATLAS experiment at CERN, web-link: <http://atlas.web.cern.ch/Atlas/Collaboration/>
- [84] S. Grinstein, et al., *Beam test studies of 3D pixel sensors irradiated non-uniformly for the ATLAS forward physics detector*, Nuclear Instruments and Methods in Physics Research A, 2013, 730(28-32).
- [85] L. Tlustos, et al., *Signal variations in high-granularity Si pixel detectors*, IEEE Transaction of Nuclear Science, 2004, 51(3006-3012).
- [86] A. B. Rosenfeld, et al., *MOSFET dosimetry of an X-ray microbeam*, IEEE Transaction of Nuclear Science, 1999, 6(1774-1780).
- [87] M. F. Hawthorne, et al., *Frontiers in Neutron Capture Therapy*, Springer, New York, 2001.
- [88] D. S. McGregor, et al., *Present status of microstructured semiconductor neutron detectors*, Journal of Crystal Growth, 2013, 379(99-110).

- [89] K.-C. Huang, et al., *Scalable large-area solid-state neutron detector with continuous p-n junction and extremely low leakage current*, Nuclear Instruments and Methods in Physics Research A, 2014, 763(260–265).
- [90] L. Evans and P. Bryant, LHC Machines, Journal of Instrumentation, 2008, 3(S08001).
- [91] ATLAS website: <http://www.atlas.ch/>.
- [92] E. Abat, et al., The ATLAS TRT Barrel Detector, Journal of Instrumentation, 2008, 3(P02014).
- [93] P. Puzo, ATLAS Calorimetry, Nuclear Instruments and Methods in Physics Research A, 2002. 494 (340–345).
- [94] Sandro Palestini, The Muon Spectrometer of the ATLAS Experiment, ATLAS Note. 494 (340–345).
- [95] G. Aad, et al., ATLAS Pixel Detector Electronics and Sensors, Journal of Instrumentation, 2008, 3(P07007).
- [96] F. Hugging, et al., Front-End electronics and integration of ATLAS pixel modules, Nuclear Instruments and Methods in Physics Research A, 2005, 549(157-164).
- [97] Ivan Peric, et al., The FEI3 readout chip for the ATLAS pixel detector, Nuclear Instruments and Methods in Physics Research A, 2006, 565(178-187).
- [98] The ATLAS IBL Collaboration, Prototype ATLAS IBL modules using the FE-I4A frontend readout chip, Journal of Instrumentation, 2012, 7(P11010).
- [99] C. Goessling et al., Evaluation of the breakdown behavior of ATLAS silicon pixel sensors after partial guard-ring removal, Nuclear Instruments and Methods in Physics Research A, 2010, 624(410-413).
- [100] C. Da Via et al., Technical Specifications and Acceptance Criteria for the 3D Sensors of the ATLAS IBL, CERN EDMS Note ATU-SYS-QC-0004, 2011.
- [101] P. Grenier et al., Test beam results of 3D silicon pixel sensors for the ATLAS upgrade, Nuclear Instruments and Methods in Physics Research A, 2011, 638(33-40).
- [102] The FE-I4 Collaboration, The FE-I4B Integrated Circuit Guide, Version 2.3, 2012.
- [103] L. Caminada, Recent Developments of HEP Pixel Detector Readout Chips, Physics Procedia, 2012, 37 (1644 – 1653).
- [104] A. L. Rosa, The ATLAS Insertable B-Layer: from construction to operation, Journal of Instrumentation, 2016, 11(C12026).

- [105] Fedrico Faccio, Total Ionizing Dose effects in 130-nm commercial CMOS technologies for HEP experiments, Nuclear Instruments and Methods in Physics Research A, 2007, 582.
- [106] D M S Sultan, Calibration and Commissioning the Dose Rate of X-RAD iR160 for Semiconductor Devices, (communicating).
- [107] M. Backhaus, Characterization of the FE-I4B pixel readout chip production run for the ATLAS Insertable B-layer upgrade, Journal of Instrumentation, 2013, 8(C03013).
- [108] RD53 Collaboration, RD53A Integrated Circuit Specifications, CERN-RD53-PUB-15-001.
- [109] ATLAS Collaboration, Operation and performance of the ATLAS semiconductor tracker, CERN-PH-EP-2014-049.
- [110] F. Campabadal, et al., Design and performance of the ABCD3TA ASIC for readout of silicon strip detectors in the ATLAS semiconductor tracker, Nuclear Instruments and Methods in Physics Research A, 2005, 552(292-328).
- [111] E. Facordi, Status of the CMS Detector, Physics Procedia, 2012, 37(119 –127).
- [112] W. Erdmann, The CMS pixel detector, International Journal of Modern Physics A, 2010, 25(1315-1337).
- [113] A. Starodumov, High rate capability and radiation tolerance of the PROC600 readout chip for the CMS pixel detector, Journal of Instrumentation, 2017, 12(C01078).
- [114] M. Raymond, et al., The CMS Tracker APV25 0.25 mm CMOS Readout Chip, Proceedings of the 6<sup>th</sup> workshop on electronics for LHC experiments, Krakow, 2000.
- [115] D. Draga, et al., Characterization of the CBC2 readout ASIC for the CMS strip-tracker high-luminosity upgrade, Journal of Instrumentation, 2014, 9(C03001).
- [116] F. Gianotti et al., *Physics potential and experimental challenges of the LHC luminosity upgrade*, The European Physical Journal C - Particles and Fields, 2005, 39 (2005).
- [117] C. Da Vià, et. al., *The geometrical dependence of radiation hardness in planar and 3D silicon detectors*, Nuclear Instruments and Methods in Physics Research A, 2009, 603.

- [118] G. Lindström et al., *Radiation hardness of silicon detectors—A Challenge from High-Energy Physics*, Nuclear Instruments and Methods in Physics Research A, 1999, 426.
- [119] V. Eremin, et. al., *Analytical Model for 3D Detectors Parametrization*, Nuclear Instruments and Methods in Physics Research A, 2010, 612.
- [120] M. Povoli, et al., *Impact of the layout on the electrical characteristics of double-sided silicon 3D sensors fabricated at FBK*, Nuclear Instruments and Methods in Physics Research A, 2013, 699.
- [121] R. Dalal, et al., *Combined Effect of Bulk and Surface Damage on Strip Insulation Properties of Proton Irradiated  $n^+p$  Silicon Strip Sensors*, Journal of Instrumentation, 2014, 9(P04007).
- [122] D. Passeri et al., *Modeling of radiation damage effects in silicon detectors at high fluences HL-LHC with Sentaurus TCAD*, Nuclear Instruments and Methods in Physics Research A, 2016, 824.
- [123] S. Parker et al., *Proposed Triple-Wall, Voltage-Isolating Electrodes for Multiple-Bias-Voltage 3D Sensors*, Nuclear Instruments and Methods in Physics Research A, 2012, 685.
- [124] M. Koehler, *Double-sided 3D silicon detectors for the High-Luminosity LHC*, PhD Dissertation, Albert-Ludwigs-Universität Freiburg im Breisgau (Germany), 2011.
- [125] G.-F. Dalla Betta, et. al., *Radiation Hardness Tests of Double-Sided 3D Strip Sensors with Passing-through Columns*, Nuclear Instruments and Methods in Physics Research A, 2014, 765.
- [126] H.C. Kaestli, et. al., *Design and Performance of the CMS Pixel Detector Readout Chip*, Nuclear Instruments and Methods in Physics Research A, 2006, 565.
- [127] D. Bisello, et. al., *X-ray radiation source for total dose radiation studies*, Radiation Physics and Chemistry, 2004, 71.
- [128] G. Kramberger, *Signal development in irradiated silicon detectors*, PhD Dissertation, University of Ljubljana (Slovenia), 2001.
- [129] A. Dierlamm, *Signal development in irradiated silicon detectors*, PhD Dissertation, University of Karlsruhe (Germany), 2003.
- [130] P. Palni, et. al., *A Method for Real Time Monitoring of Charged Particle Beam Profile and Fluence*, Nuclear Instruments and Methods in Physics Research A, 2014, 735.

- [131] D. Campbell, et. al., *Frequency and temperature dependence of the depletion voltage from CV measurements for irradiated Si detectors*, Nuclear Instruments and Methods in Physics Research A, 2002, 492.
- [132] N. Bacchetta, et. al., *Improvement in breakdown characteristics with multiguard structures in microstrip silicon detectors for CMS*, Nuclear Instruments and Methods in Physics Research A, 2001, 461.
- [133] V. Cindro, et. al., *World irradiation facilities for silicon detectors*, 23<sup>rd</sup> International Workshop on Vertex Detectors (VERTEX), Czech Republic, 2014.
- [134] A. Chilingarov, et. al., *World irradiation facilities for silicon detectors*, Journal of Instrumentation, 2013, 8(P10003).
- [135] S. Wonsak, et. al., *Measurements of the reverse current of highly irradiated silicon sensors*, Nuclear Instruments and Methods in Physics Research A, 2015, 796.
- [136] I. Mandic, et. al., *Bulk damage in DMILL npn bipolar transistors caused by thermal neutrons versus protons and fast neutrons*, IEEE Transaction of Nuclear Science, 2004, 51(1752-1758).
- [137] A. Holmes-Siedle and L. Adams, *Handbook of radiation effects*, 2nd edition, Oxford University Press Inc., U.S.A., 2002.
- [138] G.-F. Dalla Betta, et. al., *Characterization of New FBK Double-Sided 3D Sensors with Improved Breakdown Voltage*, IEEE Nuclear Science Symposium Conference Record, 2013, N41-1.
- [139] G. Lindström, et. al., *Radiation hardness of silicon detectors: A challenge from high-energy physics*, Nuclear Instruments and Methods in Physics Research A, 1999, 426.
- [140] R. Wunstorf, et. al., *Damage-induced surface effects in silicon detectors*, Nuclear Instruments and Methods in Physics Research A, 1996, 377.
- [141] J. Zhang, *X-ray Radiation Damage Studies and Design of a Silicon Pixel Sensor for Science at the XFEL*, PhD Dissertation, University of Hamburg (Germany), 2013.
- [142] T.R. Oldham, et. al., *Total Ionizing Dose effects in MOS oxides and devices*, IEEE Transaction of Nuclear Science, 2003, 50(483-499).
- [143] SEMI Standards, <http://www.semi.org/en/>

- [144] E. Vianello, et. al., *Optimization of double-side 3D detector technology for first productions at FBK*, IEEE Nuclear Science Symposium Conference Record, 2011, N10-6.
- [145] G.S. May, C.J. Spanos, *Fundamentals of semiconductor manufacturing and process control*, Wiley Interscience (2006).
- [146] D. M. S. Sultan, et. al., *Characterization of the first double-sided 3D radiation sensors fabricated at FBK on 6-inch silicon wafers*, Journal of Instrumentation, 2015, 10(C12009).
- [147] G.-F. Dalla Betta, et. al., *Development of a new generation of 3D pixel sensors for HL-LHC*, Nuclear Instruments and Methods in Physics Research A, 2016, 386.
- [148] G.-F. Dalla Betta, et. al., *The INFN-FBK "Phase-2" R& D program*, Nuclear Instruments and Methods in Physics Research A, 2016, 388.
- [149] M. Garcia-Sciveres, S. Marconi, et al., *Development of pixel readout integrated circuits for extreme rate and radiation*, CERN-LHCC-2013-002.
- [150] G.-F. Dalla Betta, et. al., *Development of New 3D Pixel Sensors for Phase 2 Upgrades at LHC*, Nuclear Science Symposium Conference Record, 2015, N3C3-5.
- [151] F. Moscatelli, et. al., *Combined Bulk and Surface Radiation Damage Effects at Very High Fluences in Silicon Detectors: Measurements and TCAD Simulations*, IEEE Transaction of Nuclear Science, 2016, 63(2716-2723).
- [152] D. M. S. Sultan, et. al., *First production of new thin 3D sensors for HL-LHC at FBK*, Journal of Instrumentation, 2017, 12(C01022).
- [153] R. Hernandez, et. al., *A Portable Readout System for Microstrip Silicon Sensors (ALIBAVA)*, IEEE Transaction on Nuclear Science, 2009, 56.
- [154] S. Lochner, et al., *The Beetle Reference Manual*, 2006, CERN-LHCb-2005-105.
- [155] H. Bichsel, et al., *Straggling in thin silicon detectors*, Reviews of Modern Physics, 1988, 60 (663-699).
- [156] K. Chain, et al., *A MOSFET electron mobility model of wide temperature range (77–400 K) for IC simulation*, Semiconductor Science and Technology, 1997, 12 (355-358).
- [157] A. G. Sabnis, et al., *Characterization of the electron mobility in the inverter Si surface*, IEEE International Electron Devices Meeting, 1979, 18–21.

- [158] P. Greniers, et al., *Test Beam Results of 3D Silicon Pixel Sensors for the ATLAS upgrade*, Nuclear Instruments and Methods in Physics Research A, 2016, 9(18–21).
- [159] G.-F. Dalla Betta, et al., *3D Silicon Detectors*, Proceedings of Science, 2014, INFN Workshop on Future Detectors for HL-LHC (IFD2014).
- [160] E. Monteil, et al., *A prototype of a new generation readout ASIC in 65nm CMOS for pixel detectors at HL-LHC*, Journal of Instrumentation, 2016, 11(C12044).
- [161] F. Hahn, et al., *NA62 Technical Design Report*, CERN-NA62-10-07.
- [162] S. Parker, et al., *Increased Speed: 3D Silicon Sensors; Fast Current Amplifiers*, IEEE Transactions on Nuclear Science, Journal of Instrumentation, 2011, 58(404-417).
- [163] M. Meschini, et al., *The INFN-FBK pixel R&D program for HL-LHC*, Nuclear Instruments and Methods in Physics Research A, 2016, 831 (116-121).
- [164] G. Verzellesi, et al., *On the Accuracy of Generation Lifetime Measurement in High-Resistivity Silicon Using PN Gated Diodes*, IEEE Transactions on Electronic Devices, 1999, 46(817-820).
- [165] A. Longoni, et al., *Instability of the behaviour of high resistivity silicon detectors due to the presence of oxide charges*, Nuclear Instruments and Methods in Physics Research A, 1990, 288 (35-43).
- [166] M. Laakso, et al., *Field oxide radiation damage measurements in silicon strip detectors*, Nuclear Instruments and Methods in Physics Research A, 1993, 327 (517-522).
- [167] J. Baudot, et al., *First Test Results of MIMOSA-26, A Fast CMOS Sensor With Integrated Zero Suppression And Digitized Output*, IEEE Nuclear Science Symposium Conference Record (NSS/MIC), 2009, N22-6 (1169-1173).
- [168] V.P. Markevich, et al., *Formation of Radiation-induced Defects in Si Crystals Irradiated with Electrons at Elevated Temperatures*, Solid State Phenomena, 2010, 156-158 (299-304).
- [169] S. M. Sze, "Physics of Semiconductor Devices", New York Wiley, 1981, pp 90.
- [170] The ATLAS Collaboration, *ATLAS Phase-II Upgrade Scoping Document*, CERN-LHCC-2015-020.

- [171] N. Flaschel, et al., *Thermal and hydrodynamic studies for micro-channel cooling for large area silicon sensors in high energy physics experiments*, Nuclear Instruments and Methods in Physics Research A, 2017, 863 (26-34).